

UNIVERSIDAD AUTÓNOMA DE MADRID
FACULTAD DE CIENCIAS
Departamento de Ingeniería Química



**Degradación de contaminantes emergentes
usando materiales híbridos órgano-metálicos
(MOFs) mediante fotocatalisis**

**Degradation of emerging contaminants using
metal organic frameworks (MOFs) by
photocatalysis**

Tesis Doctoral

Virginia Muelas Ramos

Madrid, 2022

UNIVERSIDAD AUTÓNOMA DE MADRID
FACULTAD DE CIENCIAS
Departamento de Ingeniería Química



**Degradación de contaminantes emergentes
usando materiales híbridos órgano-metálicos
(MOFs) mediante fotocatalisis**

**Degradation of emerging contaminants using
metal organic frameworks (MOFs) by
photocatalysis**

MEMORIA

que para optar al grado de

Doctor con Mención Internacional

presenta

Virginia Muelas Ramos

Directores: Dra. Carolina Belver Coldeira

Dr. Jorge Bedia García-Matamoros

Madrid, 2022

Dra. Carolina Belver Coldeira, Profesor Contratado Doctor y Dr. Jorge Bedia García Matamoros, Profesor Contratado Doctor, ambos pertenecientes al Departamento de Ingeniería Química de la Universidad Autónoma de Madrid.

HACEN CONSTAR: que el presente trabajo, titulado “*Degradación de contaminantes emergentes usando materiales híbridos órgano-metálicos (MOFs) mediante fotocatalisis*”, presentado por Dña. Virginia Muelas Ramos, ha sido realizado bajo su dirección, en los laboratorios del Departamento de Ingeniería Química, en la Universidad Autónoma de Madrid y que, a su juicio, reúne los requisitos de originalidad y rigor científico necesarios para ser presentados como Tesis Doctoral.

Y, para que conste a efectos oportunos, firmamos el presente informe en Madrid a 25 de Julio de 2022.

Carolina Belver Coldeira

Jorge Bedia García Matamoros

La realización de este trabajo ha sido posible gracias al apoyo económico del Ministerio de Economía y Competitividad (MINECO) a través del proyecto CTQ2016-78576-R, a la Agencia Estatal de Investigación (AEI) por el proyecto PID2019-106186RB-I00/AEI/10.13039/501100011033 y a la concesión de un contrato de Formación de Personal Investigador (FPI) del MINECO (Referencia BES-2017- 082613).

Para mi nueva estrella en el firmamento, mi padre y mi “crunch”.

“La mayoría de la gente dice que el intelecto es lo que hace a un gran científico. Están equivocados: es el carácter.”

Albert Einstein

Table of contents

| | |
|---|------------|
| Summary/Resumen | i |
| Summary | iii |
| Resumen | ix |
| 1. Introduction | 1 |
| 1. Water purification by photocatalysis | 3 |
| 2. Metal organic frameworks | 11 |
| 2.1. Modification of MOFs | 18 |
| 2.1.1. Functionalization..... | 18 |
| 2.1.2. Deposition of metal nanoparticles..... | 21 |
| 2.1.3. Sensitization | 22 |
| 2.1.4. Combination with other semiconductors..... | 23 |
| 2.1.5. Metal doping | 26 |
| References..... | 28 |
| 2. Objectives | 47 |
| 3. Thermal post-treatments to enhance water stability of NH₂-MIL-125 (Ti) | 51 |
| 4. Degradation of diclofenac in water under LED irradiation using combined g-C₃N₄/NH₂-MIL-125 photocatalysts | 69 |
| 5. Synthesis of noble metal-decorated NH₂-MIL-125 titanium MOF for the photocatalytic degradation of acetaminophen under solar irradiation | 85 |
| 6. Solar photocatalytic degradation of emerging contaminants using NH₂-MIL-125 grafted by heterocycles | 99 |
| 7. Conclusions/Conclusiones | 113 |
| Conclusions..... | 115 |
| Conclusiones | 118 |
| 8. Appendix | 123 |
| 8.1. Appendix Chapter 3. Thermal post-treatments to enhance water stability of NH ₂ -MIL-125 (Ti)..... | 125 |
| 8.2. Appendix Chapter 5. Synthesis of noble metal-decorated NH ₂ -MIL-125 titanium MOF for the photocatalytic degradation of acetaminophen under solar irradiation | 129 |

| | |
|---|-----|
| 8.3. Appendix Chapter 6. Solar photocatalytic degradation of emerging contaminants using NH ₂ -MIL-125 grafted by heterocycles | 135 |
| Other publications | 142 |

SUMMARY/RESUMEN



Summary

The scarcity of quality water is a growing concern in current society. In addition to this problem, recently, a new group of water contaminants, which are not readily removed by conventional technologies, are being detected. These so-called emerging contaminants (ECs) include pharmaceuticals, personal care products, detergents, steroids, hormones, etc. These pollutants are observed in low concentrations and have several harmful effects on humans and the environment. Thus, different purification technologies are worldwide investigated and implemented in the field of water and wastewater treatment. Among them, advanced oxidation processes (AOPs) are being developed as an alternative to current conventional methods for the treatment of ECs. These processes are based on the generation of radical species with high oxidizing power, which allow the oxidation of pollutants until their complete mineralization. Photocatalysis is one of the AOPs and is considered a low-cost alternative because it takes place at ambient temperature and pressure. Solar photocatalysis is the most interesting option, as it allows the use of sunlight as clean energy, avoiding the use of expensive and energy-demanding lamps. In photocatalysis, semiconductor materials are excited by light absorption to produce electron-hole pairs, which are then separated and transferred to target compounds for redox reactions. Among the different semiconductor materials used, metal organic frameworks (MOFs) have gained attention due to their excellent semiconductor properties. Titanium-based MOFs, such as MIL-125, can be found in the literature for various applications, including water decontamination. Furthermore, this material allows the incorporation of amino groups in its organic linker, which improves the light absorption in the visible region and reduces the band gap.

Therefore, the main objective of this thesis has been the development of new photocatalysts based on $\text{NH}_2\text{-MIL-125(Ti)}$ and their use in the degradation of several ECs, namely acetaminophen, diclofenac,

sulfamethoxazole and antipyrine, using solar and LED irradiations. I have initially explored the stability of the MOF in water medium, which is critical for practical applications. Subsequently, different approaches were followed to enhance the photocatalytic performance, including noble metal nanoparticles deposition, coupling with another semiconductor and grafting of the amino linker. Thus, this doctoral Thesis is presented as a compendium of four publications in scientific journals, classified in the first and second quartiles of their corresponding areas.

The first work explored the stability of NH₂-MIL-125 in water. This study demonstrated that this material leached out significant amounts of the organic linker used during its synthesis, hence, different thermal treatments were applied to improve its stability in water. Initially, the thermal resistance of the MOF was analysed by thermogravimetry, and a strong weight loss is observed from 300 to 350 °C. For this reason, temperatures in the range of 150-300 °C were selected to perform the stabilization. Firstly, the MOF was subjected to a vacuum treatment at that temperature range for 16 h. The crystalline structure was maintained up to 250 °C, higher temperatures (i.e. 300 °C) resulted in an amorphous structure. The UV-vis spectra demonstrated that amino group was not affected by the thermal treatments. Once it was demonstrated that treated MOFs maintained their structure, their stability in water was tested. Although a reduction was achieved, the leachate percentage was still high, about 15% for the samples subjected to 200 and 250 °C. Thus, the MOF was also calcined in air atmosphere at the same range of temperatures. As in the case under vacuum, the MOF maintained its crystal structure up to 250 °C, but its stability was not so high as expected. Thus, additional samples were obtained at 250 °C increasing the calcination time up to 72 h. It should be noted that the treatment for 48 h enhanced the MOF stability, while higher times caused a considerable loss of crystallinity. This work established that NH₂-MIL-125 MOF can be purified and stabilized using

a thermal treatment in air atmosphere at 250 °C for 48 h, maintaining the MOF properties.

After the first work, different modifications were carried out to enhance the photoactivity of this MOF. The second work was possible thanks to an international stay at the University of Porto, Portugal. This modification was carried out combining NH₂-MIL-125 with graphitic carbon nitride (g-C₃N₄). Three photocatalysts were synthesized with different weight ratios of MOF:g-C₃N₄ (75:25, 50:50 and 25:75). XRD patterns showed the characteristic peaks of the crystal structures of both semiconductors, NH₂-MIL-125 and g-C₃N₄. The proportions of the g-C₃N₄ and MOF in hybrid materials were confirmed by elemental analysis. The UV-vis spectra corroborated the light absorption improvement of the hybrid photocatalysts in the visible light range with a red-shift of the adsorption edge. Photoluminescence spectra confirmed the synergistic effect between semiconductors, resulting in a higher inhibition of the electron-hole recombination in the hybrid photocatalysts. Once the photocatalysts were characterized, the photoactivity was checked under LED irradiation (384 nm) for the degradation of diclofenac as a model emerging contaminant in wastewater. All photocatalysts described a similar adsorption contribution, close to 20%. The 50:50 hybrid photocatalyst showed the best diclofenac degradation, achieving a complete conversion after 2 h of irradiation, with a pseudo-first-order rate constant value of 0.0282 min⁻¹, almost three-fold that obtained with NH₂-MIL-125 and more than four-fold that determined for g-C₃N₄. Regarding the radical trapping tests, superoxide radicals and holes seemed to have the major role, while hydroxyl radicals played a minor role in the degradation process. The valence band maximum of both photocatalysts was estimated from XPS. Thus, the conduction band position was also approximated, resulting in a plausible S-scheme photocatalytic mechanism. Finally, a degradation pathway identified some intermediate by-products, as well as short-chain carboxylic acids and further

mineralization products (H_2O , CO_2 and NO_2^-). From the reaction species identified, several routes were proposed for diclofenac degradation pathway, involving, hydroxylation, coupling and oxidation reactions.

The third work studied the incorporation of metal nanoparticles (platinum, palladium and silver) on the surface of $\text{NH}_2\text{-MIL-125}$ MOF. The decorated MOF were tested in the degradation of acetaminophen under simulated solar light. The structure of the MOF was not affected by the introduction of the metal nanoparticles. The photocatalysts with metals enhanced their response in the visible light but without modification of the band gap values. The comparison of the XPS surface values of each metal with the corresponding nominal bulk contents (1 wt.%) suggested an eggshell distribution for Ag and egg-yolk distribution for Pd, while Pt seemed more evenly distributed. On the other hand, the deconvoluted spectra of Ag 3d, Pd 3d and Pt 4f confirmed a higher proportion of electro deficient Pd and Pt, while verified the successful photoreduction of the Ag precursor. Metal nanoparticles appeared as discrete spherical particles with average sizes of 3.8, 3.4 and 1.8 nm for Ag, Pt and Pd, respectively. The introduction of the metal nanoparticles seems to produce a decrease in the recombination of electron and holes, which was confirmed by the improved photodegradation of the acetaminophen. The MOF with Pt showed the best results, achieving a complete degradation of the pollutant in less than 3 h of irradiation, with a pseudo-first-order rate constant value of 0.0165 min^{-1} . The experiments with scavengers suggested that superoxide radicals were the main reactive species involved in the degradation. The stability of this MOF was confirmed after three successive cycles of use, maintaining its activity, crystalline structure and morphology unchanged. Moreover, the degradation process was not affected by the presence of chlorides, nitrates and sulphates, studied as common inorganic ions in wastewaters. However, the presence of bicarbonates exhibited a negative effect in contaminant conversion, probably

due to the decrease of superoxide radicals since these inorganic ions can interact with them. Finally, some reactions intermediates were identified, resulting from coupling and ring opening of acetaminophen molecules. Further oxidation of those by-products gave rise to formic and acetic acids. The mineralization of these short-chain acids leads to the formation of H_2O , CO_2 , and NO_3^- .

The fourth study presented the grafting of the amino linker by the incorporation of different heterocyclic carboxaldehydes, named 2-pyridinecarboxaldehyde, 3-pyridinecarboxaldehyde, 4-pyridinecarboxaldehyde and quinoline-carboxaldehyde. Thermal treatments at 200 °C for 48 h under air atmosphere were used to reduce the ligand lixiviation. The crystalline structure of the original NH_2 -MIL-125 was maintained for all photocatalysts after grafting. Solid Nuclear Magnetic Resonance (NMR) spectra revealed the successful grafting of the organic ligand by a post-synthetic procedure due to the transformation of the C-NH_2 groups to C=N=C by a Schiff reaction. The grafted materials described a slightly lower surface area than the bare NH_2 -MIL-125, more evident for the quinoline-carboxaldehyde derived-MOF. The new heterocycles acted as an antenna favouring light absorption in the visible range and reducing the band gap values. The stability in water of all grafted-MOFs was confirmed analysing the ligand lixiviation, showing lower values than the bare NH_2 -MIL-125. The 3-pyridinecarboxaldehyde grafted sample resulted the best material for the photodegradation of acetaminophen in different water matrices, deionized water, tap water and synthetic water. This improvement was ascribed to differences in the steric arrangement of the heterocycle and to a better interfacial charge transfer, as suggested by the smaller arc radius of the semicircle in the Nyquist plot. Trapping experiments showed that superoxide radicals were again the main species involved in the photodegradation process. Moreover, the abatement of antipyrine and sulfamethoxazole was

SUMMARY/RESUMEN

tested, depending the photocatalytic performance on the nature of the target compound. Finally, the photoactivity of the MOF was analyzed in continuous flow regime, showing a remarkable constant performance, and reaching a total conversion of acetaminophen for 16 h on stream.

Resumen

La escasez de agua de calidad es una preocupación creciente en la sociedad actual. Además de este problema, recientemente se ha detectado un nuevo grupo de contaminantes en el agua que no se eliminan fácilmente con las tecnologías convencionales. Conocidos como contaminantes emergentes (CEs) incluyen productos farmacéuticos, productos para el cuidado personal, detergentes, esteroides, hormonas, etc. Estos contaminantes se han detectado en bajas concentraciones y tienen varios efectos nocivos para el ser humano y el medio ambiente. Así, en todo el mundo, se investigan e implementan diferentes tecnologías para el tratamiento de aguas residuales. En este ámbito, los procesos avanzados de oxidación (PAOs) se están desarrollando como alternativa a los métodos convencionales para el tratamiento de CEs. Estos procesos se basan en la generación de especies radicalarias con alto poder oxidante, que permiten la oxidación de los contaminantes hasta su completa mineralización. La fotocatalisis es una de estas tecnologías y se considera una alternativa de bajo coste porque se realiza a temperatura y presión ambiente. En este sentido, la fotocatalisis solar surge como opción interesante, ya que permite aprovechar la luz solar como energía limpia evitando el uso de lámparas que consumen mucha energía. En la fotocatalisis, un semiconductor se excita mediante la absorción de luz produciendo pares de electrones-huecos, que si se mantienen separados y migran hacia la superficie pueden inducir reacciones redox con las especies adsorbidas. Entre los diferentes semiconductores empleados, los materiales híbridos órgano-metálicos (MOFs) han recibido especial atención, gracias a sus excelentes propiedades semiconductoras. Los MOFs basados en titanio, como el MIL-125, han sido objeto de estudio en la bibliografía para diversas aplicaciones, incluida la descontaminación del agua. Además, este material permite la incorporación de grupos amino en su ligando orgánico, lo que mejora la absorción de luz en la región visible y reduce el band gap.

Por tanto, el principal objetivo de esta tesis ha sido el desarrollo de nuevos fotocatalizadores basados en $\text{NH}_2\text{-MIL-125(Ti)}$ y su uso en la degradación de varios CE, concretamente acetaminofeno, diclofenaco, sulfametoxazol y antipirina, utilizando radiación solar y LED. Inicialmente se estudió en detalle la estabilidad del MOF en medio acuoso, que es fundamental para la aplicación real. Posteriormente, se siguieron diferentes enfoques, incluyendo la deposición de nanopartículas de metales nobles, el acoplamiento con otros semiconductores y el grafting del grupo amino del ligando. Así, esta tesis doctoral se presenta como un compendio de cuatro artículos publicados en revistas científicas, clasificadas en el primer y segundo cuartil de sus correspondientes áreas.

El primer trabajo describe la estabilidad del $\text{NH}_2\text{-MIL-125}$ en agua. Este estudio demostró que este material presentaba una lixiviación significativa del ligando orgánico que lo compone, por lo que se aplicaron diferentes tratamientos térmicos para mejorar su estabilidad en agua. Inicialmente, se analizó la resistencia térmica del MOF por termogravimetría y se observó una fuerte pérdida de masa en el rango de 300 a 350 °C. Por esta razón, se seleccionaron temperaturas en el rango de 150 a 300 °C para realizar la estabilización. El MOF fue sometido a un tratamiento a vacío a temperaturas de 150, 200, 250 y 300 °C durante 16 horas. Los difractogramas de rayos X (DRX) revelaron que la estructura cristalina se mantuvo hasta los 250 °C, obteniendo una estructura amorfa con el tratamiento a 300 °C. Los espectros UV-vis demostraron que el grupo amino del ligando no se vio afectado por los tratamientos térmicos. Una vez que se demostró que las muestras mantenían su estructura, se probó su estabilidad en agua. Aunque se consiguió una reducción significativa, el porcentaje de lixiviado seguía siendo elevado, en torno al 15% para las muestras tratadas a 200 y 250 °C. Para mejorar aún más la estabilidad, el MOF se calcinó en una mufla en atmósfera de aire en el mismo rango de temperaturas. Al igual que en el caso

del tratamiento a vacío, el MOF mantuvo su estructura cristalina hasta los 250 °C pero su estabilidad en agua no fue tan alta como se esperaba. Por tanto, dos muestras adicionales fueron preparadas alargando el tiempo de calcinación hasta las 72 h. Se observó que tras 48 h la estabilidad del MOF en agua mejoraba pero que tras 72 h había una considerable pérdida de cristalinidad. Este trabajo estableció que el NH₂-MIL-125 puede ser purificado y estabilizado mediante un tratamiento térmico en atmósfera de aire a 250 °C durante 48 horas, manteniendo las propiedades estructurales y texturales del MOF.

Tras el primer trabajo, se llevaron a cabo diferentes modificaciones para potenciar la fotoactividad de este MOF bajo radiación solar. El segundo trabajo fue posible gracias a una estancia internacional en la Universidad de Oporto, Portugal. Se llevó a cabo la combinación del NH₂-MIL-125 con nitruro de carbono grafítico (g-C₃N₄) con el objetivo de obtener una nueva heterounión. Se sintetizaron tres fotocatalizadores con diferentes proporciones de MOF/g-C₃N₄ (75:25, 50:50 y 25:75). La caracterización mediante DRX de las heterouniones mostró los picos característicos de ambos componentes, el NH₂-MIL-125 y el g-C₃N₄. Las proporciones de g-C₃N₄ y MOF en los materiales híbridos se confirmaron mediante análisis elemental. Los espectros UV-vis corroboraron que los fotocatalizadores híbridos mejoraron su absorción en el rango de luz visible con un desplazamiento de la banda de absorción. Los espectros de fotoluminiscencia confirmaron el efecto sinérgico entre los semiconductores, dando lugar a una mayor inhibición de la recombinación de huecos-electrones en los fotocatalizadores híbridos. Una vez caracterizados, se comprobó su fotoactividad bajo irradiación LED (384 nm) para degradar un contaminante emergente modelo como el diclofenaco. Todos los fotocatalizadores presentaron una contribución de la etapa de adsorción en oscuridad muy parecida, cerca del 20%. El fotocatalizador híbrido con una proporción 50:50

logró la completa degradación del diclofenaco tras 2 h de reacción, obteniendo un valor de la constante cinética de pseudo-primer orden de 0.0282 min^{-1} , casi el triple de la obtenida con el $\text{NH}_2\text{-MIL-125}$ y más de cuatro veces la del $\text{g-C}_3\text{N}_4$. En el estudio con atrapadores de radicales, los radicales superóxido y los huecos resultaron ser las principales especies oxidantes involucradas en la reacción, mientras que los radicales hidroxilo jugaron un papel minoritario. La banda de valencia máxima de ambos fotocatalizadores se estimó a partir de XPS. Conocido este valor se determinó la posición de la banda de conducción a partir del valor del band gap, observando que el movimiento de las cargas entre los semiconductores podía explicarse mediante una heterounión tipo S. Finalmente, se identificaron algunos subproductos en la ruta de degradación, así como ácidos carboxílicos de cadena corta y otros productos de mineralización (H_2O , CO_2 y NO_3^-). A partir de las especies de reacción identificadas, se propusieron varias rutas para la degradación del diclofenaco, que involucran reacciones de hidroxilación, acoplamiento y oxidación.

El tercer trabajo describe la deposición de nanopartículas metálicas, como platino, paladio y plata, en la superficie del $\text{NH}_2\text{-MIL-125}$. La estructura del MOF no se vio afectada por la incorporación de las nanopartículas metálicas. Los fotocatalizadores con metales mejoraron su respuesta en la región de luz visible, pero sin modificar los valores de band gap. El análisis de la concentración superficial de las nanopartículas mediante XPS, sugirió una distribución más uniforme en el caso del Pt. Por otro lado, los espectros deconvolucionados de Ag 3d, Pd 3d y Pt 4f confirmaron una mayor proporción de Pd y Pt electro deficientes, al tiempo que verificaron la fotorreducción del precursor de Ag. Las nanopartículas metálicas, presentes como partículas esféricas discretas, presentaron tamaños promedio de 3,8, 3,4 y 1,8 nm para Ag, Pt y Pd, respectivamente. La incorporación de las mismas conllevó una disminución en la recombinación de electrones y huecos, lo que

fue confirmado por la mejora en la fotodegradación del acetaminofeno bajo luz solar simulada. El MOF con Pt, logró una degradación completa del contaminante en menos de 3 h de irradiación, con un valor de la constante de velocidad de pseudo-primer orden de 0.0165 min^{-1} . Los experimentos con atrapadores de radicales concluyeron que los radicales superóxido fueron la principal especie reactiva involucrada en la degradación. La estabilidad de este MOF se confirmó tras tres ciclos sucesivos, manteniendo su actividad, su estructura cristalina y morfología. Por otro lado, el proceso de degradación no se vio afectado por la presencia de cloruros, nitratos y sulfatos, presentes como iones inorgánicos comunes en las aguas residuales. Sin embargo, la presencia de bicarbonatos mostró un efecto negativo en la conversión del contaminante, probablemente debido a la disminución de los radicales superóxido ya que estos iones inorgánicos pueden interactuar con ellos. Finalmente, se identificaron algunos intermedios de reacción, resultantes del acoplamiento y apertura del anillo aromático de las moléculas de acetaminofeno. La oxidación adicional de esos subproductos dio lugar a ácido fórmico y ácido acético. La mineralización de estos ácidos de cadena corta conduce a la formación de H_2O , CO_2 y NO_3^- .

El cuarto estudio presentó el grafting del grupo amino del ligando orgánico del $\text{NH}_2\text{-MIL-125}$ mediante la incorporación de diferentes carboxaldehídos heterocíclicos, como 2-piridincarboxaldehído, 3-piridincarboxaldehído, 4-piridincarboxaldehído y 2-quinolina-carboxaldehído. Para reducir la lixiviación del ligando, se utilizaron tratamientos térmicos a $200 \text{ }^\circ\text{C}$ durante 48 h en atmósfera de aire. La estructura cristalina del MOF original se mantuvo en todos los fotocatalizadores después del grafting. Los espectros de resonancia magnética nuclear (RMN) confirmaron la modificación del ligando orgánico mediante un procedimiento post-sintético debido a la transformación de los grupos C-NH_2 en C-N=C mediante una reacción de Schiff. Los nuevos

materiales describieron un área superficial ligeramente menor que el NH₂-MIL-125 original, más evidente para el MOF derivado del 2-quinolina-carboxaldehído. Los nuevos heterociclos actuaron como una antena favoreciendo la absorción de luz en el rango visible y reduciendo los valores de band gap. Por otro lado, los nuevos fotocatalizadores alcanzaron una menor lixiviación que el NH₂-MIL-125 original. La muestra con 3-piridincarboxaldehído presentó los mejores resultados para la fotodegradación de acetaminofeno en diferentes matrices de agua, como agua desionizada, agua del grifo y agua sintética. Esta mejora se atribuyó a las diferencias en la disposición estérica del heterociclo y a una mejor transferencia de carga interfacial, como sugiere el radio de arco más pequeño del semicírculo en el diagrama de Nyquist. Los experimentos con atrapadores de radicales mostraron que los radicales superóxido fueron nuevamente la principal especie involucrada en el proceso de fotodegradación. Además, se probó la fotodegradación de antipirina y sulfametoxazol, como modelos de otros CEs, observándose que la actividad fotocatalítica dependía de la naturaleza del compuesto a degradar. Finalmente, se analizó la fotoactividad del MOF en un sistema con flujo continuo, observándose una actividad constante y alcanzando una conversión total de acetaminofeno durante 16 h.

1. INTRODUCTION



1. Water purification by photocatalysis

The availability of quality water is a major problem in current societies. Water needs have increased annually, from 1990s, almost 1% per year according to the continuous growth of the worldwide population, consumption patterns and economic development [1,2]. It is noteworthy that this is a both hemispheres issue, affecting regions such as Southern Europe, Western South America, Southern Africa and countries like China or Mexico [3]. By 2025, global water demand for the most water-intensive activities, agriculture and energy production, is expected to increase about 60 and 80%, respectively. Besides this, the world population prospects establish a population growth in the range of the 22-32% by 2050.

However, the surface water availability remains almost invariable and the quality of this water is being deteriorated because of the continuous release of chemicals to the environment, mainly nutrients due to the intensification of the agricultural production [4–6]. The problem of water contamination has gained attention, giving rise a list of more than 106,000 different compounds that can be considered water pollutants. It is hard to classify them in groups, although they can be organized according to their sources and effects. Dyes are considered one of the most abundant contaminants in water, coming from textile, plastic, painting, paper and leather industries. Dyes can be carcinogenic and probably cause chronic illnesses. Moreover, these compounds can block the sunlight, due to the change of color of the aqueous medium, influencing in the aquatic organisms [7]. The presence of heavy metals is ascribed to mining industrial effluents and fertilizers used in agriculture sector. Their effect on human health depends on the specific metal, having a huge number of impacts [8]. Emerging contaminants (ECs) include the wide range of personal care products, pharmaceuticals, cyanotoxins, steroids and hormones, plasticizers, caffeine, detergents, fragrances, etc. [6,9]. ECs are compounds appeared in

the last decades, detected in low concentrations (from $\text{ng}\cdot\text{L}^{-1}$ to $\mu\text{g}\cdot\text{L}^{-1}$) in the water streams and, in most cases, without a proper regulation, resulting in a risk for human health, environment and also for economic activities due to their toxicity and/or bioaccumulation [10,11]. They have been included in the Watch List of substances recently been accepted by the European Union (Decision 840/2018/EU) [12]. Some examples of ECs are summarized in Table 1.1. All those water pollutants can be supplied to the environment by multiple pathways, like industry disposals, hospital effluents, domestic wastewater, sewage treatment plants (STPs) and water treatment plants (WTPs) [13]. Pharmaceuticals and personal care products (PPCPs) release into aquatic environment via wastewater treatment plants, landfill leachate and untreated sewage [14]. There are limited reviews of PPCPs health effects, but fecundity decrease, increase of breast and testosterone cancers and persistent antibiotic resistance can be potential risks of drinking water with these compounds [15]. On the other hand, pesticides, especially organophosphorus and organochlorines, are the most widely used in greenhouse farms. A long exposure to organochlorines is toxic, giving rise to eye irritation, Parkinson illnesses, leukemia, sarcoma and pancreas damage [16]. Steroid hormones can affect the human reproduction and fertility, male and female sexual disorders, influencing also in the fish fertility [17]. For all previous reasons, international agreements as the United Nations 2030 Agenda for Sustainable Development establish specific targets for some of these compounds, looking for improving the water quality. In this sense, wastewater treatment is a crucial step inside the water cycle. Further investigation for improving the technologies for wastewater treatments may suppose a great deal of opportunities, especially in the new context of circular economy [6,18].

Table 1.1. Examples of emerging contaminants (ECs) [19].

| | Classification | Examples |
|------------------------|-------------------------------------|---|
| Pharmaceuticals | Analgesics, anti-inflammatory drugs | acetaminophen, diclofenac, antipyrine, ibuprofen, codeine |
| | β -blockers | metoprolol, atenolol |
| | Psychiatric drugs | carbamazepine, diazepam |
| | Human antibiotics | amoxicillin, sulfamethoxazole |
| Personal care products | Fragrances | polycyclic and macrocyclic musks, phthalates |
| | Sunscreen agents | benzophenone |
| | Insect repellents | N,N-diethyltoluamide |
| | Pesticides | atrazine, malathion |
| | Steroid hormones | estriol, estrone |

The treatment and purification of wastewater consist in the removal of the contaminants by the combination of physical, biological and/or chemical processes. In the case of physical methods, gravity as a natural force (such as sedimentation), barriers such as membranes or filters are commonly used for separating and concentrating the pollutants. In this field, technologies like ultra- or nanofiltration can remove macromolecules and biological matter, while inorganic ions can be separated by reverse osmosis. However, those processes are characterized by high power consumption, thus increasing the operational costs [20]. The biological treatment of wastewater mainly includes the use of biological activated sludge for promoting the biochemical degradation routes of the different pollutants. This technology presents lower operational costs compared to physical and chemical operations, but it also has larger time requirements. Furthermore, some of the aforementioned ECs may present bioaccumulation [21,22] and persistence or inhibitory effects over the bacterial microorganisms of the activated sludge [23], drastically

reducing the effectivity of the biological process. Finally, chemical processes allow removing heavy metals by alkaline precipitation and disinfection by using UV radiation. Besides this, a family of high-power oxidant technologies, known as advanced oxidation processes (AOPs), have been deeply investigated in the last decades. These processes enable the degradation of refractory organic compounds by the in-situ generation of reactive oxygen species (ROS), mainly hydroxyl radicals ($\cdot\text{OH}$). AOPs can implement iron/ H_2O_2 (Fenton processes), O_3 (ozonation), electric power (electrochemical oxidation), ultraviolet (UV) or solar radiation (heterogeneous photocatalysis), or their combination [24,25].

Among AOPs used for water purification, heterogeneous photocatalysis can be used for the treatment of hazardous metal ions and organic pollutants [26–30]. This technology has the advantages of using O_2 as main reactive and the possibility of operating at mild conditions (ambient temperature and pressure). In heterogeneous photocatalysis, the ROS are generated after a charge separation caused by the irradiation of a semiconductor (photocatalyst) [31,32]. The photocatalyst is defined by two separated energy bands: the highest one occupied by electrons (known as valence band, VB) and the lowest without electrons (called conduction band, CB). The energetic barrier between aforementioned bands receives the name of band gap energy (E_g) [33]. In this way, as represented in Figure 1.1, when a photocatalyst is irradiated and receives an energy equal or higher to its band gap energy, an electron (e^-) is promoted from the valence band to the conduction band, thus generating a hole, h^+ , in the VB. Immediately, these photogenerated charges can recombine, releasing the excitation energy as heat, but also they can migrate to the surface and generate the ROS. In the latter case, hydroxyl radicals ($\cdot\text{OH}$) can be obtained by the oxidation of water molecules by the h^+ , while superoxide radicals ($\text{O}_2^{\cdot-}$) can be produced by the reduction of adsorbed oxygen. Moreover, superoxide radicals can be further oxidized to

hydroperoxyl radicals (HO_2^\cdot) by protonation. These oxidant species, coupled to direct oxidation by h^+ , could even mineralize the pollutant, thus achieving the complete oxidation of the organic matter to CO_2 and H_2O . However, besides the recombination of the pair e^-/h^+ , other reactions can reduce the effectivity of the global process, such as combination of HO_2^\cdot , producing H_2O_2 , or protonation of $^\cdot\text{OH}$, resulting in the formation of water [34–36].

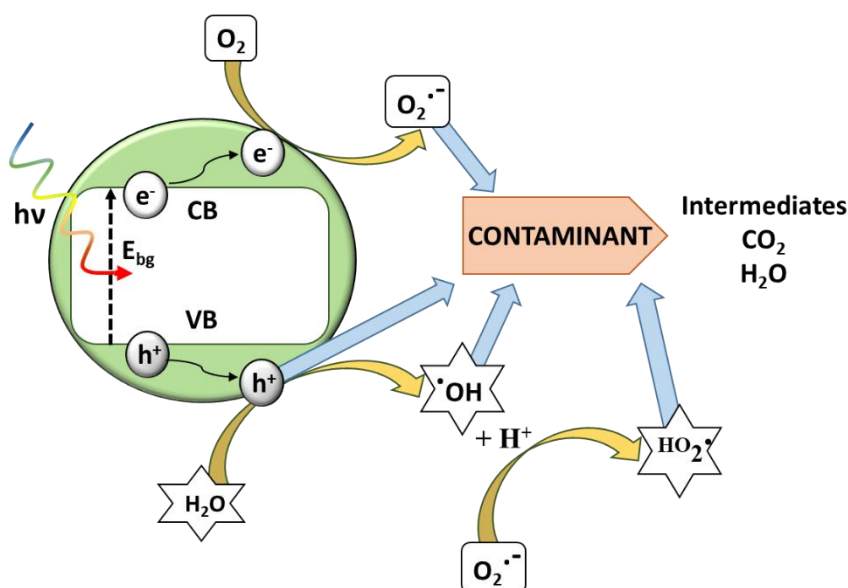


Figure 1.1. Schematic representation of reactive oxidant species generation and contaminant oxidation after the irradiation of a photocatalyst in aqueous solution [37].

The increasing attention paid in the research field of the photocatalysis for water purification has resulted in the design and development of a wide variety of photocatalysts and their modifications. Table 1.2 gathers some of the most analyzed (and some other novel) semiconductor materials studied for the photocatalytic purification of wastewater. Further investigation is necessary for outstanding the real behavior of these materials in diverse contexts, i.e., different water matrices or degradation of ECs in real

wastewaters. In addition, the stability of the material is a recurring issue. For example, metal sulfides might present low photochemical stability under irradiation, resulting in their dissolution; while corrosion in aqueous media is another major drawback for some semiconductor materials [38]. This is not the case of titanium dioxide (TiO_2), the most used and researched photocatalyst. TiO_2 has been utilized for both air and water purification [39,40]. This semiconductor is characterized by high photoactivity, besides high chemical stability and low biological toxicity [41,42]. However, the use of TiO_2 powder has the main disadvantages of low porosity, poor adsorption and the difficult management for its recovery. Moreover, the principal photocatalytic phase of TiO_2 , anatase, can be only activated by UV radiation due to its high band gap energy (3.2 eV, corresponding to $\lambda \leq 387$ nm). This results in a low utilization of the solar spectrum, as it is composed of only 5% UV light [43], in contrast with the 43% that corresponds to visible light [44]. Figure 1.2 shows the spectral irradiance of sunlight comprised a wide range of wavelengths from UV to the infrared region, with a maximum absorbance within the visible range. It can also be observed that, as sunlight crosses the atmosphere, part of that radiation is absorbed by gas molecules (O_2 , CO_2 , O_3 and water vapor) and aerosols [45].

Due to this, growing efforts have been done during the last decade to improve the photocatalytic response of TiO_2 and other semiconductors to visible light. These approaches include electronic and morphological modifications, primarily searching a displacement in the absorption region through the solar range and the development of the porous texture for increasing the contact surface between the semiconductor and the pollutant. For these reasons, TiO_2 modifications, by means of morphological (e.g., supporting on activated carbon or graphene, immobilized over fibers, forming heterojunctions with other materials) and electronic (e.g., doping with heteroatoms, metal deposition, combination with other semiconductors,

sensitization with dyes) approaches, have been frequent researching lines in photocatalysis. In any case, the synthesis of a TiO₂-based photocatalyst for real wastewater purification using not only UV light (and using visible and solar light) is still a challenging frontier for the upcoming years.

Table 1.2. Different types of photocatalysts used for the removal of pollutants in water.

| Photocatalyst type | Examples | Ref. |
|--------------------------|---|---------|
| Metal oxides | TiO ₂ , ZnO, WO ₃ , CeO ₂ , Fe ₂ O ₃ , In ₂ O ₃ , Bi ₂ O ₃ | [46–48] |
| Metal sulfides | ZnS, CdS, MoS ₂ , Bi ₂ S ₃ , CuS/ZnS | [49–51] |
| Ternary compounds | Titanates (BaTiO ₃ , SrTiO ₃ , La ₂ Ti ₂ O ₇) | [52–54] |
| | Tungstates (Bi ₂ WO ₆ , ZnWO ₄) | [55,56] |
| | Metalates [A _x B _y O _z] (such as BiVO ₄) | [57,58] |
| Multicomponent materials | Bi ₂ S ₃ /Bi ₂ O ₃ /Bi ₂ O ₂ CO ₃ Bi ₂ O ₂ CO ₃ /Bi ₂ O ₄ BiVO ₄ /Bi ₂ O ₂ CO ₃ | [59–61] |

Thus, radiation sources play an important role in the photocatalytic process. In cases where the use of artificial light is preferable, artificial light devices in the form of UV lamps, fluorescent lamps and light-emitting diodes (LEDs) have been used. Conventional UV-lamps can be divided into low, medium, and high-pressure mercury arc lamps. The drawbacks of these lamps are their short working life and fragility, as well as the risk of explosion.

Introduction

Notwithstanding their hazardous mercury content, and the fact that for medium and high pressure lamps they need cooling during reaction [62]. Fluorescent lamps present advantages such as being low cost, having a longer life time and consuming less energy [63]. Light-emitting diodes (LEDs) have been developed as light sources owing to small size, long life, low cost, friendly environmental impact, and ability of emitting light at multiple wavelengths. Thus, LEDs can emit in the infrared, visible and near-ultraviolet region, becoming an outstanding competitive option for photocatalytic processes [64]. On the other hand, the main drawback of LEDs is that they are not useful to simulate solar irradiation. Nevertheless, the activation of semiconductors by natural light source such as sunlight is considered an alternative to artificial light, due to unquestionable advantages in terms of energy saving and environmental considerations.

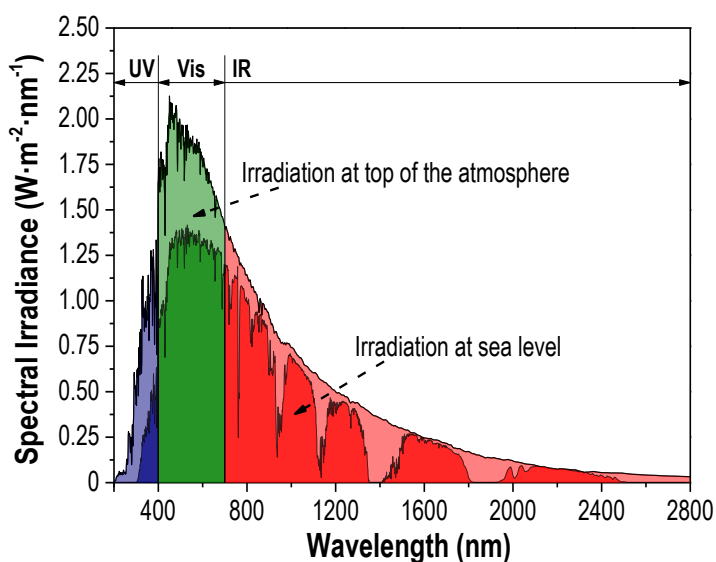


Figure 1.2. Spectral solar irradiance in the wavelength range of 200-2800 nm (Original data from NREL and ASTM).

Simultaneously, during the last two decades, metal organic frameworks (MOFs) have received special attention in photocatalysis, regarding the broad

range of possibilities that the interaction between the metal clusters and the organic linkers may present. MOFs usually present a well-defined crystalline structure and also a high developed surface area [65]. These characteristics, coupled with the wide number of different available linkers and metal clusters for their synthesis, allow obtaining semiconductor materials with redshifted absorption in the electromagnetic spectrum and suitable open porosity and very low framework density [66–68]. Therefore, the use of MOFs for the photocatalytic treatment of pollutants in water is an interesting strategy for water purification. The photodegradation of water contaminants with MOFs has been studied from the early 2000s [69], and it continues to nowadays [70]. Since that, a wide range of chemical and structural modifications has been applied to enhance the photoresponse of MOFs.

2. Metal organic frameworks

Metal organic frameworks are a class of porous materials with modular structure. This allows a very wide structural diversity and the possibility of synthesizing materials with tailored properties for specific applications such as, gas storage, drug delivery, separation processes, catalysis, light harvesting and energy conversion, sensing, among others. MOFs are formed by the assembly of two components, cluster or metal ion nodes, also called secondary building units (SBUs), and organic linkers that connect the SBUs, usually given rise to crystalline structures with significant porous texture development [71]. Figure 1.3 represents the SBU (metal node) and organic linker used for the synthesis of two well-known MOFs, namely MOF-5 and HKUST-1. The combination of these structures results in a huge number of possibilities, and therefore of different MOFs with tailored properties. Figure 1.4 represents the different MOFs obtained using the same SBU and different

Introduction

organic linkers. As can be observed, diverse pore shapes can be obtained, depending on the linker selection.

The organic linkers are generally polytopic linkers as carboxylates, phosphonates, sulphates, azole and heterocyclic compounds [72]. Some of the most representative SBUs and organic linkers used for the formulation of MOFs are depicted in Figure 1.5. The first reference to metal organic frameworks was reported by Yaghi et al. [73] who synthesized MOF-5 in 1995. Since then, many of these materials have been analyzed in the literature and grouped under different denominations. For example, UIO-based MOFs, like UIO-66, are from Universitetet i Oslo, MIL are from Materials of Institute Lavoisier or ZIF-based MOFs referred to Zeolite Imidazolate Framework, among others.

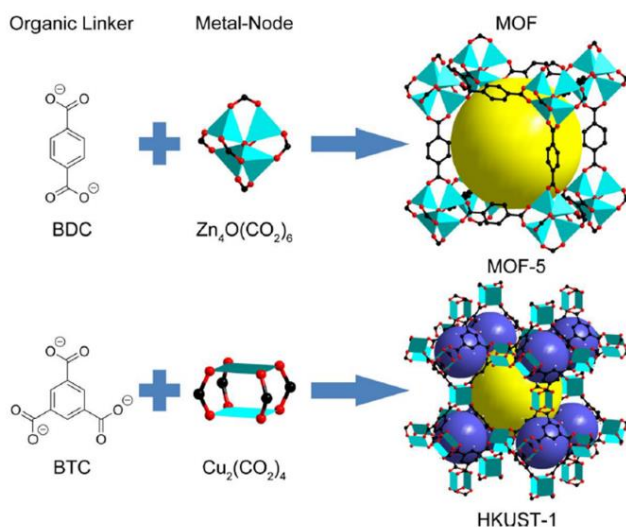


Figure 1.3. SBUs (metal node) and organic linkers used for the synthesis of MOF-5 and HKUST-1. Yellow and blue spheres represent the free spaces in the framework and have no chemical meaning (reproduced from ref. [74]).

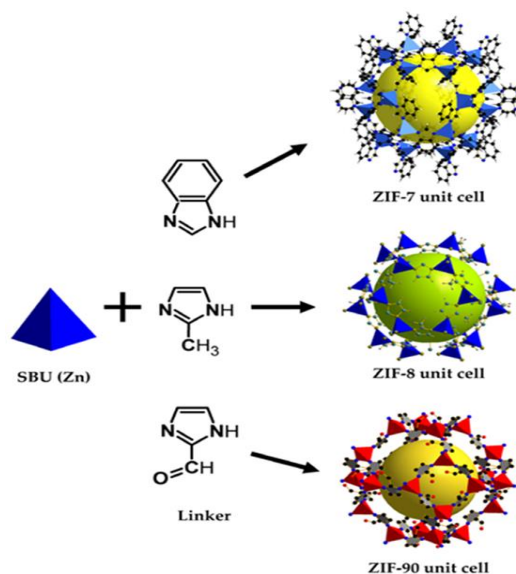


Figure 1.4. Different MOFs obtained using the same SBU and different organic linkers (reproduced from ref. [75]).

The synthesis of MOFs is usually performed in liquid-phase by mixing organic ligands, metal SBU and a solvent for a certain time at a certain temperature. The product of the reaction is filtered and dried by evaporation to obtain a purified MOF [76]. The most used method is hydrothermal/solvothermal synthesis via conventional electrical heating at controlled temperature. Generally, high-boiling organic solvents, such as dimethyl formamide, diethyl formamide, acetonitrile, acetone, ethanol or methanol, are used in solvothermal reactions. To avoid the problems related to the different solubility of the initial reagents, mixtures of solvents can be used. Solvothermal synthesis can be performed at different temperatures. At lower temperatures, glass vials can be used, while at temperatures higher than 130 °C the synthesis is generally performed in small volume Teflon-lined autoclaves [77].

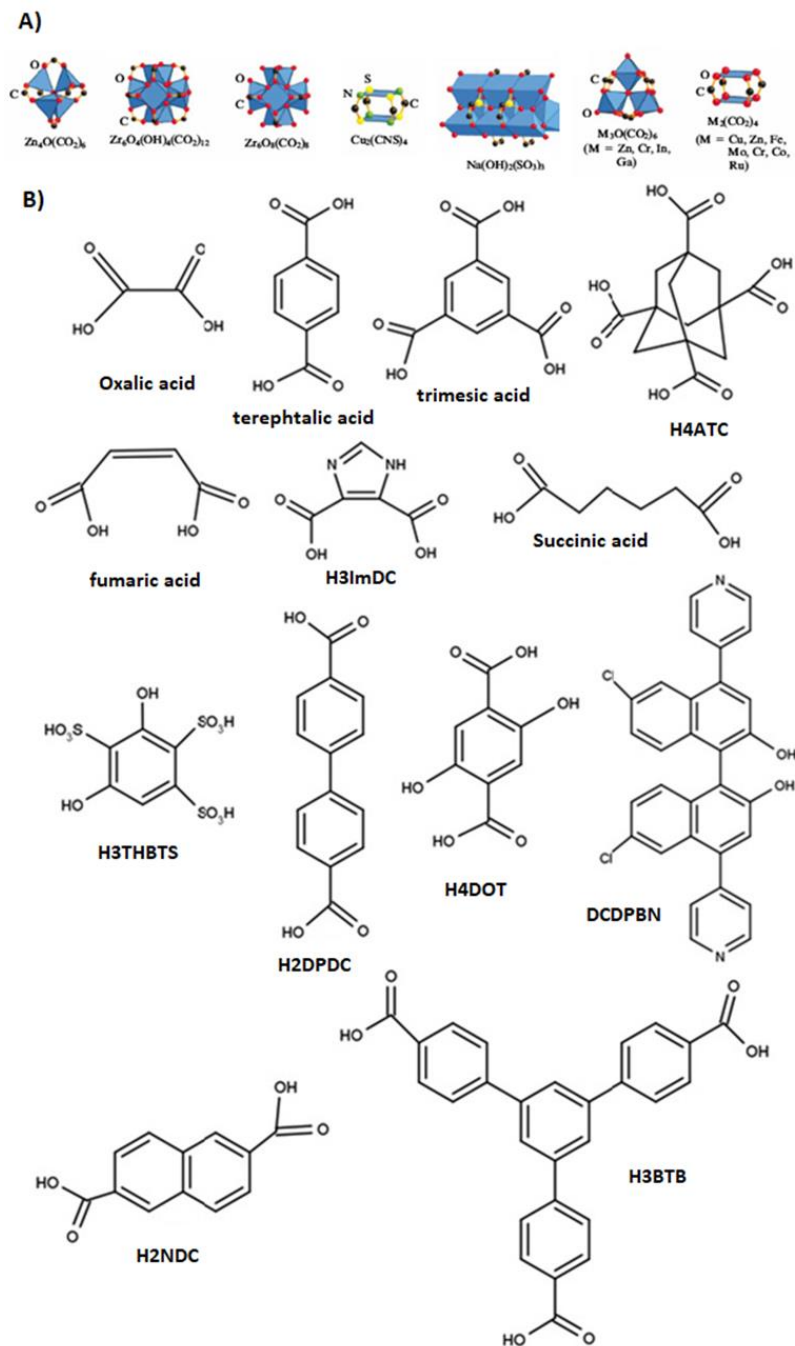


Figure 1.5. Inorganic SBUs (A) and organic linkers (B) commonly used in MOF synthesis (reproduced from ref. [78]).

Hydrothermal synthesis of MOFs constitutes a more environmental friendly approach that substitutes the use of organic solvents for water [79]. Nevertheless, these syntheses usually require long reaction times for an optimal crystallization. In order to accelerate the crystallization and obtain more uniform crystals with lower size, other alternative synthesis routes have been researched, such as microwave-assisted, electrochemical, sonochemical, mechanochemical and spray-drying synthesis. These methods try to synthesize MOFs in a shortened time and with higher crystallinity. The choice of the solvent is crucial in liquid-phase reactions and is based on different characteristics such as redox potential, reactivity, solubility or stability, among others. The nature of the solvent also determines the thermodynamic and activation energy of the reaction. Besides liquid-phase, some studies have focused on MOF synthesis by solid-state synthesis.

The synthesis of MOFs usually requires final steps of purification and/or activation. Purification consists in the removal of impurities, such as metal oxides, recrystallized linker or dense hybrid compounds, not occluded inside the pores. This can be carried out by sieving or based on the densities of the synthesized products. Nevertheless, most often impurities are removed by solvent treatment at elevated temperatures. Activation entails the removal of guest molecules from the pores. Various techniques are used to get the activation of MOFs, such as vacuum drying, solvent exchange or supercritical drying [80]. In some cases, the heating of the MOF under vacuum can be enough to assure the activation. However, it also occurs that after vacuum drying lower surface areas than expected are obtained. This behaviour can be ascribed to the framework collapse due to the high surface tension and capillary forces produced by the liquid to gas-phase transformation of the trapped solvent molecules, especially if the solvent has a high boiling point and/or high surface tension [81]. To avoid this problem the solvent can be exchanged with a lower boiling point/lower-surface tension solvent prior to

heating under vacuum. For the exchange, the MOF should be soaked in the new solvent during enough time to assure the complete solvent exchange. The soaking time can be from a few hours to several days (nuclear magnetic resonance spectroscopy can be used to assure the complete solvent exchange). Afterwards, the MOF will be activated at a temperature above the boiling point of the new solvent but below the decomposition temperature of the framework. If conventional solvent exchange is unsuccessful, activation can be achieved by exchange with supercritical carbon dioxide (scCO₂), which avoids the liquid to gas-phase transformation. Prior to use scCO₂, the MOF should be exchanged with a solvent miscible with CO₂, such as ethanol or methanol. With this last technique, activation is achieved even if the MOF has a quite breakable structure [82]. A new technique has been recently reported to activate different MOFs with UV-vis lamp [83]. The localized light-to-heat conversion produced in the MOF crystals upon irradiation enables a very fast solvent removal, thereby significantly reducing the activation time to 30 min and suppressing the need for time-consuming solvent exchange procedures and vacuum conditions. It is necessary to highlight that during all steps required for the purification and activation, the integrity of the framework must be verified, since high temperature can result in the collapse of the MOF structure or even in chemical reactions that can alter the surface chemistry and properties of the final material. In order to know if the purification/activation steps are correctly performed, it is usually convenient to compare the experimental measured surface areas with those calculated by computational modelling or previously reported in other studies. If the experimental surface area is similar to the computationally derived, the activation procedure seems well-performed. If the experimental area is significantly lower than the theoretical one, this is indicative of a collapse of the frameworks or an incomplete solvent removal [84].

MOFs are known as useful candidates for photocatalysis due to their promising photophysical/chemical properties. Many studies are focused on the photocatalytic degradation of organic pollutants, mainly dyes, and the photoreduction of heavy metals, both in water solutions. Many MOFs based photocatalysis have gained attention, being water purification one of the promising fields for using these materials. The first work with MOFs to remove pollutants was carried out by Yu et al. [69], testing the degradation of methylene blue with an uranium-nickel-organic hybrid compound under UV light. In 2007, Alvaro et al. [85] tested the photocatalytic properties of MOF-5 in the removal of phenol in aqueous medium. Since that, several MOFs have been investigated in water treatment. The most common studied MOFs for photocatalytic water treatment include MIL-125 (Ti), UiO-66 (Zr), ZIF-8 and Fe-based MOFs (MIL-101, MIL-53 and MIL-100). Titanium is considered one of the most appealing candidates to synthesize MOFs due to its biocompatibility, redox activity and photocatalytic properties. Ti-based MOFs are constituted by Ti-oxo-carboxylate SBUs with strong Ti-O bonds (Figure 1.6). MIL-125(Ti) was discovered by Hardi et al. [86] in 2009 and is constructed from $[\text{Ti}_8\text{O}_8(\text{OH})_4(\text{COO})_{12}]$ clusters and 1,4-benzenedicarboxylate (BDC). The huge deal with this material is in its light absorption edge at 350 nm (UV region). Regarding its use under solar light, it is necessary to enlarge its visible light absorption. A possibility includes a linker decoration with a functionalized group, also called functionalization of the ligand. Thus, the absorption band of the MIL-125 can be displaced to 550 nm when an amino group is incorporated to the organic linker due to its role as light absorption antenna, leading to $\text{NH}_2\text{-MIL-125}$. Thus, the interaction between the lone pair electron of the amino group and the π bond on the benzene ring of the MOF increases the electron density of the material, producing a redshifted displacement of the valence band of the MOF. Therefore, the band gap decreases from 3.6 to 2.7 eV with the introduction of

the amino group [87–89]. Moreover, this group also improves the charge transference between organic linker and metal, inhibiting electron-hole recombination.

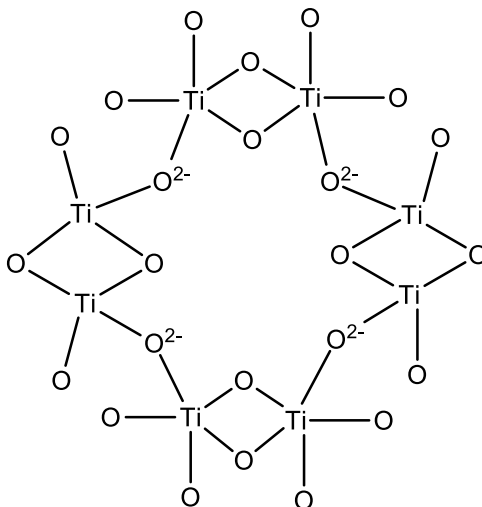


Figure 1.6. Scheme of the Ti-oxo-carboxylate SBUs with strong Ti-O bonds of the Ti-MOFs [90].

2.1. Modification of MOFs

In the case of photocatalytic applications, some of the MOFs show relatively high band gap values and therefore, they can only harvest UV light, which limits their application. The different strategies to enhance photocatalytic activity of MOFs include: (i) Functionalization; (ii) Deposition of metal nanoparticles; (iii) Combination with semiconductors in different types of heterostructures, (iv) Sensitization with dyes and (v) metal doping.

2.1.1. Functionalization

Functionalization of MOFs can be achieved by two different approaches. The first is based on the synthesis of the functionalized MOF using an organic

linker containing the desired functional groups. This approach avoids the modification of an already synthesized MOF. However, this procedure has some limitations and might not be easily generalized because either the groups could interfere with the formation of the desired material or the properties (thermal stability, solubility) of the functionalized linker might not be compatible with the synthetic conditions. The more complex are the functions to be introduced, the more difficult is the synthesis by self-assembly because of their reactivity towards the metallic precursors [91]. A clear example of this methodology is the inclusion of amino groups by replacing terephthalic acid by 2-aminoterephthalic acid as organic linker in the synthesis of MIL-125(Ti) MOF to obtain NH₂-MIL-125(Ti). This change in the organic linker resulted in a higher photocatalytic activity of the resulting MOF [89]. The second functionalization approach is post-synthetic modification (PSM), consisting in the functionalization of a previously synthesized MOF. The main difficulty with post-synthetic modification is to not distort the structure of the starting material during the process. Different routes have been developed to access post-functionalized MOFs based on different chemical interactions while keeping the same native structure [92]. PSMs can be divided in four different categories as summarized in Figure 1.7, namely: i) covalent PSM, which is produced by the covalent modification of the organic linker, ii) dative PSM, involving the coordination of a metal centre to a linker with vacant coordination site, iii) inorganic PSM, which is produced by the modification of the SBUs, and iv) ionic PSM, as result of the exchange of a counter-ion in a cationic or anionic MOF. For covalent or dative PSM, the MOF normally needs to have a reactive group present on the linker. This group is often referred to as a 'tag', which is defined as a group or functionality that is stable and non-structure-defining during MOF formation, but that can be transformed by a post-synthetic modification [92].

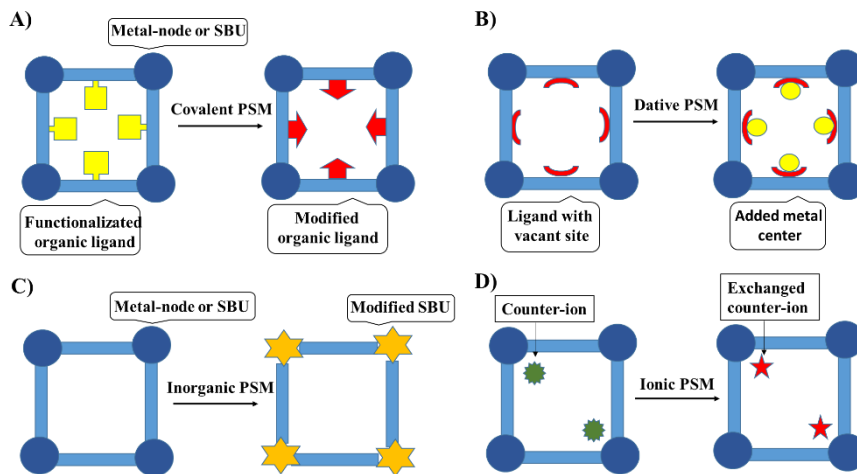


Figure 1.7. Post-functionalization strategies for MOFs modification
(Reproduced from [38]).

Different covalent transformations have been successfully carried out in the literature to modify preassembled MOFs. These transformations include varied chemical reactions, such as amide coupling, imine condensation, urea formation, salicylaldehyde condensation, N-alkylation, click reactions, bromination and protonation. Many of these reactions have been implemented in amino-functionalized MOFs, due to the higher reactivity of the amino functional group. It should be mentioned that most PSM reactions involve the increase of the size and complexity of the functional groups into the pores. However, it is also possible to make this group smaller, simultaneously unmasking a protected functional group. This class of reactions has been termed post-synthetic deprotection (PSD) [93] and can be achieved by thermolysis and photolysis reactions. Dative PSM reactions can be divided into two types: some in which the metal coordinates to a neutral site of the organic ligand, and those in which coordination occurs by the deprotonation of the ligand such as the conversion of hydroxyl groups into alkoxides (incorporating metal centres). Inorganic PSM can be included in a wider functionalization category, namely post-synthetic exchange (PSE),

which includes the modification/substitution of the SBU (inorganic PSM) or of the organic linker. Inorganic PSM reactions include transmetalation at inorganic nodes, oxidation and reduction of the framework metal centres or substitution of metal centres. On the other hand, PSE by substitution of framework ligands includes solvent-assisted linker exchange (SALE) and solvent-assisted linker incorporation (SALI) [94]. Finally, ionic MOFs are those in which the framework has a cationic or anionic charge, with counterions present in the pores to balance these charges [95]. Many ionic MOFs can undergo post-synthetic ion-exchange processes (ionic PSM) during which the cations or anions initially present in the pores are substituted for others.

2.1.2. Deposition of metal nanoparticles

There are other possible MOF transformations that can be viewed as post-synthetic modifications, including the formation of nanoparticles within the porosity of the MOF (deposition of metal nanoparticles). In recent years, metal nanoparticles (NPs) have gained popularity because of their application in heterogeneous catalysis. Different methods have been developed to load metals nanoparticles in MOFs, such as incipient wetness impregnation or double solvents method, based on the use of a hydrophilic and a hydrophobic solvents [96]. Generally, these processes require the use of strong reducing agents like NaBH_4 or H_2 , to obtain the desired metal NPs, which compromises the stability of the framework. Recently, photoreduction has been used for the reduction of the metal nanoparticles with promising results [97]. It is important to understand the migration of photogenerated charges in this system. If the light irradiated has enough energy to overcome the band gap, an electron migrates from the VB of the MOF to the metal NP via an interfacial charge transfer, acting as an electron reservoir and avoiding the recombination of charges. Particularly important is the deposition of NPs such as Ag and Au, which can absorb visible light via surface plasmon

resonance (SPR). These NPs can be excited by the light, promoting electrons to the CB of the MOF and enhancing charge separation (Figure 1.8). SPR is an inherent property of NPs, exhibiting a redistribution of the charge density when they are irradiated by light with a wavelength larger than their size [98]. Although to achieve an efficient mechanism depends on several factors such as the localization of the particles, the interaction between metal-MOF, and the loading metal amount, among others [99].

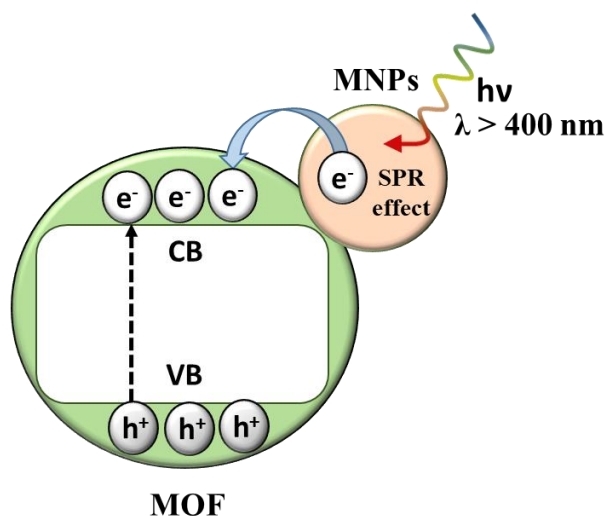


Figure 1.8. Scheme of SPR effect of NPs/MOF.

2.1.3. Sensitization

Sensitization with dyes or photosensitization of MOFs is useful to improve the photocatalytic process under sunlight. Thus, the dye molecule absorbs the light, promoting an electron from the highest occupied molecular orbital (HOMO) to the lowest occupied molecular orbital (LUMO), turning it into an excited dye (dye*) (Figure 1.9). The excited dye injects electrons to the CB of the MOF and produce radical species. The LUMO of the dye needs to be located above the bottom of the CB of the MOF. Subsequently, photosensitization improves the separation of charges and expands the light

absorption to the visible region [100]. Organic dyes, such as rhodamine B [101], Basic Yellow 24, Basic Red 14 or Methylene Blue [102], transition metal complex of polypyridine (Ru) [103], porphyrin [104] and phthalocyanine molecules [105] have been reported in literature to form viable systems with MOFs to remove pollutants from water. In all studies, authors stand out the wide visible light response of these molecules. However, the synthesis of dyes can involve organic reactions with low yields, increasing the cost. Moreover, dyes can sometimes suffer degradation under light irradiation, giving rise to changes on their structure, hence, a regeneration to recover its initial properties is necessary [106].

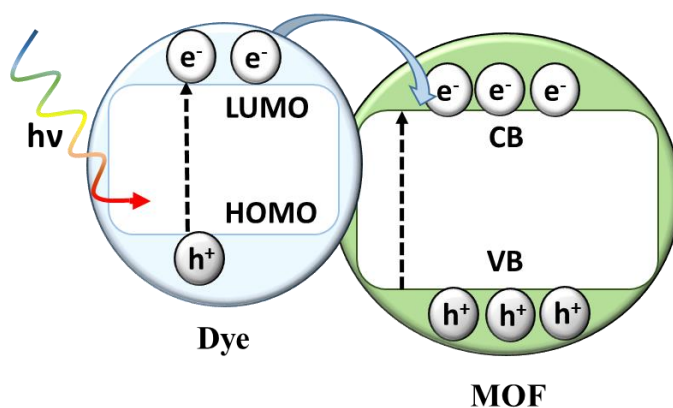


Figure 1.9. Electron transfer route in a dye sensitized MOF [100].

2.1.4. Combination with other semiconductors

Another approach to improve the photocatalytic activity of MOFs is to couple them with other semiconductors, resulting in a heterojunction, looking for attaining more efficient separation of electron-hole pairs and an enhancing absorption in the visible region. There are three types of heterojunctions depending on the alignment of VB and CB of each semiconductor: type I, II and III (Figure 1.10). In Type I, semiconductor 1 has a CB more negative than that of semiconductor 2, while its valence band is more positive than that

of semiconductor 2. Then, both charges end up accumulating in the semiconductor with lower band gap, giving rise to a better photoresponse. Type II achieves the best separation of charges, that is, longer lifetime, becoming the most studied heterojunction [107]. Two mechanisms can be observed in this type of heterojunction. In type II S-S heterojunction (Figure 1.10A), upon light absorption of both semiconductors, the electrons from the CB of the semiconductor 2 will transfer to the CB of the semiconductor 1, which presents a lower minimum CB potential. Meanwhile, the holes of the valence band of the semiconductor 1 will migrate to the VB of the semiconductor 2, which has a higher minimum VB potential. Thus, the number of available photogenerated charges increases, allowing a higher velocity of generation of ROS that can oxidize the contaminant. In contrast to this mechanism, in type II Z-Scheme heterojunction (Figure 1.10B), the photogenerated electrons from semiconductor 1 can be energetically prone to migrate to the VB of the semiconductor 2, occupying the available holes. Therefore, this recombination through semiconductors enhances the photostability of the heterojunction and its performance, by means of enabling the electrons from the semiconductor 2 (and the holes from the first one) for further generation of ROS. In Type III, the band gaps of both semiconductors do not overlap and consequently electrons and holes cannot be transferred between them [108,109]. In this case, the mobility of charges is not so efficient in comparison with other heterojunctions. MOFs can be combined with different semiconductors, such as metal oxides and chalcogenides (TiO_2 , ZnO , CdS , etc.), ternary compounds (BiVO_4 , Ag_3PO_4 , Bi_2MO_6 , etc.), metal free semiconductors (graphene and $\text{g-C}_3\text{N}_4$) or other MOFs to form heterojunctions. Then, the photocatalytic mechanism will depend on the VB and CB relative positions, leading to the formation of different ROS able to degrade the pollutant to a greater or lesser extent.

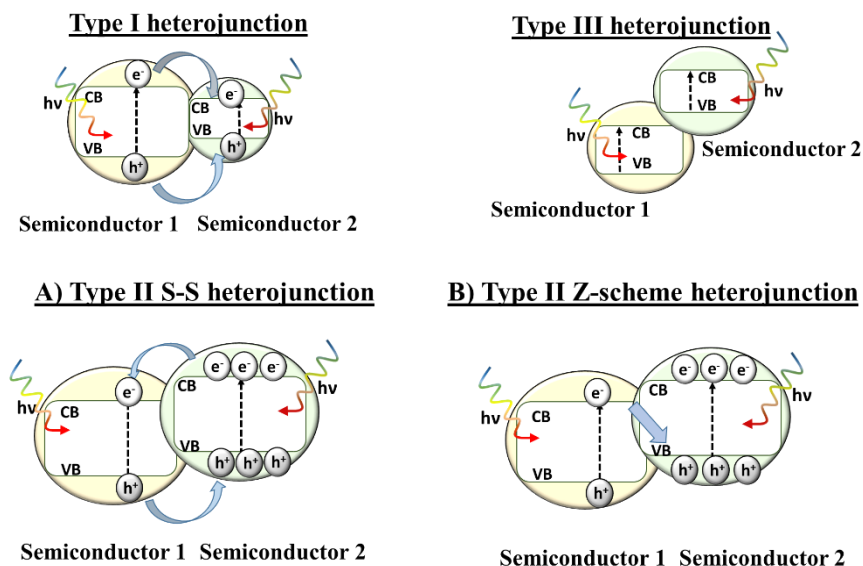


Figure 1.10. Mechanism of diverse types of heterojunctions.

Different semiconductors have been combined with MOFs in photocatalytic studies. For example, the combination of Ti-MOFs with $g\text{-C}_3\text{N}_4$ has attracted attention due to the appealing electronic structure, low cost and high stability of the latter. Thus, Salimi et al. [110] synthesized a MIL-125ML: $g\text{-C}_3\text{N}_4$ to remove different concentrations of cefixime under simulated solar light. Authors proposed a photocatalytic mechanism, where electrons in the CB of the $g\text{-C}_3\text{N}_4$ (-1.05 eV vs NHE) flow to the CB of the MIL-125ML (-0.85 eV vs NHE), while holes migrate from the VB of the MIL-125ML (2.01 eV vs NHE) to the VB of $g\text{-C}_3\text{N}_4$ (1.50 eV vs NHE). Thus, this heterojunction achieved more efficient charge separation than the pristine materials. Some works can be found in literature where a semiconductor is coupled with a Ti-MOF, such as TiO_2 , BiOI, CdS, In_2S_3 or Bi_2WO_6 . All these semiconductors have been tested in the degradation of a target EC as tetracycline [111–115].

Multicomponent heterojunctions have also been analysed, formed by more than two visible light active materials and an electron-transfer system. Then, MOFs can be combined with metal NPs and photoactive semiconductors, metal NPs and conducting carbon materials, conducting carbon materials and photoactive semiconductors, among others. Thus, the migration of charges will depend on the components of the heterojunction [116]. For example, in a multicomponent heterojunction of rGO, MIL-125 (Ti) and silver NPs (Figure 1.11), electrons oscillate collectively on the Ag surface plasmon resonance excitation, giving rise a migration of those electrons to MIL-125(Ti) or rGO. On the one hand, MOF can reduce oxygen to generate superoxide radicals, while rGO can form these latter radicals due to an interfacial charge transfer along the rGO sheets. At the same time, hydroxyl radicals ($\cdot\text{OH}$) are formed via the reaction of oxidized Ag species [117].

2.1.5. Metal doping

It is demonstrated the partial substitution of the metal centers can improve the photocatalytic performance of the MOF. The substitution of the metal by another one allows the introduction of new energy level, increasing the photogenerated charge lifetime. This new energy level can be placed close CB or VB depending on the metal dopant (Figure 1.12). Despite extensive research, no data about the effect of the new metal in the photocatalytic mechanism for the removal of ECs have been reported. Even though, it can be confirmed that the metal effect depends on factors such as dopant concentration, dopant distribution and its electronic configuration [118]. Only one work studied the effect of metal doping in NH_2 -MIL-125 to remove an emerging contaminant. Gómez-Aviles et al. [119] introduced different molar ratios of Zr^{4+} in the Ti-MOF to degrade acetaminophen under solar light, reaching the best result with a molar ratio of 15%Zr:85%Ti.

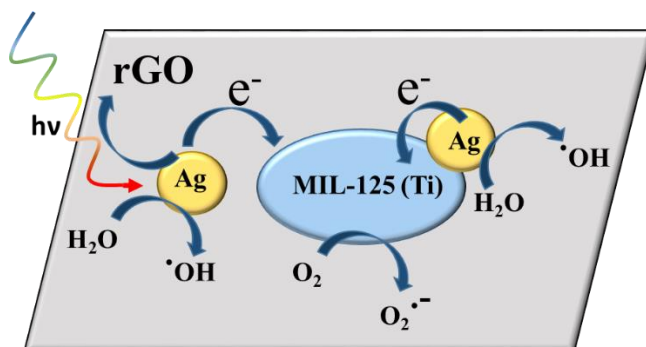


Figure 1.11. Multicomponent heterojunction formed by a MOF, Ag NPs and graphene.

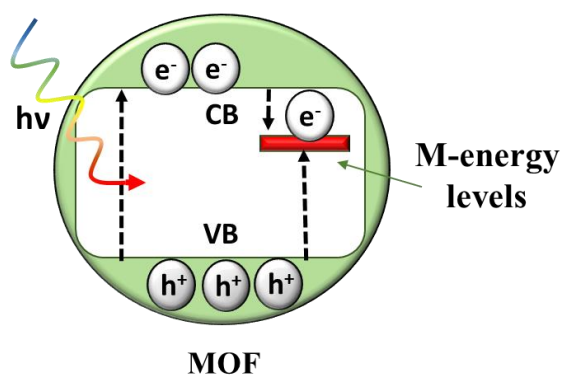


Figure 1.12. Schematic process in metal doped MOF.

References

- [1] Y. Wada, M. Flörke, N. Hanasaki, S. Eisner, G. Fischer, S. Tramberend, Y. Satoh, M.T.H. Van Vliet, P. Yillia, C. Ringler, P. Burek, D. Wiberg, Modeling global water use for the 21st century: the Water Futures and Solutions (WFaS) initiative and its approaches, *Geosci. Model Dev.* 9 (2016) 175–222. doi:10.5194/gmd-9-175-2016.
- [2] WWAP (United Nations World Water Assessment Programme)/UN-Water, *The United Nations World Water Development Report 2018: Nature-Based Solutions for Water*, Paris, (2018).
- [3] T.I.E. Veldkamp, Y. Wada, J.C.J.H. Aerts, P. Döll, S.N. Gosling, J. Liu, Y. Masaki, T. Oki, S. Ostberg, Y. Pokhrel, Y. Satoh, H. Kim, P.J. Ward, Water scarcity hotspots travel downstream due to human interventions in the 20th and 21st century, *Nat. Commun.* 8 (2017) 15697. doi:10.1038/ncomms15697.
- [4] OECD Environmental Performance Reviews: Chile 2016, OECD Publishing, (2016). doi:10.1787/9789264252615-en.
- [5] P.D. United Nations, Department of Economic and Social Affairs, *World Population Prospects: The 2017 Revision, Key Findings and Advance Tables*, (2017). doi:Working Paper No. ESA/P/WP/248.
- [6] WWAP (United Nations World Water Assessment Programme), *The United Nations World Water Development Report 2017*, UNESCO, Paris, (2017).
- [7] Z. Hasan, S.H. Jung, Removal of hazardous organics from water using metal-organic frameworks (MOFs): Plausible mechanisms for selective adsorptions, *J. Hazard. Mater.* 283 (2015) 329–339. doi:10.1016/j.jhazmat.2014.09.046.

- [8] S. Madhav, A. Ahamad, A.K. Singh, J. Kushawaha, J.S. Chauhan, S. Sharma, P. Singh, Water pollutants: sources and impact on the environment and human health, in: Springer, Singapore, (2020) 43–62. doi:10.1007/978-981-15-0671-0_4.
- [9] F. Freyria, F. Geobaldo, B. Bonelli, F.S. Freyria, F. Geobaldo, B. Bonelli, Nanomaterials for the abatement of pharmaceuticals and personal care products from wastewater, *Appl. Sci.* 8 (2018) 170. doi:10.3390/app8020170.
- [10] M. Taheran, M. Naghdi, S.K. Brar, M. Verma, R.Y. Surampalli, Emerging contaminants: Here today, there tomorrow!, *Environ. Nanotechnology, Monit. Manag.* 10 (2018) 122–126. doi:10.1016/j.enmm.2018.05.010.
- [11] United Nations Environment Programme, Good practices for regulating wastewater treatment: legislation, policies and standards, Nairobi, (2015).
- [12] M.O. Barbosa, N.F.F. Moreira, A.R. Ribeiro, M.F.R. Pereira, A.M.T. Silva, Occurrence and removal of organic micropollutants: An overview of the watch list of EU Decision 2015/495, *Water Res.* 94 (2016) 257–279. doi:10.1016/j.watres.2016.02.047.
- [13] Y. Yang, Y.S. Ok, K.H. Kim, E.E. Kwon, Y.F. Tsang, Occurrences and removal of pharmaceuticals and personal care products (PPCPs) in drinking water and water/sewage treatment plants: A review, *Sci. Total Environ.* 596–597 (2017) 303–320. doi:10.1016/j.scitotenv.2017.04.102.
- [14] H.S. Srain, K.F. Beazley, T.R. Walker, Pharmaceuticals and personal care products (PPCPs) and their sublethal and lethal effects in aquatic organisms, *Environ. Rev.* (2020) er-2020-0054. doi:10.1139/er-2020-

References

- 0054.
- [15] M.B. Ahmed, J.L. Zhou, H.H. Ngo, W. Guo, N.S. Thomaidis, J. Xu, Progress in the biological and chemical treatment technologies for emerging contaminant removal from wastewater: A critical review, *J. Hazard. Mater.* 323 (2017) 274–298. doi:10.1016/j.jhazmat.2016.04.045.
- [16] P. Amoatey, A. Al-Mayahi, H. Omidvarborna, M.S. Baawain, H. Sulaiman, Occupational exposure to pesticides and associated health effects among greenhouse farm workers, *Environ. Sci. Pollut. Res.* 27 (2020) 22251–22270. doi:10.1007/s11356-020-08754-9.
- [17] P.R. Rout, T.C. Zhang, P. Bhunia, R.Y. Surampalli, Treatment technologies for emerging contaminants in wastewater treatment plants: A review, *Sci. Total Environ.* 753 (2021) 141990. doi:10.1016/j.scitotenv.2020.141990.
- [18] D. Abu-Ghunmi, L. Abu-Ghunmi, B. Kayal, A. Bino, Circular economy and the opportunity cost of not ‘closing the loop’ of water industry: the case of Jordan, *J. Clean. Prod.* 131 (2016) 228–236. doi:10.1016/j.jclepro.2016.05.043.
- [19] A.I. Stefanakis, J.A. Becker, A review of emerging contaminants in water: Classification, sources, and potential risks, in: *Impact Water Pollut. Hum. Heal. Environ. Sustain.*, IGI Global, (2015) 55–80. doi:10.4018/978-1-4666-9559-7.ch003.
- [20] A.W. Mohammad, Y.H. Teow, W.L. Ang, Y.T. Chung, D.L. Oatley-Radcliffe, N. Hilal, Nanofiltration membranes review: Recent advances and future prospects, *DES.* 356 (2014) 226–254. doi:10.1016/j.desal.2014.10.043.
- [21] C. Grandclément, I. Seyssiecq, A. Piram, P. Wong-Wah-Chung, G.

- Vanot, N. Tiliacos, N. Roche, P. Doumenq, From the conventional biological wastewater treatment to hybrid processes, the evaluation of organic micropollutant removal: A review, *Water Res.* 111 (2017) 297–317. doi:10.1016/j.watres.2017.01.005.
- [22] P. Burkhardt-Holm, Linking water quality to human health and environment : the fate of micropollutants, *Inst. Water Policy.* (2011) 62. doi:10.1080/07900627.2010.489298.
- [23] V.S. Thomaidi, A.S. Stasinakis, V.L. Borova, N.S. Thomaidis, Is there a risk for the aquatic environment due to the existence of emerging organic contaminants in treated domestic wastewater? Greece as a case-study, *J. Hazard. Mater.* 283 (2015) 740–747. doi:10.1016/j.jhazmat.2014.10.023.
- [24] Y. Deng, R. Zhao, Advanced oxidation processes (AOPs) in wastewater treatment, *Curr. Pollut. Reports.* 1 (2015) 167–176. doi:10.1007/s40726-015-0015-z.
- [25] A.R. Ribeiro, O.C. Nunes, M.F.R. Pereira, A.M.T. Silva, An overview on the advanced oxidation processes applied for the treatment of water pollutants defined in the recently launched Directive 2013/39/EU, *Environ. Int.* 75 (2015) 33–51. doi:10.1016/j.envint.2014.10.027.
- [26] S. Singh, K.C. Barick, D. Bahadur, Fe₃O₄ embedded ZnO nanocomposites for the removal of toxic metal ions, organic dyes and bacterial pathogens, *J. Mater. Chem. A.* 1 (2013) 3325. doi:10.1039/c2ta01045c.
- [27] M.I. Litter, Mechanisms of removal of heavy metals and arsenic from water by TiO₂-heterogeneous photocatalysis, *Pure Appl. Chem.* 87 (2015) 557–567. doi:10.1515/pac-2014-0710.

References

- [28] G. Di, Z. Zhu, H. Zhang, J. Zhu, H. Lu, W. Zhang, Y. Qiu, L. Zhu, S. Küppers, Simultaneous removal of several pharmaceuticals and arsenic on Zn-Fe mixed metal oxides: Combination of photocatalysis and adsorption, *Chem. Eng. J.* 328 (2017) 141–151. doi:10.1016/j.cej.2017.06.112.
- [29] L. Zhang, M. Qin, W. Yu, Q. Zhang, H. Xie, Z. Sun, Q. Shao, X. Guo, L. Hao, Y. Zheng, Z. Guo, Heterostructured TiO₂/WO₃ nanocomposites for photocatalytic degradation of toluene under visible light, *J. Electrochem. Soc.* 164 (2017) H1086–H1090. doi:10.1149/2.0881714jes.
- [30] E. Bilgin Simsek, Solvothermal synthesized boron doped TiO₂ catalysts: Photocatalytic degradation of endocrine disrupting compounds and pharmaceuticals under visible light irradiation, *Appl. Catal. B Environ.* 200 (2017) 309–322. doi:10.1016/j.apcatb.2016.07.016.
- [31] O. Carp, C.L. Huisman, A. Reller, Photoinduced reactivity of titanium dioxide, *Prog. Solid State Chem.* 32 (2004) 33–177. doi:10.1016/j.progsolidstchem.2004.08.001.
- [32] N. Ahmed, Heterogeneous photocatalysis and its potential applications in water and wastewater treatment: a review, *Nanotechnology*. 29 (2018) 342001. doi:10.1088/1361-6528/aac6ea.
- [33] J.J. Hopfield, On the energy dependence of the absorption constant and photoconductivity near a direct band gap, *J. Phys. Chem. Solids*. 22 (1961) 63–72. doi:10.1016/0022-3697(61)90244-X.
- [34] M.N. Chong, B. Jin, C.W.K. Chow, C. Saint, Recent developments in photocatalytic water treatment technology: A review, *Water Res.* 44 (2010) 2997–3027. doi:10.1016/j.watres.2010.02.039.

- [35] C.S. Turchi, D.F. Ollis, Photocatalytic degradation of organic water contaminants: Mechanisms involving hydroxyl radical attack, *J. Catal.* 122 (1990) 178–192. doi:10.1016/0021-9517(90)90269-P.
- [36] A. Wold, Photocatalytic properties of TiO₂, *Chem. Mater.* 5 (1993) 280–283. doi:10.1021/cm00027a008.
- [37] J. Bedia, V. Muelas-Ramos, M. Peñas-Garzón, A. Gómez-Avilés, J. Rodríguez, C. Belver, A review on the synthesis and characterization of metal organic frameworks for photocatalytic water purification, *Catalysts.* 9 (2019) 52. doi:10.3390/catal9010052.
- [38] F.L. i. Xamena, J. Gascon, Metal organic frameworks as heterogeneous catalysts, *Catal. Ser.* (2013) 432. doi:10.1039/9781849737586
- [39] A.H. Mamaghani, F. Haghghat, C.S. Lee, Photocatalytic oxidation technology for indoor environment air purification: The state-of-the-art, *Appl. Catal. B Environ.* 203 (2017) 247–269. doi:10.1016/j.apcatb.2016.10.037.
- [40] O. Gimeno, J.F. García-Araya, F.J. Beltrán, F.J. Rivas, A. Espejo, Removal of emerging contaminants from a primary effluent of municipal wastewater by means of sequential biological degradation-solar photocatalytic oxidation processes, *Chem. Eng. J.* 290 (2016) 12–20. doi:10.1016/j.cej.2016.01.022.
- [41] S.Y. Lee, S.J. Park, TiO₂ photocatalyst for water treatment applications, *J. Ind. Eng. Chem.* 19 (2013) 1761–1769. doi:10.1016/j.jiec.2013.07.012.
- [42] R. Daghrir, P. Drogui, D. Robert, Modified TiO₂ for environmental photocatalytic applications: A review, *Ind. Eng. Chem. Res.* 52 (2013)

References

- 3581–3599. doi:10.1021/ie303468t.
- [43] W. Zhang, L. Zou, D. Dionysio, A parametric study of visible-light sensitive TiO₂ photocatalysts synthesis via a facile sol–gel N-doping method, *J. Exp. Nanosci.* 10 (2015) 1153–1165. doi:10.1080/17458080.2014.985751.
- [44] Z. Li, W. Luo, M. Zhang, J. Feng, Z. Zou, Photoelectrochemical cells for solar hydrogen production: Current state of promising photoelectrodes, methods to improve their properties, and outlook, *Energy Environ. Sci.* 6 (2013) 347–370. doi:10.1039/c2ee22618a.
- [45] C.A. Gueymard, D. Myers, K. Emery, Proposed reference irradiance spectra for solar energy systems testing, *Sol. Energy.* 73 (2002) 443–467. doi:10.1016/S0038-092X(03)00005-7.
- [46] K.M. Lee, C.W. Lai, K.S. Ngai, J.C. Juan, Recent developments of zinc oxide based photocatalyst in water treatment technology: A review, *Water Res.* 88 (2016) 428–448. doi:10.1016/j.watres.2015.09.045.
- [47] S.G. Kumar, K.S.R.K. Rao, Comparison of modification strategies towards enhanced charge carrier separation and photocatalytic degradation activity of metal oxide semiconductors (TiO₂, WO₃ and ZnO), *Appl. Surf. Sci.* 391 (2017) 124–148. doi:10.1016/j.apsusc.2016.07.081.
- [48] R. Fagan, D.E. McCormack, D.D. Dionysiou, S.C. Pillai, A review of solar and visible light active TiO₂ photocatalysis for treating bacteria, cyanotoxins and contaminants of emerging concern, *Mater. Sci. Semicond. Process.* 42 (2016) 2–14. doi:10.1016/j.mssp.2015.07.052.
- [49] C. Mondal, A. Singh, R. Sahoo, A.K. Sasmal, Y. Negishi, T. Pal, Preformed ZnS nanoflower prompted evolution of CuS/ZnS p–n

- heterojunctions for exceptional visible-light driven photocatalytic activity, *New J. Chem.* 39 (2015) 5628–5635. doi:10.1039/C5NJ00128E.
- [50] G.J. Lee, J.J. Wu, Recent developments in ZnS photocatalysts from synthesis to photocatalytic applications — A review, *Powder Technol.* 318 (2017) 8–22. doi:10.1016/j.powtec.2017.05.022.
- [51] C. Wang, H. Lin, Z. Xu, H. Cheng, C. Zhang, One-step hydrothermal synthesis of flowerlike MoS₂/CdS heterostructures for enhanced visible-light photocatalytic activities, *RSC Adv.* 5 (2015) 15621–15626. doi:10.1039/C4RA15632C.
- [52] H.A.J.L. Mourão, O.F. Lopes, C. Ribeiro, V.R. Mastelaro, Rapid hydrothermal synthesis and pH-dependent photocatalysis of strontium titanate microspheres, *Mater. Sci. Semicond. Process.* 30 (2015) 651–657. doi:10.1016/j.mssp.2014.09.022.
- [53] M. Rastogi, H.S. Kushwaha, R. Vaish, Highly efficient visible light mediated azo dye degradation through barium titanate decorated reduced graphene oxide sheets, *Electron. Mater. Lett.* 12 (2016) 281–289. doi:10.1007/s13391-015-5274-8.
- [54] Z. Hua, X. Zhang, X. Bai, L. Lv, Z. Ye, X. Huang, Nitrogen-doped perovskite-type La₂Ti₂O₇ decorated on graphene composites exhibiting efficient photocatalytic activity toward bisphenol A in water, *J. Colloid Interface Sci.* 450 (2015) 45–53. doi:10.1016/j.jcis.2015.02.061.
- [55] J. Zhang, X. Yuan, L. Jiang, Z. Wu, X. Chen, H. Wang, H. Wang, G. Zeng, Highly efficient photocatalysis toward tetracycline of nitrogen doped carbon quantum dots sensitized bismuth tungstate based on interfacial charge transfer, *J. Colloid Interface Sci.* 511 (2018) 296–

References

306. doi:10.1016/j.jcis.2017.09.083.
- [56] Y.A. Sethi, C.S. Praveen, R.P. Panmand, A. Ambalkar, A.K. Kulkarni, S.W. Gosavi, M. V. Kulkarni, B.B. Kale, Perforated N-doped monoclinic ZnWO₄ nanorods for efficient photocatalytic hydrogen generation and RhB degradation under natural sunlight, *Catal. Sci. Technol.* 8 (2018) 2909–2919. doi:10.1039/C8CY00521D.
- [57] S.M. Thalluri, S. Hernández, S. Bensaid, G. Saracco, N. Russo, Green-synthesized W- and Mo-doped BiVO₄ oriented along the {0 4 0} facet with enhanced activity for the sun-driven water oxidation, *Appl. Catal. B Environ.* 180 (2016) 630–636. doi:10.1016/j.apcatb.2015.07.029.
- [58] A. Kubacka, M. Fernández-García, G. Colón, Advanced nanoarchitectures for solar photocatalytic applications, *Chem. Rev.* 112 (2012) 1555–1614. doi:10.1021/cr100454n.
- [59] Y. Huang, W. Fan, B. Long, H. Li, F. Zhao, Z. Liu, Y. Tong, H. Ji, Visible light Bi₂S₃/Bi₂O₃/Bi₂O₂CO₃ photocatalyst for effective degradation of organic pollutions, *Appl. Catal. B Environ.* 185 (2016) 68–76. doi:10.1016/j.apcatb.2015.11.043.
- [60] M. Sun, S. Li, T. Yan, P. Ji, X. Zhao, K. Yuan, D. Wei, B. Du, Fabrication of heterostructured Bi₂O₂CO₃/Bi₂O₄ photocatalyst and efficient photodegradation of organic contaminants under visible-light, *J. Hazard. Mater.* 333 (2017) 169–178. doi:10.1016/j.jhazmat.2017.03.027.
- [61] P. Madhusudan, J. Ran, J. Zhang, J. Yu, G. Liu, Novel urea assisted hydrothermal synthesis of hierarchical BiVO₄/Bi₂O₂CO₃ nanocomposites with enhanced visible-light photocatalytic activity, *Appl. Catal. B, Environ.* 110 (2011) 286–295.

- doi:10.1016/j.apcatb.2011.09.014.
- [62] W.K. Jo, R.J. Tayade, New generation energy-efficient light source for photocatalysis: LEDs for environmental applications, *Ind. Eng. Chem. Res.* 53 (2014) 2073–2084. doi:10.1021/ie404176g.
- [63] M.A.I. Molla, I. Tateishi, M. Furukawa, H. Katsumata, T. Suzuki, S. Kaneco, Photocatalytic decolorization of dye with self-dye-sensitization under fluorescent light irradiation, *ChemEngineering*. 1 (2017) 8. doi:10.3390/chemengineering1020008.
- [64] O. Tokode, R. Prabhu, L.A. Lawton, P.K.J. Robertson, UV LED sources for heterogeneous photocatalysis, in: *Handb. Environ. Chem.*, (2015) 159–179. doi:10.1007/698_2014_306.
- [65] J.L.C. Rowsell, O.M. Yaghi, Metal-organic frameworks: a new class of porous materials, *Microporous Mesoporous Mater.* 73 (2004) 3–14. doi:10.1016/j.micromeso.2004.03.034.
- [66] M. Eddaoudi, J. Kim, N. Rosi, D. Vodak, J. Wachter, M. O’Keeffe, O.M. Yaghi, Systematic design of pore size and functionality in isorecticular MOFs and their application in methane storage., *Science*. 295 (2002) 469–72. doi:10.1126/science.1067208.
- [67] L. Zhu, X.Q. Liu, H.L. Jiang, L.B. Sun, Metal–organic frameworks for heterogeneous basic catalysis, *Chem. Rev.* 117 (2017) 8129–8176. doi:10.1021/acs.chemrev.7b00091.
- [68] Y.B. Huang, J. Liang, X.S. Wang, R. Cao, Multifunctional metal–organic framework catalysts: synergistic catalysis and tandem reactions, *Chem. Soc. Rev.* 46 (2017) 126–157. doi:10.1039/C6CS00250A.
- [69] Z.T. Yu, Z.L. Liao, Y.S. Jiang, G.H. Li, G.D. Li, J.S. Chen,

References

- Construction of a microporous inorganic-organic hybrid compound with uranyl units, *Chem. Commun.* 0 (2004) 1814–1815. doi:10.1039/b406019a.
- [70] D. Wang, F. Jia, H. Wang, F. Chen, Y. Fang, W. Dong, G. Zeng, X. Li, Q. Yang, X. Yuan, Simultaneously efficient adsorption and photocatalytic degradation of tetracycline by Fe-based MOFs, *J. Colloid Interface Sci.* 519 (2018) 273–284. doi:10.1016/J.JCIS.2018.02.067.
- [71] M. Eddaoudi, D.B. Moler, H. Li, B. Chen, T.M. Reineke, M. O’keeffe, O.M. Yaghi, Modular chemistry: secondary building units as a basis for the design of highly porous and robust metal-organic carboxylate frameworks, *Ann Acc. Chem. Res.* 34 (1995) 319–330. doi:10.1021/ar000034b.
- [72] E. Sharmin, F. Zafar, Introductory chapter: Metal organic frameworks (MOFs), in: *Met. Fram., InTech*, (2016). doi:10.5772/64797.
- [73] O.M. Yaghi, G. Li, H. Li, Selective binding and removal of guests in a microporous metal–organic framework, *Nature.* 378 (1995) 703–706. doi:10.1038/378703a0.
- [74] Z. Wei, New design and synthetic strategies of metal-organic frameworks, *Thesis Diss.* (2014).
- [75] E. Perez, C. Karunaweera, I. Musselman, K. Balkus, J. Ferraris, Origins and evolution of inorganic-based and MOF-based mixed-matrix membranes for gas separations, *Processes.* 4 (2016) 32. doi:10.3390/pr4030032.
- [76] J. Dai, X. Xiao, S. Duan, J. Liu, J. He, J. Lei, L. Wang, Synthesis of novel microporous nanocomposites of ZIF-8 on multiwalled carbon nanotubes for adsorptive removing benzoic acid from water, *Chem.*

- Eng. J. 331 (2018) 64–74. doi:10.1016/j.cej.2017.08.090.
- [77] O.K. Farha, J.T. Hupp, Rational design, synthesis, purification, and activation of metal-organic framework materials, *Acc. Chem. Res.* 43 (2010) 1166–1175. doi:10.1021/ar1000617.
- [78] H. Furukawa, K.E. Cordova, M. O’Keeffe, O.M. Yaghi, The chemistry and applications of metal-organic frameworks, *Science*. 341 (2013) 1230444. doi:10.1126/science.1230444.
- [79] J. Liu, T. Liu, C. Wang, X. Yin, Z. Xiong, Introduction of amidoxime groups into metal-organic frameworks to synthesize MIL-53(Al)-AO for enhanced U(VI) sorption, *J. Mol. Liq.* 242 (2017) 531–536. doi:10.1016/J.MOLLIQ.2017.07.024.
- [80] X. Zhang, Z. Chen, X. Liu, S.L. Hanna, X. Wang, R. Taheri-Ledari, A. Maleki, P. Li, O.K. Farha, A historical overview of the activation and porosity of metal-organic frameworks, *Chem. Soc. Rev.* 49 (2020) 7406–7427. doi:10.1039/d0cs00997k.
- [81] J.L. Woodliffe, R.S. Ferrari, I. Ahmed, A. Laybourn, Evaluating the purification and activation of metal-organic frameworks from a technical and circular economy perspective, *Coord. Chem. Rev.* 428 (2021) 213578. doi:10.1016/j.ccr.2020.213578.
- [82] A.P. Nelson, O.K. Farha, K.L. Mulfort, J.T. Hupp, Supercritical processing as a route to high internal surface areas and permanent microporosity in metal-organic framework materials, *J. Am. Chem. Soc.* 131 (2009) 458–460. doi:10.1021/ja808853q.
- [83] J. Espín, L. Garzón-Tovar, A. Carné, C. Sánchez, I. Imaz, D. Maspoch, Photothermal activation of metal-organic frameworks using a UV–vis light source, *ACS Appl. Mater. Interfaces*. 10 (2018)

References

52. doi:10.1021/acsami.8b00557.
- [84] J.E. Mondloch, O. Karagiari, O.K. Farha, J.T. Hupp, Activation of metal–organic framework materials, *Chem. Commun.* 15 (2013) 9258. doi:10.1039/c3ce41232f.
- [85] M. Alvaro, E. Carbonell, B. Ferrer, F.X. Llabrés I Xamena, H. Garcia, Semiconductor behavior of a metal-organic framework (MOF), *Chem. - A Eur. J.* 13 (2007) 5106–5112. doi:10.1002/chem.200601003.
- [86] M. Dan-Hardi, C. Serre, T. Frot, L. Rozes, G. Maurin, C. Sanchez, G. Férey, A new photoactive crystalline highly porous titanium (IV) dicarboxylate, *J. Am. Chem. Soc.* 131 (2009) 10857–10859. doi:10.1021/ja903726m.
- [87] J. Zhu, P.Z. Li, W. Guo, Y. Zhao, R. Zou, Titanium-based metal–organic frameworks for photocatalytic applications, *Coord. Chem. Rev.* 359 (2018) 80–101. doi:10.1016/j.ccr.2017.12.013.
- [88] L. Shen, R. Liang, L. Wu, Strategies for engineering metal-organic frameworks as efficient photocatalysts, *Chinese J. Catal.* 36 (2015) 2071–2088. doi:10.1016/S1872-2067(15)60984-6.
- [89] C.H. Hendon, D. Tiana, M. Fontecave, C.C. Sanchez, L. D'arras, C. Sasse, L. Rozes, C. Mellot-Draznieks, A. Walsh, Engineering the optical response of the titanium-MIL-125 metal-organic framework through ligand functionalization, *J. Am. Chem. Soc.* 135 (2013) 10942–10945. doi:10.1021/ja405350u.
- [90] Y. Yan, C. Li, Y. Wu, J. Gao, Q. Zhang, From isolated Ti-oxo clusters to infinite Ti-oxo chains and sheets: Recent advances in photoactive Ti-based MOFs, *J. Mater. Chem. A* 8 (2020) 15245–15270. doi:10.1039/d0ta03749d.

- [91] D. Farrusseng, *Metal-organic frameworks: applications from catalysis to gas storage*, Wiley-VCH, (2011).
- [92] Z. Wang, S.M. Cohen, Postsynthetic modification of metal–organic frameworks, *Chem. Soc. Rev.* 38 (2009) 1315–1329. doi:10.1039/b802258p.
- [93] S.M. Cohen, Postsynthetic methods for the functionalization of metal-organic frameworks, *Chem. Rev.* 112 (2012) 970–1000. doi:10.1021/cr200179u.
- [94] M. Lalonde, W. Bury, O. Karagiari, Z. Brown, J.T. Hupp, O.K. Farha, Transmetalation: Routes to metal exchange within metal-organic frameworks, *J. Mater. Chem. A* 1 (2013) 5453–5468. doi:10.1039/c3ta10784a.
- [95] A. Karmakar, A. V. Desai, S.K. Ghosh, Ionic metal-organic frameworks (iMOFs): Design principles and applications, *Coord. Chem. Rev.* 307 (2016) 313–341. doi:10.1016/j.ccr.2015.08.007.
- [96] A. Aijaz, A. Karkamkar, Y.J. Choi, N. Tsumori, E. Rönnebro, T. Autrey, H. Shioyama, Q. Xu, Immobilizing highly catalytically active Pt nanoparticles inside the pores of metal–organic framework: A double solvents approach, *J. Am. Chem. Soc.* 134 (2012) 13926–13929. doi:10.1021/ja3043905.
- [97] D. Sun, Z. Li, Double-solvent method to Pd nanoclusters encapsulated inside the cavity of NH₂–Uio-66(Zr) for efficient visible-light-promoted Suzuki coupling reaction, *J. Phys. Chem. C* 120 (2016) 19744–19750. doi:10.1021/acs.jpcc.6b06710.
- [98] J. Qiu, L. Yang, M. Li, J. Yao, Metal nanoparticles decorated MIL-125-NH₂ and MIL-125 for efficient photocatalysis, *Mater. Res. Bull.*

References

- 112 (2019) 297–306. doi:10.1016/J.MATERRESBULL.2018.12.038.
- [99] M. Meilikhov, K. Yusenko, D. Esken, S. Turner, G. Van Tendeloo, R.A. Fischer, *Metals@MOFs - loading MOFs with metal nanoparticles for hybrid functions*, *Eur. J. Inorg. Chem.* (2010) 3701–3714. doi:10.1002/ejic.201000473.
- [100] Q. Wang, Q. Gao, A.M. Al-Enizi, A. Nafady, S. Ma, *Recent advances in MOF-based photocatalysis: Environmental remediation under visible light*, *Inorg. Chem. Front.* 7 (2020) 300–339. doi:10.1039/c9qi01120j.
- [101] X. Han, X. Yang, G. Liu, Z. Li, L. Shao, *Boosting visible light photocatalytic activity via impregnation-induced RhB-sensitized MIL-125(Ti)*, *Chem. Eng. Res. Des.* 143 (2019) 90–99. doi:10.1016/J.CHERD.2019.01.010.
- [102] L.H. Zhang, Y. Zhu, B.R. Lei, Y. Li, W. Zhu, Q. Li, *Trichromatic dyes sensitized HKUST-1 (MOF-199) as scavenger towards reactive blue 13 via visible-light photodegradation*, *Inorg. Chem. Commun.* 94 (2018) 27–33. doi:10.1016/j.inoche.2018.05.027.
- [103] A.K.M. Fung, B.K.W. Chiu, M.H.W. Lam, *Surface modification of TiO₂ by a ruthenium(II) polypyridyl complex via silyl-linkage for the sensitized photocatalytic degradation of carbon tetrachloride by visible irradiation*, *Water Res.* 37 (2003) 1939–1947. doi:10.1016/S0043-1354(02)00567-5.
- [104] S.R. Thakare, S.M. Ramteke, *Postmodification of MOF-5 using secondary complex formation using 8- hydroxyquinoline (HOQ) for the development of visible light active photocatalysts*, *J. Phys. Chem. Solids.* 116 (2018) 264–272. doi:10.1016/j.jpcs.2018.01.032.
- [105] Q. Liang, M. Zhang, Z. Zhang, C. Liu, S. Xu, Z. Li, *Zinc*

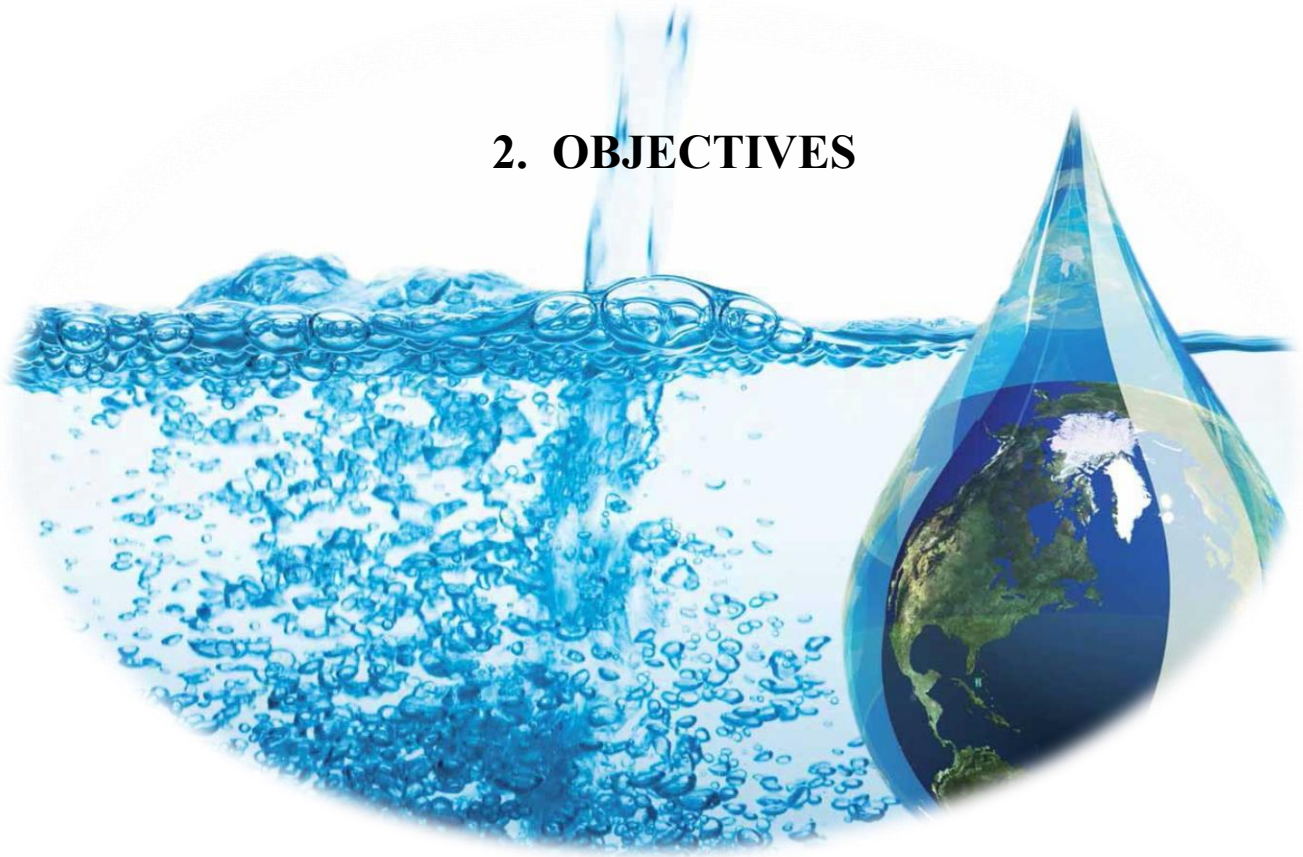
- phthalocyanine coupled with UIO-66 (NH₂) via a facile condensation process for enhanced visible-light-driven photocatalysis, *J. Alloys Compd.* 690 (2017) 123–130. doi:10.1016/j.jallcom.2016.08.087.
- [106] A. Di Paola, E. García-López, G. Marci, L. Palmisano, A survey of photocatalytic materials for environmental remediation, *J. Hazard. Mater.* 211–212 (2012) 3–29. doi:10.1016/j.jhazmat.2011.11.050.
- [107] L. Zhang, M. Jaroniec, Toward designing semiconductor-semiconductor heterojunctions for photocatalytic applications, *Appl. Surf. Sci.* 430 (2018) 2–17. doi:10.1016/j.apsusc.2017.07.192.
- [108] D. Huang, S. Chen, G. Zeng, X. Gong, C. Zhou, M. Cheng, W. Xue, X. Yan, J. Li, Artificial Z-scheme photocatalytic system: What have been done and where to go?, *Coord. Chem. Rev.* 385 (2019) 44–80. doi:10.1016/j.ccr.2018.12.013.
- [109] Y. Ren, D. Zeng, W.J. Ong, Interfacial engineering of graphitic carbon nitride (g-C₃N₄)-based metal sulfide heterojunction photocatalysts for energy conversion: A review, *Chinese J. Catal.* 40 (2019) 289–319. doi:10.1016/s1872-2067(19)63293-6.
- [110] M. Salimi, A. Esrafil, A. Jonidi Jafari, M. Gholami, H.R. Sobhi, M. Nourbakhsh, B. Akbari-Adergani, Photocatalytic degradation of cefixime with MIL-125(Ti)-mixed linker decorated by g-C₃N₄ under solar driven light irradiation, *Colloids Surfaces A Physicochem. Eng. Asp.* 582 (2019) 123874. doi:10.1016/j.colsurfa.2019.123874.
- [111] X. Li, Y. Pi, Q. Hou, H. Yu, Z. Li, Y. Li, J. Xiao, Amorphous TiO₂@NH₂-MIL-125(Ti) homologous MOF-encapsulated heterostructures with enhanced photocatalytic activity, *Chem. Commun.* 54 (2018) 1917–1920. doi:10.1039/c7cc09072b.

References

- [112] W. Jiang, Z. Li, C. Liu, D. Wang, G. Yan, B. Liu, G. Che, Enhanced visible-light-induced photocatalytic degradation of tetracycline using BiOI/MIL-125(Ti) composite photocatalyst, *J. Alloys Compd.* 854 (2021) 157166. doi:10.1016/j.jallcom.2020.157166.
- [113] H. Wang, P.H. Cui, J.X. Shi, J.Y. Tan, J.Y. Zhang, N. Zhang, C. Zhang, Controllable self-assembly of CdS@NH₂-MIL-125(Ti) heterostructure with enhanced photodegradation efficiency for organic pollutants through synergistic effect, *Mater. Sci. Semicond. Process.* 97 (2019) 91–100. doi:10.1016/j.mssp.2019.03.016.
- [114] H. Wang, X. Yuan, Y. Wu, G. Zeng, H. Dong, X. Chen, L. Leng, Z. Wu, L. Peng, In situ synthesis of In₂S₃@MIL-125(Ti) core-shell microparticle for the removal of tetracycline from wastewater by integrated adsorption and visible-light-driven photocatalysis, *Appl. Catal. B Environ.* 186 (2016) 19–29. doi:10.1016/J.APCATB.2015.12.041.
- [115] S. Yin, Y. Chen, C. Gao, Q. Hu, M. Li, Y. Ding, J. Di, J. Xia, H. Li, In-situ preparation of MIL-125(Ti)/Bi₂WO₆ photocatalyst with accelerating charge carriers for the photodegradation of tetracycline hydrochloride, *J. Photochem. Photobiol. A Chem.* 387 (2020) 112149. doi:10.1016/j.jphotochem.2019.112149.
- [116] H. Wang, L. Zhang, Z. Chen, J. Hu, S. Li, Z. Wang, J. Liu, X. Wang, Semiconductor heterojunction photocatalysts: Design, construction, and photocatalytic performances, *Chem. Soc. Rev.* 43 (2014) 5234–5244. doi:10.1039/c4cs00126e.
- [117] X. Yuan, H. Wang, Y. Wu, G. Zeng, X. Chen, L. Leng, Z. Wu, H. Li, One-pot self-assembly and photoreduction synthesis of silver nanoparticle-decorated reduced graphene oxide/MIL-125(Ti)

- photocatalyst with improved visible light photocatalytic activity, *Appl. Organomet. Chem.* 30 (2016) 289–296. doi:10.1002/aoc.3430.
- [118] J. Liu, J. Xiao, D. Wang, W. Sun, X. Gao, H. Yu, H. Liu, Z. Liu, Construction and photocatalytic activities of a series of isostructural $\text{Co}^{2+}/\text{Zn}^{2+}$ metal-doped metal-organic frameworks, *Cryst. Growth Des.* 17 (2017) 1096–1102. doi:10.1021/acs.cgd.6b01488.
- [119] A. Gómez-Avilés, M. Peñas-Garzón, J. Bedia, D.D. Dionysiou, J.J. Rodríguez, C. Belver, Mixed Ti-Zr metal-organic-frameworks for the photodegradation of acetaminophen under solar irradiation, *Appl. Catal. B Environ.* 253 (2019) 253–262. doi:10.1016/j.apcatb.2019.04.040.

2. OBJECTIVES

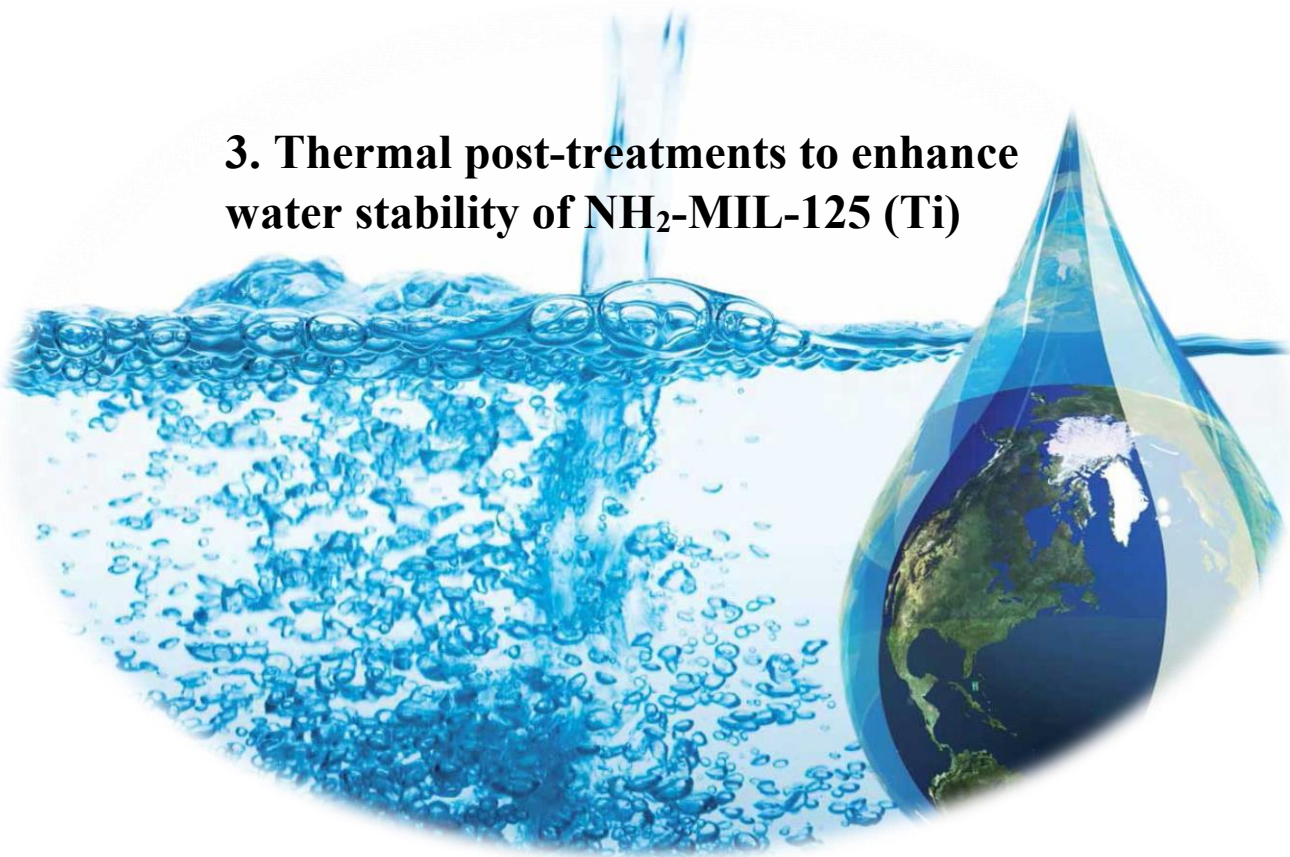


The main objective of this thesis is the synthesis of photocatalysts based on NH₂-MIL-125(Ti) metal organic framework devoted to degrading emerging contaminants from water by using solar or LED irradiation.

To achieve this main purpose, the thesis followed the steps indicated below:

1. Synthesis and characterization of NH₂-MIL-125 MOF by a solvothermal procedure.
2. Study and improvement of the stability in water of NH₂-MIL-125 by different thermal treatments, analysing the lixiviation of the organic linker on the aqueous medium.
3. Evaluation of the combination of the NH₂-MIL-125 with g-C₃N₄ in the formation of hybrid materials, to remove diclofenac under LED irradiation.
4. Study the effect of deposited metal nanoparticles, palladium, platinum and silver on MOF surface, testing these materials in the photodegradation of acetaminophen under solar simulated irradiation.
5. Grafting of the organic linker through a post-modification method, introducing heterocycles to check if the removal of acetaminophen, sulfamethoxazole and antipyrine can be improved.

3. Thermal post-treatments to enhance water stability of NH₂-MIL-125 (Ti)



Article

Thermal Post-Treatments to Enhance the Water Stability of NH₂-MIL-125(Ti)

Almudena Gómez-Avilés, Virginia Muelas-Ramos, Jorge Bedia *, Juan Jose Rodriguez and Carolina Belver *

Chemical Engineering Department, Universidad Autónoma de Madrid, Campus Cantoblanco, E-28049 Madrid, Spain; almudena.gomez@uam.es (A.G.-A.); virginia.muelas@uam.es (V.M.-R.); juanjo.rodriiguez@uam.es (J.J.R.)

* Correspondence: jorge.bedia@uam.es (J.B.); carolina.belver@uam.es (C.B.); Tel.: +34-91-497-29-11 (J.B.); +34-91-497-84-73 (C.B.)

Received: 20 April 2020; Accepted: 27 May 2020; Published: 29 May 2020

Abstract: NH₂-MIL-125(Ti) is a metal organic framework (MOF) based on Ti-oxo-clusters widely investigated in water-related applications. Such applications require MOFs with an excellent stability in the aqueous phase, but, despite this, the extent of MOFs' degradation in water is still not yet fully understood. In this study, we report a quantitative study of the water stability of NH₂-MIL-125(Ti), analyzing the ligand release along the contact time in water. This study demonstrates that NH₂-MIL-125(Ti) easily leached out over time while maintaining its structure. The effect of different thermal treatments applied to NH₂-MIL-125(Ti) was investigated to enhance its water stability. The structural and textural properties of those modified MOFs were studied in detail and those maintaining the NH₂-MIL-125(Ti) properties were exposed to aqueous medium. The analysis of the released ligand concentration in the filtrate can provide information on the water stability of this material.

Keywords: metal organic frameworks; NH₂-MIL-125(Ti); water stability; purification

1. Introduction

Metal organic frameworks (MOFs) constitute a group of materials consisting of the repetitive assembling of organic linkers and cluster metal ions. The resulting crystalline structures have a large specific surface area and a well-defined porosity. Their physicochemical properties can be tailored by selecting the nature and combination of both components yielding numerous MOFs [1,2]. MOFs have gained growing importance in many applications, such as gas storage [3,4], sensing [5,6], membrane processes [7], drug delivery [8,9], and environmental remediation [10–13]. In this last field, MOFs have been investigated in water purification, especially as: (i) adsorbents for the removal of hazardous pollutants [14–16], (ii) catalysts for the degradation of contaminants by Advanced Oxidation Processes (AOPs), such as heterogeneous Fenton and photo-assisted treatments [17–19], and (iii) membrane materials for the separation of toxic substances from water streams [20]. The growing interest in these applications is leading researchers to develop MOFs with high stability in aqueous medium.

The literature describes examples of unstable MOFs that lose their structure and pore network when exposed to water, such as MOF-5, while others showed stability in water, even after months, or have not been fully tested in this respect [21,22]. The stability of MOFs can be related to an assembly–disassembly equilibrium where both the electronic and steric effects between the linker and the metal cluster play an important role. Several studies have shown that the instability under wet conditions depends on the metal–linker bond strength [23,24]. Using highly basic ligands or acid metals results in much stronger bonds and greater stability in water, as in the cases of ZIF-8 or Al-

MIL-53 [25]. In addition, the linker structure, the nature of the metal and the coordination of the clusters also play an important role. Thus, hydrophobic linkers, inert metal cations and high-coordination clusters usually improve water stability. Moreover, high-charge metal ions lead to a stronger oxo-philic tendency that significantly strengthens the metal–linker bonds and improves the chemical stability of MOF [21]. Group-IV-metal- (Ti, Zr, Hf) based MOFs are examples of high-charge metal oxo-clusters, yielding abundant MOF structures with different coordination numbers and structural diversity [26–29]. Ti-based MOFs have received great attention because of their redox activity (Ti^{3+}/Ti^{4+} transition capacity), photochemical property and biocompatibility [30]. Those based on Ti-carboxylate complexes have high stability and their functional properties can be improved by organic functionalization, mainly by amine groups [31,32]. The degradation of MOFs exposed to water can occur by two different mechanisms, ligand displacement and hydrolysis [25]. The ligand displacement involves the exchange of a ligand by a water molecule, leading to the hydration of the metal and ligand lixiviation; while, upon hydrolysis, water dissociation occurs at the metal centers, the dissociated OH groups coordinate to the metal clusters and the metal–ligand bond is broken [33].

Nevertheless, predicting the water stability of MOFs remains qualitative and the literature is controversial, mainly due to the methodology used to assess the stability. The simplest process consists of exposing the MOF to water and comparing its properties prior and after a given contact time, mainly by weight loss, X-ray diffraction and N_2 adsorption–desorption at $-196\text{ }^\circ\text{C}$ [29]. Water adsorption–desorption isotherms are also useful since they provide information about the hydrophilic–hydrophobic character of MOFs [34]. Additionally, however, if the MOF is being considered for application in the aqueous phase, it should also be investigated whether the sample is partially dissolved [29,35]. Recently, Taheri et al. [36] performed a quantitative study of the ligand and Zn^{2+} released when ZIF-8 was immersed in water. They observed that the lixiviation of both species occurred during the first hour and after 24 h an equilibrium was achieved. No other studies deal with the analysis of the filtrate instead of the remaining solid in the literature. Lixiviation from the MOF must be considered for the sake of application in water remediation since the released metals and/or ligands can represent some hazards for the environment.

The literature contains examples concerning the post-modifications of MOFs to improve their water stability. Wen et al. [37] coated NH_2 -MIL-125(Ti) with a siloxane that increased its dye adsorption capacity while maintaining its crystal structure and morphology. Composites based on UiO -66- NH_2 and a nitrile butadiene rubber sponge are more stable in water than the bare MOF because the sponge provides a hydrophobic character that prevents hydrolysis. These composites were shown to be efficient adsorbents for 2,4-dichlorophenoxyacetic acid removal from water and were easily recoverable thanks to its sponge conformation [38]. An interesting study has recently been reported, describing the improved water stability of ZIF-8 by growing it along with UiO -66- NH_2 , giving rise to a core–shell UiO -66- NH_2 @ZIF-8 hybrid. This heterostructure showed excellent water stability, high adsorption capacity and selectivity for the separation of rare earths from water compared to other adsorbents [39]. Non-amine UiO -66 has been also incorporated in a composite membrane based on graphene oxide (GO) with a high water stability and highly efficient for dyes and antibiotics separation [40]. Although interesting, many of these modifications are not so easy to implement in technical applications.

Here, we focus the attention on NH_2 -MIL-125(Ti), a Ti-oxo-cluster MOF, due to its notable interest in water treatment by photocatalysis, a well-known AOP for the removal of different pollutants [1,41–43]. In a previous study, we demonstrated its high photocatalytic efficiency for the removal of some emerging pollutants and its stability during the reaction, comparing its structural, textural and morphologic properties before and after use [44]. However, in a preliminary test, additional organic matter was detected in the aqueous medium after reaction, thus suggesting that certain partial dissolution of the solid occurred. Thus, in this work, we initially studied the water stability of NH_2 -MIL-125(Ti) through a systematic analysis of the aqueous phase. Then, in order to improve its stability, NH_2 -MIL-125(Ti) was subjected to various thermal treatments. In particular, the study highlights that the stability of NH_2 -MIL-125(Ti) in water can be successfully improved, providing useful information for water-related applications.

2. Results and Discussion

2.1. Stability of the NH₂-MIL-125(Ti)

NH₂-MIL-125(Ti) is an amine-functionalized isostructure of the MIL-125(Ti) formed by both octahedral and tetrahedral cages [45,46]. It is composed by titanium oxo-clusters and aminoterephthalate, both providing a high density of hydrophilic sites where water molecules can be adsorbed [47]. We had previously synthesized NH₂-MIL-125(Ti), doped and successfully used as solar-light driven photocatalyst [44]. Although its structural stability under the reaction conditions was confirmed by X-ray diffraction, scanning electron microscopy and N₂ adsorption-desorption at -196 °C, some ligand release was detected in the aqueous medium. To the best of our knowledge, there are no reports about the amount of linker leached when NH₂-MIL-125(Ti) is put in contact with water. Thus, to determine the amount of released linker, NH₂-MIL-125(Ti) was suspended in aqueous medium and the filtrates were analyzed, the leachate percentage being determined by:

$$\text{Leachate (\%)} = 100 \times \frac{C_{\text{linker}}}{C_{\text{NH}_2\text{-MIL-125(Ti)}}} \cdot \frac{M_{\text{NH}_2\text{-MIL-125(Ti)}}}{6 \times M_{\text{linker}}} \quad (1)$$

where C_{linker} is the linker concentration dissolved in the liquid phase ($\text{mg}\cdot\text{L}^{-1}$), $C_{\text{NH}_2\text{-MIL-125(Ti)}}$ is the concentration of the MOF suspended in water, $M_{\text{NH}_2\text{-MIL-125(Ti)}}$ and M_{linker} are the molecular weight values of the MOF ($1653.74 \text{ g}\cdot\text{mol}^{-1}$) and the linker (2-amino benzene dicarboxylate, NH₂-BDC, $179.12 \text{ g}\cdot\text{mol}^{-1}$), respectively. Figure 1a shows the evolution of dissolved linker and the corresponding leachate percentage upon contact time. NH₂-MIL-125(Ti) undergoes relatively high linker leaching in water, which increases significantly over time to reach $40 \text{ mg}\cdot\text{L}^{-1}$ after 24 h, about 25% of the initial linker content of bare NH₂-MIL-125(Ti). This leaching process occurs continuously over time, without reaching equilibrium. Similar behavior has recently been reported for ZIF-8, whose lixiviation started during the first hour and required one day to achieve equilibrium [36]. This leaching is detrimental regarding the potential water-related applications of NH₂-MIL-125(Ti). For the sake of improving the stability of NH₂-MIL-125(Ti) by reducing ligand leaching as much as possible, this MOF was subjected to different thermal treatments at different temperatures and holding times and under different atmospheres. The temperature was selected after studying the thermal behavior of this MOF by thermogravimetric analysis in air (Figure 1b). NH₂-MIL-125(Ti) is thermally robust and suffers a strong weight loss of 54% within the 300 to 350 °C range, due to the oxidation of the organic linkers [36,48]. After increasing the temperature up to 500 °C, a small weight loss (9%) occurs, corresponding to the removal of the hydroxo-groups in the metal oxo-clusters, giving rise to TiO₂, in a similar way to the analogous non-amine MIL-125(Ti) [46,49]. Based on this analysis, the 150–300 °C range was selected for the thermal treatment addressed to stabilize the NH₂-MIL-125(Ti) without disturbing its structure and composition.

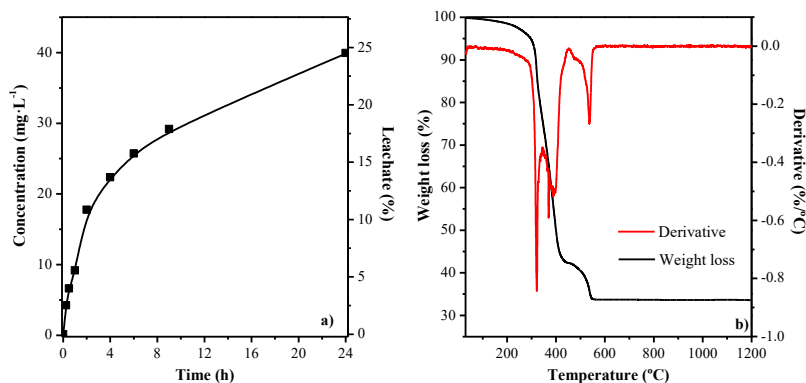


Figure 1. a) Time course of linker concentration and leachate percentage in water from NH₂-MIL-125(Ti) upon contact time; b) thermogravimetric analysis in air of NH₂-MIL-125(Ti) and its corresponding derivative.

2.2. Vacuum Treatment

During the synthesis of MOFs, excess ligand and solvent molecules can remain trapped in the pores of the framework, which can be detrimental for their future applications. In some cases, vacuum drying may be sufficient to purify the MOF, although it can lead to lower surface areas than expected due to the partial collapse of the structure [35]. NH₂-MIL-125(Ti) was thus subjected to vacuum treatment in a temperature range of 100 to 300 °C for 16 h to remove the excess linker and solvent molecules. Figure 2 shows the X-ray diffraction (XRD) patterns of the modified solids compared with that of the bare NH₂-MIL-125(Ti). In the notation, “V” refers to vacuum treatment, and the numbers represent the temperature (°C) and time in hours of the vacuum treatment. As can be seen, this treatment does not modify the crystalline structure of the MOF until reaching 300 °C. At this temperature, the NH₂-MIL-125(Ti) structure collapses, and the resulting material does not describe any crystalline XRD profile, appearing as an amorphous material. Before that, a reduction in the peaks’ intensity is evidenced, indicating a gradual loss of crystallinity. Thus, the degree of crystallinity and the crystal size, as determined by the methodologies described in Section 3.2, are collected in Table 1. The greatest reduction on crystallinity was observed when reaching 250 °C. However, since NH₂-MIL-125(Ti) is an amine-functionalized isostructure of the MIL-125(Ti), both materials would show the same XRD profile, so it would be necessary to corroborate that the amine group in the ligand is maintained. The NH₂-BDC presence was confirmed by UV-vis spectroscopy (F1 in the supplementary information). Vacuum-treated samples showed two absorption bands, at 280 and 370 nm, due to the absorption of Ti-oxo-clusters and NH₂-BDC linker, respectively. Both bands characterize the NH₂-MIL-125(Ti) and differ from the spectrum of MIL-125(Ti), which only has one band due to the absorption on Ti-oxo-clusters [49,50]. Scanning electron microscopy (SEM) and transmission electron microscopy (TEM) images of V-250-16 were taken and compared with those from the original sample (Figure 3). The MOF particles show a thin and disk-like shape with an average size close to 500 nm, very similar to those of the NH₂-MIL-125(Ti), which confirms that the vacuum treatment does not significantly modify the morphology of the MOF.

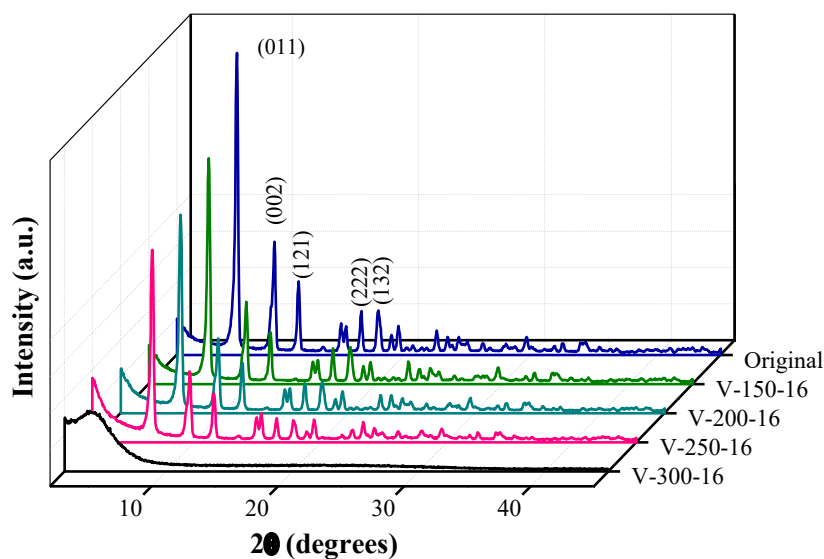


Figure 2. X-ray diffraction (XRD) patterns of the NH₂-MIL-125(Ti) treated under vacuum at different temperatures for 16 h. The original NH₂-MIL-125(Ti) pattern is included as reference.

Table 1. Crystallinity percentages and crystal size values of NH₂-MIL-125(Ti) before and after vacuum treatment at different temperatures for 16 h.

| Sample | Crystallinity (%) | Relative crystallinity ¹ (%) | Crystal size (nm) |
|----------|-------------------|---|-------------------|
| Original | 80.3 | 100.0 | 33.2 |
| V-150-16 | 75.0 | 93.4 | 30.9 |
| V-200-16 | 75.6 | 94.1 | 30.2 |
| V-250-16 | 63.6 | 79.2 | 21.2 |

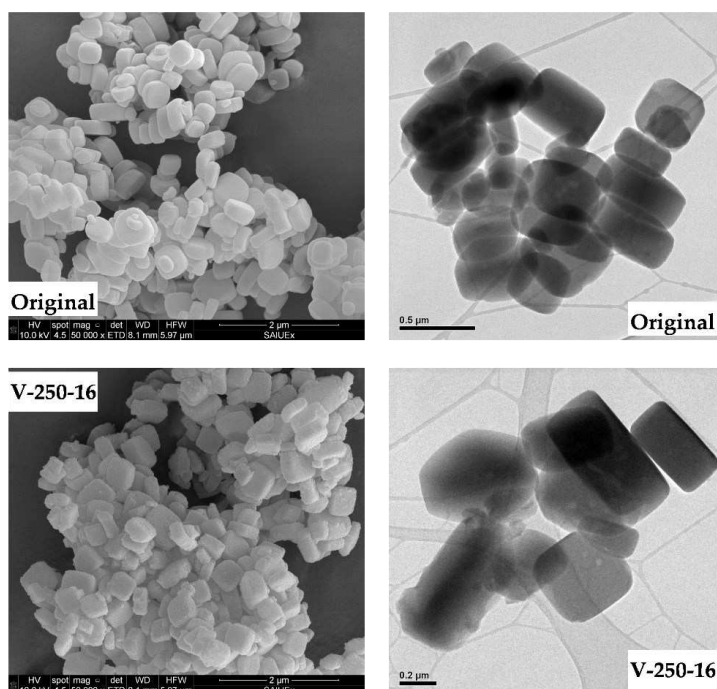
¹ Relative crystallinity to that of the original MOF.**Figure 3.** Scanning electron microscopy (SEM) and transmission electron microscopy (TEM) images of the original NH₂-MIL-125(Ti) and V-250-16 sample.

Figure 4 shows the $-196\text{ }^{\circ}\text{C}$ N₂ adsorption–desorption isotherms of the NH₂-MIL-125(Ti) subjected to the vacuum treatments and Table 2 summarizes the porous textural characteristics derived from those isotherms. Most of the solids treated under vacuum showed isotherms similar to that of the original NH₂-MIL-125(Ti), indicative of predominantly microporous texture with some relative contribution of mesoporosity and fairly high surface area values [39,44,48]. Only the V-300-16 shows remarkable differences, with very low N₂ adsorption and S_{BET} due to the linker oxidation and structure collapse. It is worth noting that an increase in the temperature, below 300 °C, is associated with some slight increase in the microporous surface, which can be related to the removal of adsorbed species, most probably excess linker and/or solvent molecules, not removed during the washing process that block the pore network [35]. According to these results, 250 °C appears to be the best temperature to carry out the vacuum-stabilization of the NH₂-MIL-125(Ti), maintaining its structure and porosity.

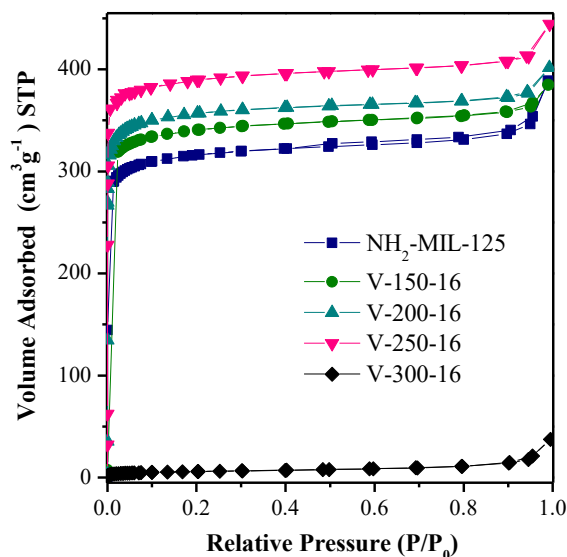


Figure 4. N₂ adsorption–desorption isotherms at -196 °C of the original NH₂-MIL-125(Ti) and after treatment under vacuum at different temperatures for 16 h.

Table 2. Porous texture characterization of the NH₂-MIL-125(Ti) and after treatment under vacuum at different temperatures for 16 h.

| Sample | S_{BET}^1 ($\text{m}^2\cdot\text{g}^{-1}$) | S_{MP}^2 ($\text{m}^2\cdot\text{g}^{-1}$) | S_{EXT}^3 ($\text{m}^2\cdot\text{g}^{-1}$) | V_{T}^4 ($\text{cm}^3\cdot\text{g}^{-1}$) | V_{MP}^5 ($\text{cm}^3\cdot\text{g}^{-1}$) |
|----------|--|---|--|---|--|
| Original | 1025 | 940 | 85 | 0.60 | 0.45 |
| V-150-16 | 1091 | 996 | 95 | 0.61 | 0.48 |
| V-200-16 | 1103 | 1016 | 87 | 0.61 | 0.49 |
| V-250-16 | 1154 | 1050 | 104 | 0.68 | 0.54 |
| V-300-16 | 24 | 8 | 16 | 0.05 | 0.002 |

¹ S_{BET} , specific surface area; ² S_{MP} and ³ S_{EXT} , microporous and non-microporous surface area; ⁴ V_{T} and ⁵ V_{MP} , total and micropore volume, respectively.

Figure 5 depicts the evolution of the linker concentration analyzed in the liquid phase and the corresponding leaching percentage, upon contact time in water. The vacuum thermal treatment allows for significantly reducing the amount of linker leaching, that effect being more pronounced at a 200–250 °C treatment temperature. However, despite this reduction, there is still a considerable amount of linker in the liquid phase, corresponding to a 15% leaching, and it is also noteworthy that the lixiviation does not reach an equilibrium, even after 24 h. Therefore V-200-16 or V-250-16 samples cannot still be considered as stable materials regarding potential applications in the aqueous phase.

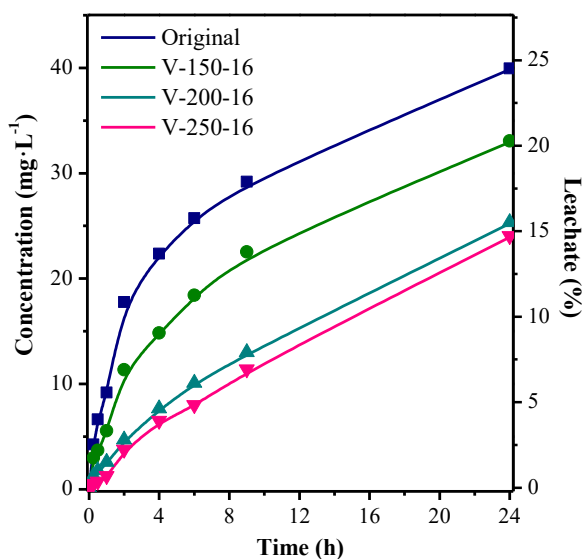


Figure 5. Linker leaching in water from NH₂-MIL-125(Ti) before and after vacuum heat treated upon contact time.

2.3. Thermal Treatment in Air Atmosphere

Figure 6 depicts the XRD diffractograms of the NH₂-MIL-125(Ti) subjected to calcination during 16 h at different temperatures in air-circulating muffle furnace. As previously observed in the vacuum treatment, the NH₂-MIL-125(Ti) structure was maintained up to 250 °C, while it collapses at 300 °C, disappearing all the characteristic peaks of NH₂-MIL-125(Ti). The degree of crystallinity and the crystal size of each sample are collected in Table 3. Increasing the temperature decreases the crystallinity of the samples, accompanied by a reduction in crystal size. These modifications can be related to the loss of solvent and excess linker molecules that are usually trapped in the MOF cages [35]. To learn more about the effect caused by air heating, additional treatments were conducted at 250 °C, but extending the treatment time. Figure 7 compares the diffraction patterns of the samples heated for 16, 48 and 72 h, where it can be seen that the characteristic peaks of the original structure are still remaining, but showing decreasing intensities as the calcination time increased, thus indicating a considerable gradual loss of crystallinity, reaching about 60% after 72 h, which means a certain amorphization of the material.

Table 3. Crystallinity percentages and crystal size values of NH₂-MIL-125(Ti) before and after heat treatment in air under different conditions. The values for M-250-48 after 24 h in contact with water are included.

| Sample | Crystallinity (%) | Relative Crystallinity ¹ (%) | Crystal Size (nm) |
|------------------|-------------------|---|-------------------|
| Original | 80.3 | 100.0 | 33.2 |
| M-150-16 | 79.2 | 98.5 | 33.5 |
| M-200-16 | 75.3 | 93.7 | 32.9 |
| M-250-16 | 63.7 | 79.2 | 31.1 |
| M-250-48 | 50.0 | 62.2 | 31.4 |
| M-250-72 | 34.1 | 42.4 | 32.9 |
| M-250-48-Exposed | 49.7 | 61.8 | 31.1 |

¹ Relative crystallinity to that of the original MOF.

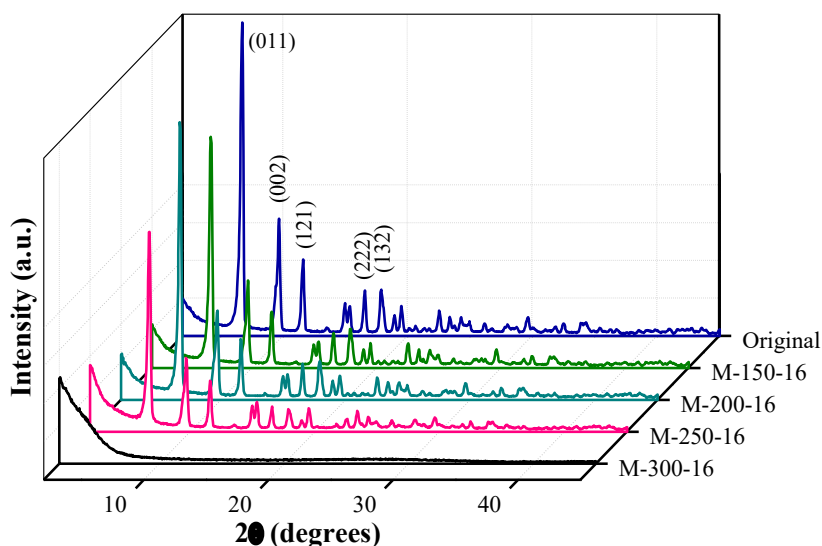


Figure 6. XRD diffraction patterns of NH₂-MIL-125(Ti) heated in air at different temperatures for 16 h. The original NH₂-MIL-125(Ti) pattern is included as reference.

Once again, the presence of NH₂-BDC in all heat-treated samples was confirmed by UV-vis spectroscopy (Figure S2 in the supplementary information). The UV-vis spectra showed the two absorption bands characteristic of the NH₂-MIL-125(Ti), unlike the single band that characterizes the MIL-125(Ti) [49,51,52]. Figure 8 collects SEM and TEM images of some calcined samples that can be compared with those of the original NH₂-MIL-125(Ti) shown in Figure 3. As can be clearly observed, the morphology of M-300-16 is very different. The well-defined disk particles of the NH₂-MIL-125(Ti) disappeared and became an amorphous morphology, corroborating the structural collapse described above. However, the morphology and disk-shape of the original MOF remained after thermal treatment at 250 °C for 48 h, as well as the particle size (\approx 500 nm).

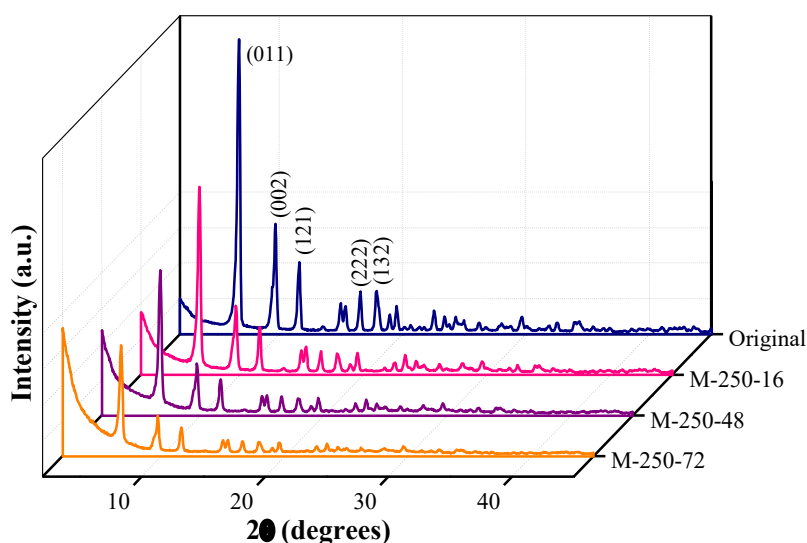


Figure 7. XRD diffraction patterns of NH₂-MIL-125(Ti) heated in air at 250 °C for 16, 48 and 72 h. The original NH₂-MIL-125(Ti) pattern is included as reference.

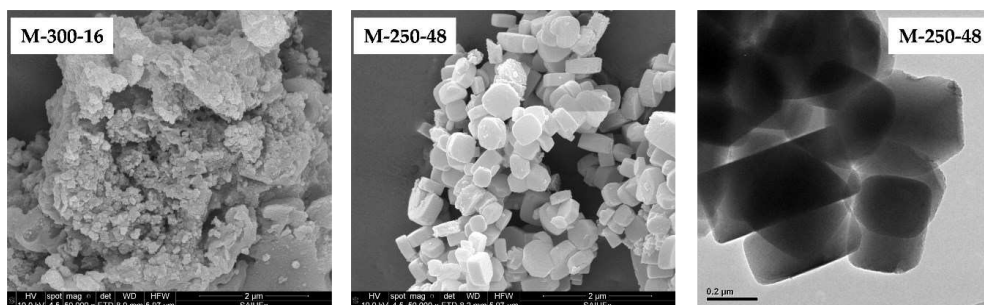


Figure 8. SEM image of M-300-16. SEM and TEM images of M-250-48.

Figure 9a depicts the $-196\text{ }^{\circ}\text{C}$ N_2 adsorption–desorption isotherms of $\text{NH}_2\text{-MIL-125(Ti)}$ subjected to thermal treatments in air and the derived porous textural characteristics are summarized in Table 4. As in the case of heat treatment under vacuum, these samples showed an isotherm typical of microporous solids [39,44,48]. Again, the calcination in air at $300\text{ }^{\circ}\text{C}$ caused the loss of structure and the collapse of the pore network, resulting in a N_2 adsorption–desorption isotherm of a non-porous material. Again, in the range below $300\text{ }^{\circ}\text{C}$, increasing the calcination temperature produces some slight increase in the microporous surface. However, in the sample treated at $250\text{ }^{\circ}\text{C}$, the observed increase in surface area corresponds to the non-microporous one. This effect can be related with the decrease in crystallinity and increased disorder observed by XRD. When comparing the vacuum and the air thermal treatments, no obvious differences were detected, so it seems evident that temperature is the main factor governing the purification process. Regarding the effect of the treatment time, the N_2 adsorption–desorption isotherms of their corresponding samples remain typical of microporous solids (Figure 9b). Increasing the treatment time led to some moderate reduction in the BET surface area, affecting to the microporous range, while the non-microporous area was increased, probably due to the loss of crystallinity seen by XRD. Therefore, thermal treatment at moderate temperature ($\approx 250\text{ }^{\circ}\text{C}$) allows purifying and improving the stability of the tested MOF, while maintaining its porous structure and surface area close to $1000\text{ m}^2\text{-g}^{-1}$, analogous to other untreated $\text{NH}_2\text{-MIL-125(Ti)}$ [41–44].

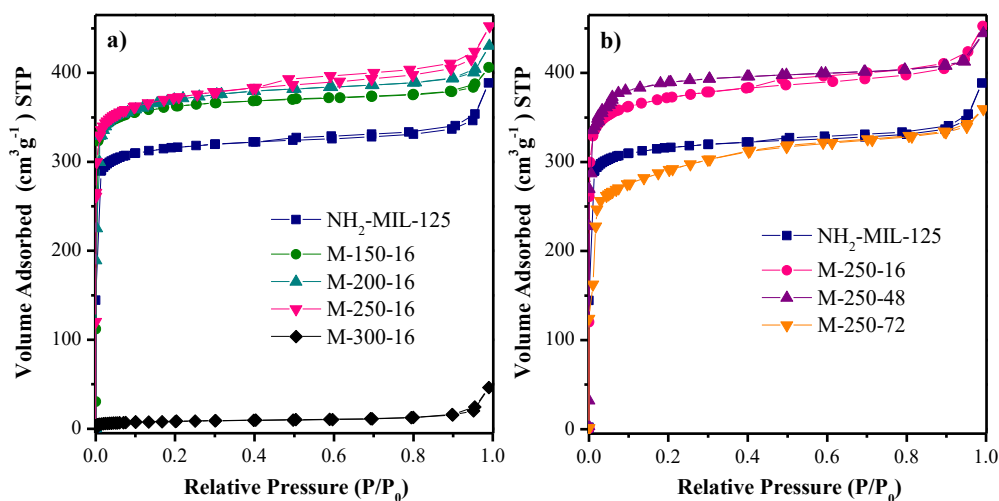


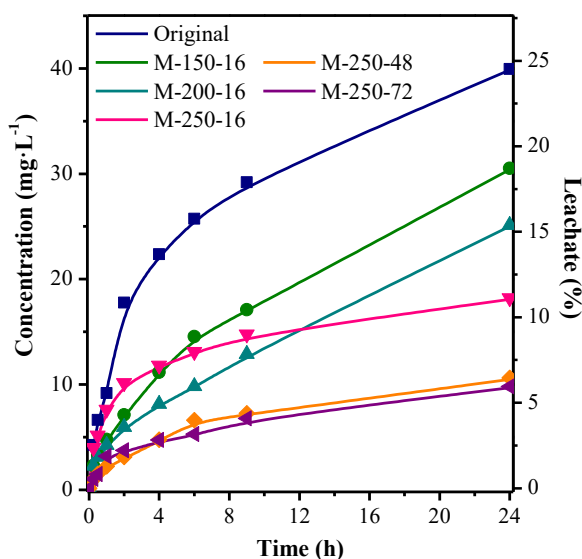
Figure 9. N_2 adsorption–desorption isotherms at $-196\text{ }^{\circ}\text{C}$ of the original $\text{NH}_2\text{-MIL-125(Ti)}$ and after heat treatment in air at different temperatures for 16 h (a) and at $250\text{ }^{\circ}\text{C}$ for different times (b).

Table 4. Porous texture characterization of NH₂-MIL-125(Ti) after heat treatment in air under different conditions.

| Sample | S _{BET} ¹ (m ² ·g ⁻¹) | S _{MP} ² (m ² ·g ⁻¹) | S _{EXT} ³ (m ² ·g ⁻¹) | V _T ⁴ (cm ³ ·g ⁻¹) | V _{MP} ⁵ (cm ³ ·g ⁻¹) |
|------------------|---|--|---|--|---|
| Original | 1025 | 940 | 85 | 0.60 | 0.45 |
| M-150-16 | 1085 | 989 | 96 | 0.63 | 0.53 |
| M-200-16 | 1173 | 1075 | 98 | 0.67 | 0.54 |
| M-250-16 | 1207 | 1058 | 149 | 0.70 | 0.53 |
| M-300-16 | 28 | 12 | 16 | 0.07 | 0.006 |
| M-250-48 | 1046 | 865 | 181 | 0.56 | 0.35 |
| M-250-72 | 962 | 684 | 278 | 0.56 | 0.33 |
| M-250-48-Exposed | 970 | 850 | 120 | 0.53 | 0.34 |

¹ S_{BET}, specific surface area; ² S_{MP} and ³ S_{EXT}, microporous and non-microporous surface area; ⁴ V_T and ⁵ V_{MP}, total and micropore volume, respectively.

Figure 10 shows the results of the stability in water of the samples subjected to calcination in air at different temperatures and times. Thermal treatment in air for 16 h stabilizes the NH₂-MIL-125(Ti) and the leachate percentage diminishes at increasing temperature. At 250 °C, this improvement of stability in water is significantly higher than the observed with the thermal vacuum treatment (see Figure 5) and now a quasi-equilibrium state is achieved. Extending the air thermal treatment up to 48 h reduces the leaching percentage to less than 7% and maintains the quasi-equilibrium state, although no further improvement was observed at higher treatment times. Characterization of the M-250-48 sample after water exposition for 24 h was carried out to check possible structural and textural changes (Figure 11). There were no significant differences in X-ray diffractograms or N₂ adsorption–desorption isotherms before and after contact with water during the above-mentioned time. The S_{BET} slightly decreased somewhat, from 1046 to 970 m²·g⁻¹, but the crystallinity remained unchanged (see values in Table 3; Table 4). The NH₂-BDC also remained in the structure, including the presence of the amine group, as confirmed by its UV-vis spectrum (Figure S3 in the supplementary information) that presents the characteristic absorption bands of this linker. These results demonstrate that it is possible to purify and stabilize the NH₂-MIL-125(Ti) MOF by a fairly simple thermal treatment in air at 250 °C for 48 h, without affecting its structure and porous texture.

**Figure 10.** Linker leaching in water from the original NH₂-MIL-125(Ti) and after heat treatment in air for 16 h at different temperatures and at 250 °C during different times.

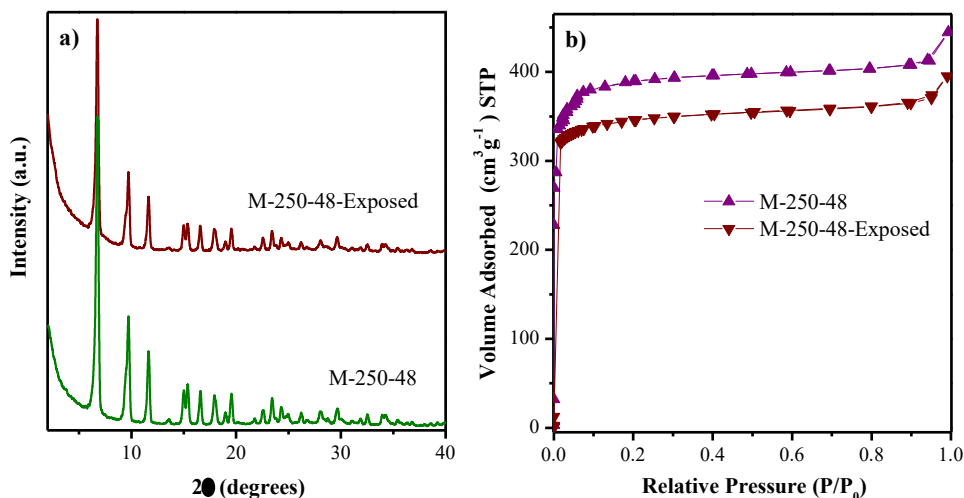


Figure 11. a) XRD patterns and b) N₂ adsorption–desorption isotherms at $-196\text{ }^{\circ}\text{C}$ of M-250-48 before and after contact with water for 24 h.

3. Materials and Methods

3.1. NH₂-MIL-125(Ti) Synthesis

NH₂-MIL-125(Ti) was prepared following the methodology reported in our previous work (chemical information included in Figure S4 in the supplementary information) [44]. Typically, 2-amino benzene dicarboxylic acid (6 mmol, NH₂-BDC, Sigma Aldrich, Madrid, Spain, 99%) was dissolved in dimethylformamide (25 mL, DMF, Sigma Aldrich, Madrid, Spain, $\geq 99.8\%$) under stirring. Titanium isopropoxide (3 mmol, Sigma Aldrich, Madrid, Spain, $\geq 98\%$) was dropped onto the mixture and stirred until homogenized, after which methanol (25 mL, CH₃OH, Sigma Aldrich, Madrid, Spain, anhydrous 99.8%) was added. The whole mixture was kept in agitation for 30 min, drawn off to a 65 mL Teflon autoclave and placed in an oven at $150\text{ }^{\circ}\text{C}$ for 16 h. The resulting solid was recovered by centrifugation (5 min, 5000 rpm) and washed three times with DMF (100 mL, 30 min) and three times with methanol (100 mL, 30 min), recovering the solid in all cases by centrifugation. The final drying of the solid was performed overnight at $60\text{ }^{\circ}\text{C}$.

NH₂-MIL-125(Ti) was subjected to different thermal treatments. The first series was obtained by heating the NH₂-MIL-125(Ti) at 150, 200, 250 and $300\text{ }^{\circ}\text{C}$ for 16 h under vacuum using a degassing station (Micromeritics VacPrep 061, Norcross, GA, USA) attached to the TriStar 123 equipment. For the second series, the NH₂-MIL-125(Ti) was heated in a muffle furnace (Fuji Electric, MOD 12 PR/400, Barcelona, Spain) in air at 150, 200, 250 and $300\text{ }^{\circ}\text{C}$ for 16 h, and also at $250\text{ }^{\circ}\text{C}$ for 48 and 72 h. The resulting samples were denoted as X-T-t, where X indicated the type of treatment, V for vacuum and M for muffle furnace, T was the treatment temperature and t the treatment time.

3.2. Characterization

Thermogravimetric analysis was carried out using a Q600 TA instruments (New Castle, DE, USA) in an alumina crucible. All measurements were carried out within the temperature range $25\text{--}1200\text{ }^{\circ}\text{C}$ at a heating rate of $10\text{ }^{\circ}\text{C}\cdot\text{min}^{-1}$ under a continuous air flow of $20\text{ mL}\cdot\text{min}^{-1}$. X-ray diffractograms (XRD) were registered in the $2\text{--}45^{\circ}$ 2θ range with a rate of $1.5^{\circ}\cdot\text{min}^{-1}$ and using a Cu K α radiation. A Bruker D8 diffractometer (Bremen, Germany) was used, equipped with a Sol-X energy dispersive detector. Crystallinity percentage was calculated after diffractogram deconvolution with OriginPro by the following expression [53,54]:

$$\text{Crystallinity (\%)} = 100 \times \frac{\text{Area of crystalline peaks}}{\text{Area of all XRD pattern}} \quad (2)$$

The average crystal size was determined by using the Scherrer's equation from the reflection peak (121) of NH₂-MIL-125(Ti), not overlapped with any other peak. UV-vis diffuse reflectance spectroscopy was carried out on Shimadzu UV2600i (Kyoto, Japan) equipment, recording the spectra in the 250–700 nm range. Scanning electron microscopy images (SEM) were taken with a Hitachi S4800 microscope (Krefeld, Germany) and transmission electron microscopy images (TEM) with a TECNAI G2 20 Twin equipment (Hillsborough, NC, USA). N₂ adsorption–desorption isotherms at −196 °C were carried out with a TriStar 123 equipment (Micromeritics II 3020, Norcross, GA, USA). Solids were outgassed before testing under vacuum at 120 °C for 18 h. Specific surface area (S_{BET}) was calculated by the Brunauer–Emmet–Teller method [55], while micropore surface area (S_{MP}) was obtained using the *t*-plot method [56] and the external or non-microporous surface area (S_{EXT}) by difference between S_{BET} and S_{MP} . The total pore volume (V_{T}) corresponded to the amount of nitrogen adsorbed at a relative pressure of 0.99, while the micropore volume (V_{MP}) was obtained from the *t*-plot method.

3.3 Stability Testing in Water

The water stability of the NH₂-MIL-125(Ti) derived solids was tested through the leaching of the NH₂-BDC in deionized water (Type II). The solid was suspended in water (250 mg·L^{−1}) and stirred for 24 h at 25 °C and 170 rpm in a water bath orbital shaker (JULABO SW22, Seelbach, Germany). At different interval times, aliquots of 2 mL were collected and filtered with Polytetrafluoroethylene (PTFE) syringe filters (Whatman 0.45 μm). The filtrates were analyzed to determine the concentration of the ligand by high performance liquid chromatography (HPLC) (Shimadzu Prominence-I LC-2030C, Kyoto, Japan), equipped with a diode array detector (SPDM30 A) and a C18 column (Eclipse Plus, 5 μm). A gradient elution method was used for the analyses, changing the mobile phase (aqueous acetic acid solution 0.1%, Sigma Aldrich, Madrid, Spain, ≥99%) by elution with acetonitrile (HPLC grade, Scharlab, Barcelona, Spain) and using a constant flow of 0.7 mL·min^{−1}. The wavelength of the detector was fixed at 358 nm for the detection of the NH₂-BDC that appeared at a 6.3 min retention time. Solid samples were recovered from the aqueous medium by centrifugation after stability test and stored for later characterization.

4. Conclusions

Water stability of NH₂-MIL-125(Ti) was studied by analyzing quantitatively the amount of ligand released to the liquid phase along the exposition time in water. In many studies, the water stability of MOFs has been mainly investigated using the X-ray diffraction, N₂ adsorption–desorption and electron microscopy of filtered powders, comparing the properties before and after exposition. This study shows that these characterization techniques are not enough to assess that stability. We demonstrated, for the first time, the quantitative lixiviation of this MOF, which achieved values up to 25% after 24 h of contact, with water still being far from equilibrium after that time. The present study also shows that the post-modification of NH₂-MIL-125(Ti) by thermal treatments stabilizes its structure, making it less susceptible to partial dissolution. Temperature and time showed to be the determining variables, while the atmosphere (air or vacuum) showed no significant effect. Thermal treatment under these two atmospheres within 150–250 °C did not alter the structure and porous texture of the MOF, except for some slight increase in the specific surface area accompanied by a small reduction in crystallinity. Increasing the treatment temperature up to 300 °C caused the collapse of the crystalline MOF structure accompanied by the loss of the pore network. Certain reduction on the surface area were observed by extending the thermal treatment but maintaining its structure.

The results obtained provide a new understanding of the effects of thermal treatments on the water stability of NH₂-MIL-125(Ti), which was improved as the temperature of the treatment increased up to 250 °C. Some significant differences were found on the effects of the atmosphere used in the thermal treatment. Under air, greater stabilization of the MOF was achieved due to the removal of excess linker molecules, with lower leaching percentages and the attainment of a quasi-equilibrium state in a relatively low contact time in water. The best results were obtained upon thermal treatment in air at 250 °C for 48 h. After that treatment, less than 7% ligand leaching occurred upon 24 h of

contact with water. These findings have significant implications regarding the potential use of MOFs in water-related applications.

Supplementary Materials: The following are available online at www.mdpi.com/2073-4344/10/6/603/s1, Figure S1: UV–vis diffuse absorbance spectra of NH₂-MIL-125(Ti) treated under vacuum at different temperatures for 16 h. Original NH₂-MIL-125(Ti) and MIL-125(Ti) spectra are included as reference, Figure S2: UV–vis diffuse absorbance spectra of NH₂-MIL-125(Ti) heated in air at different temperatures for 16 h (a) and at 250 °C for 48 and 72 h (b). Original NH₂-MIL-125(Ti) and MIL-125(Ti) spectra are included as reference, Figure S3: UV–vis diffuse absorbance spectra of M-250-48 before and after contact with water for 24 h. Original NH₂-MIL-125(Ti) and MIL-125(Ti) spectra are included as reference, Figure S4: (a) Chemical structure of Ti-oxo clusters linked to NH₂-BDC ligands, from the Cambridge Structural Database (CSD). Chemical structure of NH₂-MIL-125(Ti) viewed from a-axis (b) and c-axis (c), from cif data of Crystallography Open Database.

Author Contributions: Conceptualization, J.B., C.B. and J.J.R.; methodology, A.G.-A. and V.M.-R.; writing—original draft preparation, A.G.-A. and C.B.; writing—review and editing, A.G.-A., V.M.-R., J.B., C.B. and J.J.R.; supervision, J.B., C.B., J.J.R.; funding acquisition, J.B., C.B. and J.J.R. All authors have read and agreed to the published version of the manuscript.

Funding: This research was funded by Spanish MINECO (project CTQ2016-78576-R).

Acknowledgments: V. Muelas-Ramos thanks to Spanish MCIU for BES-2017-082613 grant.

Conflicts of Interest: The authors declare no conflict of interest.

References

1. Qiu, J.; Zhang, X.; Feng, Y.; Zhang, X.; Wang, H.; Yao, J. Modified metal-organic frameworks as photocatalysts. *Appl. Catal. B Environ.* **2018**, *231*, 317–342, doi:10.1016/j.apcatb.2018.03.039.
2. Furukawa, H.; Cordova, K. E.; O’Keeffe, M.; Yaghi, O. M. The chemistry and applications of metal-organic frameworks. *Science* **2013**, *341*, 1230444–1230444, doi:10.1126/science.1230444.
3. Szcześniak, B.; Choma, J.; Jaroniec, M. Gas adsorption properties of hybrid graphene-MOF materials. *J. Colloid Interface Sci.* **2018**, *514*, 801–813, doi:10.1016/j.jcis.2017.11.049.
4. Millward, A. R.; Yaghi, O. M. Metal–organic frameworks with exceptionally high capacity for storage of carbon dioxide at room temperature. *J. Am. Chem. Soc.* **2005**, *127*, 17998–17999, doi:10.1021/ja0570032.
5. Rasheed, T.; Nabeel, F. Luminescent metal-organic frameworks as potential sensory materials for various environmental toxic agents. *Coord. Chem. Rev.* **2019**, *401*, 213065, doi:10.1016/j.ccr.2019.213065.
6. Kreno, L. E.; Leong, K.; Farha, O. K.; Allendorf, M.; Van Duyne, R. P.; Hupp, J. T. Metal–organic framework materials as chemical sensors. *Chem. Rev.* **2012**, *112*, 1105–1125, doi:10.1021/cr200324t.
7. Qiu, S.; Xue, M.; Zhu, G. Metal–organic framework membranes: from synthesis to separation application. *Chem. Soc. Rev.* **2014**, *43*, 6116–6140, doi:10.1039/C4CS00159A.
8. Abánades Lázaro, I.; Forgan, R. S. Application of zirconium MOFs in drug delivery and biomedicine. *Coord. Chem. Rev.* **2019**, *380*, 230–259, doi:10.1016/j.ccr.2018.09.009.
9. Sun, C.-Y.; Qin, C.; Wang, X.-L.; Su, Z.-M. Metal-organic frameworks as potential drug delivery systems. *Expert Opin. Drug Deliv.* **2013**, *10*, 89–101, doi:10.1517/17425247.2013.741583.
10. Joseph, L.; Jun, B.-M.; Jang, M.; Park, C. M.; Muñoz-Senmache, J. C.; Hernández-Maldonado, A. J.; Heyden, A.; Yu, M.; Yoon, Y. Removal of contaminants of emerging concern by metal-organic framework nanoadsorbents: A review. *Chem. Eng. J.* **2019**, *369*, 928–946, doi:10.1016/J.CEJ.2019.03.173.
11. Li, X.; Wang, B.; Cao, Y.; Zhao, S.; Wang, H.; Feng, X.; Zhou, J.; Ma, X. Water contaminant elimination based on metal-organic frameworks and perspective on their industrial applications. *ACS Sustain. Chem. Eng.* **2019**, *7*, 4548–4563, doi:10.1021/acssuschemeng.8b05751.
12. Hasan, Z.; Jhung, S. H. Removal of hazardous organics from water using metal-organic frameworks (MOFs): Plausible mechanisms for selective adsorptions. *J. Hazard. Mater.* **2015**, *283*, 329–339,

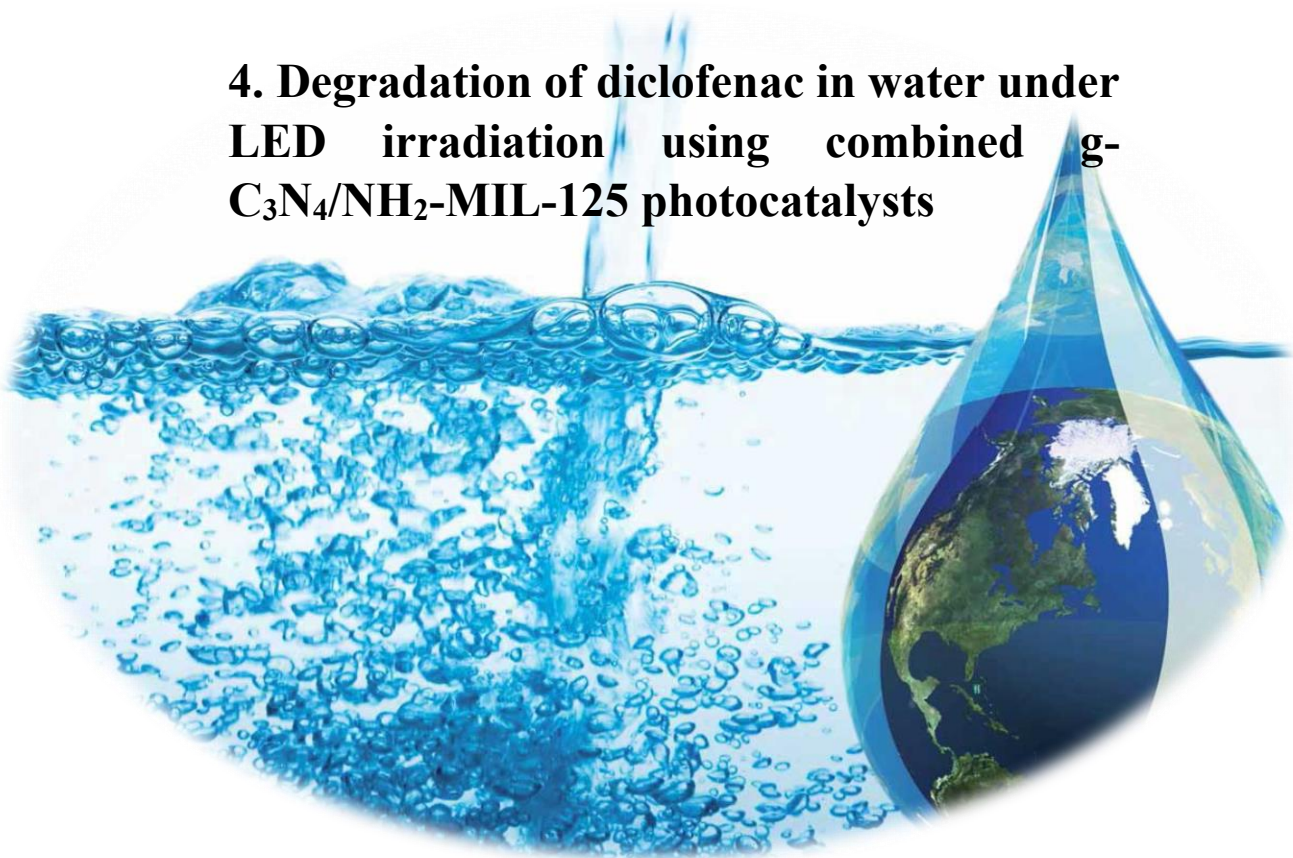
- doi:10.1016/J.JHAZMAT.2014.09.046.
13. Bedia, J.; Muelas-Ramos, V.; Peñas-Garzón, M.; Gómez-Avilés, A.; Rodríguez, J. J.; Belver, C. A review on the synthesis and characterization of metal organic frameworks for photocatalytic water purification. *Catalysts* **2019**, *9*, 52, doi:10.3390/catal9010052.
 14. Khan, N. A.; Hasan, Z.; Jhung, S. H. Adsorptive removal of hazardous materials using metal-organic frameworks (MOFs): A review. *J. Hazard. Mater.* **2013**, *244–245*, 444–456, doi:10.1016/j.jhazmat.2012.11.011.
 15. Pi, Y.; Li, X.; Xia, Q.; Wu, J.; Li, Y.; Xiao, J.; Li, Z. Adsorptive and photocatalytic removal of Persistent Organic Pollutants (POPs) in water by metal-organic frameworks (MOFs). *Chem. Eng. J.* **2018**, *337*, 351–371, doi:10.1016/j.cej.2017.12.092.
 16. Feng, M.; Zhang, P.; Zhou, H. C.; Sharma, V. K. Water-stable metal-organic frameworks for aqueous removal of heavy metals and radionuclides: A review. *Chemosphere* **2018**, *209*, 783–800, doi:10.1016/j.chemosphere.2018.06.114.
 17. Sharma, V. K.; Feng, M. Water depollution using metal-organic frameworks-catalyzed advanced oxidation processes: A review. *J. Hazard. Mater.* **2019**, *372*, 3–16, doi:10.1016/j.jhazmat.2017.09.043.
 18. Li, Y.; Xu, H.; Ouyang, S.; Ye, J. Metal-organic frameworks for photocatalysis. *Phys. Chem. Chem. Phys.* **2016**, *18*, 7563–7572, doi:10.1039/c5cp05885f.
 19. Zeng, L.; Guo, X.; He, C.; Duan, C. Metal-organic frameworks: Versatile materials for heterogeneous photocatalysis. *ACS Catal.* **2016**, *6*, 7935–7947, doi:10.1021/acscatal.6b02228.
 20. Li, W.; Zhang, Y.; Li, Q.; Zhang, G. Metal-organic framework composite membranes: Synthesis and separation applications. *Chem. Eng. Sci.* **2015**, *135*, 232–257, doi:10.1016/J.CES.2015.04.011.
 21. Canivet, J.; Fateeva, A.; Guo, Y.; Coasne, B.; Farrusseng, D. Water adsorption in MOFs: fundamentals and applications. *Chem. Soc. Rev.* **2014**, *43*, 5594–5617, doi:10.1039/C4CS00078A.
 22. Furukawa, H.; Gándara, F.; Zhang, Y.-B.; Jiang, J.; Queen, W. L.; Hudson, M. R.; Yaghi, O. M. Water adsorption in porous metal-organic frameworks and related materials. *J. Am. Chem. Soc.* **2014**, *136*, 4369–4381, doi:10.1021/ja500330a.
 23. De Toni, M.; Jonchiere, R.; Pullumbi, P.; Coudert, F. X.; Fuchs, A. H. How can a hydrophobic mof be water-unstable? Insight into the hydration mechanism of IRMOFs. *ChemPhysChem* **2012**, *13*, 3497–3503, doi:10.1002/cphc.201200455.
 24. Qian, X.; Yadian, B.; Wu, R.; Long, Y.; Zhou, K.; Zhu, B.; Huang, Y. Structure stability of metal-organic framework MIL-53 (Al) in aqueous solutions. *Int. J. Hydrogen Energy* **2013**, *38*, 16710–16715, doi:10.1016/J.IJHYDENE.2013.07.054.
 25. Low, J. J.; Benin, A. I.; Jakubczak, P.; Abrahamian, J. F.; Faheem, S. A.; Willis, R. R. Virtual high throughput screening confirmed experimentally: Porous coordination polymer hydration. *J. Am. Chem. Soc.* **2009**, *131*, 15834–15842, doi:10.1021/ja9061344.
 26. Bon, V.; Senkovska, I.; Baburin, I. A.; Kaskel, S. Zr- and Hf-based metal-organic frameworks: Tracking down the polymorphism. *Cryst. Growth Des.* **2013**, *13*, 1231–1237, doi:10.1021/cg301691d.
 27. Jeremias, F.; Lozan, V.; Henninger, S. K.; Janiak, C. Programming MOFs for water sorption: amino-functionalized MIL-125 and UiO-66 for heat transformation and heat storage applications. *Dalt. Trans.* **2013**, *42*, 15967–15973, doi:10.1039/C3DT51471D.
 28. Bai, Y.; Dou, Y.; Xie, L.-H.; Rutledge, W.; Li, J.-R.; Zhou, H.-C. Zr-based metal-organic frameworks: design, synthesis, structure, and applications. *Chem. Soc. Rev.* **2016**, *45*, 2327–2367, doi:10.1039/C5CS00837A.

29. Burtch, N. C.; Jasuja, H.; Walton, K. S. Water stability and adsorption in metal–organic frameworks. *Chem. Rev.* **2014**, *114*, 10575–10612, doi:10.1021/cr5002589.
30. Zhu, J.; Li, P. Z.; Guo, W.; Zhao, Y.; Zou, R. Titanium-based metal–organic frameworks for photocatalytic applications. *Coord. Chem. Rev.* **2018**, *359*, 80–101, doi:10.1016/j.ccr.2017.12.013.
31. Zou, D.-H.; Cui, L.-N.; Liu, P.-Y.; Yang, S.; Zhu, Q.-Y.; Dai, J. Triphenylamine derived titanium oxo clusters: an approach to effective organic–inorganic hybrid dyes for photoactive electrodes. *Chem. Commun.* **2018**, *54*, 9933–9936, doi:10.1039/C8CC05441J.
32. Kim, S.; Sarkar, D.; Kim, Y.; Park, M. H.; Yoon, M.; Kim, Y.; Kim, M. Synthesis of functionalized titanium-carboxylate molecular clusters and their catalytic activity. *J. Ind. Eng. Chem.* **2017**, *53*, 171–176, doi:https://doi.org/10.1016/j.jiec.2017.04.022.
33. Zuluaga, S.; Fuentes-Fernandez, E. M. A.; Tan, K.; Xu, F.; Li, J.; Chabal, Y. J.; Thonhauser, T. Understanding and controlling water stability of MOF-74. *J. Mater. Chem. A* **2016**, *4*, 5176–5183, doi:10.1039/C5TA10416E.
34. Canivet, J.; Bonnefoy, J.; Daniel, C.; Legrand, A.; Coasne, B.; Farrusseng, D. Structure-property relationships of water adsorption in metal-organic frameworks. *New J. Chem.* **2014**, *38*, 3102–3111, doi:10.1039/c4nj00076e.
35. Howarth, A. J.; Peters, A. W.; Vermeulen, N. A.; Wang, T. C.; Hupp, J. T.; Farha, O. K. Best practices for the synthesis, activation, and characterization of metal–organic frameworks. *Chem. Mater.* **2017**, *29*, 26–39, doi:10.1021/acs.chemmater.6b02626.
36. Taheri, M.; Enge, T. G.; Tsuzuki, T. Water stability of cobalt doped ZIF-8: A quantitative study using optical analyses. *Mater. Today Chem.* **2020**, *16*, 100231, doi:10.1016/j.mtchem.2019.100231.
37. Wen, G.; Guo, Z. Facile modification of NH₂-MIL-125(Ti) to enhance water stability for efficient adsorptive removal of crystal violet from aqueous solution. *Colloids Surfaces A Physicochem. Eng. Asp.* **2018**, *541*, 58–67, doi:10.1016/j.colsurfa.2018.01.011.
38. Li, S.; Feng, F.; Chen, S.; Zhang, X.; Liang, Y.; Shan, S. Preparation of UiO-66-NH₂ and UiO-66-NH₂/sponge for adsorption of 2,4-dichlorophenoxyacetic acid in water. *Ecotoxicol. Environ. Saf.* **2020**, *194*, 110440, doi:10.1016/j.ecoenv.2020.110440.
39. Zhang, M.; Yang, K.; Cui, J.; Yu, H.; Wang, Y.; Shan, W.; Lou, Z.; Xiong, Y. 3D-agaric like core-shell architecture UiO-66-NH₂@ZIF-8 with robust stability for highly efficient REEs recovery. *Chem. Eng. J.* **2020**, *386*, 124023, doi:10.1016/j.cej.2020.124023.
40. Fang, S.-Y.; Zhang, P.; Gong, J.-L.; Tang, L.; Zeng, G.-M.; Song, B.; Cao, W.-C.; Li, J.; Ye, J. Construction of highly water-stable metal-organic framework UiO-66 thin-film composite membrane for dyes and antibiotics separation. *Chem. Eng. J.* **2020**, *385*, 123400, doi:10.1016/J.CEJ.2019.123400.
41. Sun, D.; Ye, L.; Li, Z. Visible-light-assisted aerobic photocatalytic oxidation of amines to imines over NH₂-MIL-125(Ti). *Appl. Catal. B Environ.* **2015**, doi:10.1016/j.apcatb.2014.09.054.
42. Wang, H.; Yuan, X.; Wu, Y.; Zeng, G.; Dong, H.; Chen, X.; Leng, L.; Wu, Z.; Peng, L. In situ synthesis of In₂S₃@MIL-125(Ti) core-shell microparticle for the removal of tetracycline from wastewater by integrated adsorption and visible-light-driven photocatalysis. *Appl. Catal. B Environ.* **2016**, *186*, 19–29, doi:10.1016/J.APCATB.2015.12.041.
43. Zhu, S.-R.; Liu, P.-F.; Wu, M.-K.; Zhao, W.-N.; Li, G.-C.; Tao, K.; Yi, F.-Y.; Han, L. Enhanced photocatalytic performance of BiOBr/NH₂-MIL-125(Ti) composite for dye degradation under visible light. *Dalt. Trans.* **2016**, *45*, 17521–17529, doi:10.1039/C6DT02912D.
44. Gómez-Avilés, A.; Peñas-Garzón, M.; Bedia, J.; Dionysiou, D. D.; Rodríguez, J. J.; Belver, C. Mixed Ti-Zr

- metal-organic-frameworks for the photodegradation of acetaminophen under solar irradiation. *Appl. Catal. B Environ.* **2019**, *253*, 253–262, doi:10.1016/j.apcatb.2019.04.040.
45. Fu, Y.; Sun, D.; Chen, Y.; Huang, R.; Ding, Z.; Fu, X.; Li, Z. An amine-functionalized titanium metal-organic framework photocatalyst with visible-light-induced activity for CO₂ reduction. *Angew. Chemie Int. Ed.* **2012**, *51*, 3364–3367, doi:10.1002/anie.201108357.
 46. Dan-Hardi, M.; Serre, C.; Frot, T.; Rozes, L.; Maurin, G.; Sanchez, C.; Férey, G. A new photoactive crystalline highly porous titanium (IV) dicarboxylate. *J. Am. Chem. Soc.* **2009**, *131*, 10857–10859, doi:10.1021/ja903726m.
 47. Zhang, Y.; Chen, Y.; Zhang, Y.; Cong, H.; Fu, B.; Wen, S.; Ruan, S. A novel humidity sensor based on NH₂-MIL-125(Ti) metal organic framework with high responsiveness. *J. Nanoparticle Res.* **2013**, *15*, 2014, doi:10.1007/s11051-013-2014-6.
 48. Wang, H.; Yuan, X.; Wu, Y.; Zeng, G.; Chen, X.; Leng, L.; Wu, Z.; Jiang, L.; Li, H. Facile synthesis of amino-functionalized titanium metal-organic frameworks and their superior visible-light photocatalytic activity for Cr(VI) reduction. *J. Hazard. Mater.* **2015**, *286*, 187–194, doi:10.1016/J.JHAZMAT.2014.11.039.
 49. Kim, S.-N.; Kim, J.; Kim, H.-Y.; Cho, H.-Y.; Ahn, W.-S. Adsorption/catalytic properties of MIL-125 and NH₂-MIL-125. *Catal. Today* **2013**, *204*, 85–93, doi:10.1016/J.CATTOD.2012.08.014.
 50. Wang, F.; Li, F.-L.; Xu, M.-M.; Yu, H.; Zhang, J.-G.; Xia, H.-T.; Lang, J.-P. Facile synthesis of a Ag(*d*-doped coordination polymer with enhanced catalytic performance in the photodegradation of azo dyes in water. *J. Mater. Chem. A* **2015**, *3*, 5908–5916, doi:10.1039/C5TA00302D.
 51. Fan, Y.-H.; Zhang, S.-W.; Qin, S.-B.; Li, X.-S.; Qi, S.-H. An enhanced adsorption of organic dyes onto NH₂ functionalization titanium-based metal-organic frameworks and the mechanism investigation. *Microporous Mesoporous Mater.* **2018**, *263*, 120–127, doi:10.1016/J.MICROMESO.2017.12.016.
 52. Wu, Z.; Huang, X.; Zheng, H.; Wang, P.; Hai, G.; Dong, W.; Wang, G. Aromatic heterocycle-grafted NH₂-MIL-125(Ti) via conjugated linker with enhanced photocatalytic activity for selective oxidation of alcohols under visible light. *Appl. Catal. B Environ.* **2018**, *224*, 479–487, doi:10.1016/j.apcatb.2017.10.034.
 53. Klug, H. P.; Alexander, L. E. *X-Ray Diffraction Procedures: For Polycrystalline and Amorphous Materials*; 2nd Editio.; Wiley, 1974; ISBN 978-0-471-49369-3.
 54. Arbain, R.; Othman, M.; Palaniandy, S. Preparation of iron oxide nanoparticles by mechanical milling. *Miner. Eng.* **2011**, *24*, 1–9, doi:10.1016/J.MINENG.2010.08.025.
 55. Brunauer, S.; Emmett, P. H.; Teller, E. Adsorption of gases in multimolecular layers. *J. Am. Chem. Soc.* **1938**, *60*, 309–319, doi:10.1021/ja01269a023.
 56. Lippens, B. C.; De Boer, J. H. Studies on pore systems in catalysts V. The t method. *J. Catal.* **1965**, *4*, 319–323, doi:10.1016/0021-9517(65)90307-6.



4. Degradation of diclofenac in water under LED irradiation using combined g-C₃N₄/NH₂-MIL-125 photocatalysts





Contents lists available at ScienceDirect

Journal of Hazardous Materials

journal homepage: www.elsevier.com/locate/jhazmat

Research Paper

Degradation of diclofenac in water under LED irradiation using combined g-C₃N₄/NH₂-MIL-125 photocatalystsV. Muelas-Ramos^{a,*}, M.J. Sampaio^{b,*}, C.G. Silva^b, J. Bedia^a, J.J. Rodriguez^a, J.L. Faria^b, C. Belver^a^a Departamento de Ingeniería Química, Universidad Autónoma de Madrid, Campus Cantoblanco, E-28049 Madrid, Spain^b Laboratory of Separation and Reaction Engineering – Laboratory of Catalysis and Materials (LSRE-LCM), Departamento de Engenharia Química, Faculdade de Engenharia, Universidade do Porto, Rua Dr. Roberto Frias s/n, 4200-465 Porto, Portugal

ARTICLE INFO

Editor: Dr. L. Haizhou

Keywords:

NH₂-MIL-125g-C₃N₄

Photocatalysis

LEDs

Diclofenac degradation pathway

ABSTRACT

This study reports the photocatalytic degradation of diclofenac by hybrid materials prepared by combination of graphitic carbon nitride (g-C₃N₄) and titanium-metal organic framework (NH₂-MIL-125), in different mass proportions (MOF:C₃N₄ of 25:75, 50:50 and 75:25). The hybrid materials were fully characterized, and their properties compared to those of the individual components, whose presence was confirmed by XRD. The porous structure was the result of the highly microporous character of the MOF and the non-porous one of g-C₃N₄. The band gap values were very close to that of MOF component. Photoluminescence measurements suggested an increase on the recombination rate associated to the presence of g-C₃N₄. Photodegradation tests of diclofenac (10 mg·L⁻¹) were performed under UV LED irradiation at 384 nm. The hybrid materials showed higher photocatalytic activity than the individual components, suggesting the occurrence of some synergistic effect. The photocatalyst with a MOF:g-C₃N₄ ratio of 50:50 yielded the highest conversion rate, allowing complete disappearance of diclofenac in 2 h. Experiments with scavengers showed that superoxide radicals and holes played a major role in the photocatalytic process photodegradation, being that of hydroxyl radicals less significant. From the identification of by-products species, a degradation pathway was proposed for the degradation of diclofenac under the experimental operating conditions.

1. Introduction

The world's growing population and accelerated industrial development have notably increased wastewater effluents and their chemical complexity. This has been assessed thanks to the development of more powerful analytical techniques which enabled the identification of new pollutants, in many cases at very low concentrations (Jiménez et al., 2018). Emerging contaminants (ECs) are natural or synthetic chemicals with dangerous effects for human health and environment, which are categorized as pharmaceuticals and personal care products (PPCPs), veterinary products, pesticides, food additives and a wide diversity of industrial by-products. These compounds have shown to be recalcitrant to conventional treatments, despite founding in water in very low concentrations, resulting in their accumulation in water bodies. Nowadays, many studies are focused on the removal of these emerging contaminants from aqueous mediums (Ahmed and Jung, 2014; Arroyo and Molinos-Senante, 2018). Advanced Oxidation Processes (AOPs) are

considered very efficient methods that accelerate the oxidation of a wide variety of organic and inorganic pollutants resistant to more conventional treatment methods. This technology is based on the in-situ generation of transitory species (mainly hydroxyl radicals) with a very high oxidation capacity, which can degrade the target pollutant and even completely mineralize it to CO₂ and H₂O (Miklos et al., 2018). The term AOPs includes various of technologies, such as Fenton-like processes, ozonation, electrochemical processes, the use of ultrasound, microwaves and γ-irradiation or heterogeneous and homogeneous photocatalysis (Brillas, 2020; Kanakaraju et al., 2018). The heterogeneous photocatalysis is based on the excitation of an optical semiconductor upon irradiation with light of energy higher or equal than the catalyst bandgap. The pairs of photogenerated charges react with the species absorbed on the surface of the catalyst allowing the oxidation of the pollutant (Bahnemann, 2004). One of the most critical factors affecting the photocatalytic behavior is the light adsorption by the photocatalyst. Thus, different light sources, such as solar radiation, UV lamps, lasers

* Corresponding authors.

E-mail addresses: virginia.muelas@uam.es (V. Muelas-Ramos), mjsampaio@fe.up.pt (M.J. Sampaio).<https://doi.org/10.1016/j.jhazmat.2021.126199>

Received 17 December 2020; Received in revised form 19 May 2021; Accepted 20 May 2021

Available online 24 May 2021

0304-3894/© 2021 The Authors.

Published by Elsevier B.V. This is an open access article under the CC BY-NC-ND license

<http://creativecommons.org/licenses/by-nc-nd/4.0/>.

and light-emitting diodes (LEDs) have been analyzed. LEDs have long service life, low energy consumption and provoke a lower temperature increase than other illumination sources (Song et al., 2016).

Many different semiconductors have been analyzed as photocatalysts for the abatement of water pollutants, searching for materials with a broad light absorption spectrum, low charge recombination rate and high chemical stability. Graphitic carbon nitride ($g\text{-C}_3\text{N}_4$) is a relatively novel semiconductor tested in recent studies. It possesses a good physicochemical stability together with unique 2D and appealing electronic structure. Besides, it is active under visible light, non-toxic and unexpensive (Zeng et al., 2016; Zhao et al., 2015a, 2015b). In 2009, Wang et al. (2009a, 2009b) reported using this material as photocatalyst. This material can be synthesized from cheap precursors such as dicyanamide, urea and melamine. Unfortunately, it presents some drawbacks as photocatalyst, such as relatively low photocatalytic performance, due to fast electron-hole recombination, slow reaction kinetics and relatively low light absorbance (Cao et al., 2015; Wen et al., 2017). To overcome these limitations, the combination of $g\text{-C}_3\text{N}_4$ with other semiconductors has been evaluated (Liang et al., 2019; Xiao et al., 2019; Zhang et al., 2019; Zhou et al., 2019). One of those possible semiconductors are metal organic frameworks (MOFs) (Li et al., 2019; Panneri et al., 2017; Wang et al., 2019a, 2019b), a family of porous crystalline materials that are assembled by the combination of an organic linker and a metal oxo-cluster (Bedia et al., 2019). MOFs have many applications in different fields including water treatment, due to their high surface area, semiconductor character and tunable properties (Wang et al., 2018). Ti-containing MOFs, such as $\text{NH}_2\text{-MIL-125}$, are being widely investigated as photocatalysts (Fu et al., 2016; Wang et al., 2015; Zhu et al., 2016), due to the well-known photocatalytic properties of titania. So far, only few studies have investigated the degradation of emerging contaminants (ECs) with MOFs and $g\text{-C}_3\text{N}_4$ combinations. Panneri et al. (2017) used graphitic carbon nitride with ZIF-8 to degrade tetracycline. This compound was completely converted in 60 min, although 45% removal was due to adsorption. (Li et al., 2019) combined the same materials to remove tetracycline under visible light. The best result (75.1% conversion) was achieved with 40% of ZIF-8 at pH 8. However, the adsorption contribution was also very significant (36%). They also prepared a combination of $g\text{-C}_3\text{N}_4$, PDI (pyromellitic diimide) and $\text{NH}_2\text{-MIL-53 (Fe)}$ to remove tetracycline and carbamazepine under LED white lamp, with some addition of H_2O_2 (Li et al., 2019) MIL-53 (Fe)/urchin-like $g\text{-C}_3\text{N}_4$ has been tested by Salimi et al. (2020) to remove cefixime under simulated visible light, achieving around 80% conversion. The combination of different semiconductors can enhance the charge mobility and reduce the recombination rate, which extent the charge life and therefore can yield more reactive species and improve the photocatalytic degradation. The novelty of the present study relies on the application of an efficient photocatalytic process using $g\text{-C}_3\text{N}_4/\text{NH}_2\text{-MIL-125}$ hybrids with enhanced activity towards DCF degradation using a low-cost and energy-efficient light source.

In this study, hybrid photocatalysts with different proportions of $g\text{-C}_3\text{N}_4$ and $\text{NH}_2\text{-MIL-125(Ti)}$ were tested for the breakdown of diclofenac, as model emerging contaminant, using LEDs as the irradiation source. Diclofenac is among the most-consumed nonsteroidal anti-inflammatory drug substances. The worldwide use of this substance has generated a considerable market research interest, making it one of the most common pharmaceuticals currently detected in the environment (UNESCO/HELCOM, 2017). The challenge was to further improve the photocatalytic activity of both $\text{NH}_2\text{-MIL-125}$ and $g\text{-C}_3\text{N}_4$ through a convenient combination of both semiconductors. To the best of our knowledge, this is the first study analyzing this combination to photodegrade diclofenac under UV LEDs. Special attention has been paid on the degradation pathway of diclofenac, identifying the reaction by-products and the reactive species involved in the photocatalytic process.

2. Experimental

2.1. Synthesis of $\text{NH}_2\text{-MIL-125}$

$\text{NH}_2\text{-MIL-125}$ was synthesized following the procedure proposed by Martis et al. (2014). Briefly, 2-amino benzene dicarboxylic acid (6 mmol, Aldrich, 99%) was dissolved in N,N-dimethylformamide (25 mL, DMF, Aldrich, $\geq 99.8\%$) and stirred for 5 min. Then, titanium isopropoxide (3 mmol, Aldrich, $\geq 97\%$) was added dropwise and, finally, methanol solvent was also added (25 mL, Sigma-Aldrich, anhydrous 99.8%). After 30 min under stirring, the mixture was placed in a 65 mL Teflon-lined stainless steel autoclave and maintained at 150 °C for 16 h. The solid, separated by centrifugation, was washed three times (30 min each) with 100 mL of DMF and three additional times with 100 mL of methanol in the same conditions. Finally, a yellow solid was obtained after centrifugation and dried at 60 °C overnight. It was named $\text{NH}_2\text{-MIL-125}$.

2.2. Synthesis of $g\text{-C}_3\text{N}_4$

$g\text{-C}_3\text{N}_4$ was prepared by thermal decomposition of dicyandiamide, as described by Lima et al. (2017). The precursor was heated in a muffle furnace under static air atmosphere until 450 °C at a heating rate of 2 °C min^{-1} . After 2 h, the temperature was increased up to 550 °C at 2 °C min^{-1} and maintained for 4 h. The resulting yellow solid was washed with ultra-pure water (300 mL), filtered and dried overnight at 100 °C. It was denoted as $g\text{-C}_3\text{N}_4$.

2.3. Preparation of the $g\text{-C}_3\text{N}_4$ and $\text{NH}_2\text{-MIL-125}$ photocatalysts

The hybrid materials to be tested as photocatalysts were prepared according to the procedure previously described by Xu et al. (2017). In the case of the 50:50 (MOF: $g\text{-C}_3\text{N}_4$) material, $\text{NH}_2\text{-MIL-125}$ (100 mg) was added to a suspension with 100 mg of $g\text{-C}_3\text{N}_4$ in isopropanol (6.7 mL), to adjust a concentration of 15 $\text{g}\cdot\text{L}^{-1}$. Thus, 300 and 33 mg of $g\text{-C}_3\text{N}_4$ were dissolved in 20 and 2.2 mL of isopropanol to obtain 25:75 and 75:25 materials, respectively. The suspensions were subjected to ultrasonication for 30 min and, then, heated at 60 °C for 24 h under stirring until total solvent evaporation. Then, a yellow powder was recovered after crushing in a mortar. The samples were denoted with the mass proportion of $g\text{-C}_3\text{N}_4$ in the mixture, namely, 75% C_3N_4 , 50% C_3N_4 and 25% C_3N_4 .

2.4. Characterization

X-ray powder diffraction (XRD) patterns were obtained in a Bruker D8 diffractometer with a Sol-X energy-dispersive detector in a scanning range of 2–50°, using a $\text{Cu K}\alpha$ source. Elemental analysis was performed using a LECO CHNS-932 equipment. The porous texture was characterized by N_2 adsorption-desorption at –196 °C in a TriStar 123 equipment (Micromeritics). Before adsorption, samples were degassed in vacuum at 120 °C for at least 6 h. The specific surface area (S_{BET}) was calculated using the BET method (Brunauer et al., 1938). The t-plot method (Lippens and de Boer, 1965) was used to determine the non-microporous surface area (S_{EXT}), the micropore surface (S_{MP}) and the micropore volume (V_{M}). Total pore volume (V_{T}) was obtained by the nitrogen amount adsorbed at 0.99 relative pressure. UV–visible reflectance spectra of solid samples were recorded from 185 to 800 nm with a Shimadzu 2501PC equipment and BaSO_4 as reference. The bandgap values were determined from those spectra considering the solids as indirect semiconductors (Kampouri et al., 2018) and using the Tauc Plot technique (Tauc, 1970; Zhu et al., 2016). X-ray photoelectron spectroscopy (XPS) was employed to determine its chemical composition, using a Thermo Scientific apparatus using Al $\text{K}\alpha$ radiation (1486.68 eV). The morphology was observed using a transmission electron microscope (TEM, JEM-3000 F). EDX mapping images were obtained with an

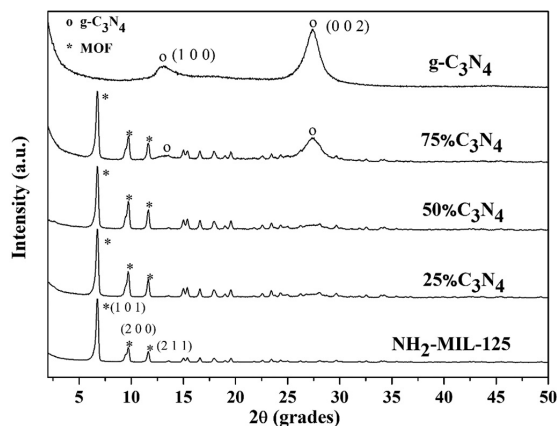


Fig. 1. XRD patterns of the bare semiconductors and the synthesized hybrid materials.

Analytical Titan apparatus (CEOSCo.) Photoluminescence spectra (PL) were obtained with a spectrofluorometer (Jasco FP-8300) with a 150 W Xenon lamp as light source. Analyses were conducted using both excitation and emission bandwidth fixed at 2.5 nm, with the excitation wavelength set at 370 nm.

2.5. Photocatalytic tests

Photodegradation of diclofenac (DCF, Aldrich, >99%) was performed in a borosilicate glass cylindrical reactor placed in a box with four LEDs (384 nm, the irradiation of each LED was $170 \text{ W}\cdot\text{m}^{-2}$). The photocatalyst ($250 \text{ mg}\cdot\text{L}^{-1}$) was dispersed in an aqueous solution (100 mL) with a DCF initial concentration equal to $10 \text{ mg}\cdot\text{L}^{-1}$. Adsorption equilibrium was reached after 30 min in the dark. Subsequently, the photocatalytic reaction was maintained for 4 h. Samples were taken at given time intervals. The photocatalyst was removed by centrifugation and the liquid phase filtrated using PTFE syringeless filters (Whatman $0.2 \mu\text{m}$). The experiments were performed by triplicate and the error bars were included. DCF was analysed by a Shimadzu Corporation Ultra High-Pressure Liquid Chromatography (UHPLC) apparatus. The chromatographic separation was carried out under isocratic mode by using a Kinetex™ XB-C18 100 \AA column ($100 \times 2.1 \text{ mm}$ i.d.; $1.7 \mu\text{m}$ particle diameter) supplied by Phenomenex, Inc. (Torrance, CA, USA) with a mobile phase composed of 0.1% formic acid aqueous solution and acetonitrile at $0.2 \text{ mL}\cdot\text{min}^{-1}$. Radical trapping experiments were carried out to check the main reactive species involved in the reaction with the most active photocatalyst. EDTA, TEMPO and tert-butanol (1 mM) were used as scavengers of holes, superoxide radicals and hydroxyl radicals, respectively. The by-products were detected by Liquid Chromatography Mass Spectrometry with electrospray ionization (LC/ESI-MS) in a Bruker Maxis II equipment using a positive ionization mode. The analyses were carried out with a 500 V end plate offset, at $200 \text{ }^\circ\text{C}$, a 3.500 V capillary voltage and $6 \text{ mL}\cdot\text{min}^{-1}$ of dry gas flow. The range of 50–3000 m/z was used to collect data. Ionic chromatography (IC) was carried out in a Metrohm 790 IC apparatus, equipped with a Metrosep A Supp 5 column, to quantify carboxylic acids and inorganic ions. $\text{Na}_2\text{CO}_3/\text{NaHCO}_3$ (3.2 mM/1.0 mM) buffer solution was used as eluent and the anionic suppressor was H_2SO_4 (100 mM).

3. Results and discussion

3.1. Characterization

Fig. 1 shows the XRD patterns of the as-prepared $\text{NH}_2\text{-MIL-125}$, $g\text{-C}_3\text{N}_4$

Table 1
Experimental and theoretical (in parentheses) elemental analysis.

| Photocatalyst | C (%) | H (%) | N (%) |
|----------------------------|-------------|-----------|-------------|
| 25% C_3N_4 | 31.7 (36.0) | 4.1 (1.6) | 19.3 (19.0) |
| 50% C_3N_4 | 33.6 (37.0) | 3.2 (1.0) | 35.9 (33.0) |
| 75% C_3N_4 | 35.5 (38.0) | 2.8 (0.5) | 49.1 (47.0) |

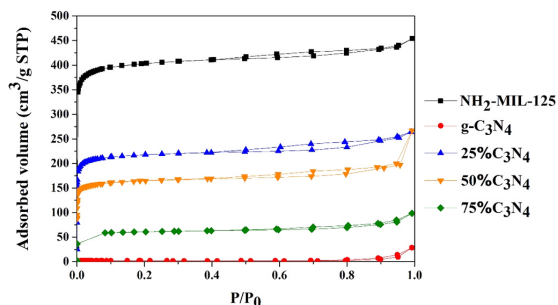


Fig. 2. Nitrogen adsorption-desorption isotherms of the bare semiconductors and the synthesized hybrid materials.

C_3N_4 and the hybrid materials prepared. In the case of pure $g\text{-C}_3\text{N}_4$, broad peaks at 13.0° and 27.6° are observed, corresponding to the (100) and (002) planes of this material, respectively (indicated with circles) (Xu et al., 2017). The peak at 13.0° indexed as the (100) plane is associated to the in-plane structural packing of tri-s-triazine units, with a calculated distance is 0.681 nm corresponding to the hole-to-hole distance in the nitride (Dong et al., 2013). This distance is smaller than that in tri-s-triazine unit (ca. 0.713 nm), probably by the presence of small tilts in the structure of the synthesized $g\text{-C}_3\text{N}_4$ (Wang et al., 2009a, 2009b). The other peak at ca. 27.6° is related to the stacking of aromatic units of $g\text{-C}_3\text{N}_4$ with an interlayer distance of 0.323 nm, corresponding to the (002) plane of the stacking of the conjugated aromatic system. In the case of $\text{NH}_2\text{-MIL-125}$ MOF, the prominent diffraction peaks are observed at 2θ values of 6.8° , 9.5° and 11.6° associated with the (101), (200) and (211) planes, respectively (indicated with asterisks) (Kim et al., 2013; Zhu et al., 2016). The diffractogram does not show the characteristic peaks of bulk titanium dioxide phases (anatase and rutile), indicating that the framework of $\text{NH}_2\text{-MIL-125}$ has been successfully crystallized (Wang et al., 2015). It should be mentioned that the intensity of the XRD peaks of $\text{NH}_2\text{-MIL-125}$ is much higher than those of $g\text{-C}_3\text{N}_4$, which indicates a higher crystallinity of the MOF. This appears clearer in the XRD patterns of 25% and 50% C_3N_4 , where only those peaks associated to the crystallographic planes of $\text{NH}_2\text{-MIL-125}$ can be clearly observed, with almost absence of the peaks of $g\text{-C}_3\text{N}_4$. In the case of the 75% C_3N_4 sample, the diffraction peaks of both $g\text{-C}_3\text{N}_4$ and $\text{NH}_2\text{-MIL-125}$ are observed due to the significantly higher proportion of the former. It can be concluded that, under the conditions of the synthesis, the crystalline structure of both semiconductors does not suffer significant modifications. Table 1 summarizes the experimental and theoretical (in parentheses) elemental analysis of 25% C_3N_4 , 50% C_3N_4 and 75% C_3N_4 . The theoretical percentages were calculated according to their elemental formulation of $g\text{-C}_3\text{N}_4$ (39.1% C; 60.9%N) and $\text{NH}_2\text{-MIL-125}$ (34.9% C; 2.1%H; 5.1% N) and the proportion of the two components used in the preparation of the mixtures. In general terms, the experimental and theoretical values fit quite well, confirming the proportion of $g\text{-C}_3\text{N}_4$ and $\text{NH}_2\text{-MIL-125}$ in the hybrid materials.

N_2 adsorption-desorption at $-196 \text{ }^\circ\text{C}$ was employed to characterized the textural properties of these materials, being the resulting isotherms depicted in Fig. 2. $\text{NH}_2\text{-MIL-125}$ MOF yielded a type I-like isotherm with a small hysteresis loop, thus, indicating an essentially microporous

Table 2

Textural properties and values of the band gap of all materials and the pseudo-first-order rate constant of DCF degradation.

| | S_{BET} (m ² /g) | S_{EXT} (m ² /g) | V_{M} (cm ³ /g) | V_{T} (cm ³ /g) | E_{g} (eV) | k (min ⁻¹) |
|-----------------------------------|--------------------------------------|--------------------------------------|-------------------------------------|-------------------------------------|---------------------|--------------------------|
| NH ₂ -MIL-125 | 1308 | 102 | 0.58 | 0.70 | 2.56 | 0.0108 |
| g-C ₃ N ₄ | 5.4 | – | 0.004 | 0.04 | 2.68 | 0.0066 |
| 25% C ₃ N ₄ | 707 | 63 | 0.31 | 0.41 | 2.60 | 0.0138 |
| 50% C ₃ N ₄ | 536 | 56 | 0.23 | 0.40 | 2.56 | 0.0282 |
| 75% C ₃ N ₄ | 188 | 28 | 0.08 | 0.15 | 2.58 | 0.0194 |

S_{BET} , BET surface area; S_{EXT} , non-microporous surface area; V_{M} and V_{T} , micropore and total pore volume, respectively; E_{g} , bandgap; k , kinetic constant.

structure with some contribution of mesoporosity (Fan et al., 2018). In contrast, g-C₃N₄ showed almost negligible N₂ adsorption except some small amount at high relative pressures, suggesting a fairly scarce mesoporosity in a basically non-porous solid (Zhang et al., 2017). As expected, the samples resulting from hybrids of both materials correlates well with the proportions of NH₂-MIL-125 and g-C₃N₄, showing a higher porosity as the relative amount of MOF increases, being that porosity of the same character. Despite this, it should be mentioned that the reduction in the amount of N₂ adsorbed does not follow a linear trend with the proportion of both components, suggesting that g-C₃N₄ may partially block MOF pores. Table 2 collects the data of the porous texture of the samples. NH₂-MIL-125 gave a BET surface area, pore volume and micropore volume very similar to the reported in previous studies (Kim et al., 2013; Martis et al., 2014; Rada et al., 2015). In contrast, the external area value was higher (Gómez-Avilés et al., 2019), which can be related to the additional washings carried out in the synthesis, allowing more efficient removal of trapped solvent molecules. In the case of g-C₃N₄, the values obtained are in agreement with the previously given in the literature (Lima et al., 2017; Liu et al., 2017; Zhao et al., 2015a, 2015b). The textural parameters of the hybrids are in the expected values depending on the MOF/g-C₃N₄ ratio. Increasing g-C₃N₄ content causes the blockage of the MOF pores, decreasing the surface area and porosity.

Fig. 3A and B represent the UV-Vis absorption spectra and the derived Tauc plots of the different samples, respectively. The bare NH₂-MIL-125 spectrum shows two absorption bands, with maxima around

280 and 390 nm. The charge transfer from O to Ti (LMCT=ligand-to-metal charge transfer) in the (Ti₈O₈(OH)₄) metal clusters is associated with the band at 280 nm, whereas the second absorption band is related to transferring charges from the amino groups to the (Ti₈O₈(OH)₄) clusters through the organic linker. This broad absorption in the visible-light region results in the characteristic yellow colour of this MOF (Gómez-Avilés et al., 2019; Huang et al., 2020). Regarding the bare g-C₃N₄, its characteristic bands appeared in the 350–380 nm range and are associated with π - π^* transitions of conjugated ring system (Panneri et al., 2017). Yan et al. (2009) concluded that the absorption edges of the g-C₃N₄ synthesized from melamine shifted significantly to longer wavelengths at increasing synthesis temperature. This behaviour is probably due to the higher number of defects in the structure. The defects are related to the alterations in the regular structural order of g-C₃N₄, usually associated to the synthesis performed at high temperatures, such as the destruction of the connected π -conjugated system (Yan et al., 2009). These defects can result in a reduction of the mobility of the charges, and thus reduce their recombination rate, resulting in an increase of the photoactivity (Gu et al., 2015). In the current study, we used a relatively high temperature for the synthesis of g-C₃N₄ (550 °C), which can justify the broad absorption observed in the visible light range. Further, a significantly stronger absorption can be observed in the visible range (specifically, 450–800 nm) in the hybrid materials. This behaviour, previously reported in the literature for NH₂-MIL-125 @g-C₃N₄ composites (Tian et al., 2018), can be ascribed to the close contact between the particles of the two components, which would facilitate the charge transfer between both semiconductors, thus, enhancing the light absorption and resulting in the observed red-shift of the adsorption edge. It should be mentioned that this absorption band is close to the wavelength of the LED irradiation (384 nm) that will be used in the photocatalytic degradation tests. The bandgap values (E_{g}) are collected in Table 2. NH₂-MIL-125 yielded a value of 2.56 eV, similar to those already reported (Hendon et al., 2013; Wang et al., 2019a, 2019b), and g-C₃N₄ displayed a band gap of 2.68 eV, also similar to the reported in the literature (Lima et al., 2017; Martínez et al., 2011; Xiao et al., 2019). The bandgap values of the hybrids were 2.60, 2.56 and 2.58 eV for 25%g-C₃N₄, 50%g-C₃N₄ and 75%g-C₃N₄, respectively. These E_{g} values are close to the pristine MOF, suggesting that this last is the determining component regarding the optical properties of the hybrid samples (Yi

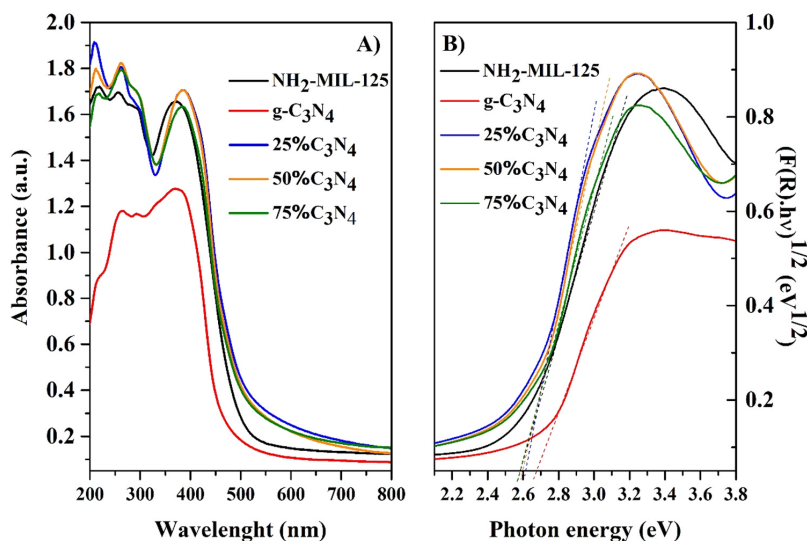


Fig. 3. (A) UV-vis absorption spectra and (B) Tauc plots of the hybrid materials synthesized.

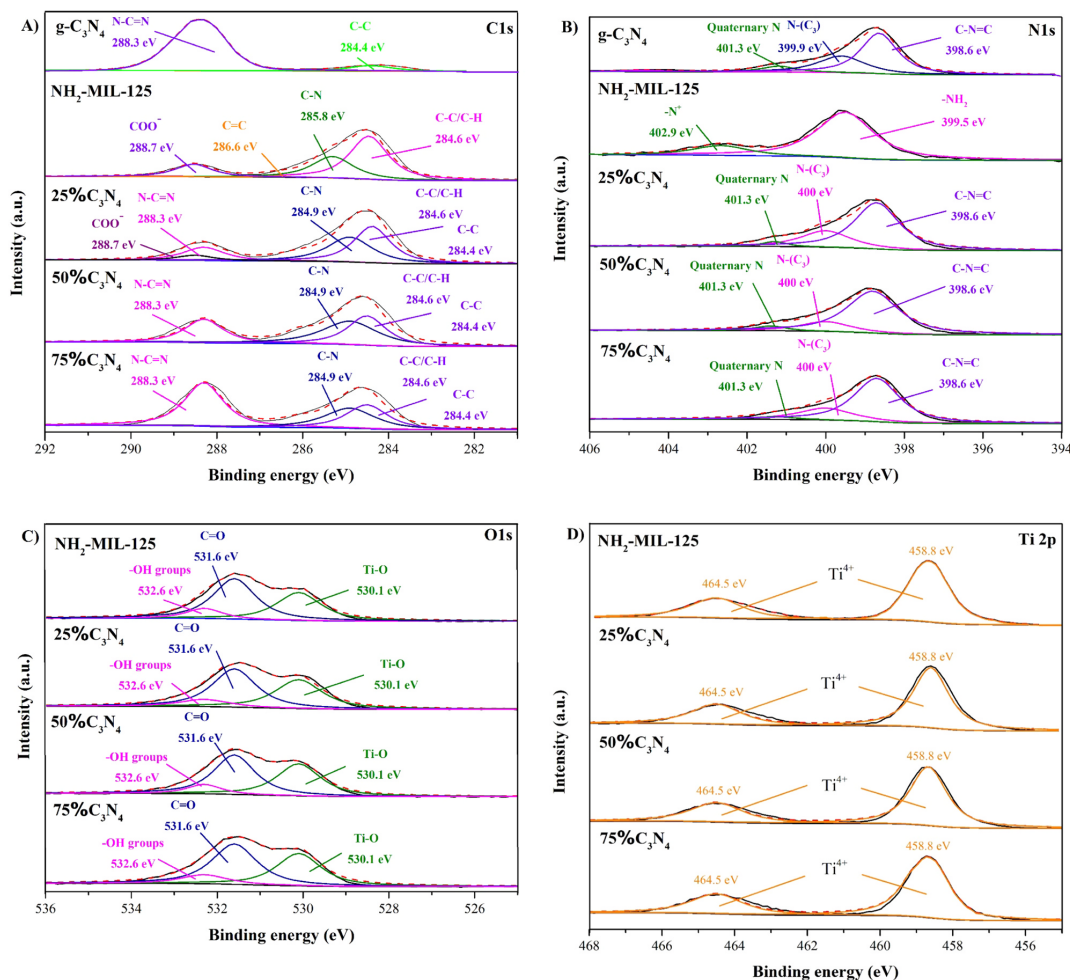


Fig. 4. XPS spectra A) C 1s, B) N 1s, C) O 1s and D) Ti 2p.

et al., 2019).

The surface composition of the materials was analysed by XPS analysis. In the case of NH₂-MIL-125, four peaks are identified in the C 1s spectrum (Fig. 4A). The peaks at 284.6, 285.8, 286.6 and 288.7 eV correspond to C–C/C–H, C–N, C⁺C and COO[−], respectively. In the case of the N 1s spectrum (Fig. 4B), this signal is deconvoluted using two peaks located at 399.5 and 402.9 eV corresponding to amine group, and N⁺, respectively (Wang et al., 2015). Three peaks are identified in the O 1s spectrum (Fig. 4C), related to Ti–O, C=O and –OH groups at 530.1, 531.6 and 532.6 eV, respectively. Finally, Ti 2p spectrum (Fig. 4D) presents two peaks at 464.5 and 458.8 eV, corresponding to the Ti⁴⁺ ions of the metal oxo-clusters that constituted this MOF (Wang et al., 2018). On the other hand, g-C₃N₄ C 1s spectrum (Fig. 4A) shows two peaks, one at 288.3 eV related to the presence of N–C⁺N, and the second peak at 284.4 eV associated to C–C bonds of g-C₃N₄. The N 1s of carbon nitride spectrum (Fig. 4B) presents three peaks associated to the presence of (i) quaternary N bonded three carbon atoms at 401.3 eV, (ii) N–(C)₃ units at 399.9 eV, and (iii) C–N–C in the triazine rings at 398.6 eV. In the case of the C 1s spectra of the hybrid samples (Fig. 4A) three peaks are observed. The first peak at 288.3 eV corresponded to N–C⁺N, while C–N bond is identified at 284.9 eV. Then, the peak at 284.6 eV has two

contributions, C–C/C–H from the MOF and C–C from the g-C₃N₄ (284.4 eV). Additionally, 25% C₃N₄ presents other peak at 288.7 eV related to COO[−] from the MOF due to its major presence in this sample. Moreover, it can be clearly seen that the relative height of the peak at 288.3 eV related to C–N⁺C increase with the amount of g-C₃N₄ in the hybrid sample, in agreement with the high intensity of this peak in the C 1s spectrum of bare g-C₃N₄. On the other hand, three peaks were identified in the N 1s spectra of the hybrids, namely quaternary N, N–(C)₃ and C–N⁺C, located at 401.3, 400 and 398.6 eV, respectively (Ye et al., 2013). These peaks are very similar to those of the pattern g-C₃N₄ in agreement with the much higher proportion of nitrogen in the g-C₃N₄ moiety. Similarly, the O 1s and Ti 2p spectra of the hybrids are very similar to that of the parent MOF, since g-C₃N₄ does not contain oxygen nor titanium. It seems that the bonds are not affected significantly by the different ratios of g-C₃N₄ to NH₂-MIL-125 used. This was expected since the samples were synthesized by a simple physical mixing at different ratios between g-C₃N₄ and NH₂-MIL-125, and thus the formation of new bonds is unlikely.

Fig. 5 shows TEM images of the two semiconductors and the 50% C₃N₄ sample. NH₂-MIL-125 exhibited plates with rounded edges between 200 and 500 nm particle size, in agreement with previous studies

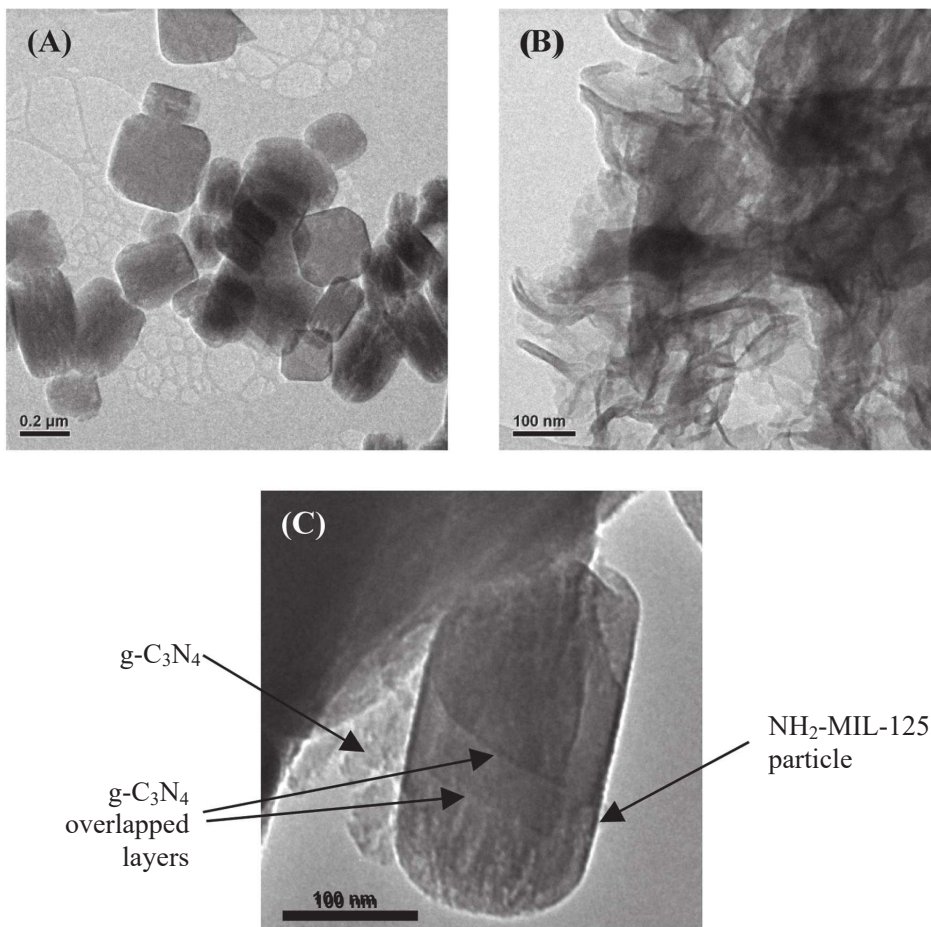


Fig. 5. TEM images of (A) $\text{NH}_2\text{-MIL-125}$, (B) $\text{g-C}_3\text{N}_4$ and (C) $50\%\text{C}_3\text{N}_4$.

(Qiu et al., 2019), while $\text{g-C}_3\text{N}_4$ presented a layered morphology similar to that described previously (Zhang et al., 2016). It can be observed that some of the layers are curled to form some vessels. This inhomogeneity has been attributed to uneven temperature distribution during the synthesis (Li et al., 2009). The $50\%\text{C}_3\text{N}_4$ sample (Fig. 3C) shows the morphological features of both components in contact between them. Fig. 6 shows the HRTEM image and EDX mapping of C, N, O and Ti from $50\%\text{C}_3\text{N}_4$. The HRTEM image (Fig. 6A) shows the presence of several disk-shape particles, associated with MOF particles, below a not so ordered structure that can be probably $\text{g-C}_3\text{N}_4$. As can be seen from the EDX mapping results, the elemental distribution fits well with the previous assumptions. The disk-shaped morphologies are mainly composed of Ti, C and O, from the metal nodes ($\text{Ti}_8\text{O}_8(\text{OH})_4$) and the organic linker ($\text{O}_2\text{C-C}_6\text{H}_3(\text{NH}_2)\text{-CO}_2$) of the MOF. Lower amounts of N form also part of this sample, due to the amino group ($-\text{NH}_2$) of the organic linker. On the other hand, the irregular morphology above in the image, is clearly only composed of C and N as corresponds to $\text{g-C}_3\text{N}_4$ moiety. These images suggest the formation of a hybrid material, which could improve the transfer efficiency and separation of photogenerated charges.

Fig. 7 summarizes the photoluminescence (PL) spectra of the materials synthesized, useful to check the transfer and recombination of photogenerated electron-hole pairs. MOF did not exhibit PL emission in this region with the excitation wavelength used (370 nm). Meanwhile,

the bare $\text{g-C}_3\text{N}_4$ and the hybrid samples showed two different bands, a more intense one at around 475 nm and another of lower intensity, at 525 nm. The latter corresponds to a radiative recombination of charge carriers captured by traps, while the first one is a result of light emission from direct pairs recombination (Lima et al., 2017). It is accepted that the intensity of the signal is related to the amount of charge recombination. Thus, the greatest relative intensity observed for $\text{g-C}_3\text{N}_4$ indicates easy recombination of electrons and holes. The hybrid samples yielded weaker PL spectra as the MOF proportion increased, indicating that this component may effectively inhibit the electron-hole recombination. Despite, $25\%\text{C}_3\text{N}_4$ exhibited the lowest PL intensity among the samples, the PL spectrum of $50\%\text{C}_3\text{N}_4$ is very similar. Considering the similar PL spectra of both samples seems reasonable predict that the higher activity of the $50\%\text{C}_3\text{N}_4$ compared with the $25\%\text{C}_3\text{N}_4$ is not only related with the charge mobility but also to light absorption and interactions with the pollutant molecules.

3.2. Photocatalytic tests

The photocatalytic tests of the different samples were checked for the degradation of diclofenac under LED irradiation (384 nm). Before irradiation, all samples were immersed in the diclofenac solution ($10\text{ mg}\cdot\text{L}^{-1}$) in the dark to achieve the adsorption equilibrium. This reduced the

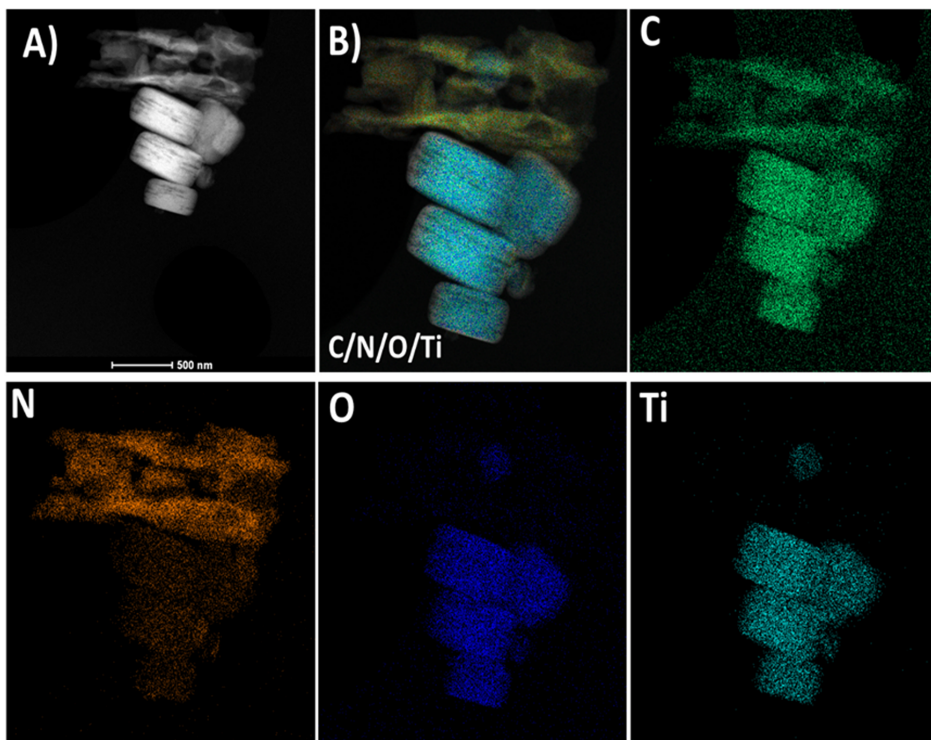


Fig. 6. A) HRTEM image, B) all elements in the same region and EDX element mapping of C, N, O, Ti of 50% C_3N_4 .

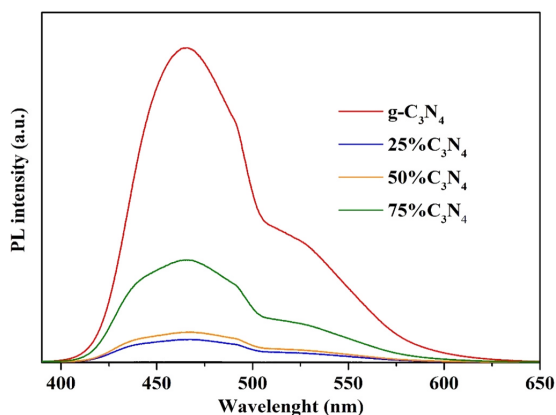


Fig. 7. Photoluminescence spectra of the synthesized hybrid materials compared with the bare $g-C_3N_4$.

diclofenac concentration down to ca. $8 \text{ mg}\cdot\text{L}^{-1}$, except for $g-C_3N_4$ that showed negligible adsorption, consistently with its poor porosity. Fig. 8 represents the concentration evolution of diclofenac upon irradiation time with all the materials checked as photocatalysts. Previous blank experiment was carried out, where diclofenac showed negligible degradation, confirming its stability in water under LED irradiation. Neat $g-C_3N_4$ displayed the lowest photocatalytic performance, achieving only 50% DCF conversion after 2 h of irradiation, while NH_2 -MIL-125 yielded 80% in the same time. Higher photocatalytic degradation rates

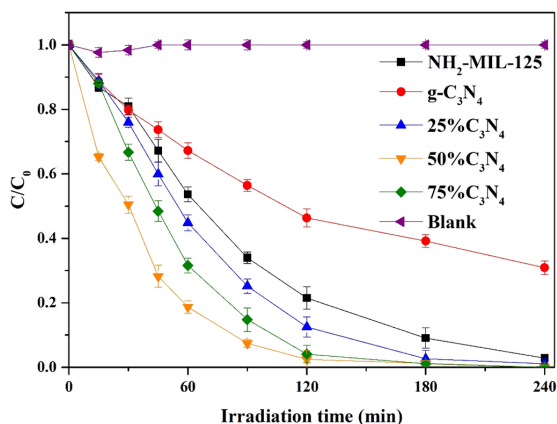


Fig. 8. Evolution of diclofenac concentration upon LED irradiation of all synthesized photocatalysts and the bare semiconductors.

were described by all the hybrid samples, suggesting the occurrence of some synergistic effect associated to the combination of both semiconductors. This enhanced activity can be ascribed to several reasons: (i) a more efficient interfacial charge transfer from $g-C_3N_4$ to MOF, hence different pathways are provided for the migration of photo-generated charges (Wang et al., 2019a, 2019b; Xu et al., 2017); (ii) a slower recombination rate of these charges as suggested by the PL measurements; and (iii) better light absorption of the hybrids materials as shown

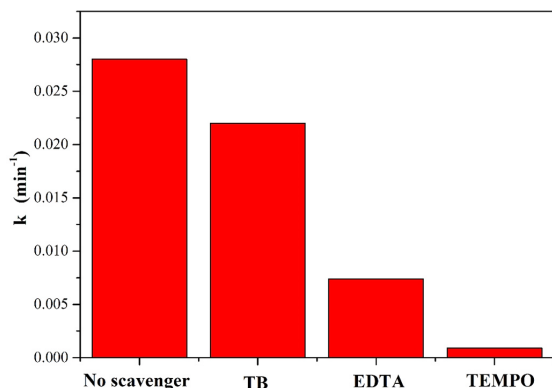


Fig. 9. Effect of EDTA (h^+), TEMPO (O_2^-) and TB (HO^\bullet) scavengers on the rate constant of diclofenac photodegradation for 50% C_3N_4 (dosage of scavengers = 1 mM).

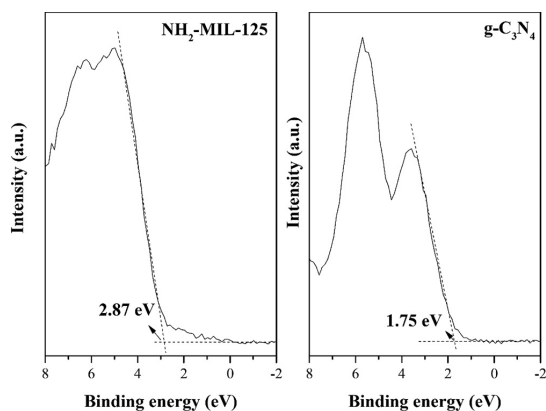


Fig. 10. XPS spectra at low binding energies for the estimation of the maximum valence band (VBM) of (A) $\text{NH}_2\text{-MIL-125}$ and (B) $\text{g-C}_3\text{N}_4$.

by the UV-vis spectra, especially in the case of 50% C_3N_4 , the one yielding the highest rate of DCF conversion.

According to Calza et al. (2006), the disappearance of diclofenac fits well to a pseudo-first-order rate equation. The values of the rate constant (k) are included in Table 2. The highest value, corresponding to 50% C_3N_4 , is almost three-fold the one for $\text{NH}_2\text{-MIL-125}$ and more than four times higher than that of $\text{g-C}_3\text{N}_4$. To the best of our knowledge, the literature does not report on the degradation of diclofenac upon UV LED or UV irradiation using MOF/ $\text{g-C}_3\text{N}_4$. To understand the photocatalytic mechanism occurring during the degradation of DCF several scavengers were used to determine the main species involved in the reaction (Fig. 9). Ethylenediaminetetraacetic acid (EDTA) was used to trap holes (h^+) (Marques et al., 2013; Tao et al., 2015), (2,2,6,6-tetramethylpiperidin-1-yl)oxyl (TEMPO) to trap superoxide radicals (Li et al., 2021), while tert-butanol (TB) was chosen to impair hydroxyl radicals (HO^\bullet) (Jiang et al., 2014; Xu et al., 2011). The corresponding doses (1 mM) were selected on the basis of previous studies (Sampaio et al., 2017; Serpone et al., 2000). EDTA caused major inhibition with almost five-fold decrease of the rate constant. This result evidences the direct contribution of the h^+ in the photocatalytic removal of DCF under LED irradiation. However, the diclofenac degradation was almost completely inhibited when TEMPO is used, suggesting that superoxide radicals are

the main specie involved in the process. Meanwhile, TB addition caused significantly smaller reduction (around 20%) of the rate constant, indicating that participation of the hydroxyl radicals in the reaction is less important. These results suggest that the active species involved in the photocatalytic mechanism are mainly superoxide radicals, with lower but significant contribution of holes.

The valence band maximum (VBM) of $\text{g-C}_3\text{N}_4$ and $\text{NH}_2\text{-MIL-125}$ has been estimated from the XPS, by linear extrapolation of the low binding energy edge of the valence band spectrum (Fig. 10). As can be seen, the VBMs of $\text{NH}_2\text{-MIL-125}$ and $\text{g-C}_3\text{N}_4$ are 2.87 and 1.75 eV, respectively. The position of the conduction band (CB) can be approximated from the VBM and band gap values ($E_{\text{CB}} = \text{VBM} - E_g$) resulting in 0.31 and -0.93 eV for $\text{NH}_2\text{-MIL-125}$ and $\text{g-C}_3\text{N}_4$, respectively. According to these results, Fig. 11 depicts a plausible S-scheme photocatalytic mechanism for the degradation of diclofenac (Xu et al., 2020). In this case, $\text{NH}_2\text{-MIL-125}$ MOF acts as oxidation photocatalyst, while $\text{g-C}_3\text{N}_4$ acts as reduction photocatalyst. The key to the process is the recombination of the electrons from the conduction band (CB) of the MOF with the holes of the valence band (VB) of $\text{g-C}_3\text{N}_4$, avoiding the recombination of the electrons of the CB in $\text{g-C}_3\text{N}_4$ and the holes in the VB of $\text{NH}_2\text{-MIL-125}$, which are those with highest redox ability. This recombination seems to be due to three factors, namely (i) the formation of an internal electric field between both semiconductors, (ii) the band bending produced by the electrons movement, and (iii) the Coulombic attraction between electrons and holes (Xu et al., 2020). The first factor can be explained as follows, when both semiconductors get in contact, the electrons flow spontaneously from $\text{g-C}_3\text{N}_4$ to the MOF with the formation of an electron depletion layer in $\text{g-C}_3\text{N}_4$ and an electron accumulation layer in $\text{NH}_2\text{-MIL-125}$. Consequently, $\text{g-C}_3\text{N}_4$ interface is positively charged, while $\text{NH}_2\text{-MIL-125}$ is negatively charged and an internal electric field from $\text{g-C}_3\text{N}_4$ to the MOF is formed. This internal electric field accelerates the photogenerated electron transfer from $\text{NH}_2\text{-MIL-125}$ to $\text{g-C}_3\text{N}_4$ (in the opposite direction to the internal electric field). The second factor is produced by the Fermi level alignment of both semiconductor when they are in contact. The Fermi level of $\text{NH}_2\text{-MIL-125}$ undergoes an upward shift, while that of $\text{g-C}_3\text{N}_4$ suffers a downward shift. These band bendings facilitate the recombination of the electrons in the CB of the MOF and the holes in the VB of $\text{g-C}_3\text{N}_4$, with the Coulombic attraction reinforcing the recombination between those electrons and holes. All these processes result in the elimination by recombination of the useless electron and holes. LED irradiation promotes electron transfer from the VB to the CB in both semiconductors, resulting in holes in the respective VB and electrons in the CB. Since the photocatalytic mechanism is mainly due to superoxide radicals with some contribution of holes, it is expected that the electrons located in the CB of the MOF (0.31 eV) migrate to the VB of the $\text{g-C}_3\text{N}_4$ (1.75 eV), leading to aforementioned recombination. Thus, the electrons in the CB of the $\text{g-C}_3\text{N}_4$ cannot recombine and can yield superoxide radicals from the oxygen dissolved in the water, since the standard redox potential of $\text{O}_2/\text{O}_2^{\bullet-}$ (-0.33 eV vs. NHE) is more positive than the CB of this material. As consequence, the holes in the VB of the MOF (2.87 eV) become available for the direct oxidation of the pollutant. The formation of hydroxyl radicals from water by the holes of $\text{g-C}_3\text{N}_4$ is impeded since the standard redox potential of the $\text{HO}^\bullet/\text{HO}^-$ (2.40 eV vs. NHE) is more positive than the VB of $\text{g-C}_3\text{N}_4$, confirming the lower participation of the HO^\bullet radicals in the photocatalytic mechanism. Moreover, the S-scheme favors the charges separation among semiconductors, reducing the recombination rate (as confirmed by PL measurements, Fig. 7).

The stability of the photocatalyst is a crucial issue regarding potential applications. The 50% C_3N_4 catalyst was characterized after reaction, by N_2 adsorption-desorption at -196 °C, XRD and TEM (Fig. 12). The diffraction pattern remained unchanged without additional peaks. The photocatalyst maintains its morphology (plate disks with rounded edges) as suggest the unaltered morphology observed in TEM image. The comparison of the N_2 adsorption-desorption isotherms of the neat and used MOF shows a slight reduction of the amount of N_2 adsorbed after

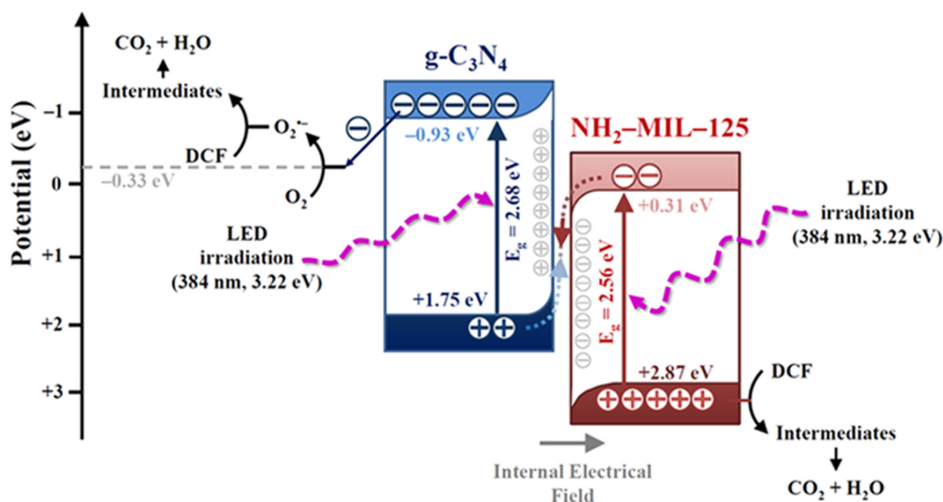


Fig. 11. Proposed S-scheme photocatalytic mechanism for the diclofenac degradation using 50% C_3N_4 .

use, and consequently, a low-significance decrease of the BET surface area (from 536 to 467 $\text{m}^2 \cdot \text{g}^{-1}$). This reduction can be associated to the adsorption of diclofenac or reaction by-products at surface of the MOF.

Moreover, TOC mineralization rates are not provided due to a limited but detectable organic linker leaching, as can be observed in a previous study (Gómez-Avilés et al., 2020). Additional effort should be applied to improve the stabilize of this MOF in water.

3.3. Reaction by-products and degradation pathway

Table 3 collects the species detected from DCF breakdown with 50% C_3N_4 , as measured by LC/ESI-MS and IC. These presented a low mass error ($< \pm 1 \text{ mDa}$) and a correct value of RDB, defined as the amount of rings and double bonds in the molecule. For instance, diclofenac yields 9, being 7 due to double bonds and 2 to the rings. Based on the detected compounds, several degradation pathways are depicted in Fig. 13. In the first route, the C-N cleavage of the side chain can result in the identification of DCF-1 (m/z 161.9872) (Gou et al., 2017). The hydroxylation of this product would give DCF-2 (m/z 177.9821) (Moctezuma et al., 2020). An alternative reaction path was proposed by Zhang et al. (2020) through the decarboxylation of the DCF molecule to give DCF-3* (m/z 252). Although this intermediate was not detected in our work, its formation may be expected since its oxidized derivative was detected, named DCF-3 (m/z 266.0135). Further hydroxylation of DCF-3 gives the DCF-4 (m/z 282.0085). A third degradation route can begin with the hydroxylation at C5 position of diclofenac, in accordance with previous studies, resulting in the DCF-5 (m/z 312.0184) (Cheng et al., 2015; Lu et al., 2017; Pérez-Estrada et al., 2005). Further oxidation produces DFC-6 (m/z 310.0032) (Calza et al., 2006). In addition, other by-products were detected from the coupling of DCF molecules. First, two DCF molecules would lead to DCF-7 (m/z 589.0252), which upon HCl loss, gives rise to DCF-8 (m/z 553.0486). Formation of dimers has been reported by Keen et al. (2013). Finally, IC analyses showed the formation of short-chain carboxylic acids, such as formic and oxalic, whose evolution can be seen in Fig. 14. The amounts of both acids increased as the reaction proceeded, due to the oxidation of previous by-products. Chloride appeared after 30 min, probably due to the loss of HCl from DCF-7 or some other chlorinated by-products not detected. Only nitrite was detected as mineralization nitrogen product.

4. Conclusions

MOF/ $\text{g-C}_3\text{N}_4$ materials to be tested as photocatalysts were successfully synthesized by a straightforward method, using different proportions of both semiconductors. The structure of these two components was observed in all photocatalysts prepared. The porous texture was the result of the highly microporous character of MOF and the non-porous one of $\text{g-C}_3\text{N}_4$, although with some lower surface area and pore volume than the expected from the relative amounts of each component, most probably due to partial blockage of the pores by $\text{g-C}_3\text{N}_4$. The morphology of the hybrids also showed the main features of both components, including plate-like particles from the MOF and fiber-like from $\text{g-C}_3\text{N}_4$. All the MOF/ $\text{g-C}_3\text{N}_4$ samples showed very similar band gap values, closer to the pristine MOF, suggesting that the optical properties are basically determined by this component. These materials have demonstrated photocatalytic activity under LED irradiation, superior to that of the individual components, suggesting the occurrence of some synergistic effect. The MOF presence reduces the electron-holes recombination rate of the $\text{g-C}_3\text{N}_4$. Regarding the photocatalytic performance, 50% C_3N_4 yielded the best result, with complete conversion of the target pollutant (diclofenac) in 2 h, with a pseudo-first-order rate constant value of 0.0282 min^{-1} , almost three-fold the obtained with the pristine $\text{NH}_2\text{-MIL-125}$ and more than four-fold the one with $\text{g-C}_3\text{N}_4$. Radical trapping experiments proved that superoxide radicals and holes played a significant role in the photocatalytic mechanism. From the reaction species identified, several routes have been proposed for diclofenac degradation pathway, involving, hydroxylation, coupling and oxidation reactions. Short-chain carboxylic acids, such as formic and oxalic acid, were identified as final by-products, as well as chloride and nitrite.

CRedit authorship contribution statement

V. Muelas-Ramos: Methodology. M.J. Sampaio: Conceptualization, Methodology, Writing - review & editing, Supervision, Funding acquisition. C.G. Silva: Writing - review & editing, Funding acquisition. J. Bedia: Conceptualization, Writing - review & editing, Supervision. J. J. Rodríguez: Writing - review & editing, Supervision, Funding acquisition. J.L. Faria: Conceptualization, Writing - review & editing, Supervision, Funding acquisition. C. Belver: Conceptualization, Writing - review & editing, Supervision, Funding acquisition. All authors have

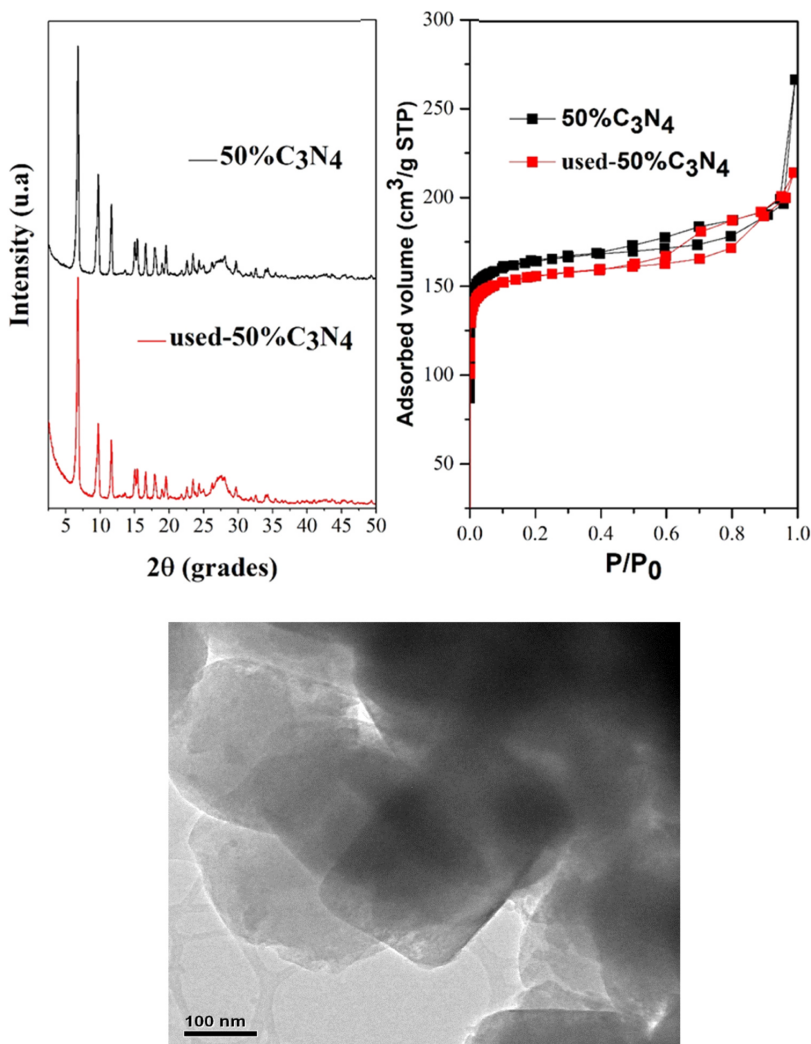


Fig. 12. XRD pattern, nitrogen adsorption-desorption isotherm and TEM image of 50%C₃N₄ sample after reaction.

Table 3

Accurate mass (m/z) values of the species identified in the photocatalytic breakdown of DCF with 50%C₃N₄.

| Name | Retention time (min) | Experimental m/z [M + H] ⁺ | Proposed formula [M + H] ⁺ | Calculated m/z [M + H] ⁺ | Mass error (mDa) | Ring Double Bond (RDB) |
|------------|----------------------|---|---|---------------------------------------|------------------|------------------------|
| Diclofenac | 17.4 | 296.0237 | C ₁₄ H ₁₂ Cl ₂ NO ₂ | 296.0235 | 0.9 | 9 |
| DCF-1 | 3.2 | 161.9872 | C ₆ H ₆ Cl ₂ N | 161.7000 | -0.6 | 4 |
| DCF-2 | 3.9 | 177.9821 | C ₆ H ₆ Cl ₂ NO | 177.9821 | -0.1 | 4 |
| DCF-3 | 6.9 | 266.0135 | C ₁₃ H ₁₀ Cl ₂ NO | 266.0134 | -0.2 | 9 |
| DCF-4 | 8.1 | 282.0085 | C ₁₃ H ₁₀ Cl ₂ NO ₂ | 282.0083 | -0.7 | 9 |
| DCF-5 | 6.2 | 312.0184 | C ₁₄ H ₁₂ Cl ₂ NO ₃ | 312.0189 | 0.6 | 9 |
| DCF-6 | 6.0 | 310.0032 | C ₁₄ H ₁₀ Cl ₂ NO ₃ | 310.0032 | 0.1 | 10 |
| DCF-7 | 31.9 | 589.0252 | C ₂₈ H ₂₁ Cl ₄ N ₂ O ₄ | 589.0266 | -0.3 | 18 |
| DCF-8 | 30.9 | 553.0486 | C ₂₈ H ₂₀ Cl ₃ N ₂ O ₄ | 553.0483 | -0.4 | 19 |

read and agreed to the published version of the manuscript.

Declaration of Competing Interest

The authors declare that they have no known competing financial

interests or personal relationships that could have appeared to influence the work reported in this paper.

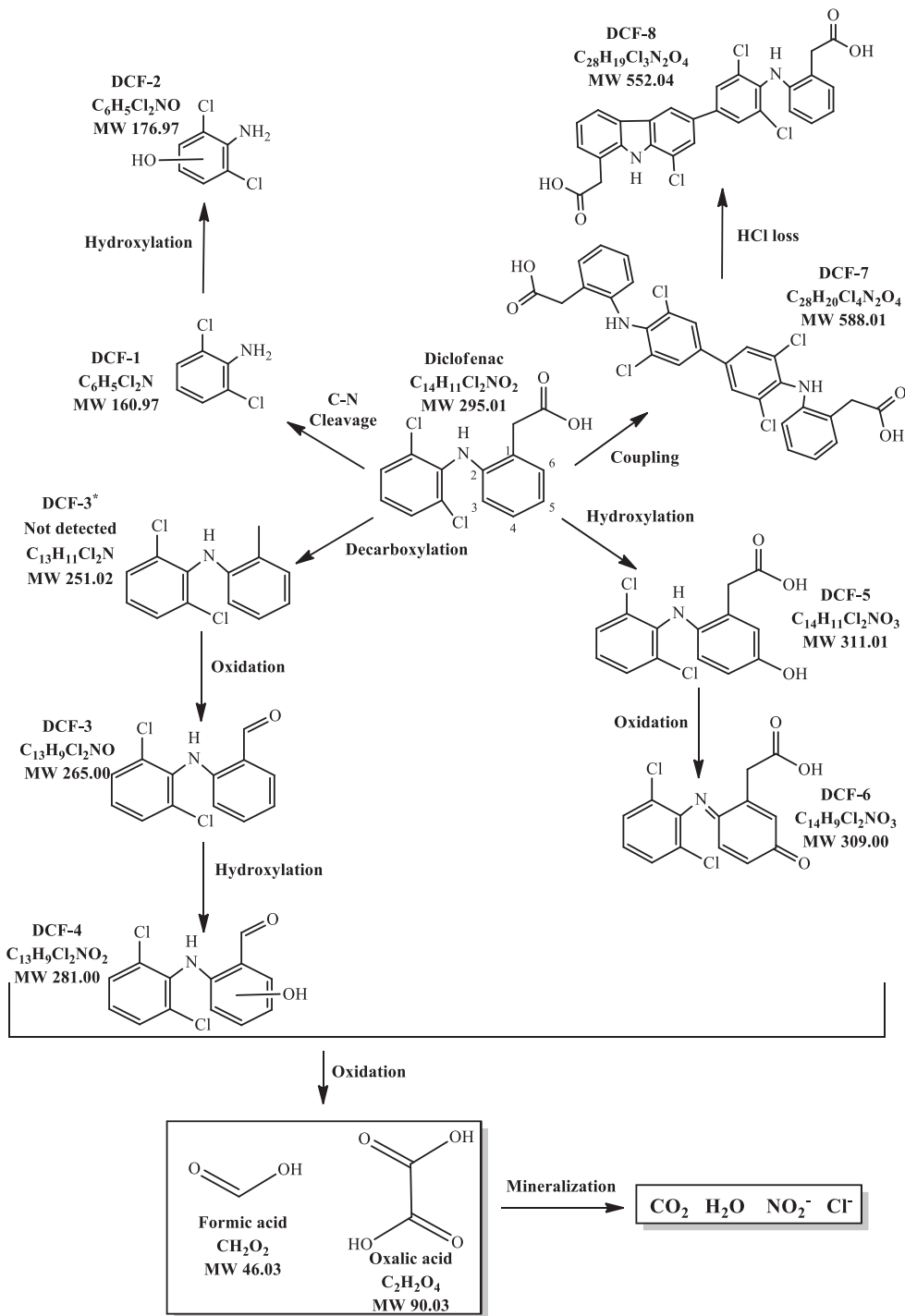


Fig. 13. Proposed reaction pathway for DCF photocatalytic breakdown with 50% C_3N_4 .

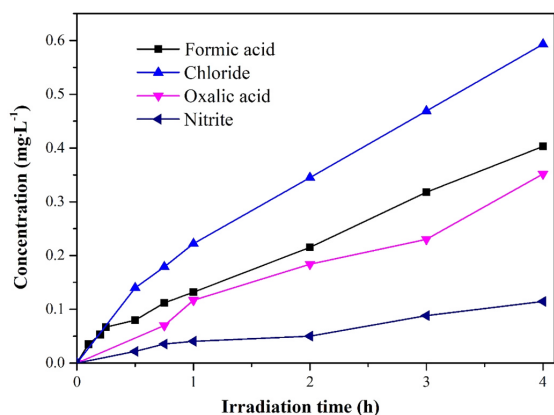


Fig. 14. Evolution of short-chain carboxylic acids, chloride and nitrite concentration upon reaction time with 50% C_3N_4 .

Acknowledgements

This work was financially supported by Associate Laboratory LSRE-LCM - UID/EQU/50020/2020 - funded by national funds through FCT/MCTES (PIDDAC) and by project POCI-01-0145-FEDER-030674, financed by the ERDF through COMPETE2020 and POCI - and by national funds through FCT (Portugal). This research was also funded by Spanish Ministry of Economy and Competitiveness (project CTQ2016-78576-R, FEDER funds) and the State Research Agency (PID2019-106186RB-I00/AEI/10.13039/501100011033) (Spain). V. Muelas-Ramos thanks to MCIU for BES-2017-082613 grant. Authors thank the TEM images from the Centro Nacional de Microscopía Electrónica (Spain). Authors would like to acknowledge the use of Servicio General de Apoyo a la Investigación-SAI for EDX mapping images, Universidad de Zaragoza (Spain) and the Research Support Service of XPS data from University of Málaga (Spain).

References

Ahmed, I., Jung, S.H., 2014. Composites of metal-organic frameworks: preparation and application in adsorption. *Mater. Today* 17, 136–146. <https://doi.org/10.1016/j.mat.2014.03.002>.

Arroyo, P., Molinos-Senante, M., 2018. Selecting appropriate wastewater treatment technologies using a choosing-by-advantages approach. *Sci. Total Environ.* 625, 819–827. <https://doi.org/10.1016/j.scitotenv.2017.12.331>.

Bahnenmann, D., 2004. Photocatalytic water treatment: solar energy applications. *Sol. Energy* 77, 445–459. <https://doi.org/10.1016/j.solener.2004.03.031>.

Bedia, J., Muelas-Ramos, V., Peñas-Garzón, M., Gómez-Avilés, A., Rodríguez, J., Belper, C., 2019. A review on the synthesis and characterization of metal organic frameworks for photocatalytic water purification. *Catalysts* 9, 52. <https://doi.org/10.3390/catal9010052>.

Brillas, E., 2020. A review on the photoelectro-Fenton process as efficient electrochemical advanced oxidation for wastewater remediation. Treatment with UV light, sunlight, and coupling with conventional and other photo-assisted advanced technologies. *Chemosphere* 250, 126198. <https://doi.org/10.1016/j.chemosphere.2020.126198>.

Brunauer, S., Emmett, P.H., Teller, E., 1938. Adsorption of gases in multimolecular layers. *J. Am. Chem. Soc.* 60, 309–319. <https://doi.org/10.1021/ja01269a023>.

Calza, P., Sakkas, V.A., Medana, C., Baiocchi, C., Dimou, A., Pelizzetti, E., Albanis, T., 2006. Photocatalytic degradation study of diclofenac over aqueous TiO_2 suspensions. *Appl. Catal. B Environ.* 67, 197–205. <https://doi.org/10.1016/j.apcatb.2006.04.021>.

Cao, S., Low, J., Yu, J., Jaroniec, M., 2015. Polymeric photocatalysts based on graphitic carbon nitride. *Adv. Mater.* 27, 2150–2176. <https://doi.org/10.1002/adma.201500033>.

Cheng, H., Song, D., Liu, H., Qu, J., 2015. Permanganate oxidation of diclofenac: the pH-dependent reaction kinetics and a ring-opening mechanism. *Chemosphere* 136, 297–304. <https://doi.org/10.1016/j.chemosphere.2014.11.062>.

Dong, F., Zhao, Z., Xiong, T., Ni, Z., Zhang, W., Sun, Y., Ho, W.K., 2013. In situ construction of $g-C_3N_4/g-C_3N_4$ metal-free heterojunction for enhanced visible-light photocatalysis. *ACS Appl. Mater. Interfaces* 5, 11392–11401. <https://doi.org/10.1021/am403653a>.

Fan, Y.H., Zhang, S.W., Qin, S., Bin, Li, X.S., Qi, S.H., 2018. An enhanced adsorption of organic dyes onto NH_2 functionalization titanium-based metal-organic frameworks and the mechanism investigation. *Microporous Mesoporous Mater.* 263, 120–127. <https://doi.org/10.1016/j.micromeso.2017.12.016>.

Fu, Y., Sun, L., Yang, H., Xu, L., Zhang, F., Zhu, W., 2016. Visible-light-induced aerobic photocatalytic oxidation of aromatic alcohols to aldehydes over Ni-doped NH_2 -MIL-125(Ti). *Appl. Catal. B Environ.* 187, 212–217. <https://doi.org/10.1016/j.apcatb.2016.01.038>.

Gómez-Avilés, A., Peñas-Garzón, M., Bedia, J., Dionysiou, D.D., Rodríguez, J.J., Belper, C., 2019. Mixed Ti-Zr metal-organic-frameworks for the photodegradation of acetaminophen under solar irradiation. *Appl. Catal. B Environ.* 253, 253–262. <https://doi.org/10.1016/j.apcatb.2019.04.040>.

Gómez-Avilés, A., Muelas-Ramos, V., Bedia, J., Rodríguez, J.J., Belper, C., 2020. Thermal post-treatments to enhance the water stability of NH_2 -MIL-125(Ti). *Catalysts* 10, 603. <https://doi.org/10.3390/catal10060603>.

Gou, J., Ma, Q., Cui, Y., Deng, X., Zhang, H., Cheng, X., Li, X., Xie, M., Cheng, Q., Liu, H., 2017. Visible light photocatalytic removal performance and mechanism of diclofenac degradation by Ag_3PO_4 sub-microcrystals through response surface methodology. *J. Ind. Eng. Chem.* 49, 112–121. <https://doi.org/10.1016/j.jiec.2017.01.015>.

Gu, Q., Gao, Z., Zhao, H., Lou, Z., Liao, Y., Xue, C., 2015. Temperature-controlled morphology evolution of graphitic carbon nitride nanostructures and their photocatalytic activities under visible light. *RSC Adv.* 5, 49317–49325. <https://doi.org/10.1039/c5ra07284k>.

Hendon, C.H., Tiana, D., Fontecave, M., Sanchez, C., D'arras, L., Sassevo, C., Rozes, L., Mellot-Draznieks, C., Walsh, A., 2013. Engineering the optical response of the titanium-MIL-125 metal-organic framework through ligand functionalization. *J. Am. Chem. Soc.* 135, 10942–10945. <https://doi.org/10.1021/ja405350u>.

Huang, H., Wang, X.S., Philo, D., Ichihara, F., Song, H., Li, Y., Li, D., Qiu, T., Wang, S., Ye, J., 2020. Toward visible-light-assisted photocatalytic nitrogen fixation: a titanium metal organic framework with functionalized ligands. *Appl. Catal. B Environ.* 267, 118686. <https://doi.org/10.1016/j.apcatb.2020.118686>.

Jiang, Y., Wang, W.N., Biswas, P., Fortner, J.D., 2014. Facile aerosol synthesis and characterization of ternary cupredoxin TiO_2 -magnetite nanocomposites for advanced water treatment. *ACS Appl. Mater. Interfaces* 6, 11766–11774. <https://doi.org/10.1021/am5025275>.

Jiménez, S., Micó, M.M., Arnaldos, M., Medina, F., Contreras, S., 2018. State of the art of produced water treatment. *Chemosphere* 192, 186–208. <https://doi.org/10.1016/j.chemosphere.2017.10.139>.

Kampouri, S., Ireland, C.P., Valizadeh, B., Oveis, E., Schouwink, P.A., Mensi, M., Stylianou, K.C., 2018. Mixed-phase MOF-derived titanium dioxide for photocatalytic hydrogen evolution: the impact of the templated morphology. *ACS Appl. Energy Mater.* 1, 6541–6548. <https://doi.org/10.1021/acsaem.8b01445>.

Kanakaraju, D., Glass, B.D., Oelgemöller, M., 2018. Advanced oxidation process-mediated removal of pharmaceuticals from water: a review. *J. Environ. Manag.* 219, 189–207. <https://doi.org/10.1016/j.jenvman.2018.04.103>.

Keen, O.S., Thurman, E.M., Ferrer, I., Dotson, A.D., Linden, K.G., 2013. Dimer formation during UV photolysis of diclofenac. *Chemosphere* 93, 1948–1956. <https://doi.org/10.1016/j.chemosphere.2013.06.079>.

Kim, S.-N., Kim, J., Kim, H.-Y., Cho, H.-Y., Ahn, W.-S., 2013. Adsorption/catalytic properties of MIL-125 and NH_2 -MIL-125. *Catal. Today* 204, 85–93. <https://doi.org/10.1016/j.cattod.2012.08.014>.

Li, D., Liu, H., Niu, C., Yuan, J., Xu, F., 2019. $Mpg-C_3N_4$ -ZIF-8 composites for the degradation of tetracycline hydrochloride using visible light. *Water Sci. Technol.* 80, 2206–2217. <https://doi.org/10.2166/wst.2020.038>.

Li, D., Huang, J., Li, R., Chen, P., Chen, D., Cai, M., Liu, H., Feng, Y., Lv, W., Liu, G., 2021. Synthesis of a carbon dots modified $g-C_3N_4/SnO_2$ Z-scheme photocatalyst with superior photocatalytic activity for PPCPs degradation under visible light irradiation. *J. Hazard. Mater.* 401, 123257. <https://doi.org/10.1016/j.jhazmat.2020.123257>.

Li, X., Zhang, J., Shen, L., Ma, Y., Lei, W., Cui, Q., Zou, G., 2009. Preparation and characterization of graphitic carbon nitride through pyrolysis of melamine. *Appl. Phys. A Mater. Sci. Process.* 94, 387–392. <https://doi.org/10.1007/s00339-008-4816-4>.

Li, Y., Fang, Y., Gao, Z., Li, N., Chen, D., Xu, Q., Lu, J., 2019. Construction of $g-C_3N_4$ /PDI/MOF heterojunctions for the highly efficient visible light-driven degradation of pharmaceutical and phenolic micropollutants. *Appl. Catal. B Environ.* 250, 150–162. <https://doi.org/10.1016/j.apcatb.2019.03.024>.

Liang, S., Zhang, D., Pu, X., Yao, X., Han, R., Yin, J., Ren, X., 2019. A novel $Ag_2O/g-C_3N_4$ p-n heterojunction photocatalysts with enhanced visible and near-infrared light activity. *Sep. Purif. Technol.* 210, 786–797. <https://doi.org/10.1016/j.seppur.2018.09.008>.

Lima, M.J., Silva, A.M.T., Silva, C.G., Faria, J.L., 2017. Graphitic carbon nitride modified by thermal, chemical and mechanical processes as metal-free photocatalyst for the selective synthesis of benzaldehyde from benzyl alcohol. *J. Catal.* 353, 44–53. <https://doi.org/10.1016/j.jcat.2017.06.030>.

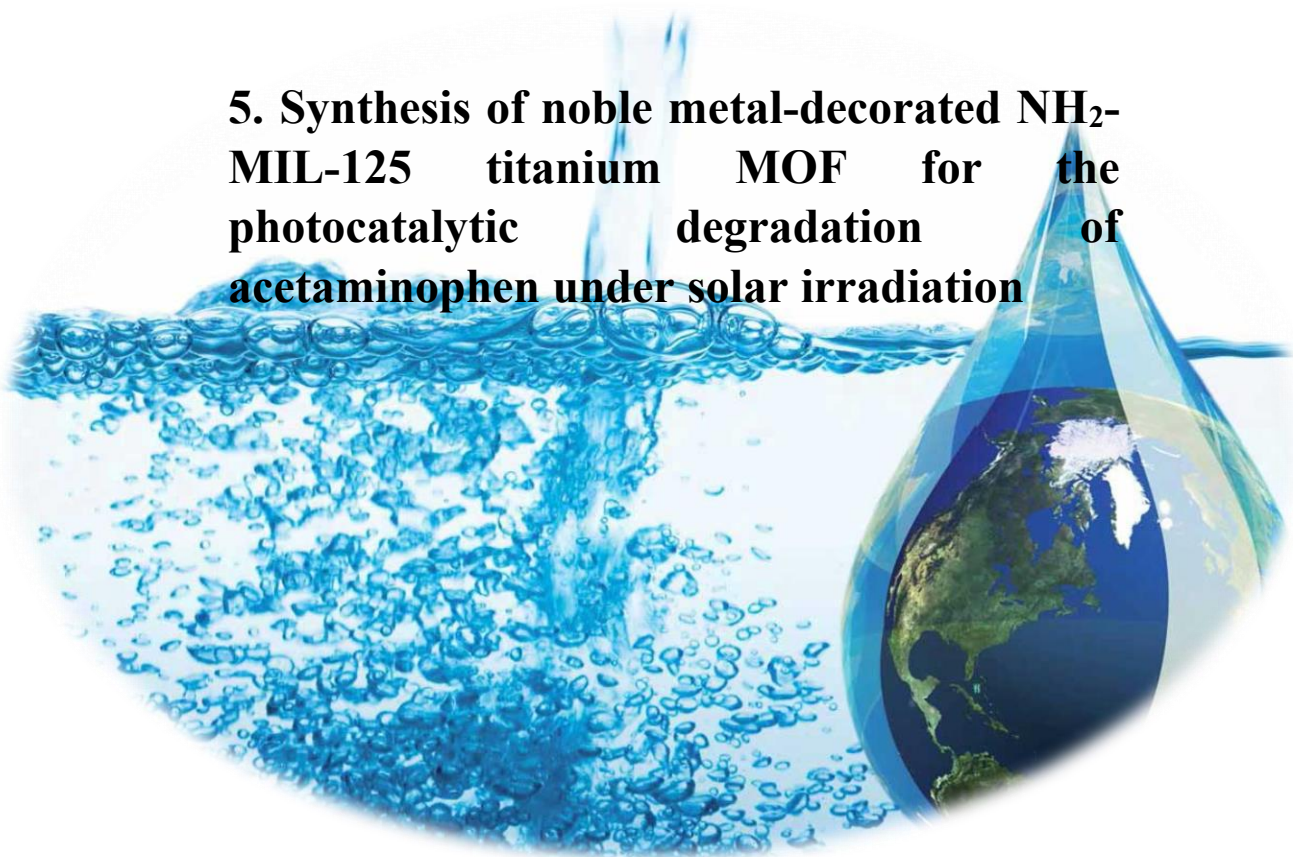
Lippens, B.C., de Boer, J.H., 1965. Studies on pore systems in catalysts. *J. Catal.* 4, 319–323. [https://doi.org/10.1016/0021-9517\(65\)90307-6](https://doi.org/10.1016/0021-9517(65)90307-6). V. t Method.

Liu, S., Chen, F., Li, S., Peng, X., Xiong, Y., 2017. Enhanced photocatalytic conversion of greenhouse gas CO_2 into solar fuels over $g-C_3N_4$ nanotubes with decorated transparent ZIF-8 nanoclusters. *Appl. Catal. B Environ.* 211, 1–10. <https://doi.org/10.1016/j.apcatb.2017.04.009>.

Lu, X., Shao, Y., Gao, N., Chen, J., Zhang, Y., Xiang, H., Guo, Y., 2017. Degradation of diclofenac by UV-activated persulfate process: kinetic studies, degradation pathways and toxicity assessments. *Ecotoxicol. Environ. Saf.* 141, 139–147. <https://doi.org/10.1016/j.ecoenv.2017.03.022>.

- Marques, R.R.N., Sampaio, M.J., Carrapiço, P.M., Silva, C.G., Morales-Torres, S., Dražić, G., Faria, J.L., Silva, A.M.T., 2013. Photocatalytic degradation of caffeine: developing solutions for emerging pollutants. *Catal. Today* 209, 108–115. <https://doi.org/10.1016/j.cattod.2012.12.008>.
- Martínez, C., Canle, L., Fernández, M., Santaballa, M.I., Faria, J. J.A., 2011. Aqueous degradation of diclofenac by heterogeneous photocatalysis using nanostructured materials. *Appl. Catal. B Environ.* 107, 110–118. <https://doi.org/10.1016/j.apcatb.2011.07.003>.
- Martis, M., Meicheng, W., Mori, K., Yamashita, H., 2014. Fabrication of metal nanoparticles in metal organic framework NH₂-MIL-125 by UV photo-assisted methods for optimized catalytic properties. *Catal. Today* 235, 98–102. <https://doi.org/10.1016/j.CATTOD.2014.02.046>.
- Miklos, D.B., Remy, C., Jekel, M., Linden, K.G., Drewes, J.E., Hübner, U., 2018. Evaluation of advanced oxidation processes for water and wastewater treatment – a critical review. *Water Res.* 139, 118–131. <https://doi.org/10.1016/j.watres.2018.03.042>.
- Moctezuma, E., Leyva, E., Lara-Pérez, C., Noriega, S., Martínez-Richa, A., 2020. TiO₂ photocatalytic degradation of diclofenac: intermediates and total reaction mechanism. *Top. Catal.* 63, 601–615. <https://doi.org/10.1007/s11244-020-01262-7>.
- Panneri, S., Minju Thomas, A., Priyanka Ganguly, A., Nair, B.N., Peer Mohamed, cd A., K Warrier, K.G., Hareesh, U.S., 2017. C₃N₄ anchored ZIF 8 composites: photo-regenerable, high capacity sorbents as adsorptive photocatalysts for the effective removal of tetracycline from water. *Catal. Sci. Technol.* 7, 2118–2128. <https://doi.org/10.1039/c7cy00348j>.
- Pérez-Estrada, L.A., Malato, S., Gernjak, W., Agüera, A., Thurman, E.M., Ferrer, I., Fernández-Alba, A.R., 2005. Photo-fenton degradation of diclofenac: Identification of main intermediates and degradation pathway. *Environ. Sci. Technol.* 39, 8300–8306. <https://doi.org/10.1021/es050794n>.
- Qiu, J., Yang, L., Li, M., Yao, J., 2019. Metal nanoparticles decorated MIL-125-NH₂ and MIL-125 for efficient photocatalysis. *Mater. Res. Bull.* 112, 297–306. <https://doi.org/10.1016/J.MATERRESBULL.2018.12.038>.
- Rada, Z.H., Abid, H.R., Shang, J., He, Y., Webley, P., Liu, S., Sun, H., Wang, S., 2015. Effects of amino functionality on uptake of CO₂, CH₄ and selectivity of CO₂/CH₄ on titanium based MOFs. *Fuel* 160, 318–327. <https://doi.org/10.1016/j.fuel.2015.07.088>.
- Salimi, M., Esrafil, A., Jafari, A.J., Gholami, M., Sobhi, H.R., 2020. Application of MIL-53(Fe)/urchin-like g-C₃N₄ nanocomposite for efficient degradation of cefixime. *Inorg. Chem. Commun.* 111, 107565 <https://doi.org/10.1016/j.inoche.2019.107565>.
- Sampaio, M.J., Lima, M.J., Baptista, D.L., Silva, A.M.T., Silva, C.G., Faria, J.L., 2017. Ag-loaded ZnO materials for photocatalytic water treatment. *Chem. Eng. J.* 318, 95–102. <https://doi.org/10.1016/j.cej.2016.05.105>.
- Serpone, N., Texier, I., Emeline, A.V., Pichat, P., Hidaka, H., Zhao, J., 2000. Post-irradiation effect and reductive dechlorination of chlorophenols at oxygen-free TiO₂/water interfaces in the presence of prominent hole scavengers. *J. Photochem. Photobiol. A Chem.* 136, 145–155. [https://doi.org/10.1016/S1010-6030\(00\)00348-8](https://doi.org/10.1016/S1010-6030(00)00348-8).
- Song, K., Mohseni, M., Taghipour, F., 2016. Application of ultraviolet light-emitting diodes (UV-LEDs) for water disinfection: a review. *Water Res* 94, 341–349. <https://doi.org/10.1016/j.watres.2016.03.003>.
- Tao, H., Liang, X., Zhang, Q., Chang, C.T., 2015. Enhanced photoactivity of graphene/titanium dioxide nanotubes for removal of Acetaminophen. *Appl. Surf. Sci.* 324, 258–264. <https://doi.org/10.1016/j.apsusc.2014.10.129>.
- Tauc, J., 1970. Absorption edge and internal electric fields in amorphous semiconductors. *Mater. Res. Bull.* 5, 721–729. [https://doi.org/10.1016/0025-5408\(70\)90112-1](https://doi.org/10.1016/0025-5408(70)90112-1).
- Tian, X., Zhou, M., Tan, C., Li, M., Liang, L., Li, K., Su, P., 2018. KOH activated N-doped novel carbon aerogel as efficient metal-free oxygen reduction catalyst for microbial fuel cells. *Chem. Eng. J.* 348, 775–785. <https://doi.org/10.1016/j.cej.2018.05.007>.
- UNESCO/HELCOM, 2017. Pharmaceuticals in the Aquatic Environment of the Baltic Sea region – A status report. UNESCO Emerging Pollutants in Water Series – No. 1. UNESCO Publishing, Paris.
- Wang, C.C., Yi, X.H., Wang, P., 2019b. Powerful combination of MOFs and C₃N₄ for enhanced photocatalytic performance. *Appl. Catal. B Environ.* 247, 24–48. <https://doi.org/10.1016/j.apcatb.2019.01.091>.
- Wang, H., Yuan, X., Wu, Y., Zeng, G., Chen, X., Leng, L., Wu, Z., Jiang, L., Li, H., 2015. Facile synthesis of amino-functionalized titanium metal-organic frameworks and their superior visible-light photocatalytic activity for Cr(VI) reduction. *J. Hazard. Mater.* 286, 187–194. <https://doi.org/10.1016/J.JHAZMAT.2014.11.039>.
- Wang, H., Cui, P.H., Shi, J.X., Tan, J.Y., Zhang, J.Y., Zhang, N., Zhang, C., 2019a. Controllable self-assembly of CdS@NH₂-MIL-125(Ti) heterostructure with enhanced photodegradation efficiency for organic pollutants through synergistic effect. *Mater. Sci. Semicond. Process.* 97, 91–100. <https://doi.org/10.1016/j.mssp.2019.03.016>.
- Wang, M., Yang, L., Yuan, J., He, L., Song, Y., Zhang, H., Zhang, Z., Fang, S., 2018. Heterostructured Bi₂S₃@NH₂-MIL-125(Ti) nanocomposite as a bifunctional photocatalyst for Cr(VI) reduction and rhodamine B degradation under visible light. *RSC Adv.* 8, 12459–12470. <https://doi.org/10.1039/c8ra00882e>.
- Wang, X., Chen, X., Thomas, A., Fu, X., Antonietti, M., 2009a. Metal-Containing Carbon Nitride Compounds: A New Functional Organic-Metal Hybrid Material. *Adv. Mater.* 21, 1609–1612. <https://doi.org/10.1002/adma.200802627>.
- Wang, X., Maeda, K., Thomas, A., Takanebe, K., Xin, G., Carlsson, J.M., Domen, K., Antonietti, M., 2009b. A metal-free polymeric photocatalyst for hydrogen production from water under visible light. *Nat. Mater.* 8, 76–80. <https://doi.org/10.1038/nmat2317>.
- Wen, J., Xie, J., Chen, X., Li, X., 2017. A review on g-C₃N₄-based photocatalysts. *Appl. Surf. Sci.* 391, 72–123. <https://doi.org/10.1016/j.apsusc.2016.07.030>.
- Xiao, N., Li, S., Liu, S., Xu, B., Li, Y., Gao, Y., Ge, L., Lu, G., 2019. Novel PtPd alloy nanoparticle-decorated g-C₃N₄ nanosheets with enhanced photocatalytic activity for H₂ evolution under visible light irradiation. *Cuihua Xuebao Chin. J. Catal.* 40, 352–361. [https://doi.org/10.1016/S1872-2067\(18\)63180-8](https://doi.org/10.1016/S1872-2067(18)63180-8).
- Xu, J., Gao, J., Wang, C., Yang, Y., Wang, L., 2017. NH₂-MIL-125(Ti)/graphitic carbon nitride heterostructure decorated with NiPd co-catalysts for efficient photocatalytic hydrogen production. *Appl. Catal. B Environ.* 219, 101–108. <https://doi.org/10.1016/j.apcatb.2017.07.046>.
- Xu, Q., Zhang, L., Cheng, B., Fan, J., Yuj, 2020. S-scheme heterojunction photocatalyst. *Chem* 6, 1–17. <https://doi.org/10.1016/j.chempr.2020.06.010>.
- Xu, T., Zhang, L., Cheng, H., Zhu, Y., 2011. Significantly enhanced photocatalytic performance of ZnO via graphene hybridization and the mechanism study. *Appl. Catal. B Environ.* 101, 382–387. <https://doi.org/10.1016/j.apcatb.2010.10.007>.
- Yan, S.C., Li, Z.S., Zou, Z.G., 2009. Photodegradation performance of g-C₃N₄ fabricated by directly heating melamine. *Langmuir* 25, 10397–10401. <https://doi.org/10.1021/la900923z>.
- Yi, X.H., Ma, S.Q., Du, X.D., Zhao, C., Fu, H., Wang, P., Wang, C.C., 2019. The facile fabrication of 2D/3D Z-scheme g-C₃N₄/UiO-66 heterojunction with enhanced photocatalytic Cr(VI) reduction performance under white light. *Chem. Eng. J.* 375, 121944 <https://doi.org/10.1016/j.cej.2019.121944>.
- Zeng, Y., Liu, C., Wang, L., Zhang, S., Ding, Y., Xu, Y., Liu, Y., Luo, S., 2016. A three-dimensional graphitic carbon nitride belt network for enhanced visible light photocatalytic hydrogen evolution. *J. Mater. Chem. A* 4, 19003–19010. <https://doi.org/10.1039/C6TA07397B>.
- Zhang, L., He, X., Xu, X., Liu, C., Duan, Y., Hou, L., Zhou, Q., Ma, C., Yang, X., Liu, R., Yang, F., Cui, L., Xu, C., Li, Y., 2017. Highly active TiO₂/g-C₃N₄/G photocatalyst with extended spectral response towards selective reduction of nitrobenzene. *Appl. Catal. B Environ.* 203, 1–8. <https://doi.org/10.1016/j.apcatb.2016.10.003>.
- Zhang, L., Liu, Y., Fu, Y., 2020. Degradation kinetics and mechanism of diclofenac by UV/peracetic acid. *RSC Adv.* 10, 9907–9916. <https://doi.org/10.1039/d0ra00363h>.
- Zhang, T., Zhao, D., Wang, Y., Chang, Y., Zhang, D., Tang, Y., Pu, X., Shao, X., 2019. Facial synthesis of a novel Ag₄V₂O₇-g-C₃N₄ heterostructure with highly efficient photoactivity. *J. Am. Ceram. Soc.* 102, 3897–3907. <https://doi.org/10.1111/jace.16254>.
- Zhang, W., Zhou, L., Deng, H., 2016. Ag modified g-C₃N₄ composites with enhanced visible-light photocatalytic activity for diclofenac degradation. *J. Mol. Catal. A Chem.* 423, 270–276. <https://doi.org/10.1016/j.molcata.2016.07.021>.
- Zhao, H.M., Di, C.M., Wang, L., Chun, Y., Xu, Q.H., 2015a. Synthesis of mesoporous graphitic C₃N₄ using cross-linked bimodal mesoporous SBA-15 as a hard template. *Microporous Mesoporous Mater.* 208, 98–104. <https://doi.org/10.1016/j.micromeso.2015.01.047>.
- Zhao, Z., Sun, Y., Dong, F., 2015b. Graphitic carbon nitride based nanocomposites: a review. *Nanoscale* 7, 15–37. <https://doi.org/10.1039/c4nr03008g>.
- Zhou, Z., Qiu, L., Wang, J., Pang, J., Yang, F., Yang, Y., Duo, S., 2019. Photocatalysts Fabricated by Depositing Ag on Co-g-C₃N₄ and Its Enhanced Visible-Light Photocatalytic Performance. *IOP Conference Series: Materials Science and Engineering* 678, 012126. <https://doi.org/10.1088/1757-899X/678/1/012126>.
- Zhu, S.-R., Liu, P.-F., Wu, M.-K., Zhao, W.-N., Li, G.-C., Tao, K., Yi, F.-Y., Han, L., 2016. Enhanced photocatalytic performance of BiOBr/NH₂-MIL-125(Ti) composite for dye degradation under visible light. *Dalton Trans.* 45, 17521–17529. <https://doi.org/10.1039/C6DT02912D>.

5. Synthesis of noble metal-decorated NH₂-MIL-125 titanium MOF for the photocatalytic degradation of acetaminophen under solar irradiation





Contents lists available at ScienceDirect

Separation and Purification Technology

journal homepage: www.elsevier.com/locate/seppur

Synthesis of noble metal-decorated NH₂-MIL-125 titanium MOF for the photocatalytic degradation of acetaminophen under solar irradiation

V. Muelas-Ramos, C. Belver, J.J. Rodriguez, J. Bedia*

Chemical Engineering Department, Universidad Autónoma de Madrid, Campus Cantoblanco, E-28049 Madrid, Spain

ARTICLE INFO

Keywords:

NH₂-MIL-125
Noble metal nanoparticles
Photocatalysis
Acetaminophen
Water treatment

ABSTRACT

This work reports the solvothermal synthesis of a titanium-based metal organic framework (NH₂-MIL-125(Ti)) and the further deposition of palladium, platinum and silver nanoparticles on its framework, with the aim to obtain visible light-driven photocatalysts. The structure of the NH₂-MIL-125 was not affected by the incorporation of the metal nanoparticles, while the textural properties changed depending on the metal used. All M/NH₂-MIL-125 (M = Pd, Pt, Ag) synthesized materials showed enhanced light absorption in the visible region due to the effect of the metal nanoparticles, which were mainly in reduced state as confirmed by XPS analyses. The metal nanoparticles were between 1.8 and 3.8 nm in size depending of the metal. They were responsible for the reduction in the recombination process, as suggested by photoluminescence measurements. The photocatalytic performance of M/NH₂-MIL-125 was tested for the degradation of acetaminophen (ACE) under simulated solar irradiation. Pt/NH₂-MIL-125 achieved the highest conversion rate (rate constant of 0.0165 min⁻¹), with complete conversion of the contaminant in less than three hours. Scavengers studies confirmed that O₂⁻ radicals play a main role in the degradation process, followed by ·OH radicals. The catalytic stability of Pt/NH₂-MIL-125 was confirmed upon three successive reaction cycles. Different water matrices were tested to understand the effect of common inorganic ions, being the presence of bicarbonates the most detrimental to the performance of the photocatalytic process.

1. Introduction

The availability of quality water is a growing concern in current society. Thus, different purification technologies are worldwide investigated and implemented in the field of water and wastewater treatment. A new group of contaminants, which are not readily removed by conventional technologies, are of growing concern. This so-called emerging contaminants (ECs) include a wide range of pharmaceuticals, personal care products, detergents, steroids, hormones, etc. [1]. The concentration of ECs in water is in general fairly low, but even at these low levels they are hazardous for human health and environment, hence the importance of their effective removal [2]. Different wastewater treatment technologies are being considered for that purpose, being advanced oxidation processes (AOPs) promising solutions due to their ability to generate reactive oxygen species (ROS) capable of degrading a wide variety of contaminants. AOPs include different approaches, such as Fenton, ozonation, sonolysis, electrolysis and photocatalysis [3]. This last is receiving growing attention, especially regarding potential application under solar light [4]. Photocatalysis exploits the ability of a

semiconductor to induce redox reactions when activated by light, being TiO₂ the most widely used photocatalyst since Fujishima and Honda discovered its properties [5]. TiO₂ presents unquestionable advantages, such as high-photoactivity and stability, low-toxicity and low-cost [6]. But, it has also some drawbacks, including a deficient exploitation of solar energy, since it only uses the UV radiation from the solar spectrum. Also, the fast recombination of electron-hole pairs and difficult recovery and recycling from the aqueous medium because of the very low particle size, limit the application of this material as photocatalyst [7]. Thus, other semiconductors have gained attention in this field to, especially for the sake of more efficient use of free solar irradiation as energy source.

Metal organic frameworks (MOFs) represent an interesting class of porous materials formed by the combination of a metal oxo-cluster and an organic linker [8]. They have been applied in many fields, such as gas storage [9,10], water splitting [11,12], sensing [13], separation processes [14,15], catalysts in green chemistry [16], and water treatment [17,18]. Regarding water purification, MOFs and derived-MOFs materials have been evaluated as promising photocatalysts due to their

* Corresponding author.

E-mail address: jorge.bedia@uam.es (J. Bedia).

<https://doi.org/10.1016/j.seppur.2021.118896>

Received 26 January 2021; Received in revised form 30 April 2021; Accepted 1 May 2021

Available online 11 May 2021

1383-5866/© 2021 The Author(s).

Published by Elsevier B.V. This is an open access article under the CC BY-NC-ND license

(<http://creativecommons.org/licenses/by-nc-nd/4.0/>).

semiconductor properties [19]. Among the different MOFs that can be synthesized by varying the metal and linker nature, Ti-MOFs are receiving great attention in photocatalysis. For instance, Dan-Hardi et al. [20] synthesized MIL-125, formed by $\text{Ti}_8\text{O}_8(\text{OH})_4$ clusters and six co-ordinated linkers with very interesting photochemical properties and thermal stability. However, this MOF has a high band gap value, close to 3.6 eV, so that to be activated needs UV light. To overcome this problem, MIL-125 has been modified to enhance its photocatalytic activity by different methods, including ligand functionalization [21] metal cluster doping [22] metal sensitization [23,24] or combination with other semiconductors [25–27]. Regarding functionalization, modifying the ligand by the incorporation of a $-\text{NH}_2$ group results in $\text{NH}_2\text{-MIL-125}$ MOF, which has a significantly lower band gap value, close to 2.6 eV [21,28]. The $-\text{NH}_2$ functionalization and metal doping were simultaneously performed by Gómez-Avilés et al. [22] giving rise to $(\text{Ti}/\text{Zr})\text{-NH}_2\text{-MIL-125}$, capable of removing acetaminophen from water in a short time under simulated solar light, where superoxide radicals were the main specie involved in the process. Among composites or heterostructures derived from MIL-125, $\text{In}_2\text{S}_3@\text{MIL-125}$ stands out for its efficiency in tetracycline breakdown under visible light again with superoxide radicals as main reactive specie in the degradation [29]. The aforementioned antibiotic, was also degraded with $\text{TiO}_2@\text{NH}_2\text{-MIL-125}$ under visible light irradiation [30]. Recently $\text{BiOI}/\text{MIL-125}$ heterojunction was employed to remove tetracycline, being holes the main reactive specie [31]. Moreover, another antibiotic, such as oxytetracycline was also removed using $\text{CdS}@\text{NH}_2\text{-MIL-125}$ [32]. MIL-125 was also combined with Bi_2WO_6 to remove tetracycline hydrochloride under visible light irradiation [33]. In this latter study, superoxide radicals and holes were identified as the main active species. A novel photocatalyst based on MIL-125 with mixed linkers was combined with different contents of $g\text{-C}_3\text{N}_4$ for the photodegradation of cefixime with a main participation in the degradation of superoxide radicals [34].

For instance, Pd and Ag were deposited on $\text{NH}_2\text{-MIL-125}$ to reduce nitro-aromatic compounds under visible light [35] attributing the better photocatalytic response to inhibition of the electron recombination due to the presence of metal nanoparticles. Pt NPs were used to improve its photocatalytic CO_2 reduction, since the metal nanoparticles reduce Ti^{4+} to Ti^{3+} , which is more active for CO_2 reduction [36] and also studied for H_2 photocatalytic production, where the metal NPs improve the charge separation [37]. Ag NPs deposition has been also investigated for the improvement of a modified $\text{NH}_2\text{-MIL-125}$ activity in the photocatalytic degradation of a dye under visible light, giving rise a better photo-degradation owing to the plasmon resonance effect [23]. However, to the best of our knowledge, only one previous study is devoted to Pt-deposited $\text{NH}_2\text{-MIL-125}$ for water treatment (Cr(VI) reduction) by solar photocatalysis. In this study, the improvement in the photoactivity is associated to a faster electron transfer and lower recombination of electron-hole pairs [38].

The current work focusses the attention on the photocatalytic behavior of $\text{NH}_2\text{-MIL-125}$ with deposited noble metal NPs on its surface. These materials are tested as photocatalysts for the removal of acetaminophen (as model emerging pollutant) under simulated solar light. To the best of our knowledge, this is the first study that uses noble metal decorated $\text{NH}_2\text{-MIL-125}$ for the solar photocatalytic degradation of a contaminant of emerging concern such as acetaminophen. We performed a systematic characterization of the synthesized materials, studying the effect of the metal NPs on the photocatalytic activity. The acetaminophen degradation was studied in detail, determining the role of the main radicals involved in the reaction, analyzing the influence of some inorganic ions commonly present in water and establishing the stability of the photocatalyst upon successive cycles. The study highlights the great activity of $\text{M}/\text{NH}_2\text{-MIL-125}$ for the removal of acetaminophen in water under solar light, providing useful information for future water treatment applications of MOFs.

2. Experimental

2.1. Synthesis of $\text{NH}_2\text{-MIL-125}(\text{Ti})$

$\text{NH}_2\text{-MIL-125}(\text{Ti})$ was synthesized following previously reported procedures [22,39]. Briefly, 6 mmol of 2-amino benzene dicarboxylic acid (Sigma-Aldrich, 99%) were dissolved in 25 mL of N,N-dimethylformamide (DMF, Sigma-Aldrich, $\geq 99.8\%$) by stirring at room temperature for 5 min. Then, 3 mmol of titanium isopropoxide (Sigma-Aldrich, $\geq 97\%$) were added dropwise, until complete homogenization, followed by 25 mL of methanol (Sigma-Aldrich, 99.8%), maintaining the final mixture under stirring for 30 min. The solution was further transferred to a 65 mL Teflon-lined stainless steel autoclave and heated at 150 °C for 16 h. The resulting solid was centrifuged (5000 rpm, 5 min) and washed three times with DMF and other three times with methanol (100 mL each time for 30 min). The final yellow solid was recovered by centrifugation, dried at 60 °C overnight and stored. This sample is named $\text{NH}_2\text{-MIL-125}$.

2.2. Deposition of Pd and Pt NPs

Pd and Pt/ $\text{NH}_2\text{-MIL-125}$ (1 wt%, Pt or Pd) were prepared by incipient wetness impregnation. Metal impregnation was carried out over the as-prepared $\text{NH}_2\text{-MIL-125}$ using an aqueous solution of PdCl_2 (Sigma-Aldrich, 99%) or H_2PtCl_6 (8 wt% in H_2O , Sigma-Aldrich, 99%). The impregnated samples were dried overnight in an oven at 60 °C and reduced under 25 mL·min⁻¹ H_2 flow at 200 °C during 2 h. These modified-MOFs were denoted as Pd/ $\text{NH}_2\text{-MIL-125}$ and Pt/ $\text{NH}_2\text{-MIL-125}$.

2.3. Deposition of Ag NPs

Ag/ $\text{NH}_2\text{-MIL-125}$ was prepared by photo-deposition of silver NPs [40]. The appropriate amount of $\text{NH}_2\text{-MIL-125}$ to achieve 1 wt% of Ag was added to 50 mL of 0.001 AgNO_3 (Alfa Aesar, 99%) ethanol solution under magnetic stirring for 30 min. Further, the suspension was irradiated at 25 °C with a commercial UV lamp (Ultra Vitalux 300 W) for 1 h under stirring. The solvent was removed by a rotary evaporator and the resulting solid was dried overnight at 60 °C.

2.4. Characterization

The Solid-State X-Ray Diffraction (XRD) patterns were registered in a Bruker D8 diffractometer equipped with a Sol-X energy dispersive detector, using a Cu K α source ($\lambda = 0.154$ nm) and a 2θ range from 2 to 50° (scan step 1.5°·min⁻¹). The average crystal size (D) was calculated by the Scherrer's equation, using the (2 1 1) peak at 11.6° of 2θ , that does not overlap with others. A TriStar 123 equipment (Micromeritics) was used to assess the porous texture by N_2 adsorption-desorption at -196 °C. The samples were previously outgassed under vacuum at 120 °C. The Brunauer-Emmet-Teller method [41] was used to calculate the specific surface area (S_{BET}). Total pore volume (V_T) was determined by the amount of N_2 adsorbed at 0.99 relative pressure (P/P_0). Micropore volume (V_{MP}) was obtained from the t-plot method [42]. The pore size distribution was determined by the density functional theory (DFT) model. UV-visible diffuse reflectance spectra were registered with a Shimadzu 2501PC UV-vis spectrophotometer in the 200–800 nm range, using BaSO_4 as reference. The band gap values were calculated from those spectra by the Tauc Plot method [28,43], considering all materials as indirect semiconductors [44]. The surface composition was analysed by X-ray photoelectron spectroscopy (XPS) with a Thermo Scientific apparatus using Al K α radiation (1486.68 eV). All binding energies were corrected using as reference the C 1s spectrum at 284.6 eV. The binding energy was taken from 0 to 1200 eV. Scanning transmission electron microscopy (STEM) images were obtained with an Analytical Titan apparatus (CEOS Co.). Chemical analyses of the solids were carried out by inductively coupled plasma mass spectrometry (ICP-MS) in a NexION

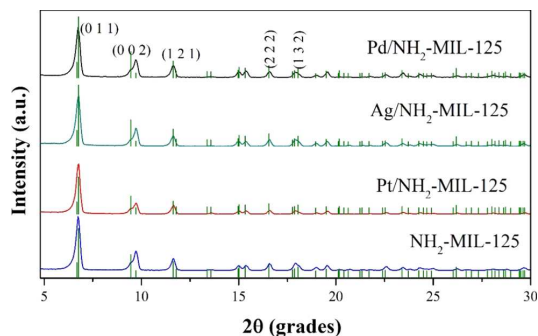


Fig. 1. X-ray diffraction patterns. Reference pattern of $\text{NH}_2\text{-MIL-125}$ from Crystal Open Database (COD) library is included in green colour (COD-7211159.cif [52]).

300 instrument. Prior to the analysis the solids were digested in acid medium and stabilize with HF. A Cary Eclipse spectrofluorometer was used to obtain the photoluminescence (PL) spectra, using an excitation wavelength of 370 nm.

2.5. Photocatalytic tests

Photodegradation of acetaminophen (ACE, Sigma-Aldrich, >99%) was undertaken in a circular Pyrex jacketed reactor (500 mL) (radius = 9.84 cm; height = 7.15 cm) at a controlled temperature of 25 °C under magnetic stirring. This reactor was located inside a solar simulator chamber (Suntest XLS+, ATLAS) with a Xe lamp and a “Daylight” filter (cuts off $\lambda \leq 290$ nm, emission spectrum shown in Fig. S1). The light intensity was fixed to $600 \text{ W} \cdot \text{m}^{-2}$ (107.14 klx). The photocatalyst ($250 \text{ mg} \cdot \text{L}^{-1}$) was suspended in 150 mL aqueous solution with an initial ACE concentration of $5 \text{ mg} \cdot \text{L}^{-1}$. Adsorption equilibrium was achieved in dark for 1 h prior to the photocatalytic reaction. Then, the light was switched on and the reaction was followed for 6 h. Aliquots were taken at given time intervals and filtered with PTFE syringeless filters (Whatman 0.2 μm) to separate the solid photocatalyst. The ACE concentration was analysed by liquid chromatography HPLC (Shimadzu Prominence-ILC-2030C) using a diode array detector (SPD-M30A) and a C18 column (Eclipse Plus 5 μm , Agilent). The mobile phase was a mixture of acetonitrile/acetic acid (0.1% v/v aqueous solution), using a gradient 10/90–40/60% method ($0.7 \text{ mL} \cdot \text{min}^{-1}$). The detection wavelength was fixed at the maximum absorption of ACE, 246 nm. Radical trapping experiments were carried out with benzoquinone (BQ) as scavenger for superoxide radicals (O_2^-) [45], isopropanol (IPA) for hydroxyl radicals ($\cdot\text{OH}$) [46], silver nitrate for holes (h^+) [47] and potassium iodide (KI) as electron (e^-) acceptor [48]. These experiments were performed under the same conditions than the reaction ones, adding the scavenger at 1 mM initial concentration to the ACE solution [49] after the dark adsorption equilibrium step. The effect of some inorganic ions commonly present in water was also studied. These tests were carried out with Cl^- ($25 \text{ mg} \cdot \text{L}^{-1}$), NO_3^- ($50 \text{ mg} \cdot \text{L}^{-1}$), SO_4^{2-} ($50 \text{ mg} \cdot \text{L}^{-1}$) and HCO_3^- ($150 \text{ mg} \cdot \text{L}^{-1}$), usual values in real waters. The stability of the photocatalyst was evaluated upon three successive cycles. After each cycle, the photocatalyst was vacuum-filtered, washed three with 300 mL of distilled water, dried at 60 °C overnight and weighed, ensuring that the reaction conditions of the following cycle were the same.

Reaction intermediates were analyzed by Liquid Chromatography Mass Spectrometry with Electrospray Ionization (LC/ESI-MS) in a Bruker Maxis II equipment using a positive ionization mode. It was employed a 500 V end plate offset, at 300 °C, a 3.500 V capillary voltage and $8 \text{ mL} \cdot \text{min}^{-1}$ of dry gas flow. The data were collected in the range of 50–3000 m/z. A Metrohm 790 IC apparatus, equipped with a Metrosep A Supp 5 column, was employed to analyze carboxylic acids and inorganic

Table 1

Porous texture, average crystal size (D) and band gap (E_g) values.

| | S_{BET} (m^2/g) | V_T (cm^3/g) | V_{MP} (cm^3/g) | D (nm) | E_g (eV) |
|----------------------------------|--|----------------------------------|--|--------|------------|
| Pt/ $\text{NH}_2\text{-MIL-125}$ | 1243 | 0.68 | 0.55 | 31.9 | 2.48 |
| Pd/ $\text{NH}_2\text{-MIL-125}$ | 1248 | 0.70 | 0.55 | 31.0 | 2.50 |
| Ag/ $\text{NH}_2\text{-MIL-125}$ | 1083 | 0.57 | 0.48 | 31.8 | 2.70 |
| $\text{NH}_2\text{-MIL-125}$ | 1109 | 0.59 | 0.47 | 32.3 | 2.56 |

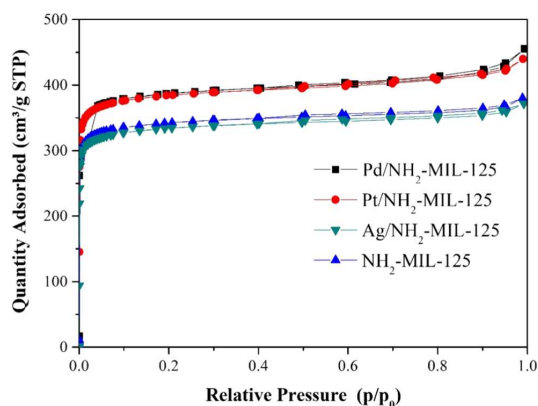


Fig. 2. N_2 adsorption-desorption isotherms at -196 °C.

ions by Ionic chromatography (IC). The eluent was a $\text{Na}_2\text{CO}_3/\text{NaHCO}_3$ (3.2 mM/1.0 mM) buffer solution, while the anionic suppressor was a H_2SO_4 (100 mM) solution.

3. Results and discussion

3.1. Characterization of the photocatalysts

Fig. 1 shows the XRD patterns of $\text{M}/\text{NH}_2\text{-MIL-125}$ compared with that of bare $\text{NH}_2\text{-MIL-125}$. All the materials synthesized described the characteristic pattern of $\text{NH}_2\text{-MIL-125}$ [22,28]. The most intense peaks appeared at 6.8, 9.5 and 11.6° values of 2θ , corresponding to the (0 1 1), (0 0 2) and (1 2 1) planes of $\text{NH}_2\text{-MIL-125}$, respectively [50]. The deposition of metal NPs did not modify significantly the XRD pattern of the bare $\text{NH}_2\text{-MIL-125}$, indicating that the crystalline structure of the MOF is maintained, without significant changes in the average crystal size (D) (see Table 1). The slight decrease observed is probably due to the thermal treatment following metal deposition. Similar results have been recently observed upon thermal stabilization of this same $\text{NH}_2\text{-MIL-125}$ MOF [51]. It is worth mentioning that no additional peaks are observed, not even those related to the impregnated metals, which can be explained by the low amount deposited (1 wt%) and more likely to the low size of the metallic nanoparticles, as will be confirmed later by the STEM images. The noble metal contents on $\text{M}/\text{NH}_2\text{-MIL-125}$ samples were quantified by ICP-MS analyses, resulting in 0.85, 0.92 and 0.98 wt % for Pt, Pd and Ag, respectively. These values are close to the theoretical 1 wt%, confirming the successful loading of the noble metals on $\text{NH}_2\text{-MIL-125}$ (Ti) MOF.

N_2 adsorption-desorption isotherms at -196 °C are depicted in Fig. 2 and Table 1 summarizes the resulting textural characteristics. All the isotherms follow the same pattern than that of the bare $\text{NH}_2\text{-MIL-125}$, indicative of essentially microporous solids with some small contribution of mesoporosity and high surface area values [53,54]. Therefore, as

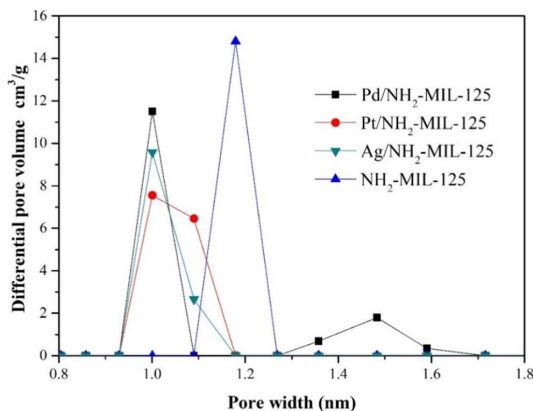


Fig. 3. DFT pore size distributions.

in the case of the crystalline structure, metal impregnation did not provoke significant changes on the porous texture of the original $\text{NH}_2\text{-MIL-125}$, except some increase of pore volume and surface area in the Pd and Pt/ $\text{NH}_2\text{-MIL-125}$ samples but maintaining similar pattern. Pore size distribution (Fig. 3) shows some small displacement of the metal-impregnated samples towards narrower microporosity. These changes can be associated to the thermal treatment following metal deposition and are related to the removal of excess linker and/or remaining solvent molecules not completely removed by washing [51].

The UV-vis spectra are shown in Fig. 4A. All the solids show two absorption bands centred at 280 and 370 nm, due to Ti-oxo-clusters and linker, respectively [55,56]. $\text{M}/\text{NH}_2\text{-MIL-125}$ samples exhibit enhanced absorption in the visible range due to photons absorption of the metal NPs [23,50,57]. The absorption displayed by $\text{Ag}/\text{NH}_2\text{-MIL-125}$ is also associated with the surface plasmon resonance of Ag^0 , an inherent property characterized by the redistribution of the charge density when the NPs are irradiated by light with a wavelength larger than their size [40,58]. The band gap values (E_g) (Table 1) were calculated using the Tauc plot method (Fig. 4B). All the materials yielded quite similar values

(2.5–2.7 eV, see Table 1), indicating that, as expected, deposition of metal NPs does not modify the $\text{NH}_2\text{-MIL-125}$ band gap [23,24].

The surface composition of photocatalysts was analyzed by XPS. Figs. S2–S5 (supplementary information) show, respectively, the Ti 2p, C 1s, N 1s and O 1s deconvoluted spectra of the samples. The deconvolution of Ti 2p region profile gave two peaks at 464.5 and 458.8 eV, ascribed to the Ti^{4+} ions of the metal oxo-clusters in the MOF [28,59]. The C 1s spectra included four peaks located at 284.6, 285.3, 286.6 and 288.7 eV, which can be assessed to $\text{C}=\text{C}/\text{C}-\text{H}$, $\text{C}-\text{N}$, $\text{C}=\text{O}/\text{N}-\text{C}=\text{O}$ and COO^- moieties, respectively [28]. These peaks correspond to different bonds of the organic linker, 2-amino benzene dicarboxylic acid ($\text{NH}_2\text{-BDC}$) [28]. The O 1s deconvolution yielded three peaks, associated with the oxygen in Ti-oxo clusters (530.1 eV), the $\text{C}=\text{O}$ bond (531.6 eV) of the linker and $-\text{OH}$ groups (532.3 eV) [60]. Finally, deconvolution of the N 1s spectra gave three deconvoluted peaks at 399.3, 400.4 and 402.9 eV, derived from $\text{C}-\text{N}/\text{N}-\text{H}$, $\text{N}-\text{C}=\text{O}$ and $-\text{N}^+$, respectively [59]. These peaks are related to the positively charged nitrogen atoms and the N element of the amine functionality spreading or protruding into the empty space of the MOF [28,54]. Table 2 collects the surface elemental composition of all the materials from XPS spectra. No significant changes in Ti, O, N and C can be observed respect to the original $\text{NH}_2\text{-MIL-125}$. Comparison of the XPS surface values of each metal with the corresponding nominal bulk content (1%) suggests more likely egg-shell distribution for Ag and egg-yolk for Pd while Pt seems more evenly distributed.

Fig. 5 shows the deconvoluted spectra of Ag 3d, Pd 3d and Pt 4f of $\text{M}/\text{NH}_2\text{-MIL-125}$ samples and Table 3 collects the metal oxidation state determined from those spectra. The Pd 3d region of Pd/ $\text{NH}_2\text{-MIL-125}$ shows two peaks at 335.0 and 340.3 eV associated to Pd^0 . Meanwhile,

Table 2
XPS surface elemental composition.

| Surface elemental composition (%) | | | | | | | |
|-----------------------------------|-------|------|-------|-------|------|------|------|
| Sample | Ti | N | O | C | Pt | Pd | Ag |
| Pt/ $\text{NH}_2\text{-MIL-125}$ | 38.45 | 4.28 | 33.03 | 23.41 | 0.83 | | |
| Pd/ $\text{NH}_2\text{-MIL-125}$ | 39.02 | 4.64 | 33.09 | 22.99 | | 0.26 | |
| Ag/ $\text{NH}_2\text{-MIL-125}$ | 37.29 | 5.08 | 32.83 | 22.58 | | | 2.23 |
| $\text{NH}_2\text{-MIL-125}$ | 36.97 | 4.89 | 33.38 | 24.75 | | | |

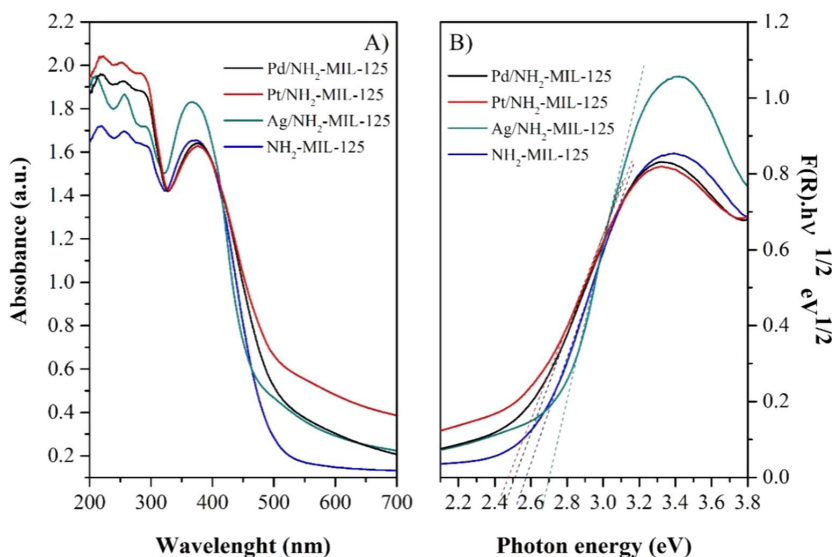


Fig. 4. (A) UV-Vis spectra and (B) Tauc plots.

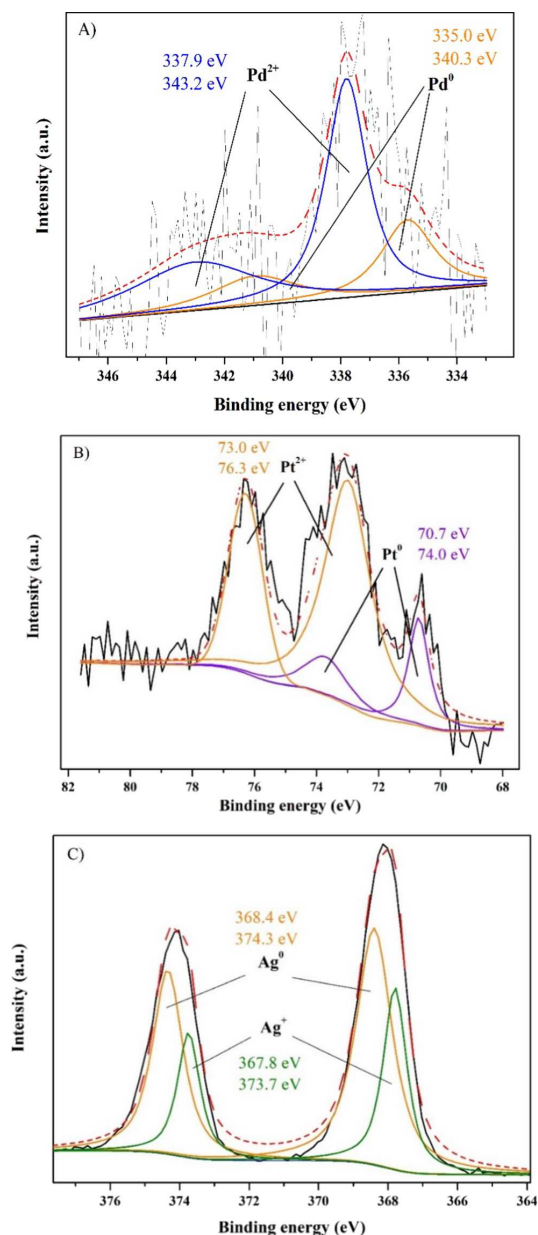


Fig. 5. (A) Pd 3d; (B) Pt 4f; (C) Ag 3d deconvoluted XPS spectra of Pd/NH₂-MIL-125, Pt/NH₂-MIL-125 and Ag/NH₂-MIL-125, respectively.

Table 3

Surface metal composition (estimated from XPS spectra) of M/NH₂-MIL-125.

| Ag/NH ₂ -MIL-125 | | | Pd/NH ₂ -MIL-125 | | | Pt/NH ₂ -MIL-125 | | |
|-----------------------------|------------------------|--------------------------------------|-----------------------------|------------------------|---------------------------------------|-----------------------------|------------------------|---------------------------------------|
| Ag ⁺ (%) | Ag ⁰ (%) | Ag ⁺ / Ag ⁰ | Pd ²⁺ (%) | Pd ⁰ (%) | Pd ²⁺ / Pd ⁰ | Pt ²⁺ (%) | Pt ⁰ (%) | Pt ²⁺ / Pt ⁰ |
| 34 | 66 | 0.50 | 65 | 35 | 1.83 | 79 | 21 | 3.81 |

two other peaks at 337.9 and 343.2 eV are ascribed to Pd²⁺. Similar results were obtained when analyzing the Pt 4f region of Pt/NH₂-MIL-125, which displays two peaks at 70.7 and 74.0 eV, attributed to Pt⁰, and two other peaks at 73.0 and 76.3 eV, assigned to Pt²⁺ [61]. The higher proportion of electrodeficient Pd and Pt on Pd/NH₂-MIL-125 and Pt/NH₂-MIL-125, respectively, can be due to the strong interaction of these metals with the MOF support and the relatively low reduction temperature (200 °C) used in order to preserve the MOF structure. Ag 3d region of Ag/NH₂-MIL-125 shows peaks at 368.4 and 374.3 eV confirming the presence of Ag⁰, although other two peaks at 367.8 and 373.7 eV reveal also the presence of Ag⁺ [40,62]. However, the Ag⁺/Ag⁰ ratio (Table 3) was quite low, verifying the successful photoreduction of the Ag precursor.

The presence of metallic NPs in the metal-loaded NH₂-MIL-125 was confirmed by STEM (Fig. 6). All synthesized materials show rectangular disk-like particles with an average size of 500 nm, characteristic of the NH₂-MIL-125 MOF [63,64]. The presence of metal NPs decorating the surface of the MOF appear as discrete spherical particles with average sizes of 3.8, 3.4 and 1.8 nm for Ag, Pt and Pd, respectively. In the case of Ag, the NPs show a bimodal distribution with most of the particles lower than 2 nm and other around 5 nm and higher in size (Fig. 6B). In contrast, both Pt and Pd show very uniform and evenly dispersed particles. Pd NPs are the smallest ones, difficult to observe in the lower magnification image (Fig. 6E). The metal NPs seem to be homogeneously distributed through the inner structure of the MOFs. It should be underlined that the location of those metal nanoparticle would have a very significant impact in the photoactivity of the resulting materials as previously show by Xiao et al. [65,66] when analysing the effect of the location of Pt nanoparticles on MOFs for the hydrogen production under visible light irradiation.

3.2. Photocatalytic tests

Adsorption of ACE onto the photocatalysts was checked prior to the reaction tests. Equilibrium was always reached in less than one hour and the adsorption capacity was in all the cases very low (Fig. S6). Those adsorption values were then used to adjust the pollutant concentration of the initial solution so that all the reaction tests started with ACE at 5 mg·L⁻¹. Fig. 7 shows the evolution of ACE concentration upon irradiation time with the photocatalysts tested. In the absence of photocatalysis (photolysis) a negligible ACE degradation is obtained, which confirms the stability of this compound versus solar light. Metal nanoparticles clearly enhanced the rate of ACE removal respect to the observed with the bare titanium MOF. This positive effect of the metal NPs can be due to lower recombination of charges, as confirmed by the decreased intensity of PL spectra (shown in Fig. S7). It can be also ascribed to the enhanced light absorption in the visible range, as can be observed in UV-vis data (Fig. 4A). We have analysed by ICP-MS the presence of leached Pt in the aqueous solution after reaction using Pt/NH₂-MIL-125. The Pt concentration in the aqueous phase after reaction is very low (87 ppb), which corresponds to less than 3.5% of the initial Pt content of the photocatalyst and confirms the aqueous stability of the metal nanoparticles in the MOF.

The disappearance of ACE fits well to a pseudo-first-order rate equation (Fig. S8). The rate constant (k) values are included in Table 4, compared with those reported with other photocatalysts. Pt/NH₂-MIL-125 yielded the highest value, 2.4 times that of bare NH₂-MIL-125. That may be due to the combined effect of a better absorption of light in the visible range (Fig. 4A) and slower charges recombination rate (Fig. S7). The k value obtained with Pt/NH₂-MIL-125 is higher than that reported by a Zr-doped NH₂-MIL-125 (85%Ti/15%Zr) tested under the same reaction conditions [22], highlighting the light harvesting caused by the incorporation of Pt nanoparticles at surface of the MOF. Moreover, Pt/NH₂-MIL-125 also showed a higher k value than other photocatalysts designed by our research group, such as Ag/ZnO-TiO₂/clay heterostructure [40] or ZnO/sepiolite [67]. Nevertheless, this value is lower

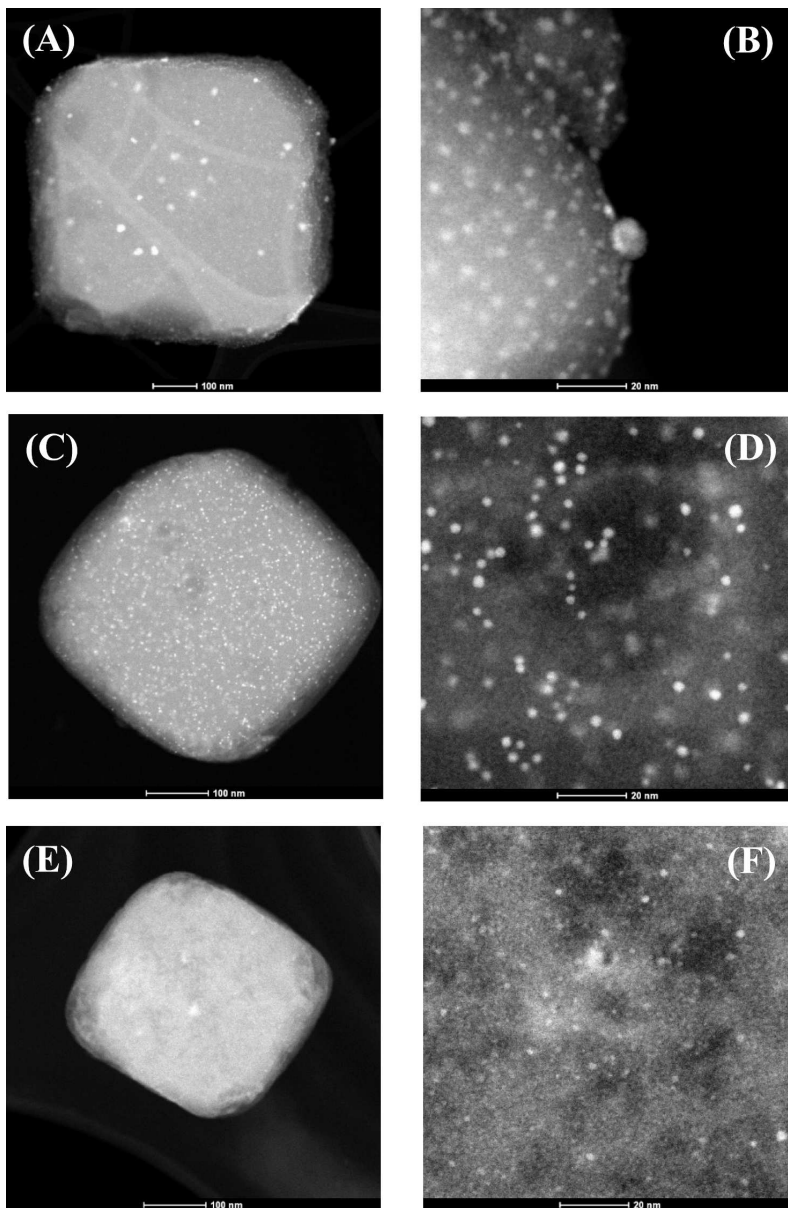


Fig. 6. STEM images of (A, B) Ag/NH₂-MIL-125, (C, D) Pt/NH₂-MIL-125 and (E, F) Pd/NH₂-MIL-125 (Bar lengths, left; 100 nm; right: 20 nm).

than that obtained with a heterojunction based on another MOF (Ag/AgCl@ZIF-8; 0.058 min^{-1}) [58], and also lower than the achieved by Pt/TiO₂ photocatalyst upon higher ACE and photocatalyst concentrations [68]. A higher rate constant was also reported by our group with C-modified TiO₂ under the same reaction conditions, related with the presence of anatase phase [69].

Several scavengers were used to learn on the main reactive species involved in the photocatalytic process. Fig. 8 A and B represent the ACE evolution upon irradiation time and the values of the pseudo-first order rate constant of ACE disappearance (k) with Pt/NH₂-MIL-125 in presence of different scavengers, respectively. KI (e^- scavenger) had no

significant effect in the photocatalytic performance, so it can be said that the electrons do not participate actively in the degradation process. Meanwhile, the slight decrease of k with IPA ($\cdot\text{OH}$ scavenger) indicate that hydroxyl radicals play a minor role in the ACE photodegradation with the catalysts tested. The breakdown rate was dramatically hindered in the presence of benzoquinone (O_2^- scavenger), hence, the main reactive specie involved in ACE removal seems to be O_2^- . Besides this, the addition of AgNO₃ had an important effect, accelerating the disappearance of ACE. This effect can be attributed to the presence of Ag⁺, which can absorb visible light giving rise to the formation of electrons and holes. These electrons can be transferred to the conduction band of

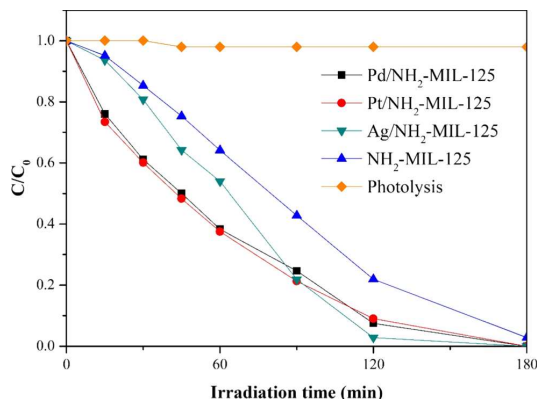


Fig. 7. Evolution of the ACE concentration under solar irradiation with the photocatalysts tested. ([ACE]₀ = 5 mg·L⁻¹; Photocatalyst load = 250 mg·L⁻¹; Illuminance = 107.14 klx).

Table 4

Values of the first order rate constant of ACE disappearance.

| Catalyst | k (min ⁻¹) | Reference |
|---|------------------------|-----------|
| Pt/NH ₂ -MIL-125 | 0.0165 | This work |
| Pd/NH ₂ -MIL-125 | 0.0159 | This work |
| Ag/NH ₂ -MIL-125 | 0.0096 | This work |
| NH ₂ -MIL-125 | 0.0067 | This work |
| NH ₂ -MIL-125 (85%Ti/15%Zr) | 0.0121 | [22] |
| ZnO/sepiolite | 0.0032 | [67] |
| Ag/ZnO-TiO ₂ /clay heterostructure | 0.0095 | [40] |
| Ag/AgCl@ZIF-8 | 0.0580 | [58] |
| Pt/TiO ₂ | 0.0260 | [68] |
| C-modified TiO ₂ | 0.0670 | [69] |

MOF, yielding more superoxide radicals [70]. The major role of superoxide radicals was also reported by Gómez-Aviles et al. [22] for the degradation of the same pharmaceutical (ACE) with Zr-doped NH₂-MIL-125 photocatalysts.

The water matrix can affect to the performance of photocatalytic degradation [75]. This potential effect was studied by mixing the starting ACE solution with chloride, nitrate, sulfate and carbonate ions, commonly present in water (Fig. 9). According to previous studies [71,72], chloride, nitrate and sulphate ions can react with hydroxyl radicals. Since these radicals do not significantly affect the reaction rate in the scavenger tests, the ACE photodegradation is not significantly affected by the presence of SO₄²⁻ ions. Conversely, the presence of HCO₃⁻ caused a detrimental effect on the reaction. According to Liu et al [73], HCO₃⁻ ions interact with superoxide radicals, decreasing the O₂⁻ concentration. Then, the observed decrease in the ACE degradation in the presence of HCO₃⁻ ions can be justified by the scavenging of superoxide radicals. A mixture of Cl⁻, NO₃⁻, SO₄²⁻ and HCO₃⁻ ions was also tested under the same operating conditions and additional damage was observed, suggesting some synergistic negative effects.

The reusability of Pt/NH₂-MIL-125 catalyst was evaluated upon three successive cycles. ACE conversion decreased from the first to the

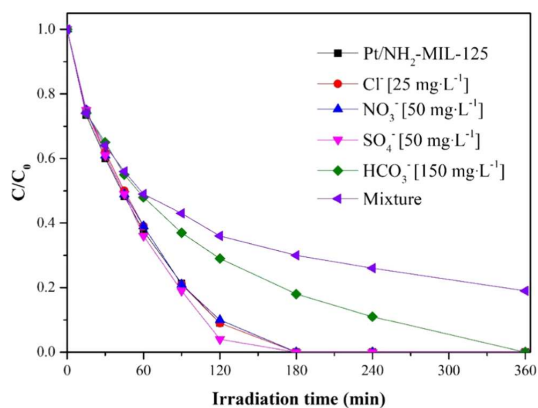


Fig. 9. Effect of some common inorganic ions on the photocatalytic degradation of ACE with Pt/NH₂-MIL-125 under solar irradiation (Operating conditions as in Fig. 7).

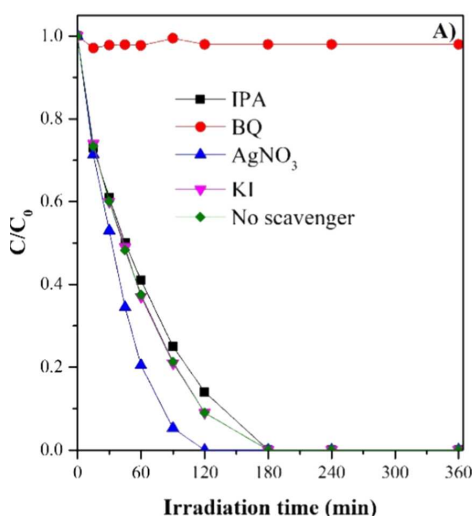


Fig. 8. (A) ACE evolution upon irradiation time and (B) values of the pseudo-first order rate constant of ACE disappearance (k) with Pt/NH₂-MIL-125 in presence of different scavengers.

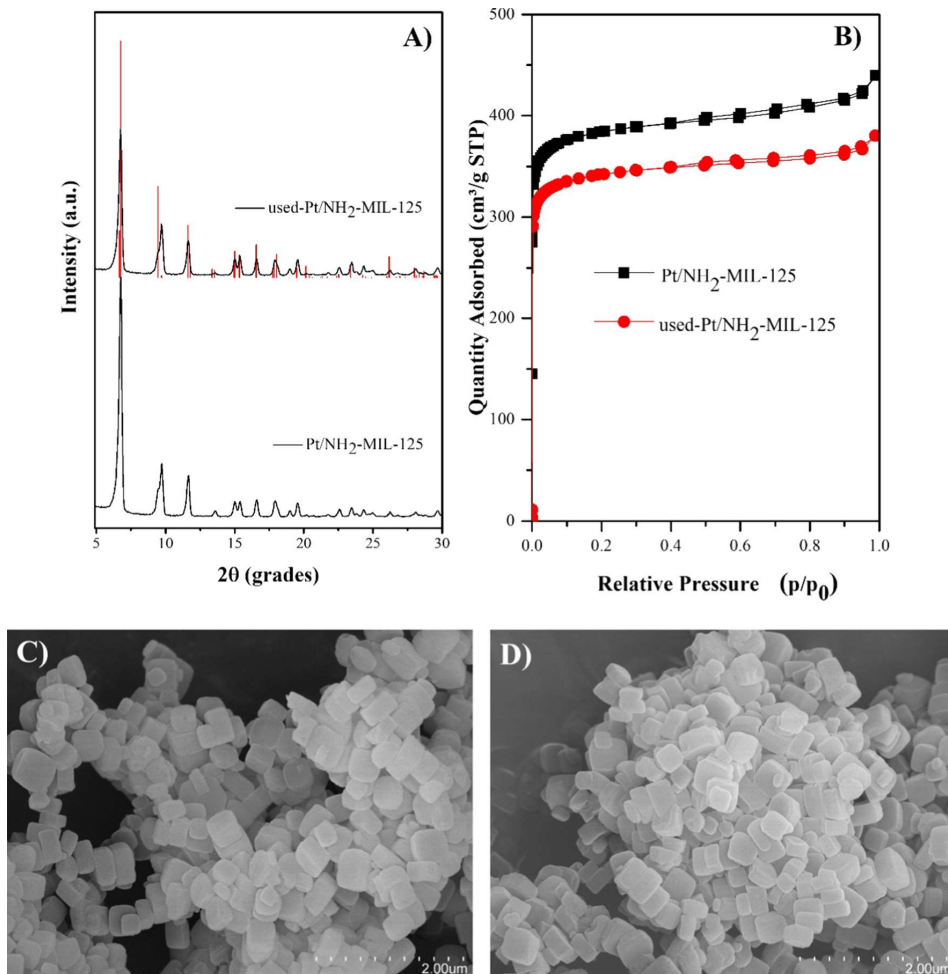


Fig. 10. Changes in the XRD pattern (A), nitrogen adsorption–desorption isotherms (B), and SEM images of Pt/NH₂-MIL-125 before (C) and after three successive cycles (D).

second cycle by about 8% and a further less than 5% decrease was observed in the third one. Similar behavior was reported for Zr-doped NH₂-MIL-125 photocatalyst [22] under the same reaction conditions. The photocatalytic activity decreased after the first cycle but remained almost unchanged from the second to the third runs, with conversion values above 90%. After the cycles, the photocatalyst was recovered and characterized by XRD, nitrogen adsorption–desorption and SEM micrographs (Fig. 10). Pt/NH₂-MIL-125 maintained its structure and porous texture, thus demonstrating its relatively high stability during the photocatalytic reaction. A small decrease ($\approx 10\%$) of BET surface area was observed, probably due to some pore blockage caused by the adsorption of ACE and/or degradation by-products, probably responsible of the minor activity. No significant morphological changes were observed comparing the SEM images before (Fig. 10C) and after reaction (Fig. 10D). The particles maintained their rectangular disk-like shape with an average size of 500 nm, in agreement with TEM images (Fig. 6).

The reaction intermediates were identified by LC/ESI-MS and IC. The accurate mass (m/z) of the detected by-products is summarized in Table S1. The low mass error ($< \pm 1$ mDa) and the value of ring and double bonds (RDB) corroborated the chemical species. RDB is related to

numbers of rings and double bonds in the molecules. Based on the detected compounds, a proposed degradation pathway is depicted in Fig. 11. One of the reaction pathways consists on the coupling of ACE molecules. Thus, two ACE molecules can form ACE-2 (m/z 301.1181), previously reported by Chen et al. [84]. Then, the direct aromatic ring hydroxylation of ACE-2 yield ACE-3 compound (non-detected, but previously observed in the literature [75]), which can be further hydroxylated in ACE-4 (m/z 349.1030). On the other hand, the ring opening of ACE molecules can give rise to the formation of ACE-1 or butylamine (m/z 74.0958), and maleic and malonic acids. These acids were also detected in previous studies [76–78]. Further oxidation of these intermediates produces formic and acetic acids. Finally, the mineralization of these short-chain acids leads the formation of CO₂, NO₃ and H₂O. Only nitrate is detected as mineralization nitrogen product.

4. Conclusions

Noble metal (Ag, Pd and Pt) nanoparticles were successfully deposited on NH₂-MIL-125 by wet impregnation followed by a reduction treatment. The characteristic structure of the MOF was maintained in all

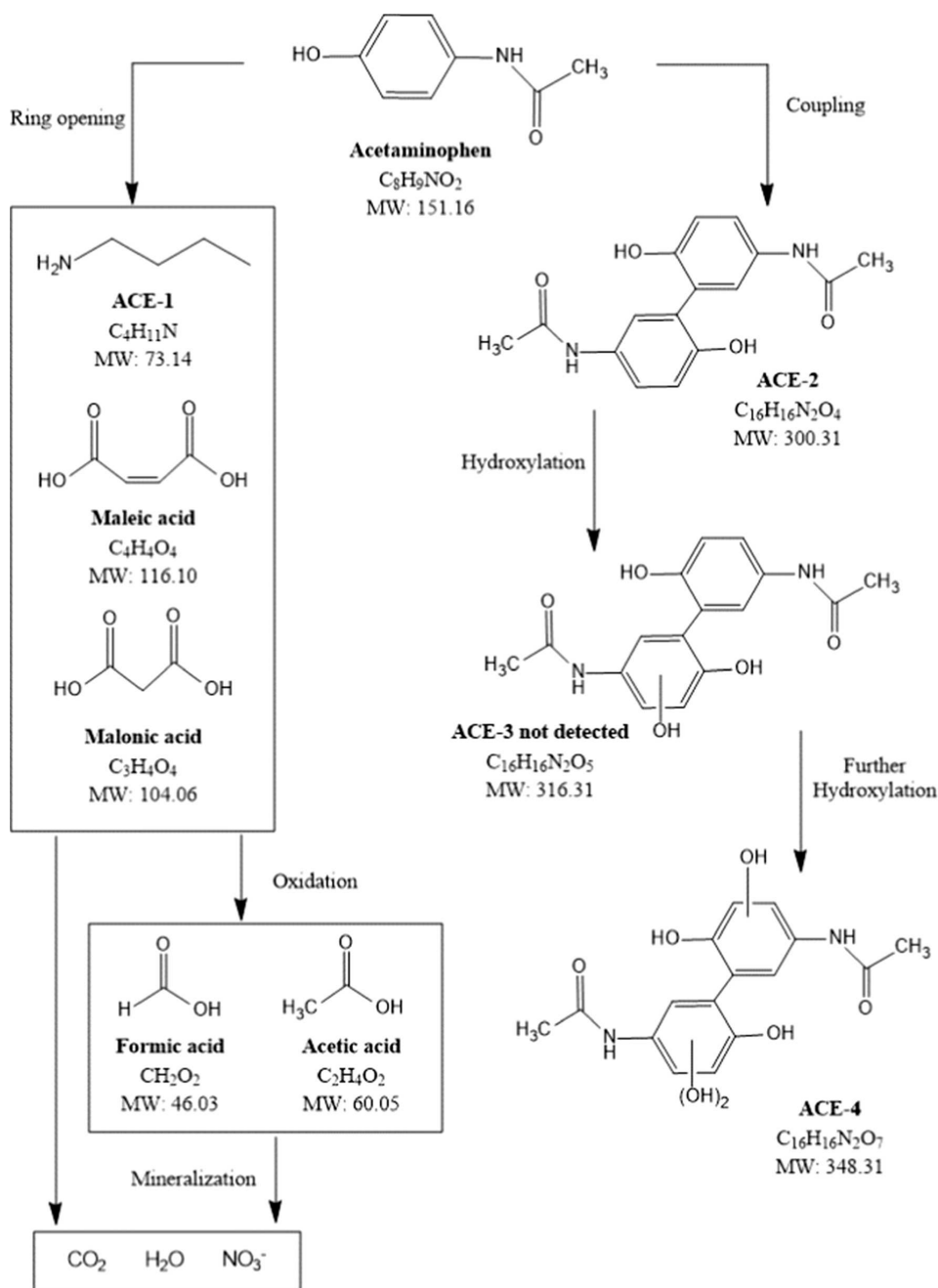


Fig. 11. Proposed reaction pathway for ACE photocatalytic degradation with Pt/NH₂-MIL-125.

M/NH₂-MIL-125 as well as the microporous texture with high surface area. Metal nanoparticles appeared decorating the surface of the MOF, with average sizes from 1.8 to 3.5 nm depending of the metal. Those nanoparticles were a mixture of M²⁺/M⁰ species responsible of light absorption in the visible region. The Pt/NH₂-MIL-125 photocatalyst yielded the best results in the degradation of the target pollutant (ACE),

due to enhanced visible light absorption and slower recombination of the photogenerated charges. O₂⁻ radicals governed the ACE photo-degradation process. The photocatalytic performance of Pt/NH₂-MIL-125 was not significantly affected by the presence of Cl⁻, NO₃⁻ and SO₄²⁻ ions, while HCO₃⁻ caused a detrimental effect due to O₂⁻ trapping. The stability and reusability of Pt/NH₂-MIL-125 was tested upon three

successive cycles, where its original crystalline structure and porous texture were maintained. Some small decrease of activity was observed as inferred from the reduction of ACE conversion (somewhat above 10% after the three cycles).

CRedit authorship contribution statement

V. Muelas-Ramos: Methodology, Writing - original draft, Writing - review & editing. **C. Belver:** Conceptualization, Writing - review & editing, Supervision, Funding acquisition. **J.J. Rodríguez:** Conceptualization, Writing - review & editing, Supervision, Funding acquisition. **J. Bedia:** Conceptualization, Writing - review & editing, Supervision, Funding acquisition.

Declaration of Competing Interest

The authors declare that they have no known competing financial interests or personal relationships that could have appeared to influence the work reported in this paper.

Acknowledgements

This research was funded by the State Research Agency (PID2019-106186RB-I00/AEI/10.13039/501100011033). V. Muelas-Ramos thanks to MCIU for BES-2017-082613 grant. Authors thank the Research Support Services of XPS data from University of Málaga (Spain) and STEM images from Instituto de Nanociencia de Aragón (University of Zaragoza, Spain).

Appendix A. Supplementary material

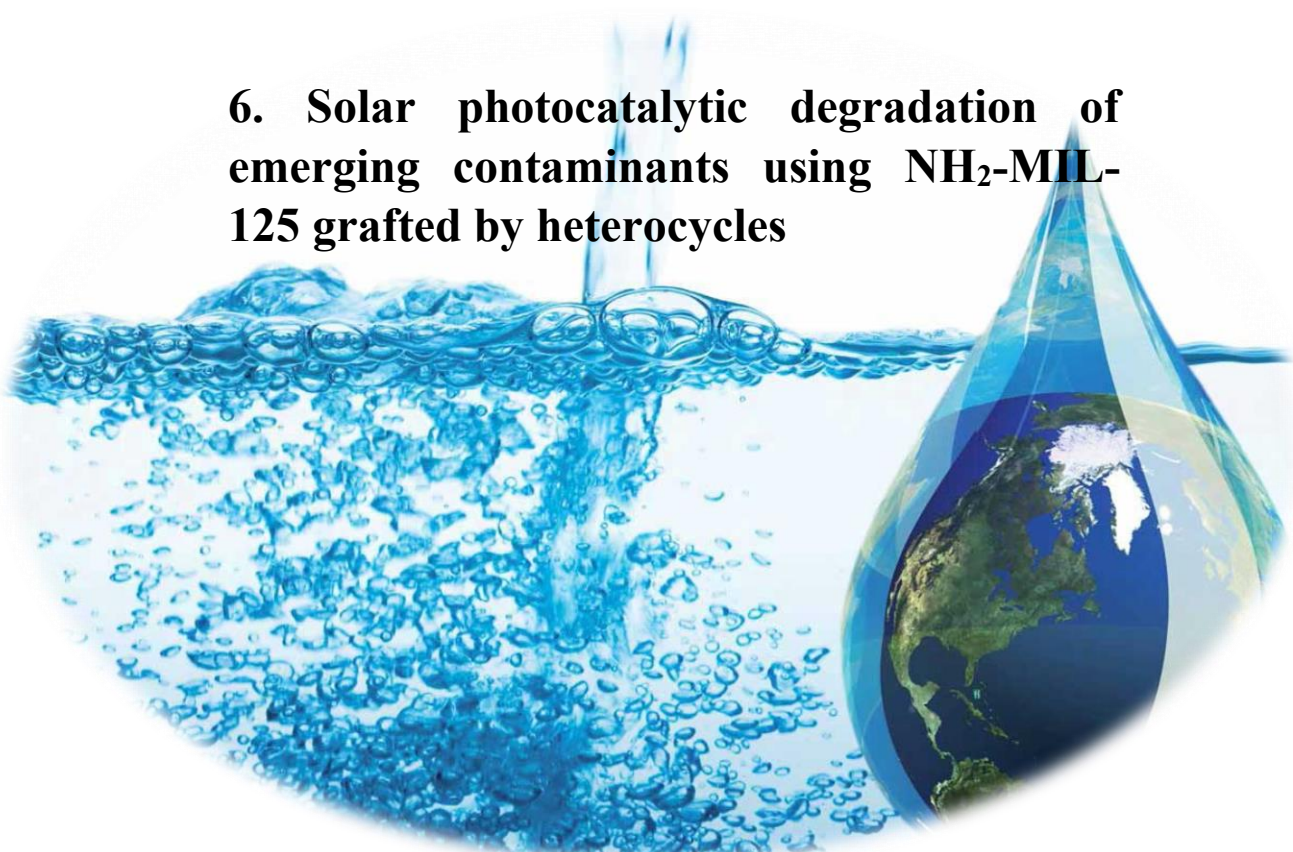
Supplementary data to this article can be found online at <https://doi.org/10.1016/j.seppur.2021.118896>.

References

- [1] J.L. Acero, F.J. Benitez, F.J. Real, F. Teva, Removal of emerging contaminants from secondary effluents by micellar-enhanced ultrafiltration, *Sep. Purif. Technol.* 181 (2017) 123–131, <https://doi.org/10.1016/j.seppur.2017.03.021>.
- [2] Y. Yang, Y.S. Ok, K.H. Kim, E.E. Kwon, Y.F. Tsang, Occurrences and removal of pharmaceuticals and personal care products (PPCPs) in drinking water and water/sewage treatment plants: A review, *Sci. Total Environ.* 596–597 (2017) 303–320, <https://doi.org/10.1016/j.scitotenv.2017.04.102>.
- [3] L. Rizzo, S. Malato, D. Antakyali, V.G. Beretsou, M.B. Dolić, W. Gernjak, E. Heath, I. Ivancev-Tumbas, P. Karaolia, A.R. Lado Ribeiro, G. Mascolo, C.S. Mc Ardell, H. Schaar, A.M.T. Silva, D. Fatta-Kassinos, Consolidated vs new advanced treatment methods for the removal of contaminants of emerging concern from urban wastewater, *Sci. Total Environ.* 655 (2019) 986–1008, <https://doi.org/10.1016/j.scitotenv.2018.11.265>.
- [4] C. Byrne, G. Subramanian, S.C. Pillai, Recent advances in photocatalysis for environmental applications, *J. Environ. Chem. Eng.* 6 (2018) 3531–3555, <https://doi.org/10.1016/j.jece.2017.07.080>.
- [5] A. Fujishima, K. Honda, Electrochemical Photolysis of Water at a Semiconductor Electrode, *Nature* 238 (1972) 37–38, <https://doi.org/10.1038/238037a0>.
- [6] R. Dagher, P. Drogui, D. Robert, Modified TiO₂ for environmental photocatalytic applications: A review, *Ind. Eng. Chem. Res.* 52 (2013) 3581–3599, <https://doi.org/10.1021/ie303468t>.
- [7] Z. Shayegan, C.S. Lee, F. Haghigat, TiO₂ photocatalyst for removal of volatile organic compounds in gas phase – A review, *Chem. Eng. J.* 334 (2018) 2408–2439, <https://doi.org/10.1016/j.cej.2017.09.153>.
- [8] Y. Cui, L. Chao Nengzi, J. Gou, Y. Huang, B. Li, X. Cheng, Fabrication of dual Z-scheme MIL-53(Fe)/A-Bi₂O₃/g-C₃N₄ ternary composite with enhanced visible light photocatalytic performance, *Sep. Purif. Technol.* 232 (2020), <https://doi.org/10.1016/j.seppur.2019.115959>.
- [9] Y. Lin, C. Kong, Q. Zhang, L. Chen, Metal-Organic Frameworks for Carbon Dioxide Capture and Methane Storage, *Adv. Energy Mater.* 7 (2017) 1601296, <https://doi.org/10.1002/aem.201601296>.
- [10] Y. He, W. Zhou, G. Qian, B. Chen, Methane storage in metal-organic frameworks, *Chem. Soc. Rev.* 43 (2014) 5657–5678, <https://doi.org/10.1039/C4CS00032C>.
- [11] K. Meyer, M. Ranocchiari, J.A. van Bokhoven, Metal organic frameworks for photocatalytic water splitting, *Energy Environ. Sci.* 8 (2015) 1923–1937, <https://doi.org/10.1039/C5EE00161G>.
- [12] H. Song, Z. Sun, Y. Xu, Y. Han, J. Xu, J. Wu, T. Sun, H. Meng, X. Zhang, Fabrication of NH₂-MIL-125(Ti) incorporated TiO₂ nanotube arrays composite anodes for highly efficient PEC water splitting, *Sep. Purif. Technol.* 228 (2019), 115764, <https://doi.org/10.1016/j.seppur.2019.115764>.
- [13] R.J. Kuppler, D.J. Timmons, Q.-R. Fang, J.-R. Li, T.A. Makal, M.D. Young, D. Yuan, D. Zhao, W. Zhuang, H.-C. Zhou, Potential applications of metal-organic frameworks, *Coord. Chem. Rev.* 253 (2009) 3042–3066, <https://doi.org/10.1016/j.ccr.2009.05.019>.
- [14] H. Li, K. Wang, Y. Sun, C.T. Lollar, J. Li, H.-C. Zhou, Recent advances in gas storage and separation using metal-organic frameworks, *Mater. Today*. 21 (2018) 108–121, <https://doi.org/10.1016/j.mattod.2017.07.006>.
- [15] J.B. DeCoste, G.W. Peterson, Metal-Organic Frameworks for Air Purification of Toxic Chemicals, *Chem. Rev.* 114 (2014) 5695–5727, <https://doi.org/10.1021/cr4006473>.
- [16] M.L. Hu, V. Safarifard, E. Doustkhah, S. Rostamnia, A. Morsali, N. Nouruzi, S. Beheshti, K. Akhbari, Taking organic reactions over metal-organic frameworks as heterogeneous catalysis, *Microporous Mesoporous Mater.* 256 (2018) 111–127, <https://doi.org/10.1016/j.micromeso.2017.07.057>.
- [17] S.W. Lv, J.M. Liu, N. Zhao, C.Y. Li, F.E. Yang, Z.H. Wang, S. Wang, MOF-derived CoFe₂O₄/Fe₂O₃ embedded in g-C₃N₄ as high-efficient Z-scheme photocatalysts for enhanced degradation of emerging organic pollutants in the presence of persulfate, *Sep. Purif. Technol.* 253 (2020), 117413, <https://doi.org/10.1016/j.seppur.2020.117413>.
- [18] J. Bedia, V. Muelas-Ramos, M. Peñas-Garzón, A. Gómez-Avilés, J. Rodríguez, C. Belver, A Review on the Synthesis and Characterization of Metal Organic Frameworks for Photocatalytic Water Purification, *Catalysts* 9 (2019) 52, <https://doi.org/10.3390/catal9010052>.
- [19] Z. Shao, D. Zhang, H. Li, C. Su, X. Pu, Y. Geng, Fabrication of MIL-88A/g-C₃N₄ direct Z-scheme heterojunction with enhanced visible-light photocatalytic activity, *Sep. Purif. Technol.* 220 (2019) 16–24, <https://doi.org/10.1016/j.seppur.2019.03.040>.
- [20] M. Dan-Hardi, C. Serre, T. Frot, L. Rozes, G. Maurin, C. Sanchez, G. Férey, A New Photoactive Crystalline Highly Porous Titanium(IV) Dicarboxylate, *J. Am. Chem. Soc.* 131 (2009) 10857–10859, <https://doi.org/10.1021/ja903726m>.
- [21] C.H. Hendon, D. Tiana, M. Fontecave, C.C. Sanchez, L. D'Arras, C. Sasseoye, L. Rozes, C. Mellot-Draznieks, A. Walsh, Engineering the optical response of the titanium-MIL-125 metal-organic framework through ligand functionalization, *J. Am. Chem. Soc.* 135 (2013) 10942–10945, <https://doi.org/10.1021/ja405350u>.
- [22] A. Gómez-Avilés, M. Peñas-Garzón, J. Bedia, D.D. Dionysiou, J.J. Rodríguez, C. Belver, Mixed Ti-Zr metal-organic-frameworks for the photodegradation of acetaminophen under solar irradiation, *Appl. Catal. B Environ.* 253 (2019) 253–262, <https://doi.org/10.1016/j.apcatb.2019.04.040>.
- [23] R.M. Abdelhameed, M.M.Q. Simões, A.M.S. Silva, J. Rocha, Enhanced Photocatalytic Activity of MIL-125 by Post-Synthetic Modification with Cr^{III} and Ag Nanoparticles, *Chem. – A Eur. J.* 21 (2015) 11072–11081, <https://doi.org/10.1002/chem.201500808>.
- [24] Y. Fu, H. Yang, R. Du, G. Tu, C. Xu, F. Zhang, M. Fan, W. Zhu, Enhanced photocatalytic CO₂ reduction over Co-doped NH₂-MIL-125(Ti) under visible light, *RSC Adv.* 7 (2017) 42819–42825, <https://doi.org/10.1039/C7RA06324E>.
- [25] Q. Hu, J. Di, B. Wang, M. Ji, Y. Chen, J. Xia, H. Li, Y. Zhao, In-situ preparation of NH₂-MIL-125(Ti)/BiOCl composite with accelerating charge carriers for boosting visible light photocatalytic activity, *Appl. Surf. Sci.* 466 (2019) 525–534, <https://doi.org/10.1016/j.apsusc.2018.10.020>.
- [26] A. Rahmani, H.B.M. Emrooz, S. Abedi, A. Morsali, Synthesis and characterization of CdS/MIL-125 (Ti) as a photocatalyst for water splitting, *Mater. Sci. Semicond. Process.* 80 (2018) 44–51, <https://doi.org/10.1016/j.mssp.2018.02.013>.
- [27] H. Wang, X. Yuan, Y. Wu, G. Zeng, X. Chen, L. Leng, H. Li, Synthesis and applications of novel graphitic carbon nitride/metal-organic frameworks mesoporous photocatalyst for dyes removal, *Appl. Catal. B Environ.* 174–175 (2015) 445–454, <https://doi.org/10.1016/j.apcatb.2015.03.037>.
- [28] S.-R. Zhu, P.-F. Liu, M.-K. Wu, W.-N. Zhao, G.-C. Li, K. Tao, F.-Y. Yi, L. Han, Enhanced photocatalytic performance of BiOBr/NH₂-MIL-125(Ti) composite for dye degradation under visible light, *Dalt. Trans.* 45 (2016) 17521–17529, <https://doi.org/10.1039/C6DT02912D>.
- [29] H. Wang, X. Yuan, Y. Wu, G. Zeng, H. Dong, X. Chen, L. Leng, Z. Wu, L. Peng, In situ synthesis of In₂S₃@MIL-125(Ti) core-shell microparticle for the removal of tetracycline from wastewater by integrated adsorption and visible-light-driven photocatalysis, *Appl. Catal. B Environ.* 186 (2016) 19–29, <https://doi.org/10.1016/j.apcatb.2015.12.041>.
- [30] X. Li, Y. Pi, Q. Hou, H. Yu, Z. Li, Y. Li, J. Xiao, Amorphous TiO₂@NH₂-MIL-125(Ti) homologous MOF-encapsulated heterostructures with enhanced photocatalytic activity, *Chem. Commun.* 54 (2018) 1917–1920, <https://doi.org/10.1039/c7cc09072b>.
- [31] W. Jiang, Z. Li, C. Liu, D. Wang, G. Yan, B. Liu, G. Che, Enhanced visible-light-induced photocatalytic degradation of tetracycline using BiOI/MIL-125(Ti) composite photocatalyst, *J. Alloys Compd.* 854 (2021), 157166, <https://doi.org/10.1016/j.jallcom.2020.157166>.
- [32] H. Wang, P.H. Cui, J.X. Shi, J.Y. Tan, J.Y. Zhang, N. Zhang, C. Zhang, Controllable self-assembly of CdS@NH₂-MIL-125(Ti) heterostructure with enhanced photodegradation efficiency for organic pollutants through synergistic effect, *Mater. Sci. Semicond. Process.* 97 (2019) 91–100, <https://doi.org/10.1016/j.mssp.2019.03.016>.
- [33] S. Yin, Y. Chen, C. Gao, Q. Hu, M. Li, Y. Ding, J. Di, J. Xia, H. Li, In-situ preparation of MIL-125(Ti)/Bi₂WO₆ photocatalyst with accelerating charge carriers for the photodegradation of tetracycline hydrochloride, *J. Photochem. Photobiol. A Chem.* 387 (2020), 112149, <https://doi.org/10.1016/j.jpphotochem.2019.112149>.

- [34] M. Salimi, A. Esrafil, A. Jonidi Jafari, M. Gholami, H.R. Sobhi, M. Nourbakhsh, B. Akbari-Adergani, Photocatalytic degradation of cefixime with MIL-125(Ti)-mixed linker decorated by g-C₃N₄ under solar driven light irradiation, *Colloids Surfaces A Physicochem. Eng. Asp.* 582 (2019) 123874, <https://doi.org/10.1016/j.colsurfa.2019.123874>.
- [35] R.M. Abdelhameed, M. El-Shahat, H.E. Emam, Employable metal (Ag & Pd)@MIL-125-NH₂@cellulose acetate film for visible-light driven photocatalysis for reduction of nitro-aromatics, *Carbohydr. Polym.* 247 (2020), 116695, <https://doi.org/10.1016/j.carbpol.2020.116695>.
- [36] D. Sun, W. Liu, Y. Fu, Z. Fang, F. Sun, X. Fu, Y. Zhang, Z. Li, Noble Metals Can Have Different Effects on Photocatalysis Over Metal-Organic Frameworks (MOFs): A Case Study on M/NH₂-MIL-125(Ti) (M=Pt and Au), *Chem. - A Eur. J.* 20 (2014) 4780–4788, <https://doi.org/10.1002/chem.201304067>.
- [37] C. Hou, Q. Xu, Y. Wang, X. Hu, Synthesis of Pt@NH₂-MIL-125(Ti) as a photocathode material for photoelectrochemical hydrogen production, *RSC Adv.* 3 (2013) 19820, <https://doi.org/10.1039/c3ra43188f>.
- [38] J. Qiu, L. Yang, M. Li, J. Yao, Metal nanoparticles decorated MIL-125-NH₂ and MIL-125 for efficient photocatalysis, *Mater. Res. Bull.* 112 (2019) 297–306, <https://doi.org/10.1016/j.matresbull.2018.12.038>.
- [39] M. Martis, W. Meicheng, K. Mori, H. Yamashita, Fabrication of metal nanoparticles in metal organic framework NH₂-MIL-125 by UV photo-assisted methods for optimized catalytic properties, *Catal. Today.* 235 (2014) 98–102, <https://doi.org/10.1016/j.cattod.2014.02.046>.
- [40] C. Belver, M. Hinojosa, J. Bedia, M. Tobajas, M. Alvarez, V. Rodríguez-González, J. Rodríguez, Ag-Coated Heterostructures of ZnO-TiO₂/Delaminated Montmorillonite as Solar Photocatalysts, *Materials (Basel)*. 10 (2017) 960, <https://doi.org/10.3390/ma10080960>.
- [41] K.S. Walton, R.Q. Snurr, Applicability of the BET method for determining surface areas of microporous metal-organic frameworks, *J. Am. Chem. Soc.* 129 (2007) 8552–8556, <https://doi.org/10.1021/ja071174k>.
- [42] A.J. Howarth, A.W. Peters, N.A. Vermeulen, T.C. Wang, J.T. Hupp, O.K. Farha, Best practices for the synthesis, activation, and characterization of metal-organic frameworks, *Chem. Mater.* 29 (2017) 26–39, <https://doi.org/10.1021/acs.chemmater.6b02626>.
- [43] J. Tauc, Absorption edge and internal electric fields in amorphous semiconductors, *Mater. Res. Bull.* 5 (1970) 721–729, [https://doi.org/10.1016/0025-5408\(70\)90112-1](https://doi.org/10.1016/0025-5408(70)90112-1).
- [44] P.V. Hloplie, L.C. Mahlalela, L.N. Dlamini, A composite of platelet-like oriented BiVO₄ fused with MIL-125(Ti): Synthesis and characterization, *Sci. Rep.* 9 (2019) 1–12, <https://doi.org/10.1038/s41598-019-46498-w>.
- [45] M. Yin, Z. Li, J. Kou, Z. Zou, Mechanism Investigation of Visible Light-Induced Degradation in a Heterogeneous TiO₂/Eosin Y/Rhodamine B System, *Environ. Sci. Technol.* 43 (2009) 8361–8366, <https://doi.org/10.1021/es902011h>.
- [46] L. Ye, J. Liu, Z. Jiang, T. Peng, L. Zan, Facets coupling of BiOBr-g-C₃N₄ composite photocatalyst for enhanced visible-light-driven photocatalytic activity, *Appl. Catal. B Environ.* 142–143 (2013) 1–7, <https://doi.org/10.1016/j.apcatb.2013.04.058>.
- [47] M. Fakhru Rulhwan Samsudin, L. Tau Siang, S. Sufian, R. Bashiri, N. Muti Mohamed, R. Mahirah Ramli, Exploring the role of electron-hole scavengers on optimizing the photocatalytic performance of BiVO₄, in: *Mater. Today Proc.*, Elsevier Ltd, 2018, pp. 21703–21709. doi: [10.1016/j.matpr.2018.07.022](https://doi.org/10.1016/j.matpr.2018.07.022).
- [48] Y. Wang, P. Zhang, Photocatalytic decomposition of perfluorooctanoic acid (PFOA) by TiO₂ in the presence of oxalic acid, *J. Hazard. Mater.* 192 (2011) 1869–1875, <https://doi.org/10.1016/j.jhazmat.2011.07.026>.
- [49] A. Gómez-Avilés, M. Peñas-Garzón, J. Bedia, D.D. Dionysiou, J.J. Rodríguez, C. Belver, Mixed Ti-Zr metal-organic-frameworks for the photodegradation of acetaminophen under solar irradiation, *Appl. Catal. B Environ.* 253 (2019) 253–262, <https://doi.org/10.1016/j.apcatb.2019.04.040>.
- [50] F.B. Li, X.Z. Li, The enhancement of photodegradation efficiency using Pt-TiO₂ catalyst, *Chemosphere* 48 (2002) 1103–1111, [https://doi.org/10.1016/S0045-6535\(02\)00201-1](https://doi.org/10.1016/S0045-6535(02)00201-1).
- [51] A. Gómez-Avilés, V. Muelas-Ramos, J. Bedia, J.J. Rodríguez, C. Belver, Thermal Post-Treatments to Enhance the Water Stability of NH₂-MIL-125(Ti), *Catalysts* 10 (2020) 603, <https://doi.org/10.3390/catal10060603>.
- [52] A.P. Smalley, D.G. Reid, J.C. Tan, G.O. Lloyd, Alternative synthetic methodology for amide formation in the post-synthetic modification of Ti-MIL125-NH₂, *CrystEngComm* 15 (2013) 9368, <https://doi.org/10.1039/c3ce41332b>.
- [53] S.-N. Kim, J. Kim, H.-Y. Kim, H.-Y. Cho, W.-S. Ahn, Adsorption/catalytic properties of MIL-125 and NH₂-MIL-125, *Catal. Today* 204 (2013) 85–93, <https://doi.org/10.1016/j.cattod.2012.08.014>.
- [54] H. Wang, X. Yuan, Y. Wu, G. Zeng, X. Chen, L. Leng, Z. Wu, L. Jiang, H. Li, Facile synthesis of amino-functionalized titanium metal-organic frameworks and their superior visible-light photocatalytic activity for Cr(VI) reduction, *J. Hazard. Mater.* 286 (2015) 187–194, <https://doi.org/10.1016/j.jhazmat.2014.11.039>.
- [55] Y. Fu, L. Sun, H. Yang, L. Xu, F. Zhang, W. Zhu, Visible-light-induced aerobic photocatalytic oxidation of aromatic alcohols to aldehydes over Ni-doped NH₂-MIL-125(Ti), *Appl. Catal. B Environ.* 187 (2016) 212–217, <https://doi.org/10.1016/j.apcatb.2016.01.038>.
- [56] Y. Fu, D. Sun, Y. Chen, R. Huang, Z. Ding, X. Fu, Z. Li, An Amine-Functionalized Titanium Metal-Organic Framework Photocatalyst with Visible-Light-Induced Activity for CO₂ Reduction, *Angew. Chem. Int. Ed.* 51 (2012) 3364–3367, <https://doi.org/10.1002/anie.201108357>.
- [57] S.H. Hsieh, W.J. Chen, C.T. Wu, Pt-TiO₂/graphene photocatalysts for degradation of AO7 dye under visible light, *Appl. Surf. Sci.* 340 (2015) 9–17, <https://doi.org/10.1016/j.apsusc.2015.02.184>.
- [58] G. Fan, X. Zheng, J. Luo, H. Peng, H. Lin, M. Bao, L. Hong, J. Zhou, Rapid synthesis of Ag/AgCl@ZIF-8 as a highly efficient photocatalyst for degradation of acetaminophen under visible light, *Chem. Eng. J.* 351 (2018) 782–790, <https://doi.org/10.1016/j.cej.2018.06.119>.
- [59] M. Wang, L. Yang, J. Yuan, L. He, Y. Song, H. Zhang, Z. Zhang, S. Fang, Heterostructured Bi₂S₃@NH₂-MIL-125(Ti) nanocomposite as a bifunctional photocatalyst for Cr(VI) reduction and rhodamine B degradation under visible light, *RSC Adv.* 8 (2018) 12459–12470, <https://doi.org/10.1039/c8ra00882e>.
- [60] H. Liu, J. Zhang, D. Ao, Construction of heterostructured ZnIn₂S₄@NH₂-MIL-125 (Ti) nanocomposites for visible-light-driven H₂ production, *Appl. Catal. B Environ.* 221 (2018) 433–442, <https://doi.org/10.1016/j.apcatb.2017.09.043>.
- [61] J. Fan, K. Qi, L. Zhang, H. Zhang, S. Yu, X. Cui, Engineering Pt/Pd Interfacial Electronic Structures for Highly Efficient Hydrogen Evolution and Alcohol Oxidation, *ACS Appl. Mater. Interfaces* 9 (2017) 18008–18014, <https://doi.org/10.1021/acsami.7b05290>.
- [62] C. Belver, C. Adán, S. García-Rodríguez, M. Fernández-García, Photocatalytic behavior of silver vanadates: Microemulsion synthesis and post-reaction characterization, *Chem. Eng. J.* 224 (2013) 24–31, <https://doi.org/10.1016/j.cej.2012.11.102>.
- [63] R.M. Abdelhameed, D.M. Tobaldi, K. Karmaoui, Engineering highly effective and stable nanocomposite photocatalyst based on NH₂-MIL-125 encirclement with Ag₃PO₄ nanoparticles, *J. Photochem. Photobiol. A Chem.* 351 (2018) 50–58, <https://doi.org/10.1016/j.jphotochem.2017.10.011>.
- [64] J. Xu, J. Gao, C. Wang, Y. Yang, L. Wang, NH₂-MIL-125(Ti)/graphitic carbon nitride heterostructure decorated with NiPd co-catalysts for efficient photocatalytic hydrogen production, *Appl. Catal. B Environ.* 219 (2017) 101–108, <https://doi.org/10.1016/j.apcatb.2017.07.046>.
- [65] J.-D. Xiao, L. Han, J. Luo, S.-H. Yu, H.-L. Jiang, Integration of Plasmonic Effects and Schottky Junctions into Metal-Organic Framework Composites: Steering Charge Flow for Enhanced Visible-Light Photocatalysis, *Angew. Chemie Int. Ed.* 57 (2018) 1103–1107, <https://doi.org/10.1002/anie.201711725>.
- [66] J. Xiao, Q. Shang, Y. Xiong, Q. Zhang, Y. Luo, S. Yu, H. Jiang, Boosting Photocatalytic Hydrogen Production of a Metal-Organic Framework Decorated with Platinum Nanoparticles: The Platinum Location Matters, *Angew. Chem.* 128 (2016) 9535–9539, <https://doi.org/10.1002/ange.201603990>.
- [67] M. Akkari, P. Aranda, C. Belver, J. Bedia, A. Ben Haj Amara, E. Ruiz-Hitzky, ZnO/sepilolite heterostructured materials for solar photocatalytic degradation of pharmaceuticals in wastewater, *Appl. Clay Sci.* 156 (2018) 104–109. doi: [10.1016/j.clay.2018.01.021](https://doi.org/10.1016/j.clay.2018.01.021).
- [68] O. Nasr, O. Mohamed, A.S. Al-Shirbini, A.M. Abdel-Wahab, Photocatalytic degradation of acetaminophen over Ag, Au and Pt loaded TiO₂ using solar light, *J. Photochem. Photobiol. A Chem.* 374 (2019) 185–193, <https://doi.org/10.1016/j.jphotochem.2019.01.032>.
- [69] A. Gómez-Avilés, M. Peñas-Garzón, J. Bedia, J.J. Rodríguez, C. Belver, C-modified TiO₂ using lignin as carbon precursor for the solar photocatalytic degradation of acetaminophen, *Chem. Eng. J.* 358 (2019) 1574–1582, <https://doi.org/10.1016/j.cej.2018.10.154>.
- [70] L. Ye, J. Liu, C. Gong, L. Tian, T. Peng, L. Zan, Two different roles of metallic Ag on Ag/AgX/BiOX (X = Cl, Br) visible light photocatalysts: Surface plasmon resonance and Z-Scheme bridge, *ACS Catal.* 2 (2012) 1677–1683, <https://doi.org/10.1021/cs300213m>.
- [71] E. Kudlek, M. Dudziak, J. Bohdziewicz, Influence of Inorganic Ions and Organic Substances on the Degradation of Pharmaceutical Compounds in Water Matrix, *Water* 8 (2016) 532, <https://doi.org/10.3390/w8110532>.
- [72] C. Hu, J.C. Yu, Z. Hao, P.K. Wong, Effects of acidity and inorganic ions on the photocatalytic degradation of different azo dyes, *Appl. Catal. B Environ.* 46 (2003) 35–47, [https://doi.org/10.1016/S0926-3373\(03\)00139-5](https://doi.org/10.1016/S0926-3373(03)00139-5).
- [73] T. Liu, K. Yin, C. Liu, J. Luo, J. Crittenden, W. Zhang, S. Luo, Q. He, Y. Deng, H. Liu, D. Zhang, The role of reactive oxygen species and carbonate radical in oxcarbazepine degradation via UV, UV/H₂O₂: Kinetics, mechanisms and toxicity evaluation, *Water Res.* 147 (2018) 204–213, <https://doi.org/10.1016/j.watres.2018.10.007>.
- [74] M. Peñas-Garzón, A. Gómez-Avilés, C. Belver, J.J. Rodríguez, J. Bedia, Degradation pathways of emerging contaminants using TiO₂-activated carbon heterostructures in aqueous solution under simulated solar light, *Chem. Eng. J.* 392 (2020), 124867, <https://doi.org/10.1016/j.cej.2020.124867>.
- [75] R. Andreozzi, V. Caprio, R. Marotta, D. Vogna, Paracetamol oxidation from aqueous solutions by means of ozonation and H₂O₂/UV system, *Water Res.* 37 (2003) 993–1004, [https://doi.org/10.1016/S0043-1354\(02\)00460-8](https://doi.org/10.1016/S0043-1354(02)00460-8).
- [76] T.X.H. Le, T. Van Nguyen, Z. Amadou Yacoubia, L. Zoungrana, F. Avril, D. L. Nguyen, E. Petit, J. Mendret, V. Bonniol, M. Bechelany, S. Lacour, G. Lesage, M. Cretin, Correlation between degradation pathway and toxicity of acetaminophen and its by-products by using the electro-Fenton process in aqueous media, *Chemosphere* 172 (2017) 1–9, <https://doi.org/10.1016/j.chemosphere.2016.12.060>.
- [77] A.M. Abdel-Wahab, A.S. Al-Shirbini, O. Mohamed, O. Nasr, Photocatalytic degradation of paracetamol over magnetic flower-like TiO₂/Fe₂O₃ core-shell nanostructures, *J. Photochem. Photobiol. A Chem.* 347 (2017) 186–198, <https://doi.org/10.1016/j.jphotochem.2017.07.030>.

6. Solar photocatalytic degradation of emerging contaminants using $\text{NH}_2\text{-MIL-125}$ grafted by heterocycles





Contents lists available at ScienceDirect

Separation and Purification Technology

journal homepage: www.elsevier.com/locate/seppur

Solar photocatalytic degradation of emerging contaminants using NH₂-MIL-125 grafted by heterocycles

V. Muelas-Ramos, M. Peñas-Garzón, J.J. Rodríguez, J. Bedia^{*}, C. Belver^{*}

Chemical Engineering Department, Universidad Autónoma de Madrid, Campus Cantoblanco, E-28049 Madrid, Spain

ARTICLE INFO

Keywords:

NH₂-MIL-125
Grafting
Emerging contaminants
Solar photocatalysis
Continuous regime

ABSTRACT

This work reports the photocatalytic performance of NH₂-MIL-125 grafted by heterocycles for the removal of contaminants of emerging concern under solar light. Grafting NH₂-MIL-125 with different heterocyclic carboxaldehydes reduces the band gap, thanks to the performance of the heterocycle as an antenna for light absorption. Grafting with 3-pyridinecarboxaldehyde (3PA) results in the best light harvesting for the degradation of acetaminophen in different water matrices. The abatement of additional emerging contaminants, i.e., antipyrine and sulfamethoxazole, was also evaluated. The photocatalytic performance depends on the nature of the target compound. Trapping experiments conclude that superoxide radicals are the main reactive species involved in the photodegradation process, while electrons and hydroxyl radicals play a minor role. The 3PA-grafted photocatalyst shows remarkable constant performance in a novel analysis in a continuous flow regime, achieving total conversion of acetaminophen (ACE) for 16 h on stream. The results herein described provide a comprehensive insight into the solar photocatalytic degradation of emerging contaminants using NH₂-MIL-125 grafted by aromatic heterocycles.

1. Introduction

The uncontrolled discharge of different compounds into aquatic sources constitutes an increasing concern. Pharmaceuticals are common emerging contaminants (ECs) detected in wastewaters and aquatic ecosystems, coming from household effluents, industrial activities, and hospital services, among others [1]. Exposure to ECs may produce harmful effects on human health and the environment, such as disruptive effects or cellular damage [2,3]. Water streams containing ECs are mixed with other water flows and treated into wastewater treatment plants (WWTPs) before final discharge into rivers, seas, or aquifers. However, the development of more accurate analytical techniques has allowed the detection of ECs in the WWTPs effluents, confirming that they are not completely removed during the process [4]. In this sense, the average removal of analgesics, anti-inflammatories, or β -blockers was estimated to be around 30–40% [5]. Acetaminophen (ACE) can be considered among the most common analgesic-antipyretic pharmaceuticals worldwide, also sold under different trade names, such as paracetamol. The consumption of ACE is situated among 60–70 daily doses per 1000 inhabitants (DDD) in European countries such as France, Spain, Denmark, and the United Kingdom, much higher than that of

other common analgesics, such as acetylsalicylic acid, with a reported consumption below 10 DDD [6]. After consumption, about 2–5% of ACE is excreted without any metabolic shift and reaches wastewater [7]. Its high solubility in water (around 14 g·L⁻¹ besides the low octanol-water partition coefficient, 0.46 [8]) can explain its common detection in water bodies. For instance, Fekadu et al. [9] compared the occurrence of certain pharmaceuticals in European and African freshwater aquatic environments. They found that the maximum ACE concentration recorded in Europe was in the Llobregat river (Spain), with a value of 1.3 μ g·L⁻¹ [10], remarkably lower than the measured in a Kenyan river, 107 μ g·L⁻¹ [11]. The incomplete elimination of these emerging contaminants would increase their overall concentration, thus representing a potential environmental risk. Therefore, it is necessary to improve strategies in the treatment of wastewaters for the complete removal of these ECs before their final discharge. For instance, advanced oxidation processes (AOPs) are based on the in-situ generation of reactive oxygen species (ROS) with high oxidation capacity [12,13], including Fenton-like processes, ozonation, electrochemical oxidation, or photocatalysis [14]. Particularly, photocatalysis, based on the conversion of light-to-chemical energy, is considered an environmentally friendly technology because it only requires the use of a light source and a solid

^{*} Corresponding authors.

E-mail addresses: jorge.bedia@uam.es (J. Bedia), carolina.belver@uam.es (C. Belver).

<https://doi.org/10.1016/j.seppur.2022.121442>

Received 16 March 2022; Received in revised form 4 June 2022; Accepted 5 June 2022

Available online 7 June 2022

1383-5866/© 2022 The Authors. Published by Elsevier B.V. This is an open access article under the CC BY-NC-ND license (<http://creativecommons.org/licenses/by-nc-nd/4.0/>).

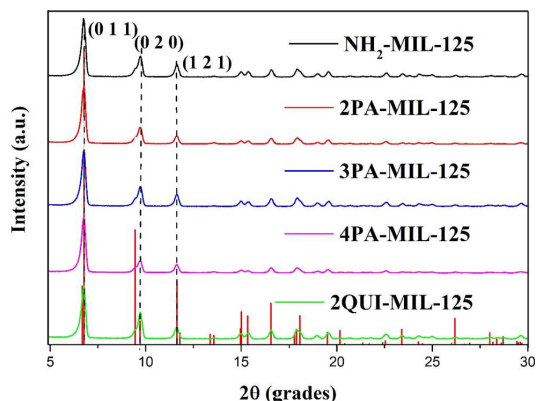


Fig. 1. X-ray diffraction patterns of the bare NH_2 -MIL-125 and the grafted materials (Reference pattern of NH_2 -MIL-125 from Crystal Open Database (COD) library is included in red colour). (For interpretation of the coloured references in this figure legend, the reader is referred to the web version of this article.)

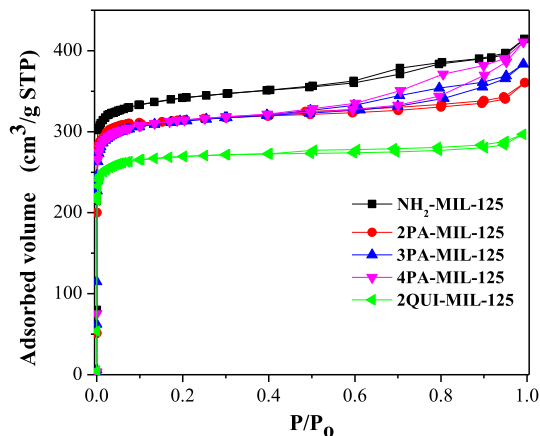


Fig. 3. N_2 adsorption–desorption isotherms at 196°C of the bare NH_2 -MIL-125 and the grafted materials.

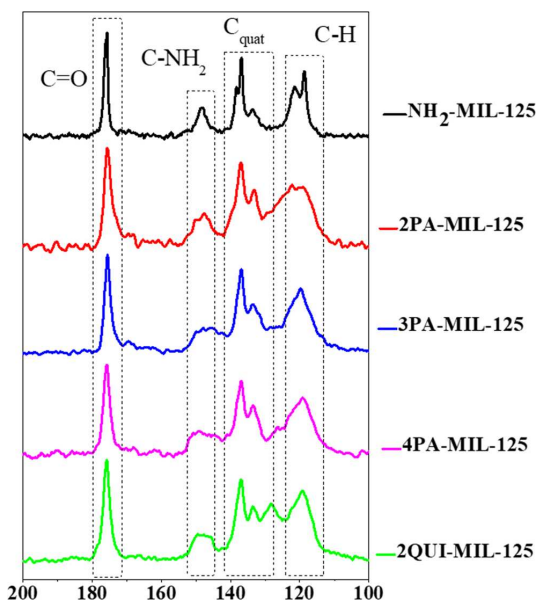


Fig. 2. ^{13}C solid-state NMR spectra of the bare NH_2 -MIL-125 and the grafted materials.

semiconductor, and can operate under mild conditions of temperature and pressure. Moreover, the use of solar light represents a cost-effective and green alternative to other more energy-demand technologies, supporting the development of photocatalysis for the abatement of contaminants in water. Thus, the removal of ECs by solar photocatalysis is the focus of many researchers, with particular emphasis on the degradation of analgesics [15–19] and antibiotics [20–22].

Since the photocatalytic process requires the absorption of light by a semiconductor, many different materials are currently under study to achieve the best solar light harvesting [23]. The main aim in this field is the absorption of light in both the UV and visible range of the solar spectrum to generate electron/hole pairs while avoiding their

Table 1

Porous texture parameters and band gap values (E_g) of the bare NH_2 -MIL-125 and the grafted materials.

| | S_{BET} ($\text{m}^2\cdot\text{g}^{-1}$) | S_{MP} ($\text{m}^2\cdot\text{g}^{-1}$) | S_{EXT} ($\text{m}^2\cdot\text{g}^{-1}$) | V_{MP} ($\text{cm}^3\cdot\text{g}^{-1}$) | V_{T} ($\text{cm}^3\cdot\text{g}^{-1}$) | E_g (eV) |
|------------------------|--|---|--|--|---|---------------|
| NH_2 -MIL-125 | 1141 | 985 | 157 | 0.46 | 0.64 | 2.67 |
| 2PA-MIL-125 | 1032 | 918 | 114 | 0.43 | 0.58 | 2.63 |
| 3PA-MIL-125 | 1053 | 927 | 126 | 0.43 | 0.59 | 2.62 |
| 4PA-MIL-125 | 1062 | 937 | 126 | 0.43 | 0.63 | 2.60 |
| 2QUI-MIL-125 | 911 | 840 | 72 | 0.38 | 0.46 | 2.60 |

S_{BET} , specific surface area; S_{MP} and S_{EXT} , microporous and non-microporous surface area; V_{T} and V_{MP} , total and micropore volume; E_g , band gap.

recombination [24]. Despite the adequate activity reported using TiO_2 as a reference photocatalyst [25], this semiconductor presents the main limitation of its large band gap value (~ 3.2 eV), avoiding the light-harvesting from the visible region and thus implying a low utilization of the solar light. In this sense, metal organic frameworks (MOFs) are being investigated for the photocatalytic treatment of contaminated water [26,27], as a consequence of their good optical, structural, and electronic properties that can be tailored through the use of different metal nodes or organic linkers [28]. After irradiation, electrons can be transferred from the organic ligand to the partially filled d-orbitals of the metal cluster in a process known as ligand-to-metal charge transfer (LMCT) [29,30]. Among the most used MOFs are Fe-based (as MIL-53, -88, and -101), Ti-MOFs (MIL-125), Zr-MOFs (UiO-66), and Zn-MOFs (ZIF-8) [31]. Moreover, the literature shows additional strategies to promote the photocatalytic performance of MOFs to enhance their light harvesting, such as doping [32], noble metal deposition [33], or combined with other semiconductors [34]. One approach consists in functionalizing the organic ligand [35]. For example, NH_2 -MIL-125 has shown high stability [36] and activity concerning the bare MIL-125 counterpart, as both the NH_2 -ligand and the Ti-cluster were excited under visible light [37]. This approach can be further extended by grafting, after synthesis, the $-\text{NH}_2$ group with other compounds that act

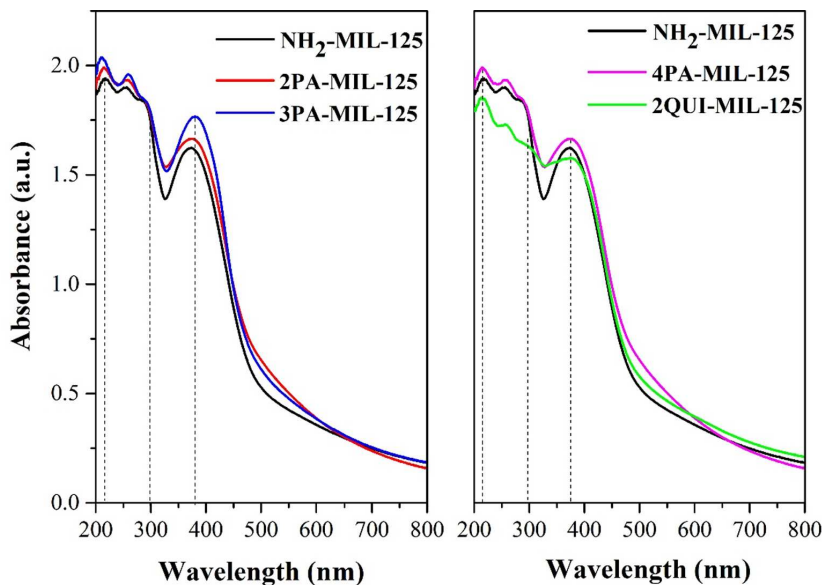


Fig. 4. UV-visible spectra of the bare $\text{NH}_2\text{-MIL-125}$ and the grafted materials.

as an antenna for light absorption [38]. In this sense, heterocyclic compounds can be successfully grafted to the $-\text{NH}_2$ group following a Schiff base reaction through an aldehyde group [39]. These heterocyclic compounds provide additional charges and improve their mobility, appearing as a promising approach to improving the photocatalytic properties of MOFs [40]. However, to the best of our knowledge, no studies have been reported dealing with the grafting of MOFs for the solar photocatalytic degradation of ECs.

This is the first work reporting the degradation of ECs for water purification using these grafted- $\text{NH}_2\text{-MIL-125}$. The grafted-MOFs were tested in the photodegradation of ACE. The photocatalytic performance of the best grafted- $\text{NH}_2\text{-MIL-125}$ was further investigated under different water matrices and with a mixture of emerging contaminants (acetaminophen, sulfamethoxazole, and antipyrine) whose presence in aqueous effluents has been also frequently reported [41]. Besides, the stability and photocatalytic performance were evaluated under a novel analysis in continuous flow tests. Remarkably, no previous works have demonstrated the performance of grafted- $\text{NH}_2\text{-MIL-125}$ in continuous flow tests or with a mixture of emerging contaminants with different chemical structures.

2. Experimental

2.1. Chemicals and reagents

2-aminoterephthalic acid (ATA, 99%), N,N-dimethylformamide (DMF, $\geq 99.8\%$), titanium (IV) isopropoxide ($\geq 97\%$), methanol (99.8%), 2-pyridinecarboxaldehyde (2PA, 99%), 3-pyridinecarboxaldehyde (3PA, 98%), 4-pyridinecarboxaldehyde (4PA, 97%), 2-quinolinecarboxaldehyde (2QUI, 97%), acetaminophen (ACE, $\geq 99\%$), sulfamethoxazole (SMX, $\geq 99\%$), antipyrine (ANT, $\geq 99\%$), acetic acid ($\geq 99\%$), benzoquinone (BQ $\geq 98\%$), silver nitrate, (AgNO_3 , $\geq 99\%$), potassium iodide (KI, 99%) and NaHCO_3 were purchased from Sigma-Aldrich. Acetonitrile (UV HPLC grade) and Na_2SO_4 ($\geq 99\%$) were acquired from Scharlab. 2-propanol (IPA, 99.7%) was acquired from AppliChem, whereas NaCl and NaNO_3 were provided from Panreac. All chemicals were used as received without further purification. All solutions were prepared with deionized water (type II).

2.2. Synthesis of bare $\text{NH}_2\text{-MIL-125}$

The $\text{NH}_2\text{-MIL-125}$ was synthesized by solvothermal synthesis following a previously described method [36]. Briefly, 6 mmol of 2-aminoterephthalic acid were dissolved in 25 ml of DMF and stirred for 5 min at 25 °C. Then, 3 mmol of titanium (IV) isopropoxide were added dropwise, followed by the addition of 25 ml of methanol. After 30 min of stirring, the mixture was placed in a 100 ml Teflon steel autoclave and heated for 16 h at 150 °C. The resulting yellow powder was recovered by centrifugation (5000 rpm, 5 min) and washed with DMF and methanol (100 ml each time for 30 min). The product was finally dried in an oven at 60 °C for 18 h.

2.3. Grafting of $\text{NH}_2\text{-MIL-125}$

The $\text{NH}_2\text{-MIL-125}$ was modified after synthesis by grafting with four heterocyclic carboxaldehydes, namely 2-pyridinecarboxaldehyde, 3-pyridinecarboxaldehyde, 4-pyridinecarboxaldehyde, and 2-quinolinecarboxaldehyde, whose chemical structures can be seen in Fig. S1. The grafting process followed the method described by Wu et al. [38]. It consists of the Schiff reaction between the amine group of the MOF and the carboxylic group of the heterocyclic carboxaldehyde, as schematized in Fig. S2. Briefly, 560 mg of $\text{NH}_2\text{-MIL-125}$ was firstly activated in a vacuum oven at 120 °C for 3 h. Then, it was dispersed in 30 ml of acetonitrile, followed by the addition of 0.8 mM of 2PA. The mixture was placed in a bath at 70 °C for three days. The resulting solid was collected by centrifugation (5000 rpm and 5 min), washed with methanol three times, and dried at 60 °C for 18 h in a vacuum oven. For complete removal of organic precursors and solvent, the solid was heated in air at 200 °C for 48 h. The material thus obtained was named 2PA-MIL-125, according to the abbreviation of the heterocyclic carboxaldehyde. The $\text{NH}_2\text{-MIL-125}$ was grafted by the other heterocyclic carboxaldehydes, 3PA, 4PA, and 2QUI, following the same methodology, and the resulting materials were labelled as 3PA-MIL-125, 4PA-MIL-125, and 2QUI-MIL-125, respectively.

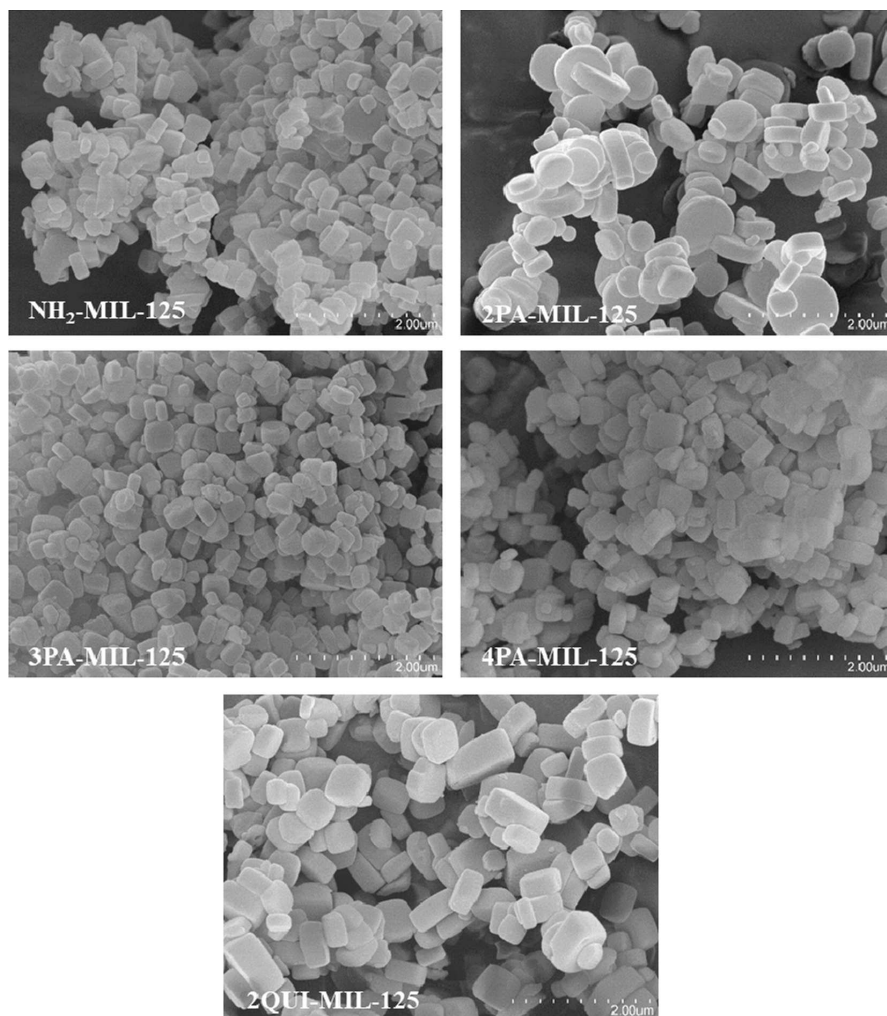


Fig. 5. SEM images of the bare NH_2 -MIL-125 and the grafted materials.

2.4. Characterization of photocatalysts

A Bruker D8 diffractometer (Cu $K\alpha$ source) in a 2θ scanning range of 2 to 50° and with a $5^\circ\cdot\text{min}^{-1}$ rate, was used to record the X-ray diffraction (XRD) patterns. The ^{13}C solid-state NMR spectra were acquired with a Bruker AV 400 WB spectrometer at 100.61 MHz in ZrO rotors sealed with Kel-F caps at room temperature. The analysis conditions were contact time 3 ms, spinning frequency 10 kHz, and pulse delay 4 s. Chemical shifts were all reported concerning external tetramethylsilane (TMS). The porous texture was characterized by N_2 adsorption-desorption at -196°C performed with a TriStar 123 equipment (Micromeritics). All photocatalysts were previously outgassed under vacuum at 120°C . The specific surface area (S_{BET}) was obtained from the BET method [42], while the microporous surface area (S_{MP}) and the non-microporous surface area (S_{EXT}) were quantified by the t-plot [43]. The amount of nitrogen adsorbed at a relative pressure (P/P_0) of 0.99 was used to estimate the total pore volume. UV-vis diffuse reflectance spectra were collected in a Shimadzu 2600 UV-vis spectrophotometer in the 185–800 nm range, using BaSO_4 as reference. The

band gap (E_g) values were determined by the Tauc Plot method [35,44], considering all materials as indirect semiconductors [45]. Scanning electron microscopy (SEM) images were acquired with HITACHI S-4800 equipment. Photoluminescence (PL) spectra were recorded in a Cary Eclipse spectrofluorometer using an excitation wavelength of 370 nm. A Metrohm Autolab potentiostat (PGSTAT204) was used to determine the electrochemical properties of the synthesized materials. This system comprises an indium tin oxide (ITO) working electrode, with counter and reference counterparts of carbon and silver electrodes, respectively. The material suspension ($1\text{ mg}\cdot\text{mL}^{-1}$) was prepared in 0.1 M Na_2SO_4 ($\text{pH} \sim 4.3$ at 25°C) and placed into the electrochemical cell (DropSens ITO10). Electrochemical impedance spectroscopy (EIS) was recorded scanning the frequency range from 10^5 to 10^{-1} Hz at a fixed potential of -1.2 V , whereas Mott-Schottky plots were obtained applying a voltage between 0.4 and -1.0 V under a constant frequency of 100 Hz. The flat band potential of the material, V_{fb} , was obtained following Mott-Schottky equation (Eq. (1)) [46]:

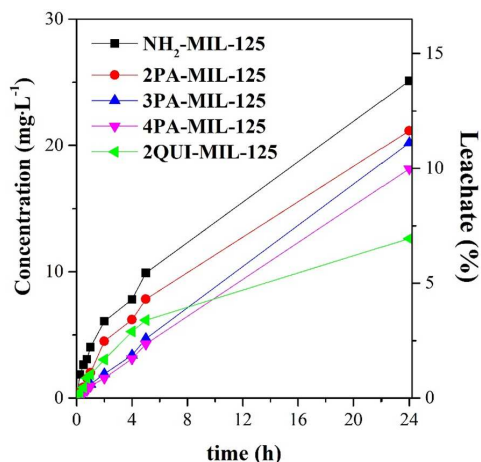


Fig. 6. Evolution of the linker leaching in the water of the bare $\text{NH}_2\text{-MIL-125}$ and the grafted materials.

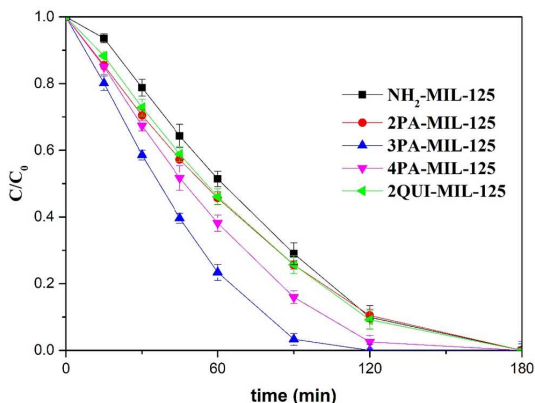


Fig. 7. Evolution of ACE degradation with the bare $\text{NH}_2\text{-MIL-125}$ and the grafted materials under solar irradiation ($[\text{ACE}]_0 = 5 \text{ mg}\cdot\text{L}^{-1}$; Photocatalyst load = $250 \text{ mg}\cdot\text{L}^{-1}$; Intensity = $600 \text{ W}\cdot\text{m}^{-2}$).

Table 2

Values of the pseudo-first-order rate constant (k) of ACE degradation under solar irradiation.

| Photocatalyst | k (min^{-1}) | Reference |
|---------------------------------------|---------------------------|-----------|
| $\text{NH}_2\text{-MIL-125}$ | 0.0082 | This work |
| 2PA-MIL-125 | 0.0126 | This work |
| 3PA-MIL-125 | 0.0194 | This work |
| 4PA-MIL-125 | 0.0151 | This work |
| 2QUI-MIL-125 | 0.0137 | This work |
| Zr-doped $\text{NH}_2\text{-MIL-125}$ | 0.0121 | [32] |
| Pt@ $\text{NH}_2\text{-MIL-125}$ | 0.0165 | [33] |

$$\frac{1}{C^2} = \frac{2}{\epsilon \hat{A} \cdot \epsilon_0 \hat{A} \cdot e \hat{A} \cdot N_D} \hat{A} \cdot \left(V - V_{fb} - \frac{k \hat{A} \cdot T}{e} \right)_{1/C^2=0} V_{fb} = V - \frac{k \hat{A} \cdot T}{e} \quad (1)$$

being C the capacitance of the semiconductor-electrolyte junction at applied voltage V ; ϵ and ϵ_0 the permittivity of the semiconductor and the void, respectively; e the electron charge ($1.602 \cdot 10^{-19} \text{ J}$); k the

Boltzmann's constant ($8.617 \cdot 10^{-5} \text{ eV}\cdot\text{K}^{-1}$); and T the temperature (298 K). V_{fb} is estimated from the intercept point of the tangent line with the potential axis ($1/C^2 = 0$) in the plot of $1/C^2$ vs V . The potential of the conduction band (V_{CB}) can be calculated concerning the normal hydrogen electrode (NHE) at pH 7 following a Nernstian shift using Eq. (2) [47]:

$$V_{CB} = V_{fb(\text{Ag}/\text{AgCl}, \text{pH})} + \Delta V_{(\text{Ag}/\text{AgCl}, \text{NHE})} - 0.059 \cdot (7 - \text{pH}), \quad (2)$$

where $\Delta V_{(\text{Ag}/\text{AgCl}, \text{NHE})}$ is the Ag/AgCl potential against NHE (0.21 V). Finally, the valence band potential (V_{VB}) can be estimated following Eq. (3):

$$V_{VB} = V_{CB} + \frac{E_g}{e}, \quad (3)$$

where E_g is the bandgap of the semiconductor.

2.5. Photocatalytic assays

Photocatalytic assays were performed in a Pyrex jacketed reactor under simulated solar light (Suntest XLS+, Xe lamp, ATLAS). The light intensity was fixed at $600 \text{ W}\cdot\text{m}^{-2}$ and restrained to $\lambda \geq 320 \text{ nm}$ with an ID65 filter. An aqueous solution (150 ml) of the target contaminant was placed in the reactor with the photocatalyst ($250 \text{ mg}\cdot\text{L}^{-1}$) under stirring, setting the temperature at $25 \text{ }^\circ\text{C}$. For all assays, the initial concentration of the target compound was set at $5 \text{ mg}\cdot\text{L}^{-1}$ after reaching the adsorption equilibrium in the dark. Aliquots of $400 \mu\text{L}$ were taken during reaction at different intervals, filtered with PTFE syringeless filters (Whatman $0.45 \mu\text{m}$) and analysed by High Performance Liquid Chromatography (HPLC), using a reverse phase C18 column. The mobile phase used was a mixture of acetic acid 0.1% (v/v) and acetonitrile using a gradient elution method (10/90 to 40/60%), with a constant flow equal to $0.7 \text{ ml}\cdot\text{min}^{-1}$ for the identification of ACE and ANT, while SMX was determined by an isocratic 70/30% method. The detection wavelength was fixed at the maximum absorption of each target contaminant, i.e., 246, 254, and 242 nm for ACE, SMX, and ANT, respectively. The possible lixiviation of the organic linker of the MOFs was also monitored by using the same chromatographic method, setting the detection wavelength at 358 nm . The photodegradation of a mixture of these three pharmaceuticals was evaluated using the material with the best performance, setting the initial concentration of each contaminant at $5 \text{ mg}\cdot\text{L}^{-1}$ after adsorption under the same conditions previously described. Radical trapping experiments were carried out with p-benzoquinone (BQ) as a scavenger for superoxide radicals (O_2^-), isopropanol (IPA) for hydroxyl radicals ($\text{HO}\cdot$), silver nitrate for electrons (e^-), and potassium iodide (KI) as hole quenchers (h^+). These experiments were performed under the same conditions as the reaction ones, adding the scavenger at 1 mM initial concentration to the ACE solution after the dark adsorption equilibrium step [33]. The photocatalytic performance was also investigated in different water matrices. Specifically, tap water and synthetic water with Cl^- ($25 \text{ mg}\cdot\text{L}^{-1}$), NO_3^- ($50 \text{ mg}\cdot\text{L}^{-1}$), SO_4^{2-} ($50 \text{ mg}\cdot\text{L}^{-1}$), and HCO_3^- ($150 \text{ mg}\cdot\text{L}^{-1}$) as usual concentrations of these ions in real water samples [33]. Tests were carried out in triplicate and the average value was included. A continuous experiment was carried out in the experimental setup schematized in Fig. S3, coupling an inlet and outlet flow by two different pumps at $0.9 \text{ ml}\cdot\text{min}^{-1}$. A filter was placed in the outlet pipe to avoid photocatalyst loss. After the reaction, the photocatalyst was recovered by filtration (PTFE, Whatman $0.45 \mu\text{m}$), washed three times with 300 ml of water, and dried at $60 \text{ }^\circ\text{C}$ overnight. This used photocatalyst was characterized by X-ray diffraction and N_2 adsorption-desorption ($-196 \text{ }^\circ\text{C}$). The quantification of short-chain carboxylic acids was performed using a Supelcogel C-610H column. The mobile phase consisted of an isocratic 0.1% H_3PO_4 solution at a flow rate of $0.5 \text{ ml}\cdot\text{min}^{-1}$ ($30 \text{ }^\circ\text{C}$), fixing the excitation wavelength at 210 nm . The corresponding standard solutions were used to identify the carboxylic acids.

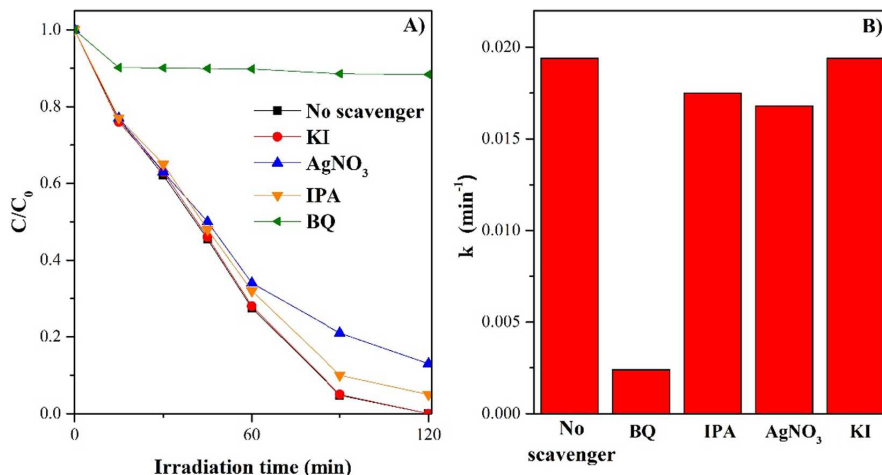


Fig. 8. A) ACE evolution in presence of different scavengers, and B) corresponding pseudo-first-order rate under solar light using 3PA-MIL-125 ($[ACE]_0 = 5 \text{ mg}\cdot\text{L}^{-1}$; $[\text{scavenger}] = 1 \text{ mM}$; Photocatalyst load = $250 \text{ mg}\cdot\text{L}^{-1}$; Intensity = $600 \text{ W}\cdot\text{m}^{-2}$).

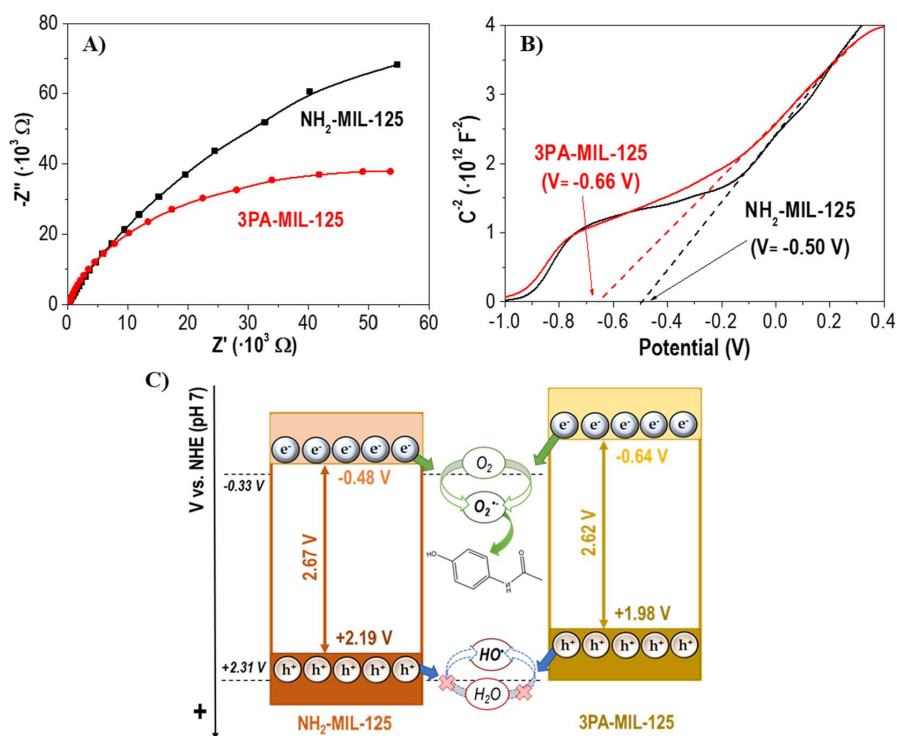


Fig. 9. (a) EIS Nyquist and (b) Mott-Schottky plots of NH_2 -MIL-125 and 3PA-MIL-125. (c) Proposed photocatalytic mechanism of ACE removal.

3. Results and discussion

3.1. Characterization

The XRD diffractograms of all materials are depicted in Fig. 1. All grafted materials have very similar diffractograms to that of NH_2 -MIL-125 [32,35], characterized by intense peaks at 6.8 , 9.5 , and 11.6° of 2θ

assigned to the (101), (200), and (211) reflections, respectively, (COD-7211159.cif [48]). Thus, it can be confirmed that NH_2 -MIL-125 maintains its structural framework after grafting with the different heterocycles. Fig. 2 shows the solid ^{13}C MAS NMR spectra of all synthesized materials. The peak at 180 ppm is characteristic of C atoms from the carboxylic group of the ligand bonded to the Ti-clusters, common to all synthesized materials (see chemical structure in Fig. S4) [49,50]. The

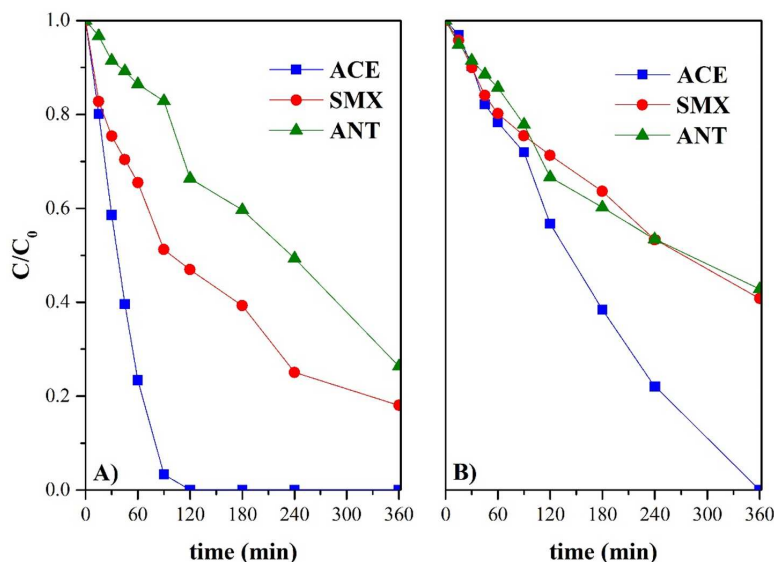


Fig. 10. Evolution of ACE, SMX and ANT upon reaction time with 3PA-MIL-125: A) individual experiments and B) mixture experiment ($[ACE]_0 = 5 \text{ mg}\cdot\text{L}^{-1}$; $[SMX]_0 = 5 \text{ mg}\cdot\text{L}^{-1}$; $[ANT]_0 = 5 \text{ mg}\cdot\text{L}^{-1}$; Photocatalyst load = $250 \text{ mg}\cdot\text{L}^{-1}$; Intensity = $600 \text{ W}\cdot\text{m}^{-2}$).

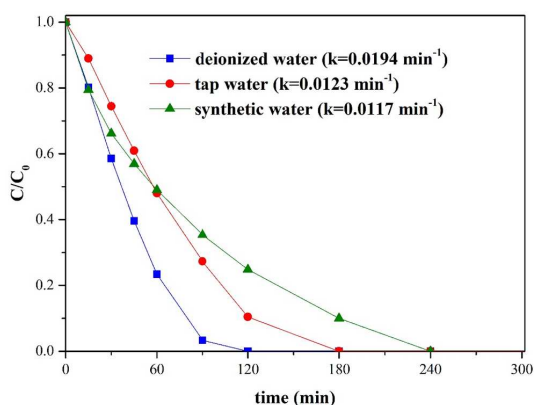


Fig. 11. Time-course of ACE concentration with 3PA-MIL-125 under solar irradiation in different water matrices.

resonance corresponding to carbon atoms bonded to the amine group of $\text{NH}_2\text{-MIL-125}$, i.e. C-NH_2 , is visible at 150 ppm [49]. This signal suffers a broadening after grafting with the heterocycles, since some C-NH_2 groups are transformed to $\text{C-N}=\text{C}$ by a Schiff reaction (Fig. S2). The resonances of the quaternary aromatic carbon atoms appear in the range 140–130 ppm [49,50], which undergo significant modification after grafting due to the incorporation of pyridinic groups. This change is even more evident in the case of 2QUI since the ligand is grafted by the inclusion of a quinolinic group (Fig. S4). The signals observed at a lower chemical shift (≈ 120 ppm) are assigned to the carbon atoms bonded to a proton, i.e. $-\text{CH}$ group [49,50]. Once again, grafting with heterocycles causes a signal broadening due to the addition of new $-\text{CH}$ groups from the pyridine ring (2PA, 3PA, and 4PA), and quinoline ring on 2QUI-MIL-125. It should be mentioned that the spectra of the 2PA-, 3PA-, and 4PA-MIL-125 are very similar because the three heterocycles used are isomers. These results confirm the successful grafting of the ATA ligand by

a post-synthetic procedure in all cases under study, resulting in the chemical structures schematized in Fig. S4.

The porous texture parameters of all synthesized materials were determined from N_2 adsorption-desorption isotherms at -196°C (Fig. 3) and are summarized in Table 1. The isotherms can be classified as type I (IUPAC classification [51]) characteristic of microporous materials. All materials show high surface area values (between 911 and $1141 \text{ m}^2\cdot\text{g}^{-1}$) due mainly to the contribution of micropores. Grafted materials showed a slightly lower amount of nitrogen adsorbed and, consequently, lower surface area values than the pristine $\text{NH}_2\text{-MIL-125}$, being this reduction more evident for 2QUI-MIL-125. This effect can be due to the larger size of the organic molecules anchored to the ligand that can partially block the porosity [38].

The optical properties of all synthesized materials were determined by UV-vis spectroscopy. Fig. 4 represents the absorbance spectra. All materials show the same absorption bands in the 200–300 nm range due to the presence of the Ti-oxo-clusters [52,53]. The band located at higher wavelengths is due to the linker absorption that shifts slightly from 390 to 400 nm after grafting with heterocycles. Thus, the grafted materials show some shift of absorption to the visible range, suggesting that the heterocycle molecules act as an antenna favouring light absorption [54]. The grafting process also showed an effect in the band gap values (Table 1), obtained from the Tauc plot (Fig. S5), whose values are slightly reduced after grafting. The morphology of all synthesized materials can be observed in the SEM images shown in Fig. 5. All samples describe thin and disk-like particles with a smooth surface similar to that of $\text{NH}_2\text{-MIL-125}$ [52,55], with a mean size of 400–650 nm. Thus, the grafting post-treatment does not affect the particle morphology.

MOFs stability in water is a very important issue to consider in the practical use of these materials for water purification [56–59]. Following our previous work dealing with the $\text{NH}_2\text{-MIL-125}$ stability [36], the amount of released ligand was determined by analyzing the filtrates after suspending the materials in an aqueous medium. The leachate percentage was determined by Eq. (4):

$$\text{Leachate}(\%) = \frac{C_{\text{ligand}}}{C_{\text{MOF}}} \times \frac{M_{\text{MOF}}}{6 \times M_{\text{ligand}}} \times 100 \quad (4)$$

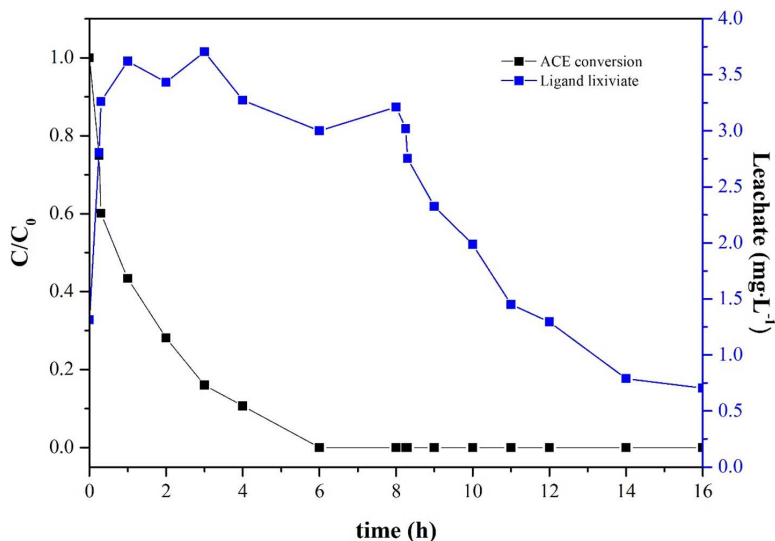


Fig. 12. Time-course of ACE and ligand leachate on stream in a continuous experiment with 3PA-MIL-125.

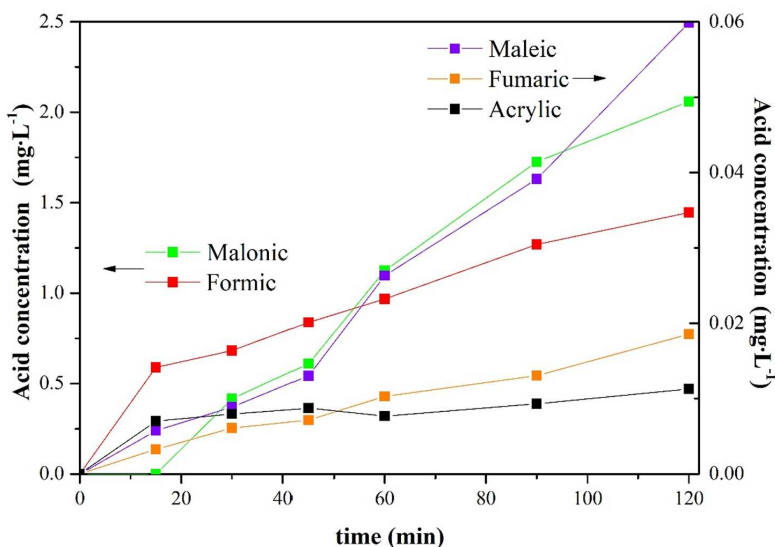


Fig. 13. Evolution of short-chain acids from the oxidation route of ACE ($[ACE]_0 = 100 \text{ mg}\cdot\text{L}^{-1}$; Photocatalyst load = $250 \text{ mg}\cdot\text{L}^{-1}$; Intensity = $600 \text{ W}\cdot\text{m}^{-2}$).

where C_{ligand} is the ligand concentration detected in water ($\text{mg}\cdot\text{L}^{-1}$), C_{MOF} is the concentration of the MOF suspended in water, M_{MOF} and M_{ligand} are the molecular weight values of the MOF and the ligand, respectively. Fig. 6 shows both the evolution in the concentration of the ligand detected and the percentage leached in relation to the total ligand content of the MOF. All grafted materials present lower ligand lixiviation than that of the bare $\text{NH}_2\text{-MIL-125}$, hence, it seems that the grafting improves the stability in water. In fact, ligand grafting is considered an approach to enhance the stability of MOFs in water, as it can lead to changes in surface hydrophobicity and steric size [60]. It should be noted that the low leaching could broaden the potential applications of these materials in aqueous media processes.

3.2. Photocatalytic performance assays

The photocatalytic performance of all materials herein synthesized was evaluated for ACE degradation under simulated solar light irradiation. Fig. 7 shows the evolution of ACE concentration with irradiation time after reaching the adsorption equilibrium in the dark. All grafted materials describe a better photocatalytic performance than the bare MOF, being 3PA-MIL-125 the most active, achieving almost total ACE degradation in 90 min. All degradation profiles were successfully fitted to a pseudo-first order kinetic reaction, being the kinetic constant values collected in Table 2. It is noteworthy that the kinetic constant of 3PA-MIL-125 is 2.4 times higher than that of the original $\text{NH}_2\text{-MIL-125}$.

These values have been compared with those already reported under the same reaction conditions with NH₂-MIL-125 MOF with other modifications, i.e., Zr-doping [32] and Pt decoration [33]. It should be noted that the grafting of the ATA ligand with heterocycles promotes the photocatalytic reaction to a greater extent than those other modifications. This is most likely due to the aforementioned action of the heterocycle as an antenna favoring the ligand-to-metal charge transfer (LMCT) mechanism characteristic of MOFs [29,30]. Regarding the differences in photoactivity observed when using the different heterocyclic carboxaldehydes for the grafting, since the abovementioned properties were very similar, i.e. structure, porous properties and band gap, even the rate of electron-hole recombination was similar (shown in Fig. S6), the difference could be attributed to the steric arrangement of the heterocycle (schematized in Fig. S4).

To learn more about the reactive species involved in the ACE breakdown mechanism using 3PA-MIL-125, Fig. 8 represents the ACE evolution upon irradiation time in trapping experiments with different scavengers. KI had a negligible effect on the reaction, indicating that holes should not contribute to the process. The inhibitory effect of IPA was very low, suggesting a minor role of HO[•] radicals, and a similar effect was observed by the addition of AgNO₃, also suggesting a low contribution of the electrons. However, the incorporation of BQ suppressed remarkably the ACE degradation, indicating that O₂^{•-} radicals are the most likely reactive species in the photocatalytic process. This main contribution of O₂^{•-} radicals is in agreement with other works dealing with NH₂-MIL-125 previously reported by our group [32–34].

Electrochemical characterization was also assessed to rationalize the likely causes of the better photocatalytic activity of 3PA-MIL-125 with respect to NH₂-MIL-125. In this sense, the resistance for surface charge transfer has been previously analyzed by EIS through the Nyquist plot [37,61]. As observed in Fig. 9a by the smaller arc radius of the semicircle, the higher performance of 3PA-MIL-125 can be attributed to a better interfacial charge transfer. Besides, Mott-Schottky plots were used to examine the bands alignment. From the intercept of the tangent lines with the potential axis in Fig. 9b and using Eq. (1), the flat band potentials (V_{fb}) of 3PA-MIL-125 and NH₂-MIL-125 were estimated to be -0.69 and -0.53 V, respectively. Following Eq. (2), the V_{CB} of both MOFs was determined to be -0.64 and -0.48 V, respectively, Eq. (3) was used to obtain the values of the V_{VB} considering the E_g of each photocatalyst (Table 1). The V_{CB} value estimated in this study for NH₂-MIL-125 lies within the range of those reported for this MOF in the literature (-0.32 < V_{CB} < -0.87 V [62,63]). Fig. 9c schematizes a tentative band structure for both MOFs. Grafting the NH₂-MIL-125 with 3PA heterocyclic carboxaldehyde resulted in a slight reduction of the band gap (Table 1) and a displacement of the position of both CB and VB. This displacement favors and supports the generation of the O₂^{•-} described above. The formation of this radical through the dissolved oxygen reduction (-0.33 V vs NHE at pH 7 [64]) is energetically favored, even more than on the NH₂-MIL-125, while the generation of HO[•] after water oxidation (+2.31 V vs NHE at pH 7 [65]) is energetically prevented due to the position of the valence band.

Since 3PA-MIL-125 proved its promising photocatalytic performance in the conversion of ACE, the degradation of other emerging contaminants, i.e. SMX and ANT, was also tested. Fig. 10A shows the evolution of SMX and ANT concentration with irradiation time in individual tests (in the presence of only one of the pollutants). The photocatalytic degradations of SMX and ANT were slower than that of ACE, revealing the more refractory character of these compounds. This issue can be associated with their chemical structure (shown in Fig. S7). Unlike ACE, which has an aromatic ring easier to open [66,67], SMX has a second heterocycle, i.e. a sulfonamide group, that makes its degradation more difficult [68]. Something similar occurs with ANT, whose pyrazolone group makes it more refractory to oxidation [17]. The removal of the three pharmaceuticals was also evaluated in a mixture (Fig. 10B). 3PA-MIL-125 was able to degrade the three of them simultaneously, although the conversion rates achieved were lower than those obtained when they

are degraded separately. This difference can be ascribed to several factors: i) the competition among ACE, SMX, and ANT molecules for the photocatalyst surface, ii) the oxidative species have a more organic matter to degrade, and/or iii) the formation of reaction by-products that can interfere in the degradation process. Remarkably, no works have been previously reported dealing with the photodegradation of these contaminants with NH₂-MIL-125 grafted with 3-pyridinecarboxaldehyde.

The effect of the water matrix was also assessed for ACE removal with 3PA-MIL-125. Fig. 11 depicted the photocatalytic degradation of ACE in deionized water, tap water, and synthetic water. Total conversion of ACE was achieved in all cases, but the reaction rate is reduced when tap water is used and even more when using synthetic water. This decrease is due to the presence of inorganic ions (such as Cl⁻, NO₃⁻, SO₄²⁻ or HCO₃⁻) capable of trapping the photogenerated charges and radicals. This behavior is in agreement with previous results dealing with other photocatalysts based on MOFs [33].

Batch systems present a huge disadvantage since it is necessary to separate the photocatalyst from the treated water [46–48]. Thus, the photocatalytic performance of 3PA-MIL-125 was evaluated in a 16 h continuous flow system (set-up schematized in Fig. S3). Fig. 12 shows the time-course of ACE and leached ligand on stream during this test. Once the steady-state was reached (about 6 h), the photocatalytic performance remained constant, achieving a total conversion of ACE, and thus demonstrating the stability of 3PA-MIL-125. Ligand leaching was also monitored, and a low concentration of leachate was observed (<4 mg·L⁻¹), which continuously decreases from 8 h of reaction and practically disappeared after 16 h on stream. After reaction, the photocatalyst was recovered and characterized to analyze its structural stability. XRD and N₂ adsorption-desorption results were very similar to those described above for the neat 3PA-MIL-125 (Fig. S8). Only a slight reduction of the surface area was detected, which may be associated with the deposition of by-products, which can slightly block the porous network. Thus, 3PA-MIL-125 appears as an active and stable photocatalyst to remove emerging contaminants from water under solar irradiation in a continuous flow system.

The acetaminophen degradation pathway has been previously reported by our research group [15,17,33]. We proposed several reaction routes involving ring-opening, coupling, hydroxylation, acetamide loss, and oxidation processes. Short-chain acids were detected as succinic, malonic, formic, and acetic acids. In the current study, up to five different carboxylic acids, namely maleic, malonic, formic, fumaric, and acrylic acids, were identified from the photocatalytic degradation of ACE by 3PA-MIL-125, as detailed in Fig. 13. Malonic and formic acids are continuously formed along with the experiment, while malonic acid appeared after 30 min under solar light irradiation. Similar behaviour was shown for maleic, fumaric, and acrylic acids, although their concentrations were lower. It seems that the grafted MOF allows the transformation of ACE giving rise to compounds of lower complexity.

4. Conclusions

The photocatalytic performance of NH₂-MIL-125 was improved by grafting the amine ligand with heterocycles that act as an antenna for visible light absorption. 3PA-MIL-125 exhibited the best performance in acetaminophen degradation due to its high specific surface area and microporosity, slightly lower band gap, improved light absorption, better interfacial charge transference, and reduced electron-hole recombination. Experiments with scavengers lead to the conclusion that superoxide radicals play a major role in the photodegradation of acetaminophen, although electrons and hydroxyl radicals are also partly involved. The inorganic ions commonly found in water reduced the acetaminophen photodegradation. 3PA-MIL-125 was able to remove other emerging contaminants, i.e. sulfamethoxazole and antipyrine, and even a mixture of them, although the reaction rate depends on the nature of the target compound. In a continuous flow regime, total

degradation of acetaminophen was reached after 6 h and then maintained for the rest of the 16 h experiment. The current results revealed the stability and activity of the grafted-NH₂-MIL-125 with 3-pyridine-carboxaldehyde photocatalyst for the remediation of pharmaceuticals in water on stream under solar irradiation.

Declaration of Competing Interest

The authors declare that they have no known competing financial interests or personal relationships that could have appeared to influence the work reported in this paper.

Acknowledgement

This research was funded by State Research Agency (PID2019-106186RB-I00/AEI/10.13039/501100011033). V. Muelas-Ramos thanks to MCIU for BES-2017-082613 grant. M. Peñas-Garzón is indebted to Spanish MECD (FPU16/00576 grant). The authors thank the Research Support Services of the University of Extremadura (SAIUEX) for SEM images.

Appendix A. Supplementary material

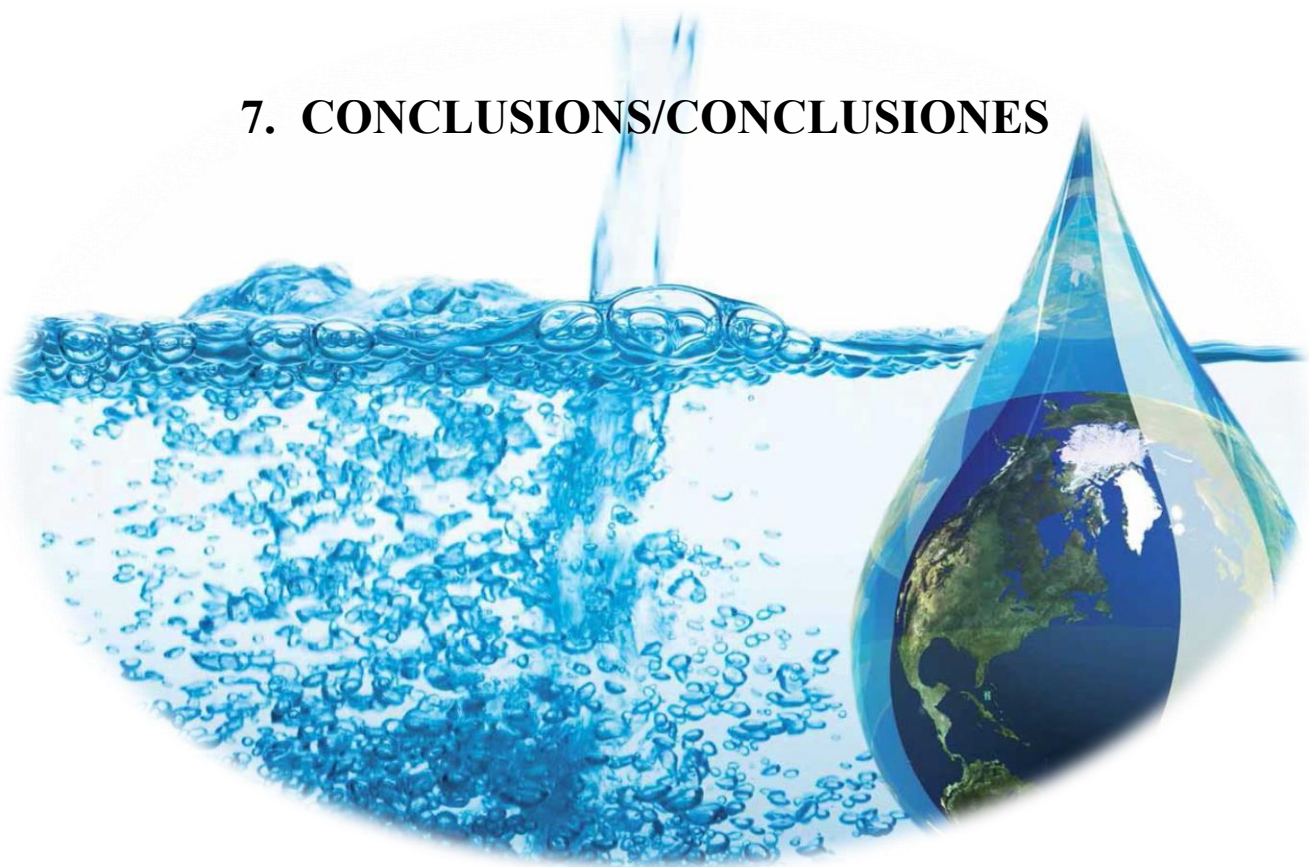
Supplementary data to this article can be found online at <https://doi.org/10.1016/j.seppur.2022.121442>.

References

- Rivera-Utrilla, M. Sánchez-Polo, M.Á. Ferro-García, G. Prados-Joya, R. Ocampo-Pérez, Pharmaceuticals as emerging contaminants and their removal from water. A review, *Chemosphere* 93 (2013) 1268–1287, <https://doi.org/10.1016/j.chemosphere.2013.07.059>.
- C. Regmi, E. Maya-Flores, S.W. Lee, V. Rodríguez-González, Cerium-doped β-Ni(OH)₂ hexagonal nanosheets: an effective photocatalyst for the degradation of the emerging water pollutant, naproxen, *Nanotechnology*. 29 (2018) 375603, <https://doi.org/10.1088/1361-6528/AACE14>.
- M.Q. Cai, R. Wang, L. Feng, L.Q. Zhang, Determination of selected pharmaceuticals in tap water and drinking water treatment plant by high-performance liquid chromatography-triple quadrupole mass spectrometer in Beijing, China, *Environ. Sci. Pollut. Res.* 22 (2014) 1854–1867, <https://doi.org/10.1007/s11356-014-3473-8>.
- M. Papageorgiou, C. Kosma, D. Lambropoulou, Seasonal occurrence, removal, mass loading and environmental risk assessment of 55 pharmaceuticals and personal care products in a municipal wastewater treatment plant in Central Greece, *Sci. Total Environ.* 543 (2016) 547–569, <https://doi.org/10.1016/j.scitotenv.2015.11.047>.
- T. Deblonde, C. Cossu-Leguille, P. Hartemann, Emerging pollutants in wastewater: A review of the literature, *Int. J. Hyg. Environ. Health.* 214 (2011) 442–448, <https://doi.org/10.1016/j.IJHEH.2011.08.002>.
- K. Hider-Mlynarz, P. Cavalié, P. Maison, Trends in analgesic consumption in France over the last 10 years and comparison of patterns across Europe, *Br. J. Clin. Pharmacol.* 84 (2018) 1324–1334, <https://doi.org/10.1111/bcp.13564>.
- E. Yoon, A. Babar, M. Choudhary, M. Kutner, N. Pyrsopoulos, Acetaminophen-induced hepatotoxicity: a comprehensive update, *J. Clin. Transl. Hepatol.* 4 (2016) 131, <https://doi.org/10.14218/JCTH.2015.00052>.
- R. Taylor, J.V. Pergolizzi, Acetaminophen (paracetamol): Properties, clinical uses, and adverse effects, in: *Pharmacol. Res. Saf. Test. Regul.*, 2012; pp. 1–24.
- S. Fekadu, E. Alemayehu, R. Dewil, B. Van der Bruggen, Pharmaceuticals in freshwater aquatic environments: A comparison of the African and European challenge, *Sci. Total Environ.* 654 (2019) 324–337, <https://doi.org/10.1016/j.scitotenv.2018.11.072>.
- M.R. Boleda, M.T. Galceran, F. Ventura, Validation and uncertainty estimation of a multiresidue method for pharmaceuticals in surface and treated waters by liquid chromatography-tandem mass spectrometry, *J. Chromatogr. A.* 1286 (2013) 146–158, <https://doi.org/10.1016/j.chroma.2013.02.077>.
- K.O. K'oreje, L. Vergeynst, D. Ombaka, P. De Wispelaere, M. Okoth, H. Van Langenhove, K. Demeestere, Occurrence patterns of pharmaceutical residues in wastewater, surface water and groundwater of Nairobi and Kisumu city, Kenya, *Chemosphere*. 149 (2016) 238–244, <https://doi.org/10.1016/j.chemosphere.2016.01.095>.
- J. Wang, S. Wang, Activation of persulfate (PS) and peroxymonosulfate (PMS) and application for the degradation of emerging contaminants, *Chem. Eng. J.* 334 (2018) 1502–1517, <https://doi.org/10.1016/j.cej.2017.11.059>.
- Y. Deng, R. Zhao, Advanced oxidation processes (AOPs) in wastewater treatment, *Curr. Pollut. Reports.* 1 (2015) 167–176, <https://doi.org/10.1007/s40726-015-0015-z>.
- A.R. Ribeiro, O.C. Nunes, M.F.R. Pereira, A.M.T. Silva, An overview on the advanced oxidation processes applied for the treatment of water pollutants defined in the recently launched Directive 2013/39/EU, *Environ. Int.* 75 (2015) 33–51, <https://doi.org/10.1016/j.envint.2014.10.027>.
- Y.L. Wang, S. Zhang, Y.F. Zhao, J. Bedia, J.J. Rodriguez, C. Belver, UiO-66-based metal organic frameworks for the photodegradation of acetaminophen under simulated solar irradiation, *J. Environ. Chem. Eng.* 9 (2021) 106087, <https://doi.org/10.1016/j.jece.2021.106087>.
- A. Gómez-Avilés, M. Peñas-Garzón, J. Bedia, J.J. Rodriguez, C. Belver, C-modified TiO₂ using lignin as carbon precursor for the solar photocatalytic degradation of acetaminophen, *Chem. Eng. J.* 358 (2019) 1574–1582, <https://doi.org/10.1016/j.cej.2018.10.154>.
- M. Peñas-Garzón, A. Gómez-Avilés, C. Belver, J.J. Rodriguez, J. Bedia, Degradation pathways of emerging contaminants using TiO₂-activated carbon heterostructures in aqueous solution under simulated solar light, *Chem. Eng. J.* 392 (2020) 124867, <https://doi.org/10.1016/j.cej.2020.124867>.
- M. Akkari, P. Aranda, C. Belver, J. Bedia, A. Ben Haj Amara, E. Ruiz-Hitzky, ZnO/sepilolite heterostructured materials for solar photocatalytic degradation of pharmaceuticals in wastewater, *Appl. Clay Sci.* 156 (2018) 104–109, <https://doi.org/10.1016/j.clay.2018.01.021>.
- H. Ji, W. Liu, F. Sun, T. Huang, L. Chen, Y. Liu, J. Qi, C. Xie, D. Zhao, Experimental evidences and theoretical calculations on phenanthrene degradation in a solar-light-driven photocatalysis system using silica aerogel supported TiO₂ nanoparticles: Insights into reactive sites and energy evolution, *Chem. Eng. J.* 419 (2021), 129605, <https://doi.org/10.1016/j.cej.2021.129605>.
- M. Miranda-García, S. Suárez, B. Sánchez, J.M. Coronado, S. Malato, M. I. Maldonado, Photocatalytic degradation of emerging contaminants in municipal wastewater treatment plant effluents using immobilized TiO₂ in a solar pilot plant, *Appl. Catal. B Environ.* 103 (2011) 294–301, <https://doi.org/10.1016/j.apcatb.2011.01.030>.
- A. Petala, D. Spyrou, Z. Frontists, D. Mantzavinos, D.I. Kondarides, Immobilized Ag₃PO₄ photocatalyst for micro-pollutants removal in a continuous flow annular photoreactor, *Catal. Today.* 328 (2019) 223–229, <https://doi.org/10.1016/j.cattod.2018.10.062>.
- P. Ding, H. Ji, P. Li, Q. Liu, Y. Wu, M. Guo, Z. Zhou, S. Gao, W. Xu, W. Liu, Q. Wang, S. Chen, Visible-light degradation of antibiotics catalyzed by titania/zirconia/graphitic carbon nitride ternary nanocomposites: a combined experimental and theoretical study, *Appl. Catal. B Environ.* 300 (2022), 120633, <https://doi.org/10.1016/j.apcatb.2021.120633>.
- X. Li, J. Xie, C. Jiang, J. Yu, P. Zhang, Review on design and evaluation of environmental photocatalysts, *Front. Environ. Sci. Eng.* 12 (2018) 1–32, <https://doi.org/10.1007/s11783-018-1076-1>.
- J. Wen, J. Xie, X. Chen, X. Li, A review on g-C₃N₄-based photocatalysts, *Appl. Surf. Sci.* 391 (2017) 72–123, <https://doi.org/10.1016/j.apsusc.2016.07.030>.
- C. Belver, J. Bedia, A. Gómez-Avilés, M. Peñas-Garzón, J.J. Rodriguez, Semiconductor Photocatalysis for Water Purification, in: *Nanoscale Mater. Water Purif.*, Elsevier, 2018; pp. 581–651, doi:10.1016/B978-0-12-813926-4.00028-8.
- G. Zahn, H.A. Schulze, J. Lippke, S. König, U. Sazama, M. Fröba, P. Behrens, A water-born Zr-based porous coordination polymer: Modulated synthesis of Zr-fumarate MOF, *Microporous Mesoporous Mater.* 203 (2015) 186–194, <https://doi.org/10.1016/j.micromeso.2014.10.034>.
- J. Bedia, V. Muelas-Ramos, M. Peñas-Garzón, A. Gómez-Avilés, J. Rodríguez, C. Belver, A review on the synthesis and characterization of metal organic frameworks for photocatalytic water purification, *Catalysts.* 9 (2019) 52, <https://doi.org/10.3390/catal9010052>.
- L. Zeng, X. Guo, C. He, C. Duan, Metal-Organic Frameworks: Versatile materials for heterogeneous photocatalysis, *ACS Catal.* 6 (2016) 7935–7947, <https://doi.org/10.1021/acscatal.6b02228>.
- M. Alvaro, E. Carbonell, B. Ferrer, F. LlabrésXamena, H. Garcia, Semiconductor behavior of a metal-organic framework (MOF), *Chem. A Eur. J.* 13 (18) (2007) 5106–5112, <https://doi.org/10.1002/chem.200601003>.
- J. Qiu, X. Zhang, Y. Feng, X. Zhang, H. Wang, J. Yao, Modified metal-organic frameworks as photocatalysts, *Appl. Catal. B Environ.* 231 (2018) 317–342, <https://doi.org/10.1016/j.apcatb.2018.03.039>.
- Z.U. Zango, K. Jumri, N.S. Sambudi, A. Ramli, N.H.H.A. Bakar, B. Saad, M.N. H. Rozaini, H.A. Isiyaka, A.H. Jagaba, O. Aldaghri, A. Suleiman, A critical review on metal-organic frameworks and their composites as advanced materials for adsorption and photocatalytic degradation of emerging organic pollutants from wastewater, *Polymers (Basel).* 12 (2020) 2648, <https://doi.org/10.3390/POLY12112648>.
- A. Gómez-Avilés, M. Peñas-Garzón, J. Bedia, D.D. Dionysiou, J.J. Rodríguez, C. Belver, Mixed Ti-Zr metal-organic-frameworks for the photodegradation of acetaminophen under solar irradiation, *Appl. Catal. B Environ.* 253 (2019) 253–262, <https://doi.org/10.1016/j.apcatb.2019.04.040>.
- V. Muelas-Ramos, C. Belver, J.J. Rodriguez, J. Bedia, Synthesis of noble metal-decorated NH₂-MIL-125 titanium MOF for the photocatalytic degradation of acetaminophen under solar irradiation, *Sep. Purif. Technol.* 272 (2021), 118896, <https://doi.org/10.1016/j.seppur.2021.118896>.
- V. Muelas-Ramos, M.J. Sampaio, C.G. Silva, J. Bedia, J.J. Rodriguez, J.L. Faria, C. Belver, Degradation of diclofenac in water under LED irradiation using combined g-C₃N₄/NH₂-MIL-125 photocatalysts, *J. Hazard. Mater.* 416 (2021), 126199, <https://doi.org/10.1016/j.jhazmat.2021.126199>.
- S.R. Zhu, P.F. Liu, M.K. Wu, W.N. Zhao, G.C. Li, K. Tao, F.Y. Yi, L. Han, Enhanced photocatalytic performance of BiOBr/NH₂-MIL-125(Ti) composite for dye degradation under visible light, *Dalt. Trans.* 45 (2016) 17521–17529, <https://doi.org/10.1039/C6DT02912D>.

- [36] A. Gómez-Avilés, V. Muelas-Ramos, J. Bedia, J.J. Rodríguez, C. Belver, Thermal Post-Treatments to Enhance the Water Stability of NH₂-MIL-125(Ti), Catalysts. 10 (2020) 603, <https://doi.org/10.3390/catal10060603>.
- [37] R.R. Solís, A. Gómez-Avilés, C. Belver, J.J. Rodríguez, J. Bedia, Microwave-assisted synthesis of NH₂-MIL-125(Ti) for the solar photocatalytic degradation of aqueous emerging pollutants in batch and continuous tests, J. Environ. Chem. Eng. 9 (5) (2021) 106230, <https://doi.org/10.1016/j.jece.2021.106230>.
- [38] Z. Wu, X. Huang, H. Zheng, P. Wang, G. Hai, W. Dong, G. Wang, Aromatic heterocycle-grafted NH₂-MIL-125(Ti) via conjugated linker with enhanced photocatalytic activity for selective oxidation of alcohols under visible light, Appl. Catal. B Environ. 224 (2018) 479–487, <https://doi.org/10.1016/j.apcatb.2017.10.034>.
- [39] H.M.A. Hassan, M.A. Betiha, S.K. Mohamed, E.A. El-Sharkawy, E.A. Ahmed, Salen-Zr(IV) complex grafted into amine-tagged MIL-101(Cr) as a robust multifunctional catalyst for biodiesel production and organic transformation reactions, Appl. Surf. Sci. 412 (2017) 394–404, <https://doi.org/10.1016/j.apsusc.2017.03.247>.
- [40] O.A.M. Ali, S.M. El-Medani, D.A. Ahmed, D.A. Nassar, Synthesis, characterization, fluorescence and catalytic activity of some new complexes of unsymmetrical Schiff base of 2-pyridinecarboxaldehyde with 2,6-diaminopyridine, Spectrochim. Acta - Part A Mol. Biomol. Spectrosc. 144 (2015) 99–106, <https://doi.org/10.1016/j.saa.2015.02.078>.
- [41] S.Y. Bunting, D.J. Lapworth, E.J. Crane, J. Grima-Olmedo, A. Koroša, A. Kuczyńska, N. Mali, L. Rosenqvist, M.E. van Vliet, A. Togola, B. Lopez, Emerging organic compounds in European groundwater, Environ. Pollut. 269 (2021) 115945, <https://doi.org/10.1016/j.envpol.2020.115945>.
- [42] K.S. Walton, R.Q. Snurr, Applicability of the BET method for determining surface areas of microporous metal-organic frameworks, J. Am. Chem. Soc. 129 (2007) 8552–8556, <https://doi.org/10.1021/ja071174k>.
- [43] A.J. Howarth, A.W. Peters, N.A. Vermeulen, T.C. Wang, J.T. Hupp, O.K. Farha, Best practices for the synthesis, activation, and characterization of metal-organic frameworks, Chem. Mater. 29 (2017) 26–39, <https://doi.org/10.1021/acs.chemmater.6b02626>.
- [44] J. Tauc, Absorption edge and internal electric fields in amorphous semiconductors, Mater. Res. Bull. 5 (1970) 721–729, [https://doi.org/10.1016/0025-5408\(70\)90112-1](https://doi.org/10.1016/0025-5408(70)90112-1).
- [45] S. Kampouri, C.P. Ireland, B. Valizadeh, E. Oveisi, P.A. Schouwink, M. Mensi, K. C. Stylianou, Mixed-Phase MOF-Derived titanium dioxide for photocatalytic hydrogen evolution: the impact of the templated morphology, ACS Appl. Energy Mater. 1 (2018) 6541–6548, <https://doi.org/10.1021/acs.aem.8b01445>.
- [46] C. Baumanis, D.W. Bahnemann, TiO₂ thin film electrodes: Correlation between photocatalytic activity and electrochemical properties, J. Phys. Chem. C. 112 (2008) 19097–19101, <https://doi.org/10.1021/jp807655a>.
- [47] T. Giannakopoulou, I. Papailias, N. Todorova, N. Boukos, Y. Liu, J. Yu, C. Trapalis, Tailoring the energy band gap and edges' potentials of g-C₃N₄/TiO₂ composite photocatalysts for NO_x removal, Chem. Eng. J. 310 (2017) 571–580, <https://doi.org/10.1016/j.cej.2015.12.102>.
- [48] A.P. Smalley, D.G. Reid, J.C. Tan, G.O. Lloyd, Alternative synthetic methodology for amide formation in the post-synthetic modification of Ti-MIL125-NH₂, CrystEngComm. 15 (2013) 9368, <https://doi.org/10.1039/c3ce41332b>.
- [49] A. Rossini, A.J. Zagdoun, A. Lelli, M. Canivet, J. Aguado, S. Ouari, O. Tordo, P. Rosay, M. Maas, W.E. Copéret, C. Farrusseng, D. Emsley, L. Lesage, Dynamic nuclear polarization enhanced solid-state NMR spectroscopy of functionalized metal-organic frameworks, Angew. Chem. Int. Ed. Engl. 51 (2012) 123–127, <https://doi.org/10.1002/anie.201106030>.
- [50] S. Devautour-Vinot, G. Maurin, C. Serre, P. Horcajada, D. Paula da Cunha, V. Guillerm, E. de Souza Costa, F. Taulelle, C. Martineau, Structure and Dynamics of the Functionalized MOF Type UiO-66(Zr): NMR and Dielectric Relaxation Spectroscopies Coupled with DFT Calculations, Chem. Mater. 24 (11) (2012) 2168–2177, <https://doi.org/10.1021/CM300863C>.
- [51] K. Sing, Reporting physisorption data for gas/solid systems, Pure Appl. Chem. 54 (1982) 2201–2218, <https://doi.org/10.1351/pac198254112201>.
- [52] Y.H. Fan, S.W. Zhang, S. Bin Qin, X.S. Li, S.H. Qi, An enhanced adsorption of organic dyes onto NH₂ functionalization titanium-based metal-organic frameworks and the mechanism investigation, Microporous Mesoporous Mater. 263 (2018) 120–127, <https://doi.org/10.1016/j.micromeso.2017.12.016>.
- [53] H. Huang, X.S. Wang, D. Philo, F. Ichihara, H. Song, Y. Li, D. Li, T. Qiu, S. Wang, J. Ye, Toward visible-light-assisted photocatalytic nitrogen fixation: A titanium metal organic framework with functionalized ligands, Appl. Catal. B Environ. 267 (2020), 118686, <https://doi.org/10.1016/j.apcatb.2020.118686>.
- [54] A. Dhakshinamoorthy, Z. Li, H. Garcia, Catalysis and photocatalysis by metal organic frameworks, Chem. Soc. Rev. 47 (2018) 8134–8172, <https://doi.org/10.1039/c8cs00256h>.
- [55] H. Wang, X. Yuan, Y. Wu, G. Zeng, X. Chen, L. Leng, Z. Wu, L. Jiang, H. Li, Facile synthesis of amino-functionalized titanium metal-organic frameworks and their superior visible-light photocatalytic activity for Cr(VI) reduction, J. Hazard. Mater. 286 (2015) 187–194, <https://doi.org/10.1016/j.jhazmat.2014.11.039>.
- [56] G. Wen, Z.G. Guo, Facile modification of NH₂-MIL-125(Ti) to enhance water stability for efficient adsorptive removal of crystal violet from aqueous solution, Colloids Surfaces A Physicochem. Eng. Asp. 541 (2018) 58–67, <https://doi.org/10.1016/j.colsurfa.2018.01.011>.
- [57] X. Qian, B. Yadian, R. Wu, Y. Long, K. Zhou, B. Zhu, Y. Huang, Structure stability of metal-organic framework MIL-53 (Al) in aqueous solutions, Int. J. Hydrogen Energy. 38 (2013) 16710–16715, <https://doi.org/10.1016/j.ijhydene.2013.07.054>.
- [58] K.A. Cychosz, A.J. Matzger, Water stability of microporous coordination polymers and the adsorption of pharmaceuticals from water, Langmuir. 26 (2010) 17198–17202, <https://doi.org/10.1021/la103234u>.
- [59] K.S. Park, Z. Ni, A.P. Côté, J.Y. Choi, R. Huang, F.J. Uribe-Romo, H.K. Chae, M. O'Keeffe, O.M. Yaghi, Exceptional chemical and thermal stability of zeolitic imidazolate frameworks, Proc. Natl. Acad. Sci. U. S. A. 103 (2006) 10186–10191, <https://doi.org/10.1073/pnas.0602439103>.
- [60] B. Liu, K. Vikrant, K.-H. Kim, Y. Kumar, S.K. Kailasa, Critical role of water stability in metal-organic frameworks and advanced modification strategies for the extension of their applicability, Environ. Sci. Nano 7 (2020) 1319–1347, <https://doi.org/10.1039/C9EN01321K>.
- [61] H. Diarmand-Khalilabad, A. Habibi-Yangjeh, D. Seifzadeh, S. Asadzadeh-Khaneghah, E. Vesali-Kermani, g-C₃N₄ nanosheets decorated with carbon dots and CdS nanoparticles: Novel nanocomposites with excellent nitrogen photofixation ability under simulated solar irradiation, Ceram. Int. 45 (2019) 2542–2555, <https://doi.org/10.1016/j.ceramint.2018.10.185>.
- [62] S. Luo, C. Zhang, X. Liu, Y. Li, L. Tang, M. Fu, S. Wang, J. Wu, M. Xu, X. Wang, Y. He, Protonated NH₂-MIL-125 via HCl vapor to introduce the moiety with charge and ample hydrogen as a novel bifunctional photocatalyst: Enhanced photocatalytic H₂ production and NO purification, Chem. Eng. J. 432 (2022), 134244, <https://doi.org/10.1016/j.cej.2021.134244>.
- [63] Y. Du, L. Zhao, H. Chen, Z. Huang, X. He, W. Fang, W. Li, F. Zhang, G. Wang, Synthesis and enhanced visible light-induced photocatalytic activity of a hierarchical porous biomorphic N/Zn-TiO₂@NH₂-MIL-125 photocatalyst, J. Mater. Sci. Mater. Electron. 29 (2018) 20356–20366, <https://doi.org/10.1007/s10854-018-0171-1>.
- [64] X. Li, J. Yu, M. Jaroniec, Hierarchical photocatalysts, Chem. Soc. Rev. 45 (2016) 2603–2636, <https://doi.org/10.1039/c5cs00838g>.
- [65] W.H. Koppenol, D.M. Stanbury, P.L. Bounds, Electrode potentials of partially reduced oxygen species, from dioxygen to water, Free Radic. Biol. Med. 49 (2010) 317–322, <https://doi.org/10.1016/j.freeradbiomed.2010.04.011>.
- [66] R. Andreozzi, V. Caprio, R. Marotta, D. Vogna, Paracetamol oxidation from aqueous solutions by means of ozonation and H₂O₂/UV system, Water Res. 37 (2003) 993–1004, [https://doi.org/10.1016/S0043-1354\(02\)00460-8](https://doi.org/10.1016/S0043-1354(02)00460-8).
- [67] A.M. Abdel-Wahab, A.S. Al-Shirbini, O. Mohamed, O. Nasr, Photocatalytic degradation of paracetamol over magnetic flower-like TiO₂/Fe₂O₃ core-shell nanostructures, J. Photochem. Photobiol. A Chem. 347 (2017) 186–198, <https://doi.org/10.1016/j.jphotochem.2017.07.030>.
- [68] Y. Song, J. Tian, S. Gao, P. Shao, J. Qi, F. Cui, Photodegradation of sulfonamides by g-C₃N₄ under visible light irradiation: Effectiveness, mechanism and pathways, Appl. Catal. B Environ. 210 (2017) 88–96, <https://doi.org/10.1016/j.apcatb.2017.03.059>.

7. CONCLUSIONS/CONCLUSIONES



Conclusions

The removal of emerging contaminants in wastewater is a key issue in the re-use of water resources. Their elimination is limited in wastewater-treatment plants (WWTPs) by conventional methods. Thus, advanced oxidation processes (AOPs) have received major attention. In this context, photocatalysis using MOFs materials represents a powerful option for the degradation of emerging contaminants in water. After the results have been exposed, the following general conclusions can be sum up.

- The stability of NH₂-MIL-125 was improved with a thermal treatment under air atmosphere at 250 °C for 48 h. This procedure maintained the crystalline structure and the porous texture of the original MOF, while significantly reducing the linker lixiviation in water. These findings have significant implications regarding the potential use of MOFs in water-related applications.
- MOF/g-C₃N₄ materials to be tested as photocatalysts were successfully synthesized by a straightforward method, using different proportions of both semiconductors. The structure of both components was observed in all photocatalysts prepared. The porous texture was the result of the highly microporous character of MOF and the non-porous one of g-C₃N₄, although with some lower surface area and pore volume than the expected from the relative amounts of each component, most probably due to the partial blockage of the MOF porosity by g-C₃N₄. The morphology of the hybrids also showed the main features of both components, including plate-like particles from the MOF and fiber-like ones from g-C₃N₄. All MOF/g-C₃N₄ samples showed very similar band gap values, closer to the pristine MOF, suggesting that the optical properties are basically determined by this component. These hybrids have demonstrated

photocatalytic activity under LED irradiation, superior to that of the individual components, suggesting the occurrence of some synergistic effect. The MOF presence reduces the electron-hole recombination rate of the g-C₃N₄. Regarding the photocatalytic performance, 50%C₃N₄ yielded the best result, with complete conversion of diclofenac in 2 h and a pseudo-first-order rate constant value of 0.0282 min⁻¹, almost three-fold the obtained with the pristine NH₂-MIL-125 and more than four-fold the one with g-C₃N₄. Radical trapping experiments proved that superoxide radicals, holes and ·OH radicals are involved in the reaction, although superoxide radicals and holes played the most significant role. From the reaction species identified, several routes have been proposed for diclofenac degradation pathway, involving, hydroxylation, coupling and oxidation reactions. Short-chain carboxylic acids, such as formic and oxalic acid, were identified as final by-products, as well as chloride and nitrite.

- Noble metal (Ag, Pd and Pt) nanoparticles were successfully deposited on NH₂-MIL-125 by wet impregnation followed by a reduction treatment. The characteristic structure of the MOF was maintained in all M/NH₂-MIL-125 materials as well as the microporous texture with high surface area. Metal nanoparticles appeared decorating the surface of the MOF, with average sizes from 1.8 to 3.5 nm depending on the metal. Those nanoparticles were a mixture of M²⁺/M⁰ species responsible of light absorption in the visible region. The Pt/NH₂-MIL-125 photocatalyst yielded the best results in the degradation of the target pollutant (ACE), due to enhanced visible light absorption and slower recombination of the photogenerated charges. O₂^{·-} radicals governed the ACE photodegradation process. The photocatalytic performance of

Pt/NH₂-MIL-125 was not significantly affected by the presence of Cl⁻, NO₃⁻ and SO₄⁻ ions, while HCO₃⁻ caused a detrimental effect due to O₂⁻ trapping. The stability and reusability of Pt/NH₂-MIL-125 was tested upon three successive cycles, where its original crystalline structure and porous texture were maintained. Some small decrease of activity was observed as inferred from the reduction of ACE conversion (somewhat above 10% after the three cycles).

- The photocatalytic performance of NH₂-MIL-125 was improved by grafting the amino-ligand with heterocycles that act as an antenna for visible light absorption. 3PA-MIL-125 exhibited the best performance in the acetaminophen degradation due to its high specific surface area and microporosity, slightly lower band gap, improved light absorption, better interfacial charge transference and reduced electron-hole recombination. Experiments with scavengers lead to the conclusion that O₂⁻ radicals play the mayor role in the photodegradation of ACE, although electrons and hydroxyl radicals are also partly involved. The inorganic ions commonly found in water (Cl⁻, NO₃⁻, SO₄⁻ y HCO₃⁻) reduced the acetaminophen photodegradation. 3PA-MIL-125 was able to remove other emerging contaminants, i.e. sulfamethoxazole and antipyrine, and even a mixture of them, although the reaction rate depends on the nature of the target compound. In continuous flow regime, total degradation of acetaminophen was reached after 6 h and then maintained for the rest 16 h experiment. The current results revealed the high stability and activity of the grafted-NH₂-MIL-125 with 3-pyridinecarboxaldehyde photocatalyst for the remediation of pharmaceuticals in water on stream under solar irradiation.

Conclusiones

La eliminación de contaminantes emergentes en las aguas residuales es un tema clave en la reutilización de los recursos hídricos. Su eliminación está limitada en las estaciones depuradoras de aguas residuales (EDAR) mediante los métodos convencionales. Por lo tanto, se han estudiado nuevos métodos de eliminación, como los procesos avanzados de oxidación (PAOs). En este contexto, el desarrollo de la fotocatalisis solar empleando materiales tipo MOFs surge como una interesante opción para la degradación de contaminantes emergentes en el agua. Una vez expuestos los resultados, se pueden establecer las siguientes conclusiones generales.

- La estabilidad del $\text{NH}_2\text{-MIL-125}$ fue mejorada realizando un tratamiento térmico en atmósfera de aire a $250\text{ }^\circ\text{C}$ durante 48 h. Este procedimiento mantuvo la estructura cristalina y la textura porosa del MOF original, al tiempo que redujo significativamente la lixiviación del ligando en agua. Estos resultados tienen implicaciones significativas con respecto al potencial uso del $\text{NH}_2\text{-MIL-125}$ en aplicaciones que requieran medio acuoso.
- Los materiales $\text{MOF/g-C}_3\text{N}_4$ se sintetizaron con éxito mediante un método sencillo, variando las proporciones de ambos semiconductores. La estructura de ambos componentes se mantuvo sin modificaciones en todos los fotocatalizadores preparados. Las propiedades superficiales de los híbridos preparados fueron mezcla del carácter altamente microporoso del MOF y del no poroso del $\text{g-C}_3\text{N}_4$, aunque con un área superficial y un volumen de poros más bajos de lo esperado respecto a las cantidades relativas de cada componente, probablemente debido a un bloqueo parcial de los poros por el $\text{g-C}_3\text{N}_4$. Los híbridos preparados también mostraron la

morfología mezcla de ambos componentes, observándose partículas en forma de disco del MOF junto a láminas del g-C₃N₄. Todos los materiales MOF/g-C₃N₄ presentaban valores de band gap muy similares, más cercanos al MOF original, lo que sugiere que las propiedades ópticas están determinadas básicamente por este componente. Estos materiales híbridos presentaron una actividad fotocatalítica bajo radiación LED superior a la de los componentes individuales, lo que sugiere la aparición de un efecto sinérgico. La presencia del MOF redujo la tasa de recombinación de los pares hueco-electrón del g-C₃N₄. En cuanto a la actividad fotocatalítica, el fotocatalizador con 50% C₃N₄ logró el mejor resultado, alcanzando conversión completa del diclofenaco en 2 h, con un valor de la constante de velocidad de pseudo-primer orden de 0.0282 min⁻¹, casi el triple del obtenido con el NH₂-MIL-125 y más de cuatro veces el del g-C₃N₄. Los experimentos realizados con atrapadores de radicales demostraron que los radicales O₂⁻, los huecos y los radicales [•]OH estaban involucrados en la reacción, aunque los radicales O₂⁻ y los huecos jugaron un papel más importante. La identificación de diversos subproductos de reacción permitió proponer varias rutas para la degradación del diclofenaco, que involucraban reacciones de hidroxilación, acoplamiento y oxidación. Los ácidos carboxílicos de cadena corta, como el ácido fórmico y el oxálico, se identificaron como productos finales, así como el cloruro y el nitrito.

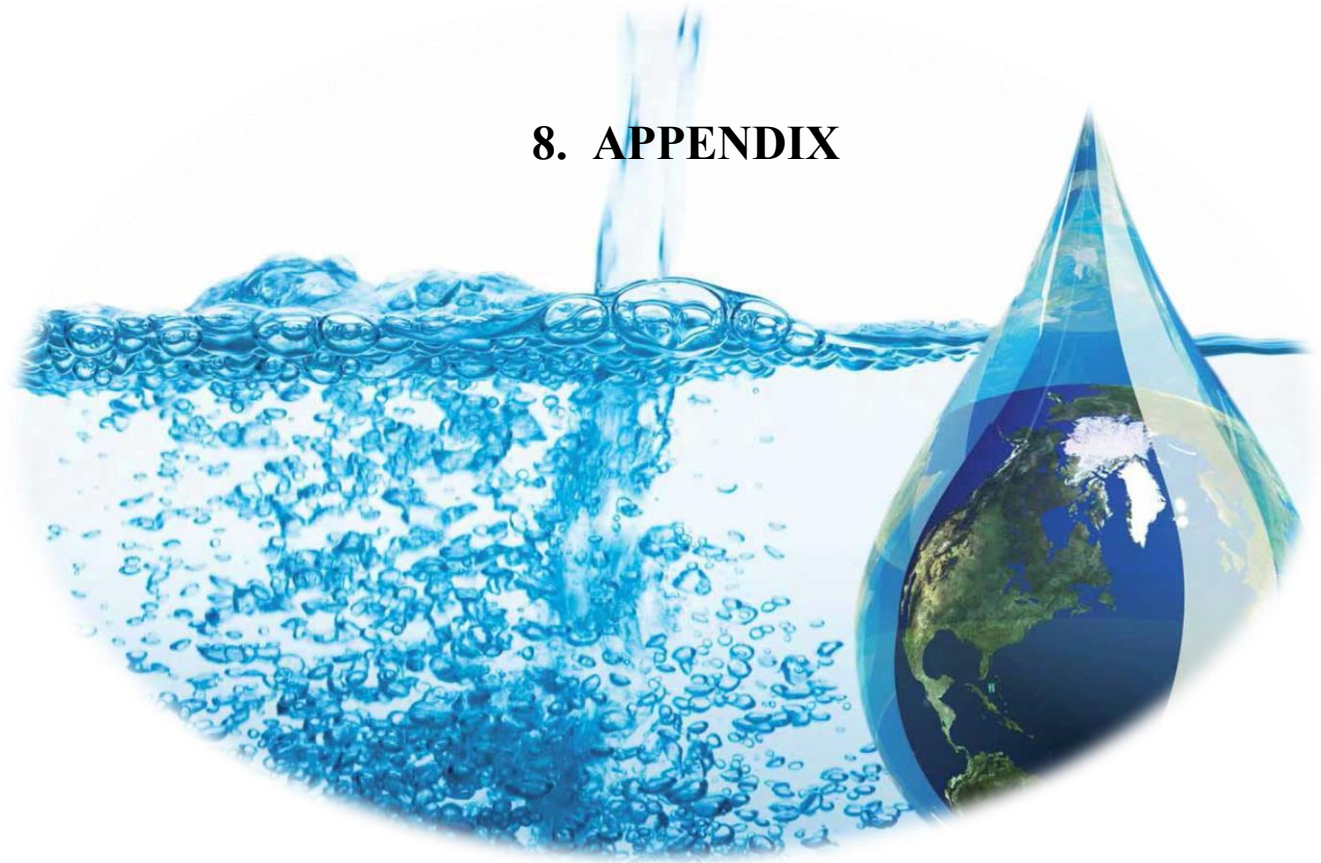
- Se depositaron con éxito nanopartículas de metales nobles (Ag, Pd y Pt) sobre el NH₂-MIL-125 mediante impregnación húmeda seguida de un tratamiento de reducción. La estructura característica del MOF se mantuvo en todos los M/NH₂-MIL-125 sintetizados, así como su textura microporosa y alta área superficial. Las nanopartículas metálicas se presentaban decorando la superficie del MOF, con

tamaños promedio de 1,8 a 3,5 nm dependiendo del metal. Esas nanopartículas resultaron ser una mezcla de especies M^{2+}/M^0 responsables de la absorción de luz en la región visible. El Pt/NH₂-MIL-125 logró los mejores resultados en la degradación del acetaminofeno (ACE), al presentar una mayor absorción de luz visible y una recombinación más lenta de las cargas fotogeneradas. Los radicales $O_2^{\cdot-}$ fueron los principales responsables del proceso de fotodegradación del ACE. La actividad fotocatalítica del Pt/NH₂-MIL-125 no se vio afectada por la presencia de iones Cl^- , NO_3^- y SO_4^- en el medio de reacción, mientras que el HCO_3^- causó un efecto perjudicial al capturar los radicales $O_2^{\cdot-}$. La estabilidad y reutilización del Pt/NH₂-MIL-125 fueron evaluadas tras tres ciclos de reacción. La estructura cristalina y porosidad del MOF se mantuvo sin modificaciones y tan sólo se observó cierta disminución de la actividad fotocatalítica, cerca del 10%, tras los tres ciclos.

- La actividad fotocatalítica del NH₂-MIL-125 se mejoró al modificar el ligando acoplando heterociclos que actúan como antena para la absorción de luz visible. El 3PA-MIL-125 fue el fotocatalizador más activo en la degradación de ACE, debido a su elevada área superficial y microporosidad, su ligeramente menor band gap, su mayor absorción de luz, mejor transferencia de carga interfacial y reducción de la recombinación de los pares hueco-electrón. Los experimentos con atrapadores de radicales identificaron a los radicales $O_2^{\cdot-}$ como principales responsables de la fotodegradación de ACE, aunque los electrones y los radicales $\cdot OH$ también estaban parcialmente involucrados. La presencia de iones inorgánicos (Cl^- , NO_3^- , SO_4^- y HCO_3^-) que se encuentran comúnmente en el agua redujeron la actividad fotocatalítica. El 3PA-MIL-125 mantuvo su actividad fotocatalítica en la degradación de otros contaminantes emergentes,

como el sulfametoxazol y la antipirina, e incluso una mezcla de ellos, aunque la velocidad de reacción dependía de la naturaleza del compuesto. El 3PA-MIL-125 también operaba de forma efectiva en régimen de flujo continuo, alcanzando la degradación total de ACE tras 6 h y manteniendo la actividad durante las 16 h restantes del experimento. Los resultados revelaron la alta estabilidad y actividad del fotocatalizador preparado mediante la modificación del NH₂-MIL-125 con 3-piridincarboxaldehído para la degradación de diversos productos farmacéuticos en agua empleando radiación solar.

8. APPENDIX



8.1. Appendix Chapter 1: Thermal post-treatments to enhance water stability of NH₂-MIL-125(Ti)

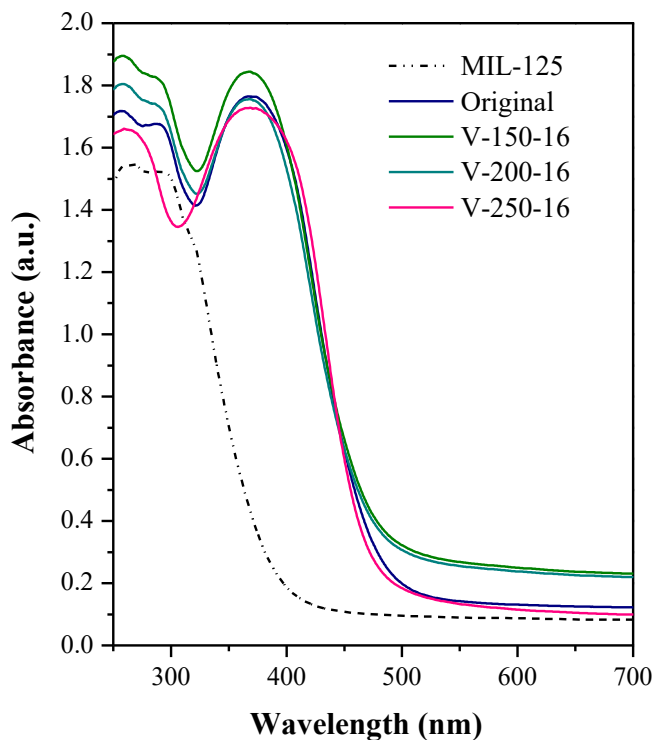


Figure S1. UV-vis diffuse absorbance spectra of NH₂-MIL-125(Ti) treated under vacuum at different temperatures for 16 h. Original NH₂-MIL-125(Ti) and MIL-125(Ti) spectra are included as reference.

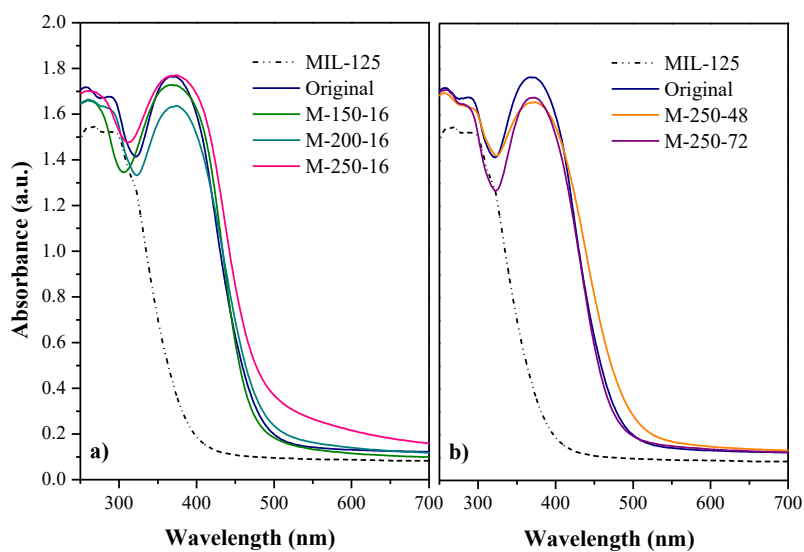


Figure S2. UV-vis diffuse absorbance spectra of $\text{NH}_2\text{-MIL-125(Ti)}$ heated in air at different temperatures for 16 h (a) and at 250 °C for 48 and 72 h (b). Original $\text{NH}_2\text{-MIL-125(Ti)}$ and MIL-125(Ti) spectra are included as reference.

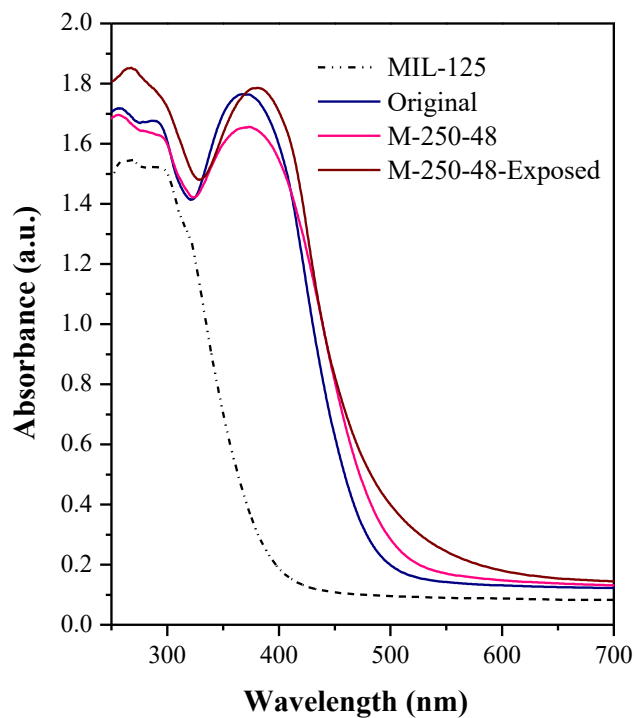


Figure S3. UV-vis diffuse absorbance spectra of M-250-48 before and after contact with water for 24 h. Original NH₂-MIL-125(Ti) and MIL-125(Ti) spectra are included as reference.

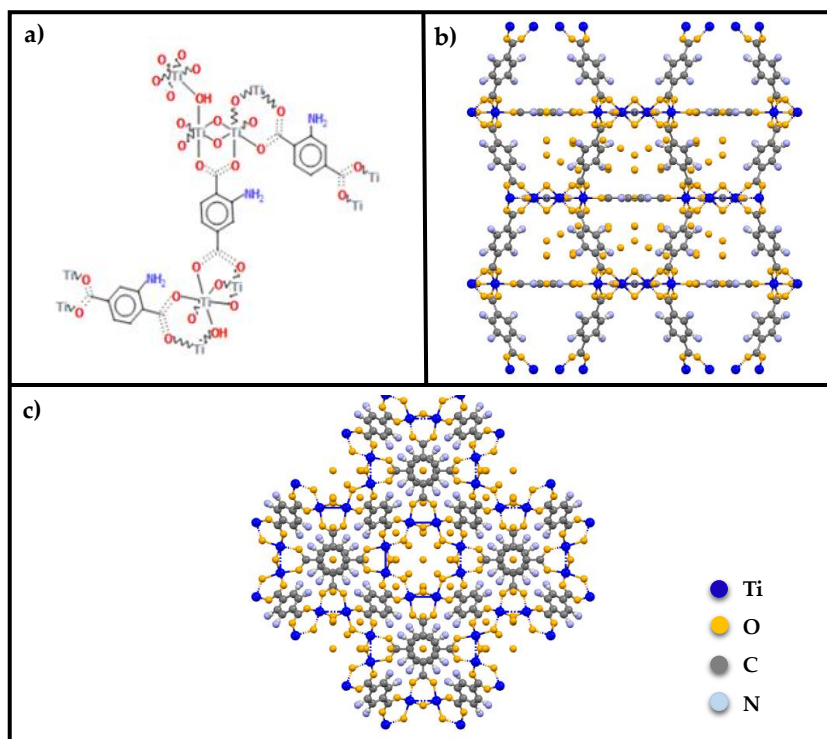


Figure S4. (a) Chemical structure of Ti-oxo clusters linked to NH₂-BDC ligands, from the Cambridge Structural Database (CSD). Chemical structure of NH₂-MIL-125(Ti) viewed from a-axis (b) and c-axis (c), from cif data of Crystallography Open Database.

8.2. Appendix Chapter 5: Synthesis of noble metal-decorated NH₂-MIL-125 titanium MOF for the photocatalytic degradation of acetaminophen under solar irradiation

Table S1. Accurate mass (m/z) values for ACE degradation by-products.

| Name | Retention time (min) | Experimental m/z [M + H] ⁺ | Proposed formula [M + H] ⁺ | Calculated m/z [M + H] ⁺ | Mass error (mDa) | Ring Double Bond (RDB) |
|---------------|----------------------|---------------------------------------|---|-------------------------------------|------------------|------------------------|
| Acetaminophen | 4.6 | 152.0702 | C ₈ H ₁₀ NO ₂ | 152.0706 | 0.4 | 5 |
| ACE-1 | 1.9 | 74.0958 | C ₄ H ₁₂ N | 74.0964 | 0.6 | 0 |
| ACE-2 | 8.0 | 301.1181 | C ₁₆ H ₁₇ N ₂ O ₄ | 301.1183 | 0.2 | 10 |
| ACE-4 | 4.1 | 349.1030 | C ₁₆ H ₁₇ N ₂ O ₇ | 349.1030 | 0.1 | 10 |

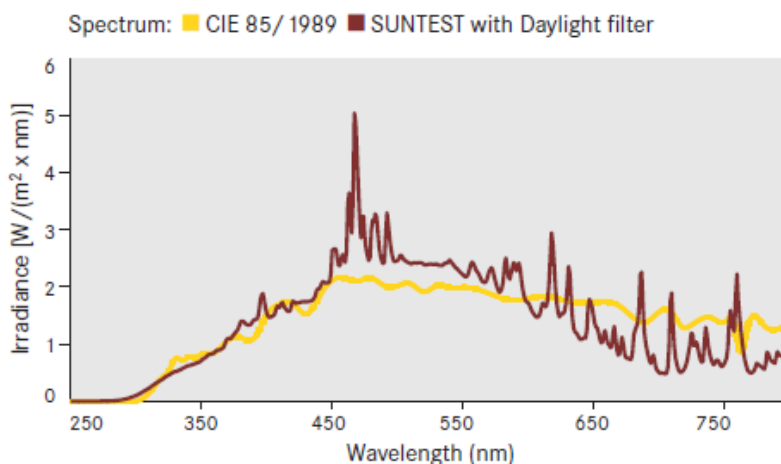


Figure S1. Emission spectrum of the solar lamp (<https://www.atlants.com/products/standard-instruments/xenon-arc-weathering-test/suntest/xls>).

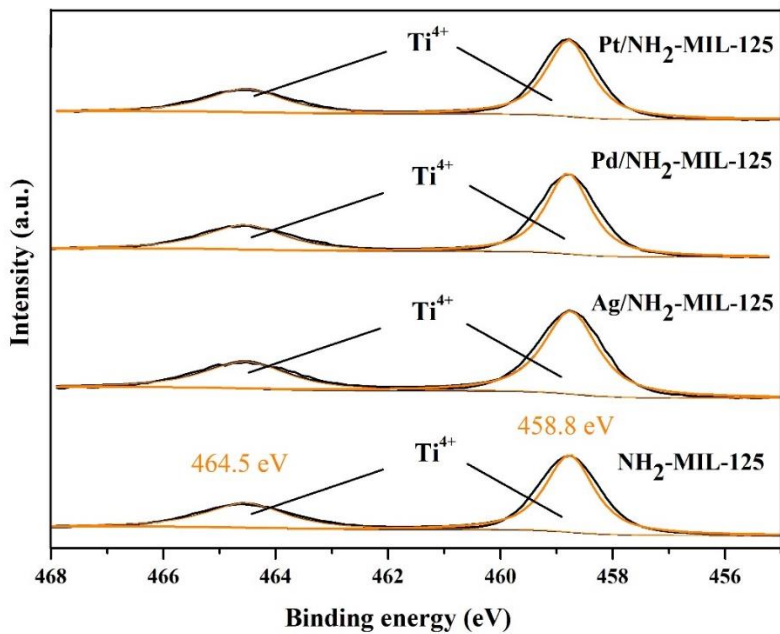


Figure S2. Ti2p deconvoluted XPS spectra.

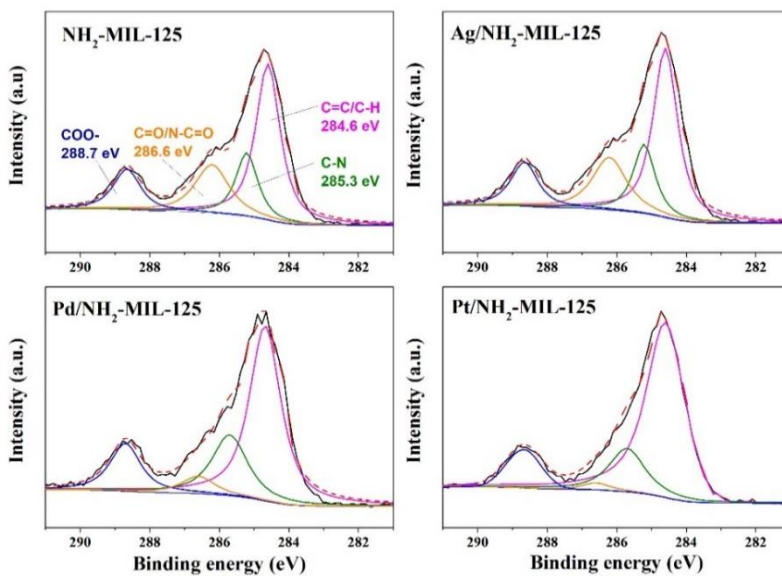


Figure S3. C1s deconvoluted XPS spectra.

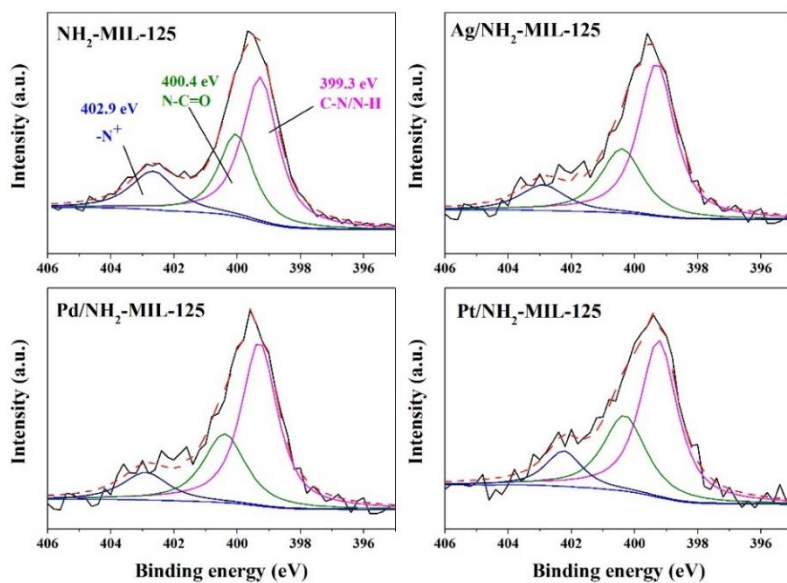


Figure S4. N1s deconvoluted XPS spectra.

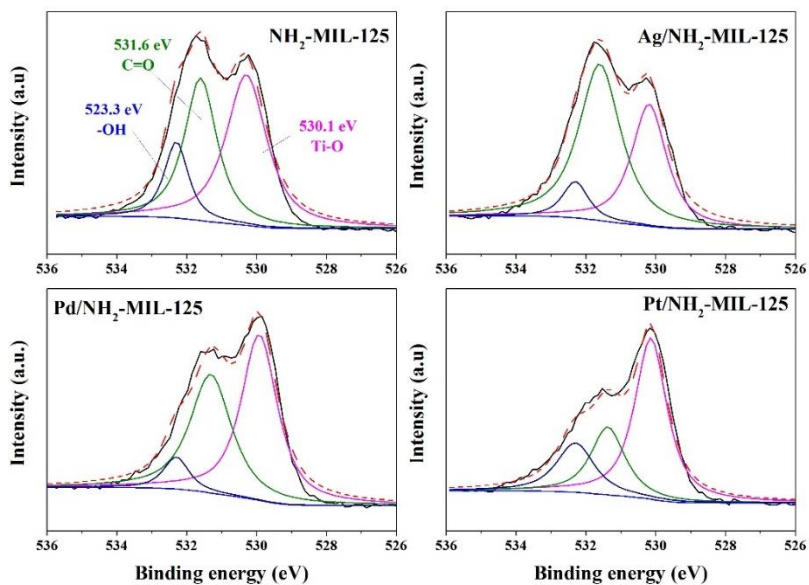


Figure S5. O1s deconvoluted XPS spectra.

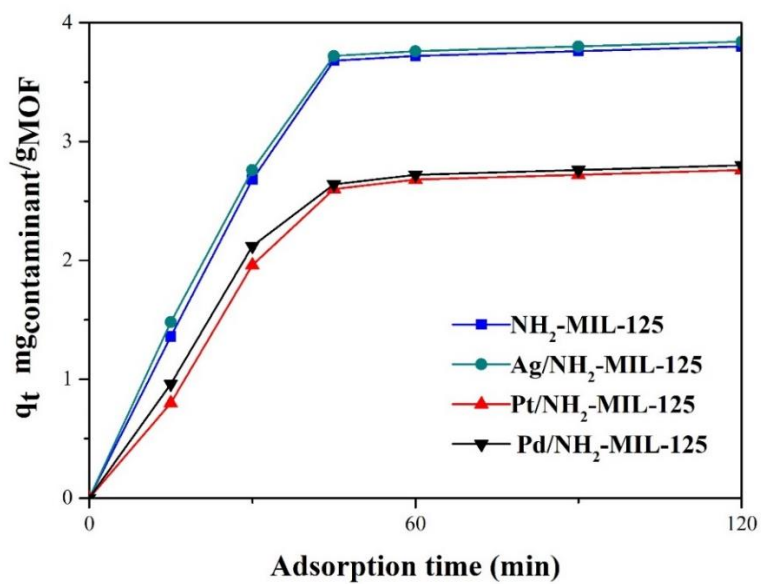


Figure S6. ACE adsorption tests in dark.

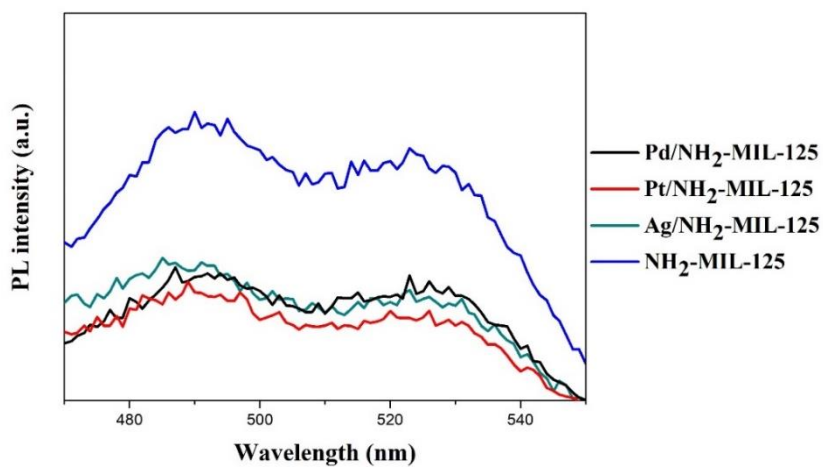


Figure S7. Photoluminescence spectra.

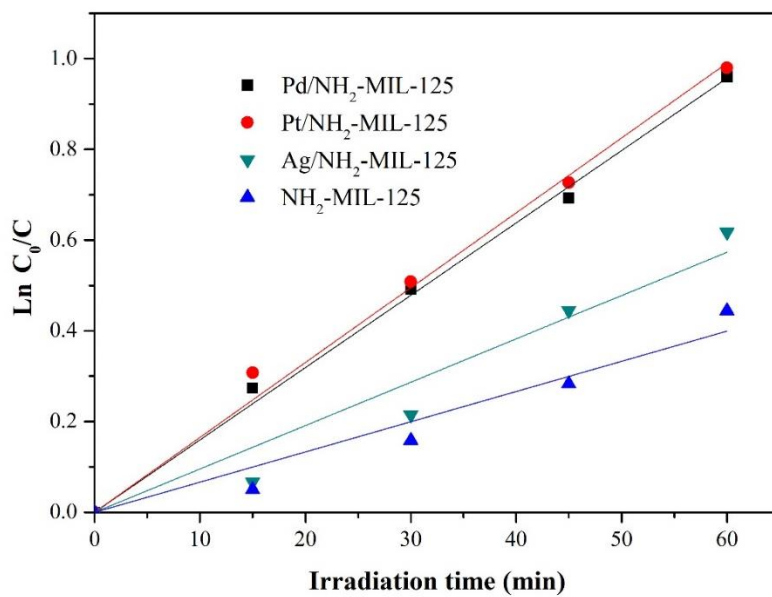


Figure S8. Fitting of ACE degradation to pseudo-first-order rate equation ($[ACE]_0 = 5 \text{ mg}\cdot\text{L}^{-1}$; Photocatalyst load = $250 \text{ mg}\cdot\text{L}^{-1}$; Illuminance = 107.14 klx).

8.3. Appendix Chapter 6: Solar photocatalytic degradation of emerging contaminants using NH₂-MIL-125 grafted by heterocycles

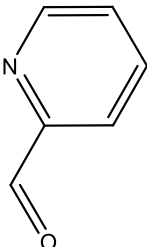
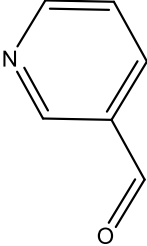
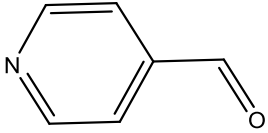
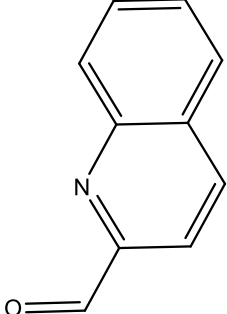
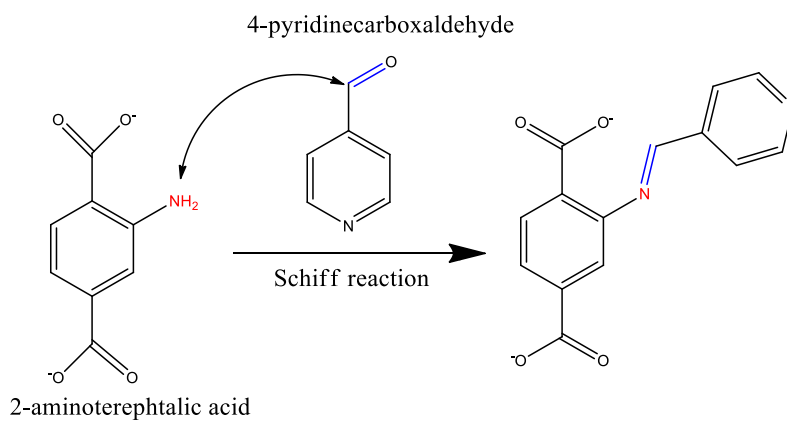
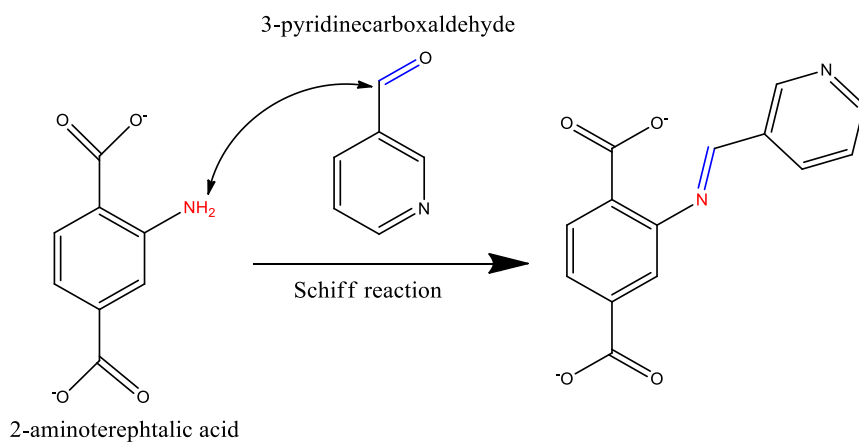
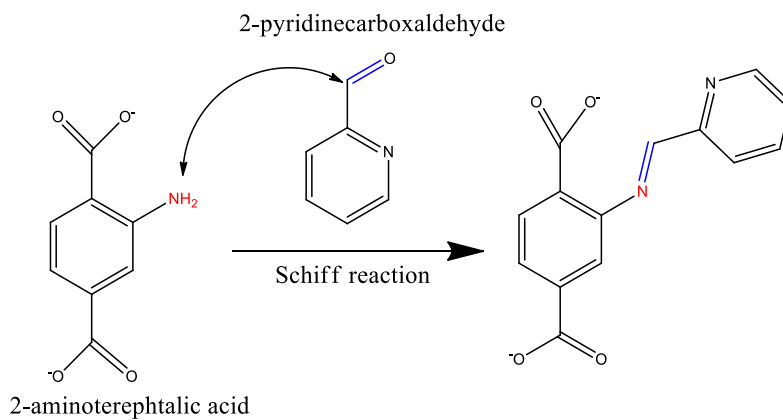
| | |
|---|--|
| 2- pyridinecarboxaldehyde (2PA) |  |
| 3- pyridinecarboxaldehyde (3PA) |  |
| 4- pyridinecarboxaldehyde (4PA) |  |
| 2- quinolinecarboxaldehyde (2QUI) |  |

Figure S1. Chemical formulas of the heterocyclic carboxaldehydes used for the grafting process.



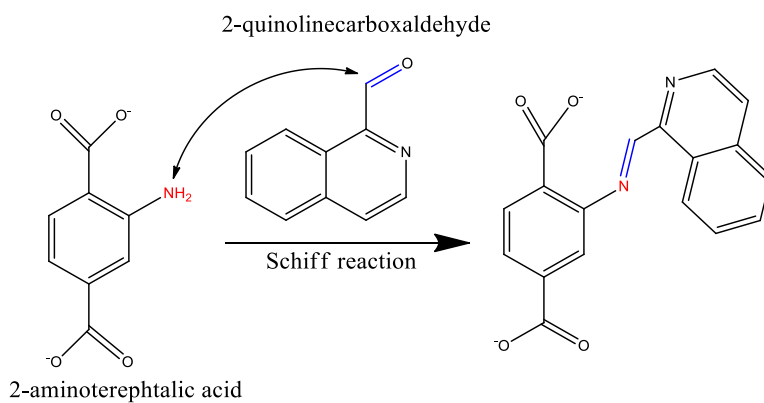


Figure S2. Post-grafting of NH₂-MIL-125 with aromatic heterocycles.

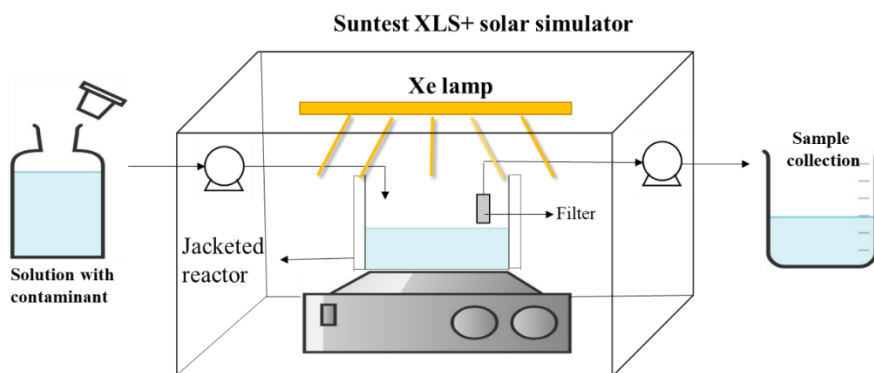


Figure S3. Scheme of the photocatalytic reactor under continuous flow.

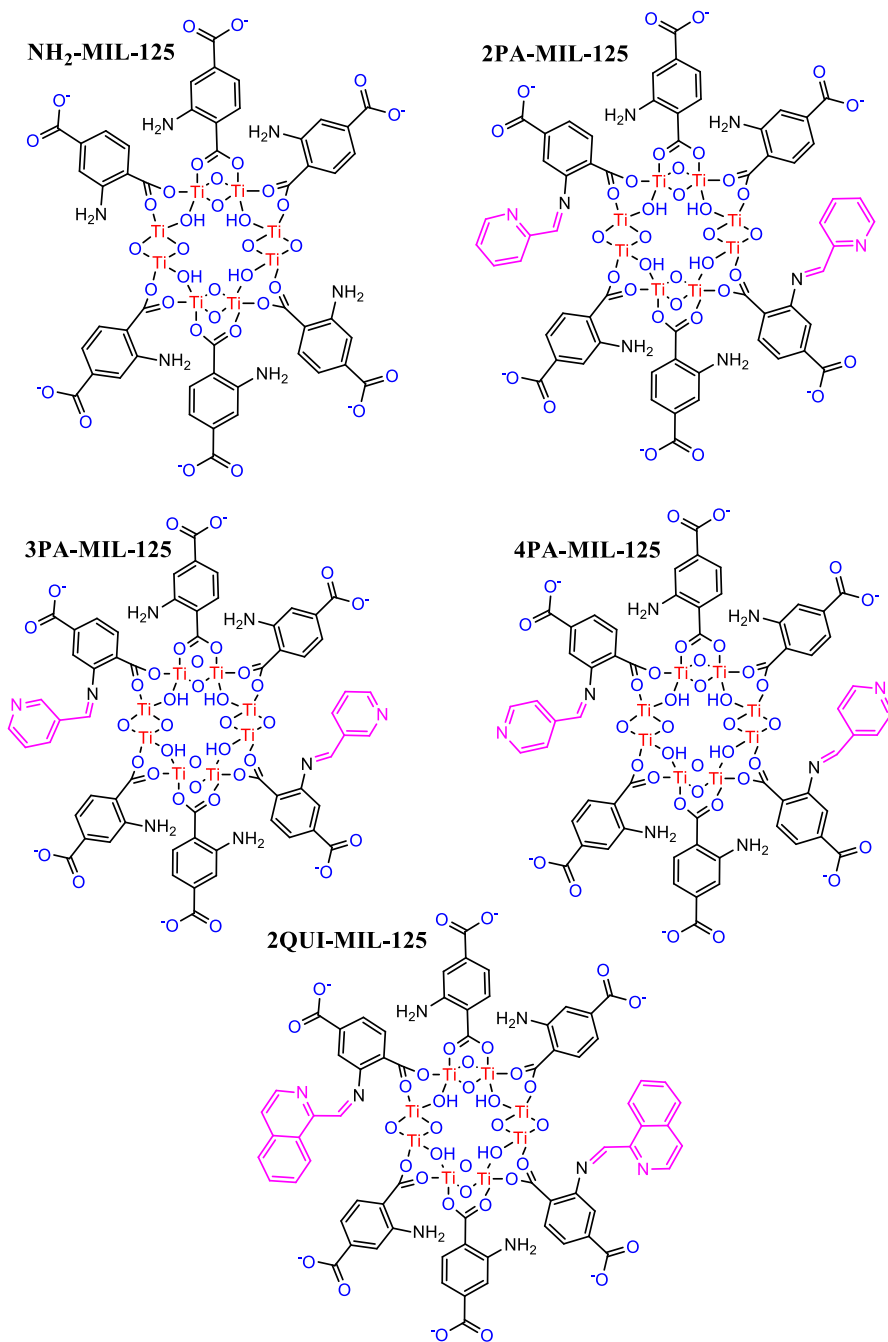


Figure S4. Chemical structures of the bare NH₂-MIL-125 and the grafted materials.

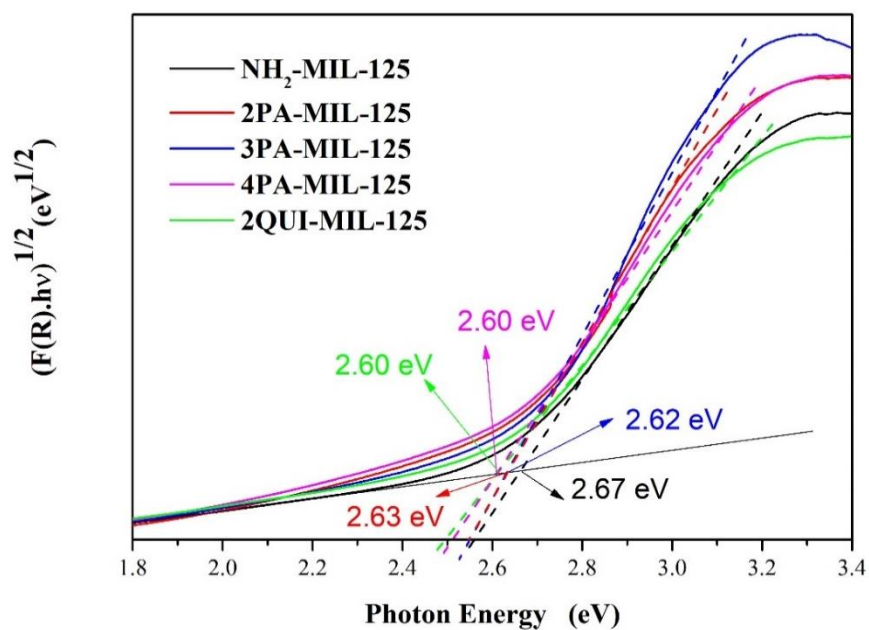


Figure S5. Tauc plots of the bare $\text{NH}_2\text{-MIL-125}$ and the grafted materials.

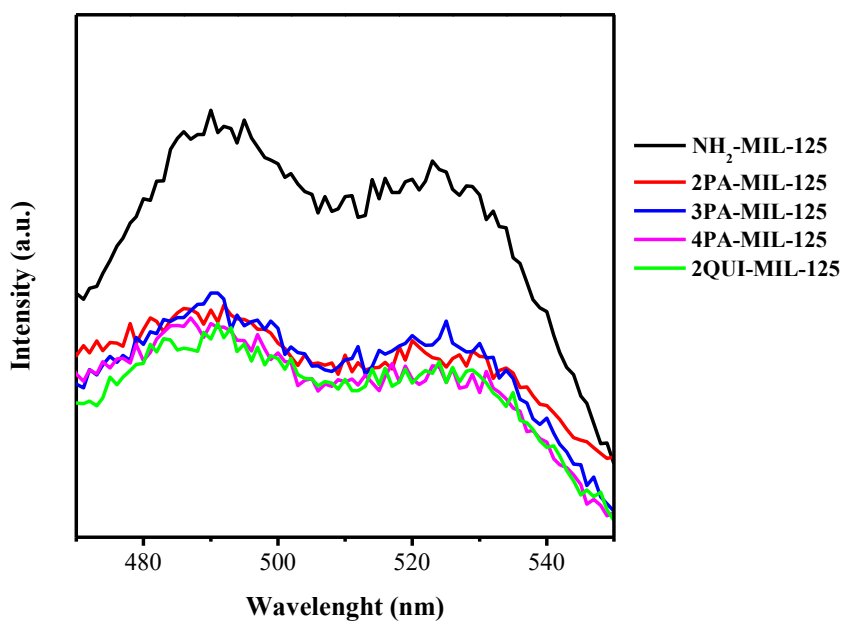


Figure S6. Photoluminescence spectra (PL).

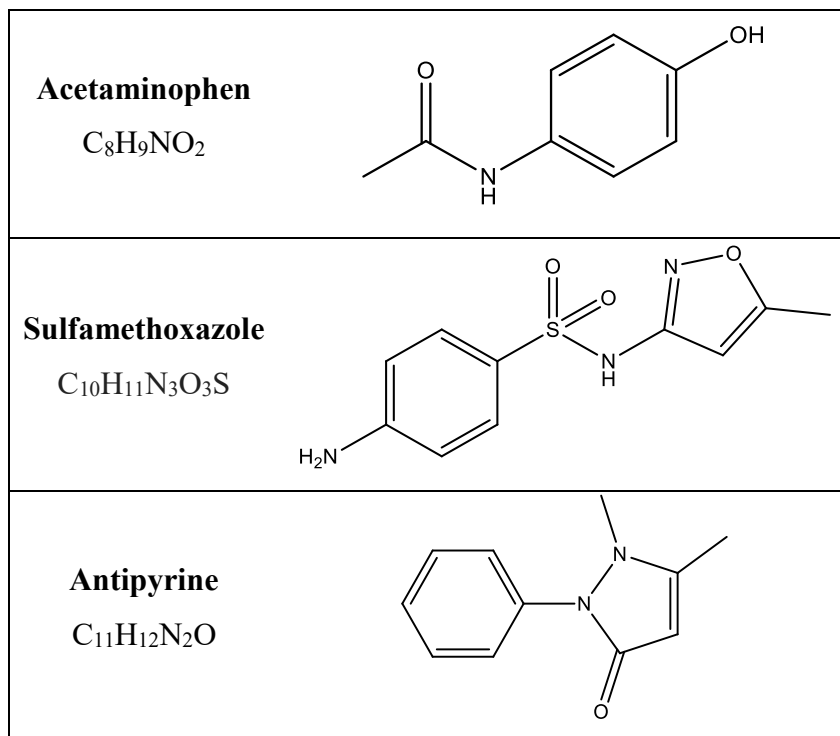


Figure S7. Chemical structure of acetaminophen, sulfamethoxazole and antipyrine.

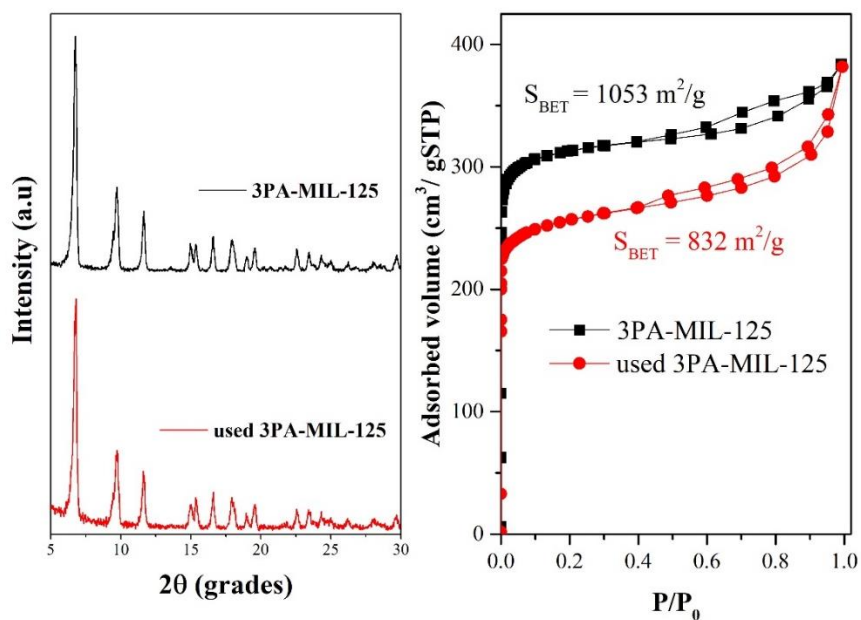


Figure S8. XRD, nitrogen adsorption isotherms at $-196 \text{ }^\circ\text{C}$ and BET surface areas of 3PA-MIL-125 before and after reaction.

Other publications

Book chapters

- J. Bedia, **V. Muelas-Ramos**, M. Peñas-Garzón, A. Gómez-Avilés, J.J. Rodríguez, C. Belver. Metal-organic frameworks for water purification. In: Bonelli, B., Freyria, F.S., Rossetti, I., Sethi, R. (Eds.) Nanomaterials for the detection and removal of wastewater pollutants. Elsevier, (2020) 241-284. ISBN: 978-0-12-818489-9
- C. Belver, J. Bedia, M. Peñas-Garzón, **V. Muelas-Ramos**, A. Gómez-Avilés, J.J. Rodríguez. Structured photocatalysts for the removal of emerging contaminants under visible or solar light. In: Sacco, O., Vaiano, V. (Eds.) Visible light active structured photocatalysts for the removal of emerging contaminants: Science and Engineering. Elsevier, (2019) 41-98. ISBN: 978-0-12-818334-2

Research papers

- J. Bedia, **V. Muelas-Ramos**, M. Peñas-Garzón, A. Gómez-Avilés, J.J. Rodríguez, C. Belver. A review on the synthesis and characterization of metal organic frameworks for photocatalytic water purification. *Catalysts* 9, (2019) 52-95. doi:10.3390/catal9010052